

AFCRL-70-0531

AD 715301

FULL WAVE SOLUTION FOR THE TRANSMISSION OF ULF AND ELF WAVES THROUGH THE IONOSPHERE

by

Yuji Inoue and D. Lynn Shaeffer

Earth and Planetary Sciences Department
University of Pittsburgh
Pittsburgh, Pennsylvania 15213

Contract No. F19628-67-C-0109

Project No. 5631

Task No. 563116

Work Unit No. 56311601

FINAL REPORT

Contract Period: 1 November 1966 to 30 September 1970

Date of Report: 30 September 1970

Contract Monitor: Samuel Horowitz
Ionospheric Physics Laboratory

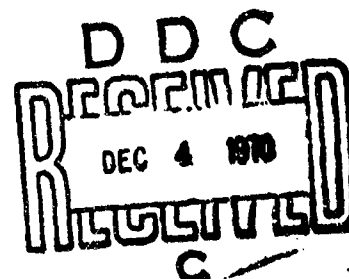
This document has been approved for public
release and sale; its distribution is unlimited.

Submitted in partial fulfillment for a Doctorate in Physics,
University of Pittsburgh, Pittsburgh, Pennsylvania, 15213

Reproduced by
NATIONAL TECHNICAL
INFORMATION SERVICE
Springfield, Va. 22151

prepared for

Air Force Cambridge Research Laboratories
AIR FORCE SYSTEMS COMMAND
United States Air Force
Bedford, Massachusetts 01730



ACCESSION NO.		
REF ID	WRITE SECTION <input checked="" type="checkbox"/>	
REF ID	REF SECTION <input type="checkbox"/>	
UNANNOUNCED	<input type="checkbox"/>	
JUSTIFICATION		
BY		
RESTRICTION/AVAILABILITY CODE		
DISC.	AVAIL. CODE/OF SPECIAL	
/		

Qualified requestors may obtain additional copies from the Defense Documentation Center. All others should apply to the Clearinghouse for Federal Scientific and Technical Information.

AFCRL-70-0531

FULL WAVE SOLUTION FOR THE TRANSMISSION OF ULF
AND ELF WAVES THROUGH THE IONOSPHERE

by

Yuji Inoue and D. Lynn Shaeffer

Earth and Planetary Sciences Department
University of Pittsburgh
Pittsburgh, Pennsylvania 15213

Contract No. F19628-67-C-0109
Project No. 5631
Task No. 563116
Work Unit No. 56311601

FINAL REPORT

Contract Period: 1 November 1966 to 30 September 1970
Date of Report: 30 September 1970

Contract Monitor: Samuel Horowitz
Ionospheric Physics Laboratory

This document has been approved for public
release and sale; its distribution is unlimited.

Submitted in partial fulfillment for a Doctorate in Physics,
University of Pittsburgh, Pittsburgh, Pennsylvania, 15213

prepared for

Air Force Cambridge Research Laboratories
AIR FORCE SYSTEMS COMMAND
United States Air Force
Bedford, Massachusetts 01730

ABSTRACT

Full wave solutions have been found for plane wave and localized disturbances in the ULF (micropulsation) and ELF frequency ranges. Slow and fast wave disturbances incident at 5000 km. altitude at the frequencies 100, 3.0, 1/3, and 1/300 cps. were analyzed. A model ionosphere developed from existing rocket and satellite data for conditions of midday and midlatitude at sunspot minimum was used in the calculations. The cold plasma dispersion relation was written conveniently in terms of the localized disturbance factor and the ionospheric conductivity tensor elements. The localized disturbances were found to produce large vertical electric fields in the neutral atmosphere for the incident slow waves in the micropulsation range and the incident fast wave at 100 cps. Localization causes strong mode coupling in the lower D region and the coupling coefficients are larger than the quartic roots at 1/300 c/s. Charge exchange of O^+ and O results in an enhanced Pedersen conductivity region which in some cases acts as a cavity wall for wave energy storage. Charge exchange also causes some absorption at Pc1 frequencies in the range 150-250 km. The conductivity of the Earth's surface is included and found to result in almost total reflection at ground level for all frequencies considered. Incident slow mode signals at 3.0 cps. undergo polarization reversal at 1000 km. and then propagate mostly in the R mode through the ionosphere. At 4000 km. plasma drift velocities between 0.1 and 1.0 km/sec. are sufficient for the incident slow waves to excite typical Pc1 and Pc5 ground observed signals.

LIST OF CONTRIBUTORS

Yuji Inoue

Contractor

D. Lynn Shaeffer

Graduate Student

RELATED PUBLICATIONS

"A Model Ionosphere for Mid-day and Mid-latitude During Sunspot Minimum," by D. Lynn Shaeffer and Yuji Inoue, Space Magnetism University of Pittsburgh (SMUP) Report No. 4, July 1968.

"Full Wave Solution for the Transmission of ELF Waves through the Ionosphere," by D. Lynn Shaeffer and Yuji Inoue, presented at conference on Antennas and Trans-Ionospheric Propagation as Related to ELF/VLF Downlink Satellite Communications, Naval Research Laboratory, Washington, D.C., 8-10 June 1970.

TABLE OF CONTENTS

	<u>Page</u>
Abstract	i
List of Contributors	ii
Table of Contents	iii
 PART I - FULL WAVE SOLUTION FOR THE TRANSMISSION OF ULF AND ELF WAVES THROUGH THE IONOSPHERE	 1-1
 PART II - IONOSPHERIC CONDUCTIVITY	 2-1
 PART III - A MODEL IONOSPHERE FOR MID-DAY AND MID-LATITUDE DURING SUNSPOT MINIMUM.	 3-1

PART I

FULL WAVE SOLUTION FOR THE TRANSMISSION OF ULF
AND ELF WAVES THROUGH THE IONOSPHERE

TABLE OF CONTENTS

	<u>Page</u>
List of Figures	1-iv
List of Tables	1-vii
1.0 INTRODUCTION	1- 1
2.0 THEORETICAL CONSIDERATIONS	1- 4
2.1 Formulation of the Wave Equation	1- 4
2.2 Dispersion Relation	1- 8
2.3 Computer Program for Full Wave Solution	1-13
2.31 Program for Part I	1-13
2.32 Program for Part II	1-16
2.33 Program for Part III	1-19
3.0 THE TRANSMISSION OF ELF WAVES THROUGH THE IONOSPHERE	1-26
3.1 Ion Cyclotron Resonance	1-26
3.2 Localized Disturbance at 100 c/s	1-34
3.21 Booker Quartic Roots	1-34
3.22 Magneto-Ionic Coupling Coefficients	1-37
3.23 Characteristic Wave Mixing Ratios	1-40
3.24 Wave Fields	1-44
3.25 Wave Field Polarization	1-46
3.3 Comparison of Plane Wave with Localized Disturbance at 100 c/s	1-48
3.4 Ionospheric Electric and Magnetic Field Measurements	1-50
4.0 THE TRANSMISSION OF ULF WAVES THROUGH THE IONOSPHERE	1-52
4.1 Localized Disturbance at 3.0 c/s	1-52
4.11 Booker Quartic Roots	1-52
4.111 Effect of Charge Exchange on the Booker Quartic Roots	1-55
4.12 Magneto-Ionic Coupling Coefficients	1-55
4.13 Characteristic Wave Mixing Ratios	1-59
4.14 Wave Fields	1-62
4.15 Wave Field Polarization	1-65
4.2 Localized Disturbance at 1/3 c/s	1-73
4.21 Booker Quartic Roots	1-73

4.22	Magneto-ionic Coupling Coefficients	1- 77
4.23	Characteristic Wave Mixing Ratios	1- 80
4.24	Wave Fields	1- 82
4.25	Wave Field Polarization	1- 86
4.3	Localized Disturbance at $1/300$ c/s	1- 89
4.31	Booker Quartic Roots	1- 89
4.32	Magneto-ionic Coupling Coefficients	1- 93
4.33	Characteristic Wave Mixing Ratios	1- 95
4.34	Wave Fields	1- 98
4.35	Wave Field Polarization	1-103
4.36	Comparison of Localized Disturbance and Plane Wave Cases at $1/300$ c/s	1-108
5.0	OVERALL COMPARISON OF THE DISTURBANCE PROPAGATION CHARACTERISTICS AT THE VARIOUS FREQUENCIES INVESTIGATED	1-118
6.0	CONCLUSIONS AND RECOMMENDATIONS	1-132
6.1	Conclusions	1-132
6.2	Recommendations	1-135
	REFERENCES	1-137

LIST OF FIGURES

<u>Figure</u>	<u>Page</u>
3.1 Ion cyclotron resonance profile	1-27
3.2 Effect of multiple ions on R and L at 1000 km	1-29
3.3 Effect of collisions on R and L at 200 km. for a model ionosphere with multiple ions and for an average ion suffering collisions	1-31
3.4 Booker quartic roots vs. altitude for the localized disturbance at 100 c/s	1-36
3.5 Magneto-ionic coupling coefficients vs. altitude for the localized disturbance at 100 c/s	1-38
3.6 Characteristic wave mixing ratios vs. altitude for the localized incident fast wave at 100 c/s	1-41
3.7 Mixing ratios, wave fields, and polarization of localized incident slow wave at 100 c/s	1-43
3.8 Wave fields vs. altitude for the localized incident fast wave at 100 c/s	1-45
3.9 Wave field polarization vs. altitude for the localized incident fast wave at 100 c/s	1-47
4.1 Booker quartic roots vs. altitude for the localized disturbance at 3.0 c/s	1-54
4.2 Effect of charge exchange on the Booker quartic roots for the localized disturbance at 3.0 c/s	1-56
4.3 Magneto-ionic coupling coefficients vs. altitude for the localized disturbance at 3.0 c/s	1-57
4.4 Characteristic wave mixing ratios vs. altitude for the localized incident slow and fast waves at 3.0 c/s	1-60

4.5	Wave fields vs. altitude for the localized incident slow wave at 3.0 c/s	1-63
4.6	Wave fields vs. altitude for the localized incident fast wave at 3.0 c/s	1-65
4.7	Wave field polarization vs. altitude for the localized incident slow wave at 3.0 c/s	1-67
4.8	Wave field polarization vs. altitude for the localized incident fast wave at 3.0 c/s	1-68
4.9	Booker quartic roots vs. altitude for the localized disturbance at 1/3 c/s	1-75
4.10	Magneto-ionic coupling coefficients vs. altitude for the localized disturbance at 1/3 c/s	1-78
4.11	Characteristic wave mixing ratios vs. altitude for the localized incident slow and fast waves at 1/3 c/s	1-81
4.12	Wave fields vs. altitude for the localized incident slow wave at 1/3 c/s	1-83
4.13	Wave fields vs. altitude for the localized incident fast wave at 1/3 c/s	1-85
4.14	Wave field polarization vs. altitude for the localized incident slow wave at 1/3 c/s	1-87
4.15	Wave field polarization vs. altitude for the localized incident fast wave at 1/3 c/s	1-88
4.16	Booker quartic roots vs. altitude for the localized disturbance at 1/300 c/s	1-91
4.17	Magneto-ionic coupling coefficients vs. altitude for the localized disturbance at 1/300 c/s	1-94

4.18	Characteristic wave mixing ratios vs. altitude for the localized incident slow and fast waves at $1/300$ c/s	1- 96
4.19	Wave fields vs. altitude for the localized incident fast wave at $1/300$ c/s	1- 99
4.20	Wave fields vs. altitude for the localized incident slow wave at $1/300$ c/s	1-102
4.21	Wave field polarization vs. altitude for the localized incident fast wave at $1/300$ c/s	1-104
4.22	Wave field polarization vs. altitude for the localized incident slow wave at $1/300$ c/s	1-106
4.23	Booker quartic roots vs. altitude in the lower ionosphere for the incident plane wave at $1/300$ c/s	1-109
4.24	Effect of charge exchange on the Booker quartic roots for the incident plane wave at $1/300$ c/s	1-112
4.25	Magneto-ionic coupling coefficients vs. altitude in the lower ionosphere for the incident plane wave at $1/300$ c/s	1-114
4.26	Wave fields vs. altitude for the incident slow mode plane wave at $1/300$ c/s	1-115
4.27	Wave fields vs. altitude for the incident fast mode plane wave at $1/300$ c/s	1-116

LIST OF TABLES

<u>Table</u>	<u>Page</u>
2.31 Some important variables in Part I and their meaning	1- 14
2.32 Description of subroutines used in Part I	1- 15
2.33 Variables read into Part II from data card	1- 17
2.34 Description of Subroutines used in Part II	1- 17
2.35 Variables read into Part III from data card	1- 23
2.36 Description of subroutines used in Part III	1- 24
3.1 Medium characteristics at 100 c/s for a localized disturbance incident at an oblique angle from the vertical at 5000 km.	1- 35
4.1 Medium characteristics at 3.0 c/s for a localized disturbance incident at an oblique angle from the vertical at 5000 km.	1- 53
4.2 Medium characteristics at 1/3 c/s for a localized disturbance incident at an oblique angle from the vertical at 5000 km.	1- 74
4.3 Medium characteristics at 1/300 c/s for a localized disturbance incident at an oblique angle from the vertical at 5000 km.	1- 90
4.4 Medium characteristics at 1/300 c/s for a plane wave incident at 5000 km.	1-110
5.1 Disturbance parameters for the slow mode at 5000 km.	1-119
5.2 Disturbance parameters for the fast mode at 5000 km.	1-120
5.3 Reflection coefficients for incident slow and fast waves	1-121

5.4	Incident fast mode electric and magnetic wave field transmission coefficients	1-123
5.5	Incident slow mode electric and magnetic wave field transmission coefficients	1-124
5.6	Comparison of magnetic field transmission coefficients obtained by various investigators for two different wave frequencies	1-126
5.7	Electric and magnetic wave field magnitudes of the incident fast wave at various altitudes	1-129
5.8	Electric and magnetic wave field magnitudes of the incident slow wave at various altitudes	1-130

1.0 INTRODUCTION

Variations in the intensity of the geomagnetic field as observed at the Earth's surface are well known to exist in the frequency range 1 cps. down to around 10^{-3} cps. These oscillations are referred to as geomagnetic micropulsations and have been given a morphological classification by Jacobs et. al. [1964]. It is now generally accepted that micropulsations as observed on the Earth's surface are caused by hydromagnetic disturbances generated in the magnetosphere and propagated along the geomagnetic field lines through the ionosphere down to ground surface. The ultimate aim of the present investigation is to determine the modification of these waves and to study the reflection and magnetoionic coupling processes as the disturbances propagate down to ground level. A full wave solution is obtained utilizing a numerical technique developed by Inoue and Horowitz [1966a,b].

Hydromagnetic wave propagation has been studied extensively ever since its discovery by Alfven [1942]. Theoretical studies led Dungey [1954a,b] to suggest that some micropulsations are of hydromagnetic origin. This suggestion has since led to a number of investigations devoted to the study of hydromagnetic wave propagation through the Earth's ionosphere [Akasofu, 1965; Field, 1963; Field and Greifinger, 1965, 1966; Francis and Karplus, 1960; Greifinger and Greifinger, 1965; Jacobs and Watanabe, 1962; Karplus et. al., 1962; Prince and B. stick, 1964; Prince et. al., 1964].

The solutions to these studies have been effected by two basic means, i.e., analytical and numerical. All of the investigations mentioned above have neglected to consider magnetoionic coupling, which has been found in the present investigation to be of considerable importance in determining the final wave fields. Analytical solutions, such as those obtained by Greifinger and Greifinger [1965] and Field and Greifinger [1965, 1966], have been effected only by making some drastic simplifying assumptions.

For high and medium frequencies the wave equation is often solved using the WKB method and the approximations of geometric optics. For low frequencies, however, the concept of ray optics becomes invalid and partial reflection is not properly treated. A more accurate solution to the wave equation must then be sought by utilizing known functions or numerical methods; this is referred to as a "full wave solution." In general full wave solutions are necessary when the scale size of the variations in the ionospheric parameters becomes less than the wavelength of the electromagnetic disturbance. A general discussion of the full wave and phase integral (i.e., WKB) methods and their advantages and disadvantages may be found in an excellent review article by Budden [1969].

Various full wave methods have been proposed for the solution of the problem of electromagnetic wave propagation in a horizontally stratified magnetoionic medium. These include Budden [1955], Barron and Budden [1959], Jöhler and Harper [1962], Pittaway [1965], and

more recently, Walsh [1967] and Altman and Cory [1969a,b]. None of these methods, with the exception of that due to Altman and Cory, has been applied to the micropulsation frequency range. The simple thin-film optical method due to Altman and Cory [1969a] is valid only for constant wave polarization, when magnetoionic coupling is zero. In general this condition is not fulfilled in the micropulsation frequency range, even for vertical propagation. The generalized thin-film optical method (Altman and Cory, [1969b]) allows for oblique incidence and intermode coupling. However, the wave fields do not appear to have been calculated with this method.

In the present investigation three different frequencies (3.0, 0.333, and 0.00333 cps.) are considered in the micropulsation frequency range. In addition one frequency (100 cps.) is studied in the ELF range, which is of interest in the possible effect of ion cyclotron resonance. For each frequency a localized disturbance (See section 2.1) is considered. Also, at 100 cps. and at 0.00333 cps. plane wave cases are studied. For each case considered the incident slow and incident fast waves are introduced separately at the top of the ionosphere.

2.0 THEORETICAL CONSIDERATIONS

2.1 Formulation of the Wave Equation

The assumption is made that an electromagnetic disturbance is incident at 5000 km. altitude. The propagation characteristics of this disturbance are determined by Maxwell's equations and the constitutive relations for the medium. The disturbance is assumed to be of sufficiently small amplitude that nonlinearities of the governing equations may be neglected. The ionosphere is assumed to be horizontally stratified in the presence of a vertical magnetic field.

The disturbance function F_D is represented by a double Fourier series over the spatial coordinates x and y .

$$F_D = \sum_{\ell'} \sum_{m'} A(\ell', m') F(z) \exp[ik_{\ell'} \ell' x + ik_{m'} m' y] e^{-i\omega t}$$

where ℓ' and m' are the Fourier numbers.

The Fourier series is expanded over an interval equal to the Earth's circumference so that the fundamental wavelength gives

$$\text{where } k_g = \frac{2\pi}{2\pi R_e} = \frac{1}{R_e} \\ R_e = \text{Earth's radius}$$

Maxwell's equations may be written as

$$\begin{aligned} \nabla \times \vec{E} &= ik_0 \vec{H} \\ \nabla \times \vec{H} &= -ik_0 \vec{K} \cdot \vec{E} \\ k_0 &= \frac{2\pi}{\lambda_0} \end{aligned}$$

λ_0 = free space wavelength

$$\vec{\mathcal{N}} = z_0 \vec{H}$$

$$z_0 = \left[\frac{\mu_0}{\epsilon_0} \right]^{\frac{1}{2}}$$

where z_0 , ϵ_0 , and μ_0 are the characteristic impedance, dielectric constant, and magnetic permeability of free space and \vec{E} and \vec{H} are the electric and magnetic wave fields, respectively. The quantity $\vec{\mathcal{N}}$ has the same units as \vec{E} . \vec{K} is the dielectric tensor of the ionosphere and is given by

$$\vec{K} = \vec{I} + i \frac{\vec{\sigma}}{\omega \epsilon_0}$$

where \vec{I} is the unity matrix with the diagonal elements being unity and the off-diagonal elements being zero. The conductivity tensor $\vec{\sigma}$ is determined from the equations of motion of the charged particles (See Part II).

The x and y components of the nabla differential operator may be written as

$$\frac{\partial}{\partial x} \rightarrow i k_y l$$

$$\frac{\partial}{\partial y} \rightarrow i k_x m$$

If r is defined as

$$r = \frac{k_0}{k_y} = \frac{2\pi R_0}{\lambda_0}$$

then Maxwell's equations in component form may be written as

$$mE_z - \frac{1}{ik_g} \frac{\partial}{\partial z} E_y = r\mathcal{H}_x = \mathcal{H}'_x$$

$$\frac{1}{ik_g} \frac{\partial}{\partial z} E_x - lE_z = r\mathcal{H}_y = \mathcal{H}'_y$$

$$lE_y - mE_z = r\mathcal{H}_z = \mathcal{H}'_z$$

$$m\mathcal{H}'_z - \frac{1}{ik_g} \frac{\partial}{\partial z} \mathcal{H}'_y = -(K'_{xx}E_x + K'_{xy}E_y + K'_{xz}E_z)$$

$$\frac{1}{ik_g} \frac{\partial}{\partial z} \mathcal{H}'_x - l\mathcal{H}'_z = -(K'_{yx}E_x + K'_{yy}E_y + K'_{yz}E_z)$$

$$l\mathcal{H}'_y - m\mathcal{H}'_x = -(K'_{zx}E_x + K'_{zy}E_y + K'_{zz}E_z)$$

where

$$\vec{\mathcal{H}}' = r\vec{\mathcal{H}}$$

$$\vec{K}' = r^2\vec{K}$$

These equations may be written more concisely by introducing a matrix notation due to Clemmow and Heading [1954].

$$\frac{d\vec{\mathcal{E}}}{dz_s} = i\vec{T}'\vec{\mathcal{E}}$$

$$z_s = k_g z$$

$$\vec{\mathcal{E}} = \begin{bmatrix} E_x \\ E_y \\ \mathcal{H}'_x \\ \mathcal{H}'_y \end{bmatrix}$$

where \vec{T}' is the 4 x 4 propagation tensor having the functional form

$$\vec{T}' = \vec{T}'(\vec{K}', l, m)$$

and is the same as equation (10) given by Inoue and Horowitz [1966a]

with \bar{K} being replaced by \bar{K}' .

Although the propagation tensor \bar{T}' is here represented as a function of both ℓ and m , a coordinate transformation is performed so that the disturbance is propagating only in the x and z directions.

Then the Fourier numbers become

$$\ell = [\ell'^2 + m'^2]^{\frac{1}{2}}$$

$$m = 0$$

Also, in order to simplify the calculations only a single Fourier component is considered so that the disturbance function is now represented by

$$F_D \sim F(z) \exp(i k_g \ell x) e^{-i \omega t}$$

$F(z)$ is the height dependent portion of the disturbance function which is determined from the solution to the wave equation.

The above differential equation represents the wave equation reduced to a set of four linear, homogeneous, first order differential equations. This equation was integrated using the technique developed by Inoue and Horowitz [1966a,b] from deep in the interior of the earth out to 5000 km. altitude.

In order to carry out the numerical solutions to this problem a model ionosphere was developed from existing rocket and satellite data for conditions of midlatitude and midday at sunspot minimum. (See Part III for the details of this model.) The neutral atmosphere ($0 - 50$ km.) was considered to be free space with zero conductivity. The surface conductivity of the earth was taken from data published by Green and Hoffman [1967] and the conductivity of the Earth's

interior was obtained from graphs given by Price [1965].

2.2 Dispersion Relation

Maxwell's equations may be written as

$$\nabla \times \vec{E} = i\omega\mu_0 \vec{H}$$

$$\nabla \times \vec{H} = -i\omega\epsilon_0 \vec{K} \cdot \vec{E}$$

where \vec{K} , the dielectric tensor, is given in the notation of Stix [1962].

$$\vec{K} = \begin{bmatrix} S & -iD & 0 \\ iD & S & 0 \\ 0 & 0 & P \end{bmatrix}$$

where

$$S \equiv \frac{1}{2}(R+L)$$

$$D \equiv \frac{1}{2}(R-L)$$

$$R \equiv 1 - \sum_k \frac{\pi_k^2}{\omega^2} \left[\frac{\omega}{\omega + \epsilon_k \Omega_k} \right]$$

$$L \equiv 1 - \sum_k \frac{\pi_k^2}{\omega^2} \left[\frac{\omega}{\omega - \epsilon_k \Omega_k} \right]$$

$$P \equiv 1 - \sum_k \frac{\pi_k^2}{\omega^2}$$

$$\pi_k^2 = \frac{n_k^2 e^2}{m_k \epsilon_0}$$

= plasma frequency of k th particle

$$\Omega_k = \left| \frac{z_k e B_0}{m_k} \right| = \text{magnitude of cyclotron frequency of } k \text{ th particle}$$

ω = angular wave frequency of the disturbance

The quantities n_k , m_k , z_k represent the particle density, mass, and charge multiplicity of the k th particle species. In this work z_k is assumed to be unity. e is the magnitude of the electrical charge of an electron. ϵ_k is +1 or -1, if the k th particle is positively or negatively charged, respectively. B_0 is the Earth's static magnetic field.

The curl of a vector \vec{A} is $\nabla \times \vec{A}$ and may be written as an antisymmetric tensor times the vector where the tensor is given by

$$\overline{\nabla \times} = \begin{bmatrix} 0 & -\frac{\partial}{\partial z} & \frac{\partial}{\partial y} \\ \frac{\partial}{\partial z} & 0 & -\frac{\partial}{\partial x} \\ -\frac{\partial}{\partial y} & \frac{\partial}{\partial x} & 0 \end{bmatrix}$$

Because of the coordinate transformation which makes $\ell = (\ell'^2 + m'^2)^{\frac{1}{2}}$ and $m = 0$, none of the variables have any y dependence. Then the derivatives become

$$\begin{aligned} \frac{\partial}{\partial x} &\rightarrow i k_y \ell \\ \frac{\partial}{\partial y} &\rightarrow 0 \\ \frac{\partial}{\partial z} &\rightarrow i k_y q \end{aligned}$$

where q is the Booker quartic root (See Budden, 1961, p. 120).

$$\overline{\nabla} \times = ik_g \begin{bmatrix} 0 & -q & 0 \\ q & 0 & -l \\ 0 & l & 0 \end{bmatrix}$$

From Maxwell's equations

$$\nabla \times (\nabla \times \vec{E}) \equiv \overline{\nabla} \times \cdot (\overline{\nabla} \times \cdot \vec{E}) = i\omega\mu_0 (\overline{\nabla} \times \cdot \vec{H})$$

$$\begin{aligned} \overline{\nabla} \times \cdot (\overline{\nabla} \times \cdot \vec{E}) &= \omega^2 \mu_0 \epsilon_0 \overline{K} \cdot \vec{E} \\ &= \frac{\omega^2}{c^2} \overline{K} \cdot \vec{E} \end{aligned}$$

which may be reduced to

$$\begin{bmatrix} -q^2 & 0 & ql \\ 0 & -(q^2+l^2) & 0 \\ ql & 0 & -l^2 \end{bmatrix} \cdot \begin{bmatrix} E_x \\ E_y \\ E_z \end{bmatrix} = -r^2 \overline{K} \cdot \vec{E}$$

$$r = \frac{\omega}{k_g c} = \frac{k_0}{k_g}$$

Now substituting the expression for \overline{K} and transposing to the left side of the equation

$$\begin{bmatrix} r^2 s - q^2 & -ir^2 D & ql \\ ir^2 D & r^2 s - (q^2 + l^2) & 0 \\ ql & 0 & r^2 P - l^2 \end{bmatrix} \cdot \begin{bmatrix} E_x \\ E_y \\ E_z \end{bmatrix} = 0$$

$$\begin{bmatrix} s - \frac{q^2}{r^2} & -iD & \frac{ql}{r^2} \\ iD & s - \frac{q^2 + l^2}{r^2} & 0 \\ \frac{ql}{r^2} & 0 & P - \frac{l^2}{r^2} \end{bmatrix} \cdot \begin{bmatrix} E_x \\ E_y \\ E_z \end{bmatrix} = 0$$

In order that the solution to this system of equations be nontrivial the determinant of the 3 x 3 matrix must be zero. The following quartic equation representing the dispersion relation is then obtained.

$$Aq^4 - Bq^2 + C = 0$$

where

$$A = \frac{P}{r^4}$$

$$B = \frac{l^2}{r^4} (S - P) + \frac{2S}{r^2} (P - \frac{l^2}{r^2})$$

$$C = \left[RL - \frac{l^2 S}{r^2} \right] \left[P - \frac{l^2}{r^2} \right]$$

$$r^2 = \left[\frac{2\pi R_e}{\lambda_0} \right]^2$$

P, R, L may be written in terms of σ_{\parallel} , σ_H , and σ_{\perp} , the parallel, Hall, and Pedersen conductivities, respectively. (See Part II, section 4.1.)

$$R = 1 + \frac{\sigma_{Hr} - \sigma_{Li}}{\omega \epsilon_0} + i \frac{\sigma_{Li} + \sigma_{Hi}}{\omega \epsilon_0}$$

$$L = 1 - \frac{\sigma_{Hr} + \sigma_{Li}}{\omega \epsilon_0} + i \frac{\sigma_{Li} - \sigma_{Hi}}{\omega \epsilon_0}$$

$$P = 1 - \frac{\sigma_{Hi}}{\omega \epsilon_0} + i \frac{\sigma_{Hr}}{\omega \epsilon_0}$$

where the subscripts "r" and "i" mean the real and imaginary parts, respectively.

Comparing the 3 x 3 matrix from which the dispersion relation is derived with equation (1-20) given by Stix [1962], q is seen to be related to n , the total index of refraction, by

$$\frac{q}{r} = n \cos \theta$$

where θ is the angle between the wave normal and the magnetic field. We also have the relation

$$\begin{aligned} \theta &= \tan^{-1} \frac{k_x}{k_z} = \tan^{-1} \left[\frac{l k_g}{q k_g} \right] \\ &= \tan^{-1} \left[\frac{l}{q} \right] \end{aligned}$$

Thus we see that

$$q = r n \cos \theta$$

$$l = r n \sin \theta$$

Now θ can be eliminated to give the relationship between q , n , and l .

$$\sin^2 \theta = 1 - \frac{q^2}{r^2 n^2}$$

or

$$q^2 = r^2 n^2 - l^2$$

If $l = 0$, i.e., completely vertical propagation, then

$$q^2 = r^2 n^2$$

Also, in this case,

$$A = \frac{P}{r^4}$$

$$B = \frac{2PS}{r^2}$$

$$C = PRL$$

and the dispersion relation becomes

$$\frac{P}{r^4} q^4 - \frac{2PS}{r^2} q^2 + PRL = 0$$

Substituting $q^2 = r^2 n^2$ we have

$$Pn^4 - 2PSn^2 + PRL = 0$$

which is identical to the dispersion relation given by Stix for $\Theta = 0$.

2.3 Computer Program for Full Wave Solution

The computer program for the full wave solution consists of three separate programs (Part I, Part II, and Part III) which are interfaced by means of magnetic tapes. Quantities calculated in Part I which are necessary for the computations in Part II are stored on the binary magnetic tape which interfaces Part I and Part II. The same situation is true for the relationship between Part II and Part III.

The integration procedure used in this program is based on the theoretical work of Inoue and Horowitz (1966a,b) and these two papers shall hereinafter be referred to as Papers I and II, respectively.

2.31 Program for Part I

Part I of the full wave program has the following primary functions:

	Variable	Meaning
Wave data	FREQ; LDF, MDF	Wave frequency; Fourier numbers L and m
Station data	GML, GMM, GMN BG	Magnetic field direction cosines Magnetic field value at ground level
Medium data	IMED = 0, 1, 2 IDATA = 0 = 1 → SP1 = 2 → SP2 = 3 H, ELD, DN CFPN, CFEN, CFEP PIM, ANM EPSI, PERM, COND	Plasma, free space, and interior of the earth treatments, respectively No data interpolation is performed within the current slab Current height interval divided into the number of intervals given by the variable SP1 SP2 used to divide the height interval Flag to indicate last height Height; electron and neutral densities (cm^{-3}) Ion-neutral, electron-neutral, electron-ion collision frequencies Ion and neutral masses (a.m.u.) ϵ, μ, σ
	F, T	dielectric and propagation tensors

TABLE 2.31. Some important variables in Part I and their meaning.

1. Performs a coordinate transformation so that the propagation vector lies in the x - z plane at an angle Θ to the z axis.
2. Calculates the magneto-ionic quantities X, Y, Z.
3. Uses the coupled equations of motion for electrons and ions (See Part II, chapter 1 of this report) to calculate the ionospheric conductivity tensor.
4. Calculates the dielectric and propagation tensors.
5. The altitude (or depth), the Fourier number ρ , and the dielectric and propagation tensors are stored on magnetic tape for later use in the full wave program.

A few of the important variables used in Part I are given in Table 2.31 along with their interpretation. The wave data, station data, and medium data are read into Part I on cards.

A brief description of the various subroutines used in Part I is given below.

TABLE 2.32

<u>Subroutine</u>	<u>Description</u>
DTRM	Finds the determinant of a 3 x 3 matrix having complex elements.
DETERM	Computes the determinant of a 4 x 4 matrix having complex elements using the method of pivot condensation.
MTMLTP	Finds the product of two 3 x 3 matrices each having complex elements.
MATINV	Determines the inverse of a 3 x 3 matrix having

complex elements.

DUMP A dump is forced if the program finds itself in the wrong location.

FTRAP A University of Pittsburgh subroutine which sets to zero any number which becomes too small for the computer.

Magnetic tapes used in the program are

INP	BCD scratch tape which reads in data cards
IOUT	BCD scratch tape which prints out desired information
IW1	Binary Tapes used for manipulating and storing quantities which are to be used in Part II and/or Part III.
IW2	

2.32 Program for Part II

Part II of the full wave program has the following primary functions:

1. A binary search is initiated if the invariant test fails (Paper I, p. 433). This test will fail when a singularity occurs within a given slab. The purpose of the binary search is to try to squeeze the singularity into as small a slab as possible.
2. The slab width is adjusted so that the difference in the amplitude changes of the slow and fast modes within a slab is not too great.
3. The slab is determined to be isotropic or anisotropic and the Booker quartic roots and eigenvectors are calculated accordingly.
4. The coupling coefficients (See Paper I, p. 431) are calculated and stored on tape IW4, which is used as a permanent storage tape for all quantities which are later retrieved and plotted automatically.

The following variables are read into Part II from a data card.

TABLE 2.33

<u>Variable</u>	<u>Description</u>
HMAX	Maximum data height (km.). For purposes of the work here, HMAX=5000 km.
HMIN	Minimum data height (km.). In order to take into account the conducting properties of the earth this value was set to HMIN= -400 km.
EPSINV	Numerical value assigned to the invariant test.
WLNTH	$\frac{1}{k_g} = R_e =$ Earth's radius
LIMBSR	The limit on the number of binary searches to be preformed for a given slab.

A brief description of the various subroutines used in Part II, but not in Part I, is given below.

TABLE 2.34

<u>Subroutine</u>	<u>Description</u>
COEFIC	Computes the coefficients of the Booker quartic equation from the propagation tensor.
POLAR	Changes the cartesian coordinates x and y to polar coordinates r and ϕ .
LEIGEN	Calculates the normalized \bar{D} matrix. (See Paper I, p. 434).
CMEXP	Given the real and imaginary parts x_r and x_i , respectively, of the variable x, calculates $e^{x_r + ix_i}$.

BOOKER

Calculates the roots of the Booker quartic equation.

Finding a root requires making a good initial guess for the root, as is done in the following method. The

quartic equation is differentiated three times and the zero crossing of the 3rd

derivative is used to find

the maximum or minimum

of the 2nd derivative. A

Taylor series expansion is

then made about the maximum

or minimum to find the roots of the 2nd derivative.

Newton's method is used to improve on these roots,

which are then used to find the maxima and minima

of the 1st derivative. The whole process is repeated

for finding the roots of the 1st derivative and then for

finding the roots of the quartic equation. Redundant

roots are thrown out. The roots are then arranged

in the order

D_s, D_f, U_s, U_f

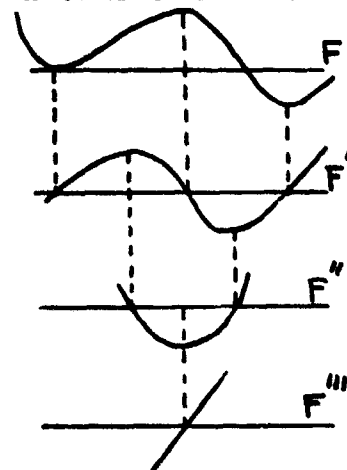
i.e., downgoing slow, downgoing fast, upgoing slow,

upgoing fast. In the eventuality that the slow

mode has larger attenuation than the fast mode

then the slow and fast modes are interchanged in

order to prevent swamping.



EIGENV

Computes the eigenvectors associated with the Booker quartic roots. For any given quartic root the characteristic matrix has 16 different 3×3 determinants which may be obtained by elimination of the i th row and j th column. For each eigenvalue the two largest of the 16 determinants are found. The eigenvectors associated with each of the two largest determinants are then calculated. Thus for each eigenvalue two different sets of equations have been used to calculate two eigenvectors. The eight eigenvectors associated with the four eigenvalues may be combined in sixteen different ways to give the eigenvector matrix. The eigenvector matrix which has the maximum determinant is chosen because the columns of that particular eigenvector matrix are as independent as possible.

BOBM

This is a University of Pittsburgh subroutine which causes the computer to halt at the next "pause" statement. A message is then printed to the operator to mount a third private tape, i.e., tape IW4.

2.33 Program for Part III

The basic function of Part III is to perform the actual integration of the wave equation. The forward integration proceeds in the upward direction, starting deep in the interior of the Earth and proceeding

out to HMAX, at which point the boundary conditions for the disturbance source are applied. Because of the problem of numerical swamping (See Paper II for a complete discussion) corrections frequently have to be made to the solutions in the various horizontal slabs in order to preserve good linear independence. In order to be efficient the corrections are all made in one backward integration process, which is performed after the boundary conditions are applied at HMAX. The matricant method of matrix algebra (Gantmacher, 1959; Pease, 1965; Inoue and Horowitz, 1966b) is utilized in performing the forward integration.

In general the solution to the wave equation is given by

$$\vec{e} = \vec{W} \cdot \vec{b}$$

(Paper I, equation (14)) where \vec{e} is the wave field solution vector, \vec{W} the 4 x 4 integral matrix whose columns are four linearly independent solutions to the wave equation, and the superposition vector \vec{b} consisting of four constants given by the boundary conditions. Because the disturbance source is considered to be above the layers over which the integration is performed two of the superposition constants will be zero (See Table 3, Paper II). Consequently only two independent solutions are necessary for the final solution. These will correspond to the incident slow mode and the incident fast mode and are selected by the variables SB1 and SB2 in the computer program (See Table 2.35 below).

The following basic operations are performed by the program for Part III:

1. The synthesis matrix from Part II is fed into the wave properties matrix (equation (31), Paper II) and the third and fourth columns are zeroed out because only two independent solutions are required as a result of the boundary conditions.
2. The average propagation tensor is found by linear interpolation of the values at the upper and lower heights of a slab.
3. The Booker quartic roots and the hybridizing matrices (equations (19) and (27), Paper II) are calculated in accordance with whether the slab is isotropic or anisotropic, indicated by the variable IANISO which was given a value in Part II.
4. The modification matrix (equations (9), (10), (18), and (22), Paper II) and the eigenvectors are then calculated.
5. Undesirable wave components are excluded from the wave properties matrix by a linear combination of solutions (section 5.2, Paper II).
6. The boundary conditions are applied at HMAX according to whether the first independent solution ($IRL = 1$) or the second independent solution ($IRL = 2$) is desired. Either case utilizes the same forward integration. Only the backward integration is different.
7. On the backward integration the correction to the integral matrix is performed by use of the \overline{COR} matrix (equation (47), Paper II). The amplitude and phase factors (equation (32), Paper II) and the mixing ratios are also calculated. The mixing ratios are defined in the following manner.

$$\begin{aligned}\vec{e} &= \vec{W} \cdot \vec{b} \\ \vec{W} &= \vec{S} \cdot \vec{W}\end{aligned}$$

where \vec{S} is the principal axis transformation of the propagation tensor and \vec{W} contains the amplitude characteristics. Then

$$\begin{aligned}\vec{e} &= \vec{S} \cdot \vec{W} \cdot \vec{b} \\ &= \vec{S} \cdot \vec{f} \\ \vec{f} &= \vec{S}^{-1} \cdot \vec{e}\end{aligned}$$

where \vec{f} is the column matrix of elements defined as the mixing ratios because they indicate the magnitude of the "mixing" of the characteristic waves, which are the columns of the \vec{S} matrix.

8. The final form of the wave fields is then calculated in the background integration.

9. The Booker quartic roots, the electric and magnetic wave field magnitudes and the mixing ratios for the first and second independent solutions are stored on magnetic tape IW4 for subsequent automatic plotting.

The variables read into the computer on cards as data are as follows.

TABLE 2.35

<u>Variable</u>	<u>Description</u>
HMAX	Upper limit (km.) of integration
HMIN	Lower limit (km.) of integration
EUXB (1) EUXB (2) EUYB (1) EUYB (2)	These variables represent the real and imaginary parts of the x and y components of the electric field of downgoing wave at the upper limit HMAX of integration, i.e.,

$$\vec{E}_u = \begin{bmatrix} E_{xu} \\ E_{yu} \end{bmatrix} = \begin{bmatrix} (E_x)_{u1} & (E_x)_{u2} \\ (E_y)_{u1} & (E_y)_{u2} \end{bmatrix} \cdot \begin{bmatrix} b'_1 \\ b'_2 \end{bmatrix}$$

where all quantities are evaluated at HMAX, the subscripts 1 and 2 refer to the 1st and 2nd independent solutions, and the superposition constants b'_1 and b'_2 are given by

$$b'_j = b_j Q_{jj}$$

where the Q_{jj} are the amplitude and phase functions (equation (32), Paper II) and the b_j are constants determined by the boundary conditions.

There are two different ways that the source may be specified at HMAX. Either the constants b'_1 and b'_2 are given, in which case \vec{E}_u is given by the equation above, or else \vec{E}_u is specified at HMAX and b'_1 and b'_2 are then predetermined by the equations

$$b'_1 = \frac{\begin{vmatrix} \text{EUXB} & \text{EUX2} \\ \text{EUYB} & \text{EUY2} \end{vmatrix}}{\Delta}$$

$$b'_2 = \frac{\begin{vmatrix} \text{EUX1} & \text{EUXB} \\ \text{EUY1} & \text{EUYB} \end{vmatrix}}{\Delta}$$

$$\Delta = (\text{EUX1}) (\text{EUY2}) - (\text{EUY1}) (\text{EUX2})$$

When it is preferred that b'_1 and b'_2 be specified then EUXB and EUYB are given the value zero on the input data card.

SB1 (1)
SB1 (2)
SB2 (1)
SB2 (2)

These variables represent the real and imaginary parts of b'_1 and b'_2 , respectively. For the example calculations given in this work, if IRL = 1 then $b'_1 = 1.0$ and $b'_2 = 0.0$ and if IRL = 2 then $b'_1 = 0.0$ and $b'_2 = 1.0$. Separate backward integrations are performed for IRL = 1 and IRL = 2.

A brief description of the various subroutines used in Part III, but not in Part I or Part II, is given below.

TABLE 2.36

<u>Subroutine</u>	<u>Description</u>
DECOMP	Used to check the linear independency of the columns of the wave properties matrix. Each column is normalized with respect to the magnitude of that column. It is then easier to compare different

columns and ascertain the degree of numerical swamping and degradation in the linear independence of the columns.

LGRISO	Computes the hybridizing matrices for the isotropic case.
LGRNG	Computes the hybridizing matrices for the anisotropic case.
CMLOG	Calculates the natural logarithm of a complex number.
SKIP	This is a University of Pittsburgh subroutine which takes the form CALL SKIP (NF, NR, NTAPE), where NF is the number of file marks to be skipped, NR the number of records to be skipped, and NTAPE is the number of the tape to which these commands apply.

Copies of the program object deck and flow chart may be obtained from the Air Force Cambridge Research Laboratories, Ionospheric Physics Laboratory, L.G. Hanscom Field, Bedford, Mass. 01730.

3.0 THE TRANSMISSION OF ELF WAVES THROUGH THE IONOSPHERE

3.1 Ion Cyclotron Resonance

Figure 3.1 depicts the ion cyclotron resonance profile (i.e., the $L = \infty$ surface on the CMA diagram) for the particular model ionosphere used in this work. The ions primarily responsible for each portion of the curve are indicated. That part of the profile which tails off to the left above 2000 km. is due to the constancy of the ion mass (H^+) and the r^{-3} dependence of the magnetic field.

In this analysis a two component plasma was assumed and the effects of ions of different charge to mass ratio were not examined. Propagation effects in a plasma containing several ion species have been discussed by Stix [1965]. Gurnett et. al. [1965] have applied the theory of propagation in a multi-component plasma to ion cyclotron whistlers and Hayakawa et. al. [1969] have calculated the dispersion of waves in the lower exosphere containing multiple ion species for the frequency range 0-150 c/s. Also, experimental evidence has been found for the existence of various ion resonances in the ionosphere. Smith et. al. [1964] reported the discovery of the proton whistler in satellites. Barrington et. al. [1966] observed the helium whistler in Alouette 2 satellite data. More recently Gurnett et. al. report the observation of an ion cyclotron whistler due to an ion with a mass to charge ratio of 8 amu/unit charge. This ion is thought to be either O^{++} or He_2^+ , but its identity has not been clearly established. There

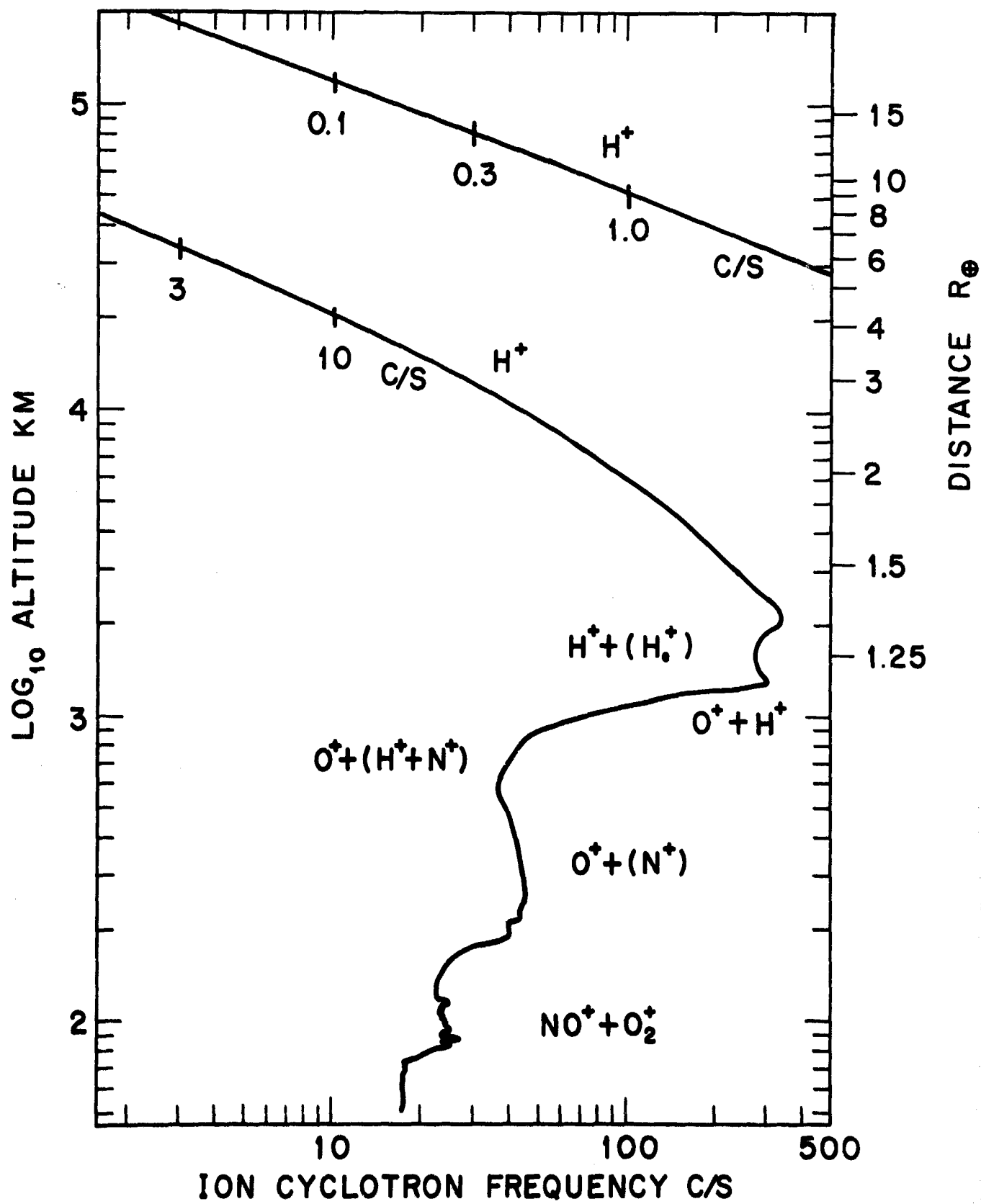


Figure 3.1

is every reason to believe that other ion resonances, such as Ne^+ , O_2^+ , N^+ , O^+ , etc., will be discovered.

The effect that multiple ions have on R and L (the squares of the indices of refraction for the right and left circularly polarized waves, respectively; See Stix [1962]) at 1000 km for the model ionosphere used in this work may be seen in Figure 3.2. In this graph collisions are excluded and L goes to infinity at the gyrofrequency for each ion present in the plasma. For a two component plasma there will appear only one resonance, which corresponds to the gyrofrequency of the effective ion. In addition between each gyrofrequency there appears a point at which $D = 1/2 (R - L) = 0$, ie, R and L cross over each other. The frequency at which this occurs is called the "crossover" frequency. Smith and Brice [1964] find that both modes are linearly polarized at the crossover frequency. Polarization reversal occurs for a wave passing through the crossover frequency. This situation corresponds to the phase velocity surfaces being tangent in the direction parallel to the magnetic field. At this point the R and L labels are interchanged. Such a phenomena does not occur for a two component plasma because D can strictly vanish only for a plasma containing positive ions of different charge-to-mass ratio, provided the magnetic field and electron density are not zero (See problem 2, chapter 1, Stix [1962]). In fact D may vanish only at frequencies greater than the minimum ion cyclotron frequency and less than the maximum ion cyclotron frequency.

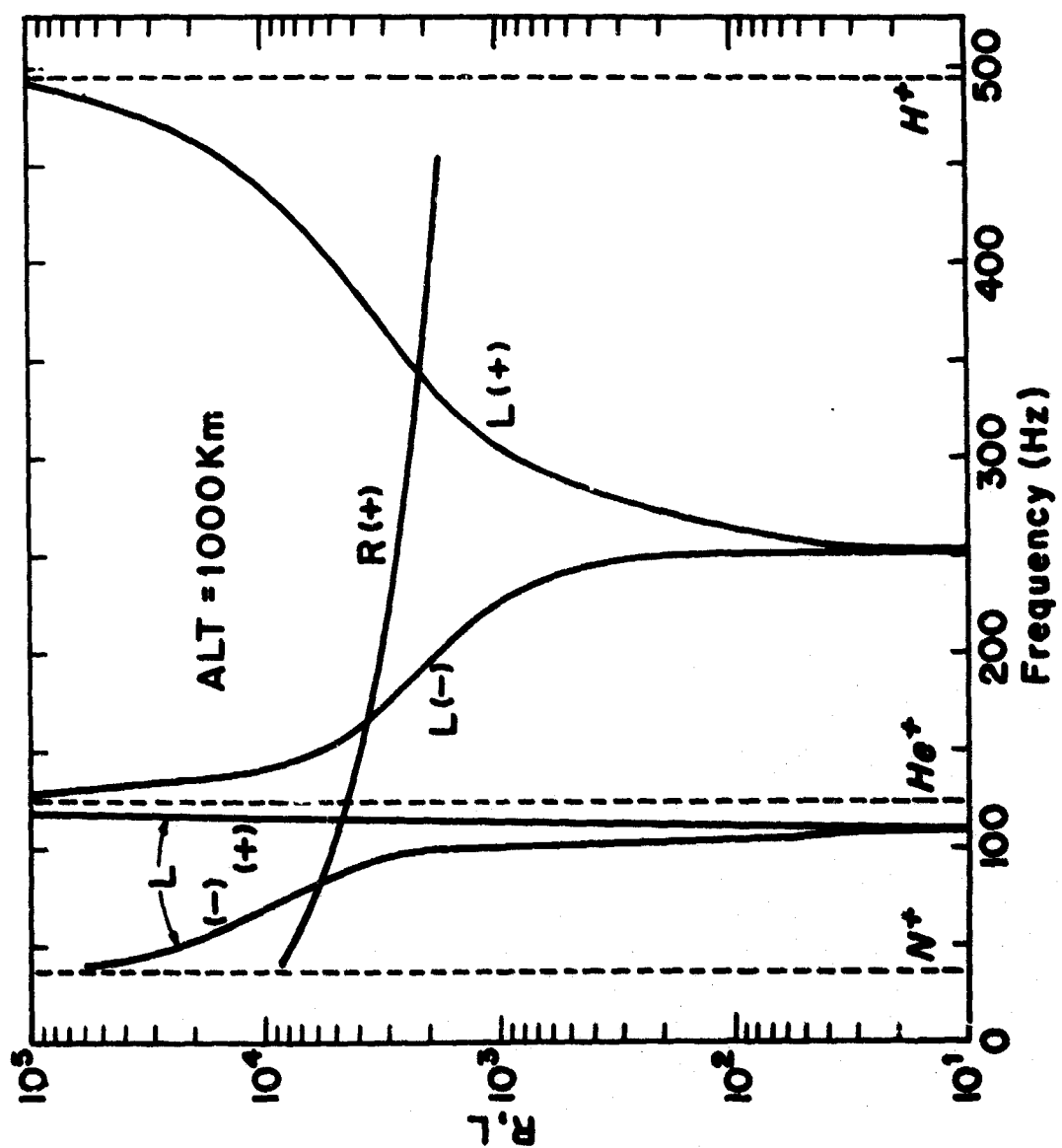


Figure 3.2

The discussion so far has been limited to the case of a collisionless plasma. Including collisions causes the quantities R , L , and D to contain imaginary as well as real parts. A plot of the real parts of R and L with and without collisions for a model ionosphere with multiple ions and also for the case of an effective ion suffering collisions is shown in Figure 3.3. A representative altitude of 200 km is chosen. The subscripts "O" and "I" refer to the quantities calculated excluding collisions and including collisions, respectively, but for a multi-component plasma in both cases. The subscript "eff" refers to a two component plasma containing electrons and an effective ion, with both species suffering collisions.

It is evident from Figure 3.3 that the inclusion of collisions at 200 km has no significant affect on the value of R . This is consistent with the result obtained by Gurnett et. al. [1965] that the real part of R for the collisionless case is the same as the real part of R with collisions when R is expanded to first order in the parameter ν/ω (i.e., the ratio of collision frequency to angular wave frequency). This same result is seen to be true for L when sufficiently far away from the gyrofrequencies. However, collisions do significantly affect the value of L near the gyrofrequencies. The value of L is moderated by collisions and no longer tends to infinity at the gyrofrequencies. Also L may go through zero near the gyrofrequencies and at some point between any two ion gyrofrequencies may become equal to R . Thus even with collisions included there may still be frequencies between the ion

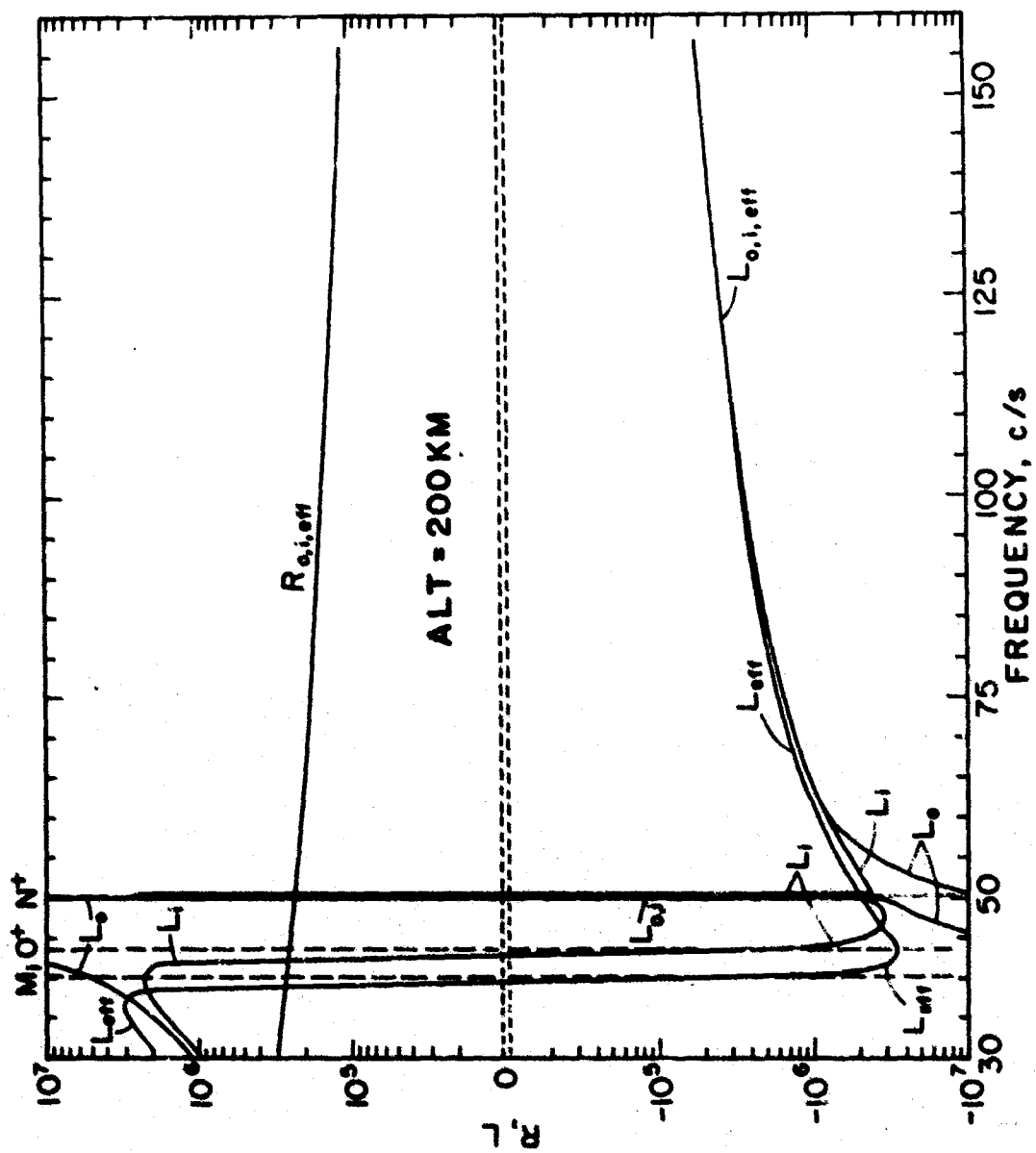


Figure 3.3

gyrofrequencies at which the real part of D is zero.

The question still remains as to whether the vanishing of the real part of D corresponds to a polarization reversal. Gurnet et. al. claim that when the magnitudes of the imaginary parts of R, L, P, and H ($H = RL - PS$) are much less than the real parts of the corresponding quantities then there exists a critical coupling angle Θ_c near $D_o = 0$ determined by the relation

$$\sin^2 \Theta_c \tan^2 \Theta_c = -4 P_o^2 D_i D_o / H_i H_o$$

where the subscripts "o" and "i" refer to the real and imaginary parts, respectively. Thus, in the presence of collisions the wave normal surfaces at $D_o = 0$ intersect over a cone of directions making an angle Θ_c with the magnetic field. This cone is called the critical coupling cone. If a wave passes through this critical coupling cone near $D_o = 0$ a wave of opposite polarization is generated.

However, in Stix' notation, the condition of critical coupling is the vanishing of F^2 , i.e.,

$$F^2 = (RL - PS) \sin^4 \Theta + 4(PD)^2 \sin^2 \Theta = 0$$

Then, in the case of small collisions, the exact condition for critical coupling is

$$\frac{\text{Im}(RL - PS)}{\text{Re}(RL - PS)} + \frac{\text{Re}(PD)}{\text{Im}(PD)} = 0$$

and the critical coupling angle θ_c is given by

$$\sin^2 \theta_c \tan^2 \theta_c = 4 \left[\frac{\text{Im}(PD)}{\text{Re}(RL-PS)} \right]^2$$

Therefore critical coupling does not necessarily take place near the level of

$\text{Re}[D] = 0$. In fact even if $|\text{Im}[D]| \ll |\text{Re}[D]|$, critical coupling may occur.

Also, with collisions included, polarization reversal may arise from the quadrant change of F^2 in the complex plane at a certain angle without causing critical coupling.

Consideration of an effective ion and collisions gives rise to a moderated resonance effect only in the vicinity of the gyrofrequency corresponding to the effective ion (see Figure 3.3). Also, there may exist one crossover frequency (i.e., $D_0 = 0$) when only the effective ion is considered, provided collisions are included. However, at most one such frequency exists.

Therefore, this discussion serves to show that even in the presence of collisions it is necessary to include all the ions in order to determine the wave characteristics of a disturbance propagating with a wave frequency near any of the ion gyrofrequencies.

3.2 Localized disturbance at 100 c/s

3.21 Booker Quartic Roots

Table 3.1 summarizes the nature of the slow and fast waves at 100 c/s in the various regions of the Earth's environment. Figure 3.4 shows the altitude dependence of the Booker quartic roots for the slow (s) and fast (f) waves. The abbreviations QR and QI stand for the real and imaginary parts of the quartic roots, respectively. The indices of refraction for propagation in the z - direction are obtained by multiplying the Q values by a factor of .075. Downgoing and upgoing waves are represented by the same curves and differ only by a minus sign.

The Booker quartic roots are almost entirely real in the region above 1070 km. The slow and fast waves are quite similar in this region and are both propagating. At 1070 km the ion cyclotron resonance is encountered. Below this level the slow and fast waves are interchanged and the fast wave is evanescent. This resonance condition corresponds to a crossing of the $L = \infty$ surface in parameter space on the CMA diagram. The magneto-ionic quantity Y_1 is equal to one. As we shall see later from the mixing ratios and coupling coefficients this resonance causes the L mode to be almost completely reflected back to the magnetosphere. The slow mode is highly propagating down to the neutral atmosphere. Above the resonance level the ionosphere is slightly anisotropic. Below the resonance level the ionosphere is highly anisotropic.

REGION	REFRACTIVE INDEX	PROPAGATION CHARACTERISTICS	
		FAST WAVE	SLOW WAVE
Magnetosphere Alt > 1060 Km	Anisotropic	Propagating	Propagating
Resonance Level 1060 Km	$L = \infty$ Wave normal surfaces interchanged	Wave normal surface disappears	Propagating
Ionosphere 70 < Alt < 1060 Km	Anisotropic	Evanescant	Propagating
Lower D region Alt < 70 Km	Quasi-isotropic	Evanescant	Propagating
Neutral Atmosphere	Isotropic $\text{Re } q = 0$	Evanescant $\text{Im } q = 4.67$	Evanescant $\text{Im } q = 4.67$
Earth's Interior	Isotropic $\text{Re } q = \text{Im } q$	Propagating $ q \sim 10^4$	Propagating $ q \sim 10^4$

TABLE 3.1 Medium characteristics at 100 c/s for a localized disturbance incident at an oblique angle from the vertical at 5000 Km.

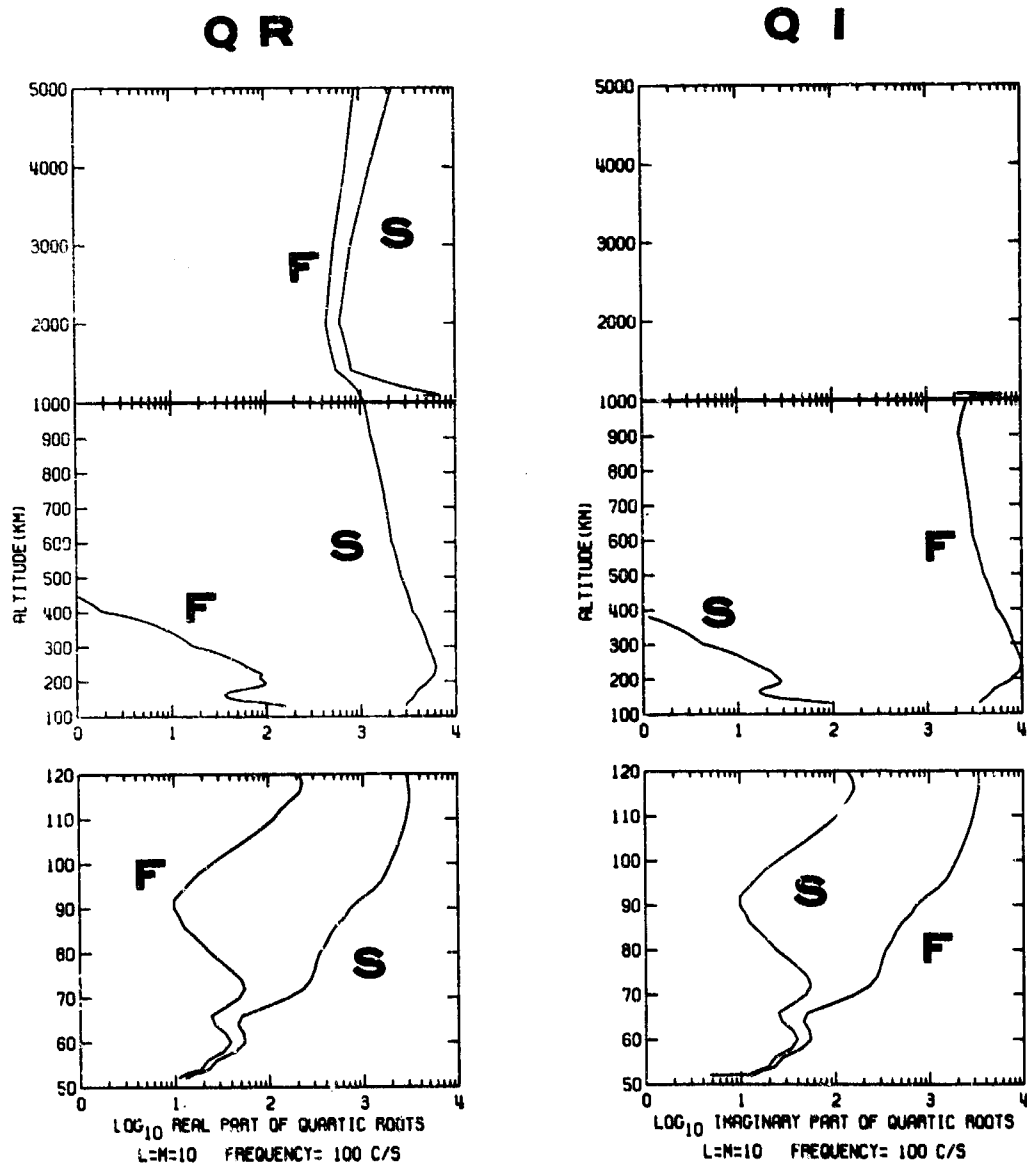


Figure 3.4

In the neutral atmosphere the quartic roots are pure imaginary and both modes are evanescent. This effect is due to the presence of a horizontal component in the propagation vector. In the neutral atmosphere the electron and ion densities are zero. Therefore, in Stix' notation:

$$R = L = P = S = 1$$

$$A = C = 1$$

$$B = 2$$

The dispersion relation then becomes

$$n^4 - 2n^2 + 1 = 0$$

or

$$(n^2 - 1)^2 = 0$$

$$n^2 = 1 = n_x^2 + n_z^2$$

thus

$$n_z^2 = 1 - \frac{c^2}{v_x^2}$$

If $v_x^2 \ll c^2$, then

$$n_z^2 < 0$$

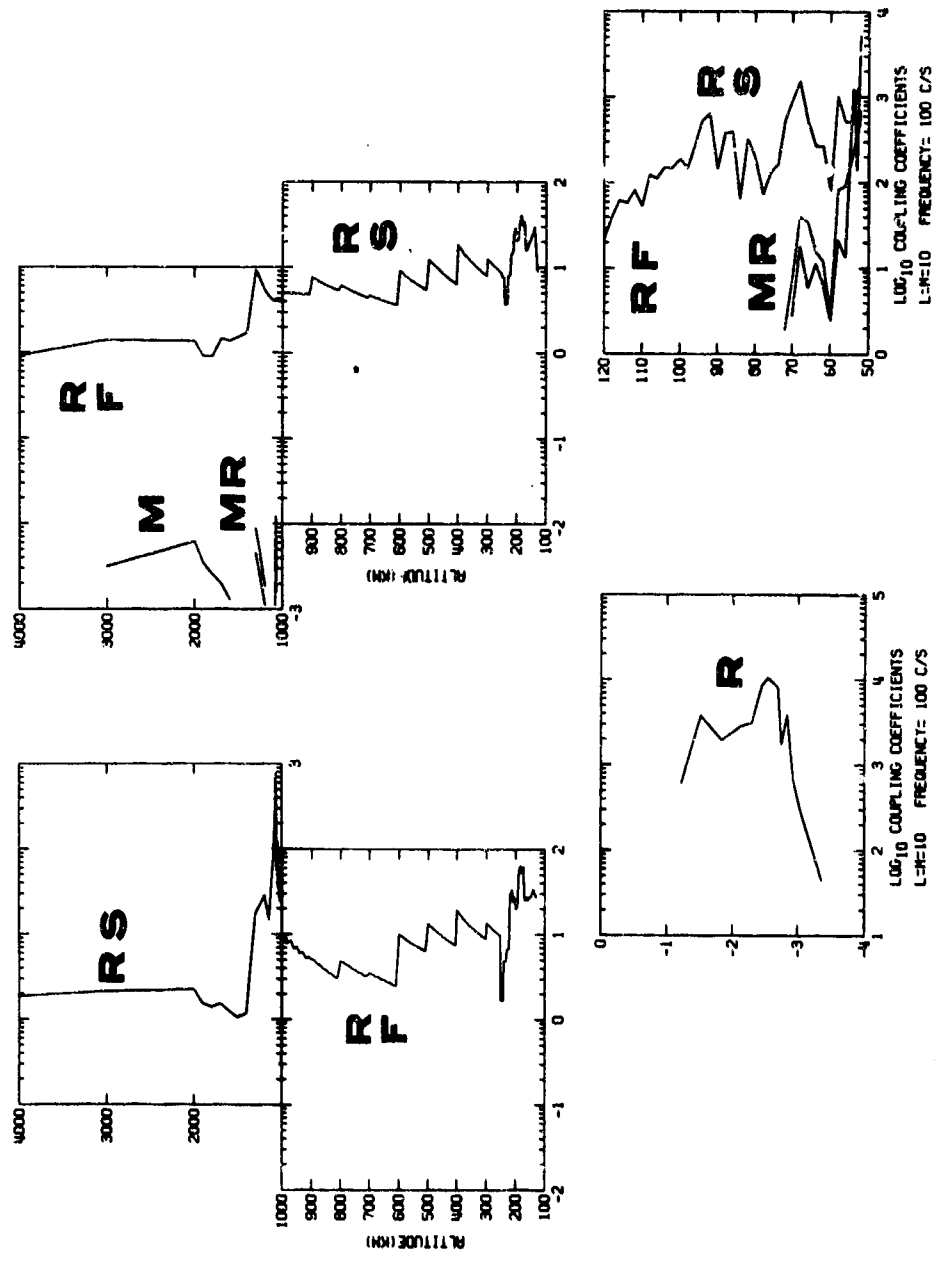
and hence n_z is pure imaginary.

Thus the neutral atmosphere acts as an elastic medium for the vertically propagating component of the particular localized disturbance being considered. If v_x had been greater than c then $0 \leq n_z < 1$ and the neutral atmosphere would have been dispersive for the vertically propagating component.

Inside the Earth the magnitudes of the real and imaginary parts of the quartic roots are all equal. Thus the Earth's interior is isotropic and "dense resistive", ie. behaves like a metal.

3.22 Magneto-ionic Coupling Coefficients

Figure 3.5 shows the magneto-ionic coupling coefficients (See



MAGNETO-IONIC COUPLING

Figure 3.5

Inoue and Horowitz, 1966a) for the localized disturbance at 100 c/s.

The abbreviations S, F, M, R stand for slow, fast, mode coupling and reflection, respectively. Thus RS means reflection of the slow wave.

M means generation of a downgoing slow wave from a downgoing fast wave or an upgoing fast wave from an upgoing slow wave, etc. MR means generation of a upgoing fast wave from a downgoing slow wave or an upgoing slow wave from a downgoing fast wave, etc.

Reflection is the dominant type of coupling at almost all heights. At 1070 km reflection type coupling for the slow wave becomes very large because of the ion cyclotron resonance. For the fast wave below this level the magnitude of the coupling is larger than or comparable to the quartic roots. For the slow wave below the resonance level coupling is of less importance than the quartic roots down to the D region. In the lower D region coupling becomes very large for the slow and fast modes. Mode reflection type coupling also appears. The plane wave case produces no mode reflection type coupling in the lower D region. Therefore this effect is due to the localized nature of the disturbance.

Reflection type coupling occurs within the surface layer of the earth and is a maximum at a depth of about 2.5 km. This reflection region corresponds to the rapid change in the earth conductivity. In this region the coupling coefficients are in general smaller than the quartic roots but are of comparable magnitude at a depth of 2.5 km.

3.23 Characteristic Wave Mixing Ratios

The mixing ratios (See section 2.33 for definition) for the incident fast wave are given in Figure 3.6. Above 1070 km. the resultant wave fields consist primarily of a downgoing fast (DF) wave but with some partial reflection occurring as may be seen by the presence of a small amount of the upgoing fast wave (UF). The mixing ratio for the upgoing fast wave exhibits a standing wave nature due to reflection from the ion cyclotron resonance level. The downgoing slow wave (DS) is generated by mode coupling, which may also be seen in the coupling coefficients in Figure 3.5. The upgoing slow (US) wave is generated by mode reflection type coupling, again also seen in Figure 3.5. However, these last two waves offer only a small contribution to the total wave field.

From 1070 km. down through the D region the dominant mixing ratio is that of the downgoing slow wave. (Remember that below the critical reflection layer the R mode becomes a slow wave). Some partial reflection is seen throughout this altitude range as evidenced by the mixing ratio for the upgoing slow wave. Between 700 and 1000 km. there is a standing wave due to the ion mass changing very rapidly. The standing wave between 300 and 600 km. is caused by the upper slope of the F maximum electron density. There is also a standing wave centered on the F region maximum.

In the D region the mixing ratios for the downgoing and upgoing fast waves grow rapidly as a consequence of the mode reflection type

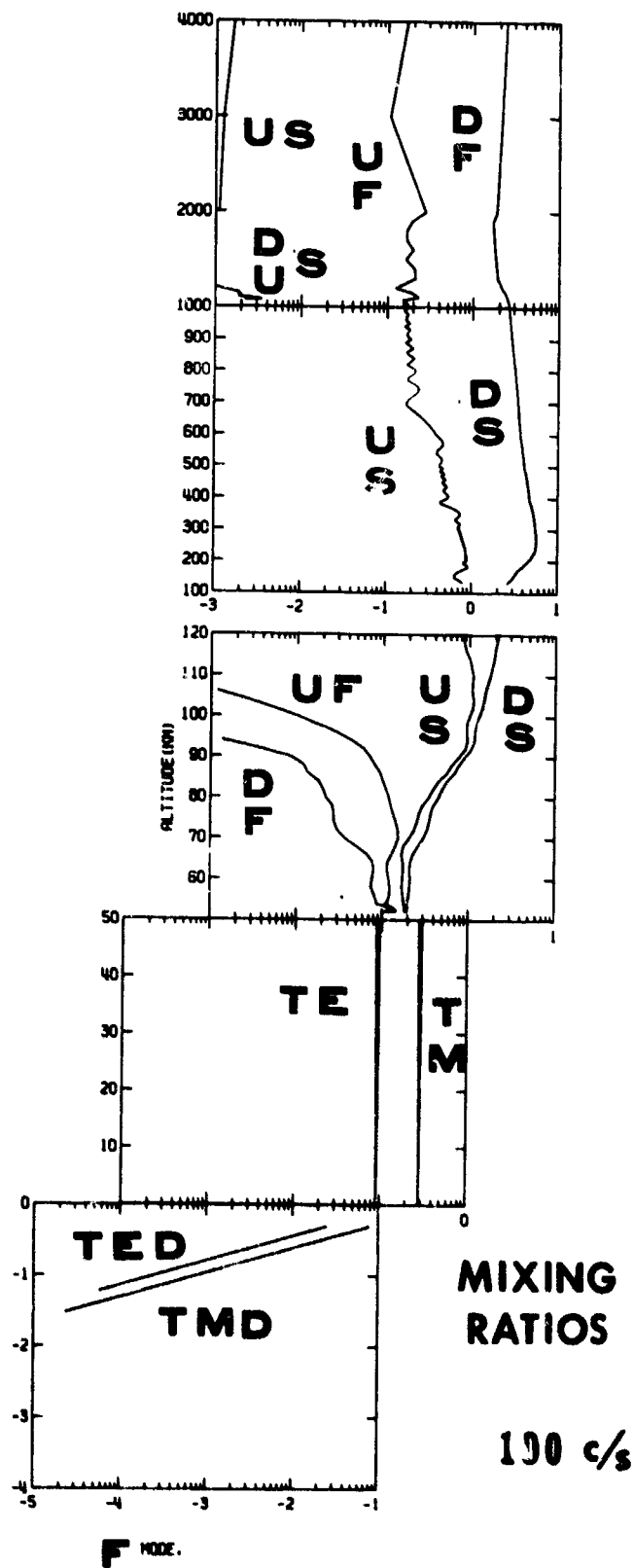
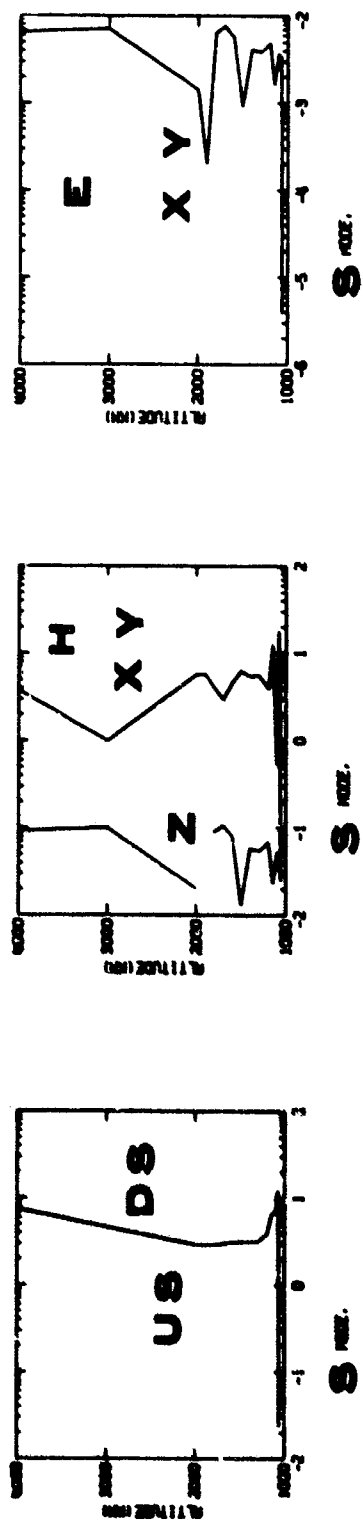


Figure 3.6

coupling already seen in Figure 3.5. This effect is due to the localized nature of the disturbance.

In the neutral atmosphere and in the ground the transverse magnetic (TM) wave is larger than the transverse electric (TE). The earth acts as a good conductor and almost complete reflection occurs as seen from the approximate equality of the downgoing and upgoing parts of the TM and of the TE waves. The mixing ratios are attenuated logarithmically in the ground and only downgoing waves are present. Although the coupling coefficients indicate that reflection occurs for both the transverse magnetic and transverse electric modes between about 1 and 3 km. depth this process has negligible effect on the resultant mixing ratios and wave fields due to the fact that the quartic roots are larger than the coupling coefficients and are therefore more important in determining the final wave field characteristics.

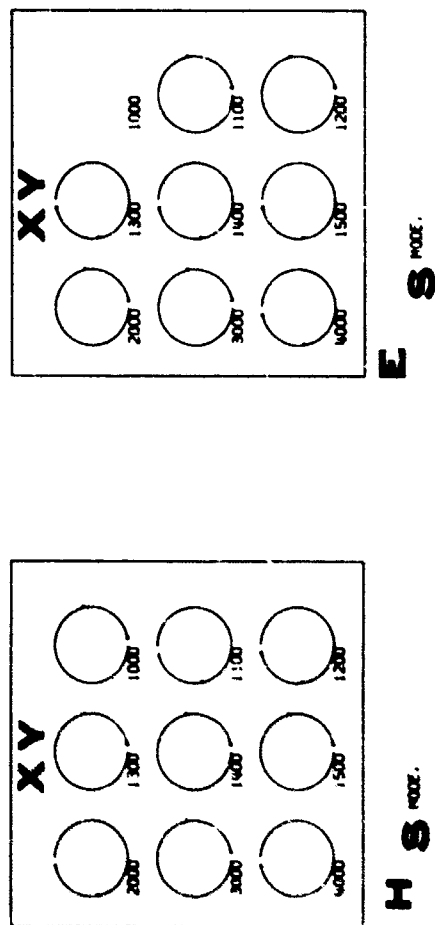
The mixing ratios for the incident slow wave may be seen in Figure 3.7. The equality of the mixing ratios for the downgoing slow and upgoing slow waves indicates that complete reflection takes place at 1070 km., the ion cyclotron resonance level. Thus the slow mode (ie. the L mode) is completely non-penetrating below this level. This result is in agreement with the prediction of the CMA diagram that the wave normal surface for the L mode disappears upon crossing the $L = \infty$ surface from lower to higher frequencies.



MIXING RATIOS

100 c/s

WAVE FIELD



POLARIZATION

Figure 3.7

3.24 Wave Fields

The wave fields of the incident fast wave are shown in Figure 3.8.

The magnitudes of the electric and magnetic fields are all relative to the values at 4000 km. If the magnetic field values are multiplied by a factor of 0.25 the B field is then obtained in gammas (1 gamma = 10^{-5} gauss). The electric field is read directly in volts/meter. The letters x, y, z stand for the corresponding components of the field quantities.

The wave fields exhibit the same standing wave characteristics as the mixing ratios in the F region. The standing wave above 1070 km. is due to partial reflection above the ion cyclotron resonance level. The standing wave between 300 and 600 km. is caused by partial reflection from the upper slope of the F maximum electron density. A standing wave is also centered on the F layer maximum. Standing waves are visible in the wave fields down through the E region but are less obvious in the D region and neutral atmosphere. In the D region mode coupling produces the separation in the x and y components of the electric and magnetic fields and an increase in the z - component of the electric field. The electric field remains essentially vertical throughout the neutral atmosphere and must cause charge separation to occur between the Earth's surface and the lower ionosphere. In the ground the fields are attenuated logarithmically.

The wave fields for the incident slow wave display a standing wave effect above 1070 km. due to reflection from the ion cyclotron

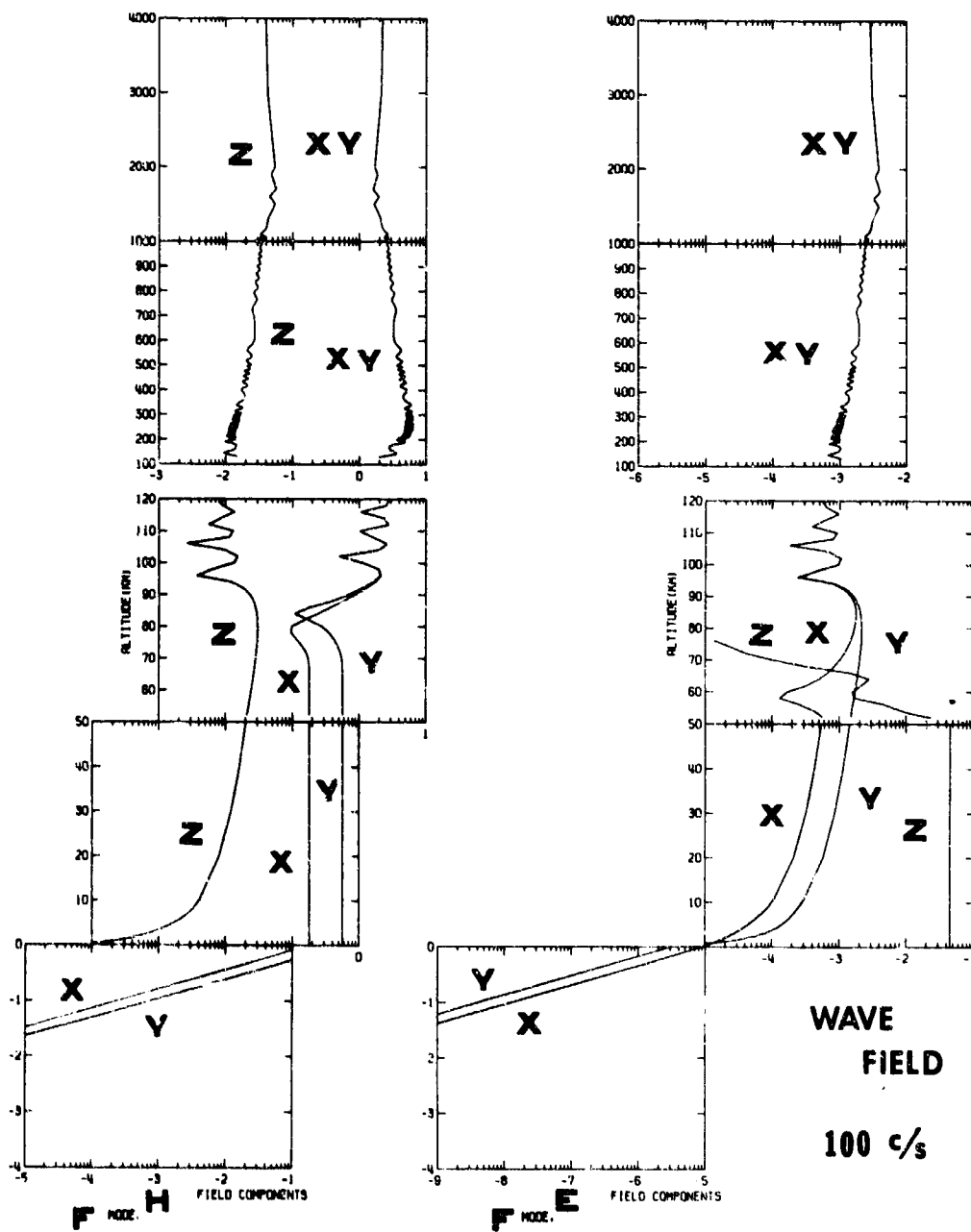


Figure 3.8

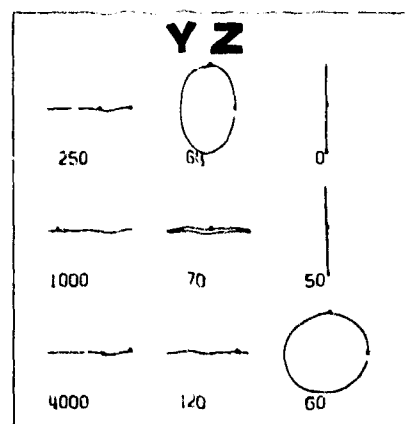
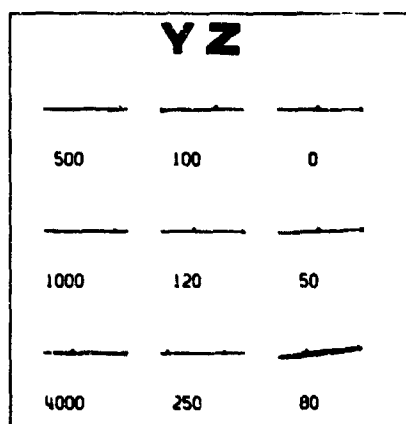
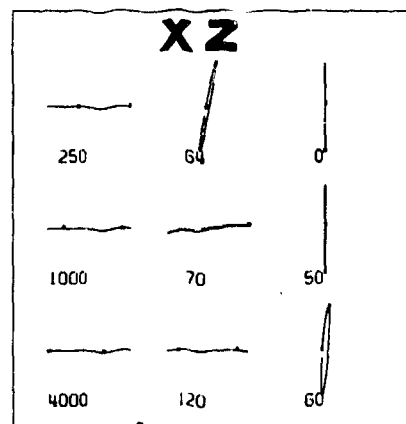
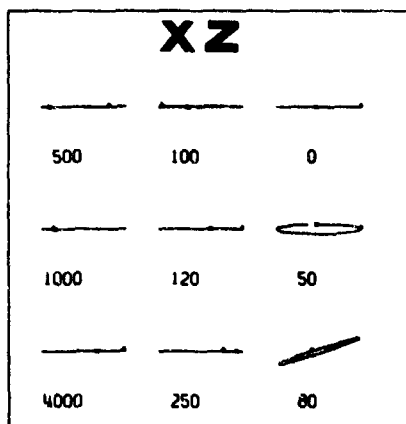
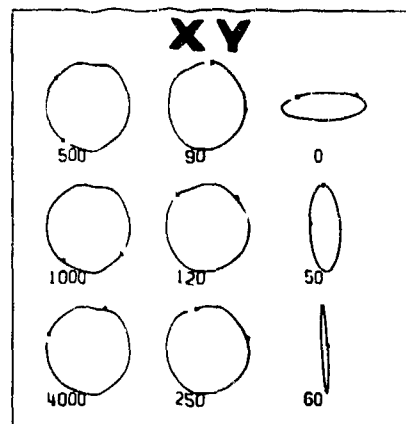
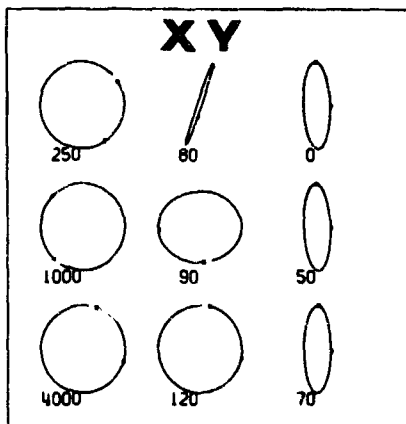
resonance level. The fields are completely zero below this level and further substantiate the fact that the L mode is non-penetrating beyond the ion resonance level.

3.25 Wave Field Polarization

The polarizations of the electric and magnetic wave fields for the incident fast wave are given in Figure 3.9. The labeling at the top of each diagram specifies the plane in which the polarization is plotted. For example, "YZ" implies that the y component of the field quantity is plotted along the horizontal direction and the z component is plotted along the vertical direction. The number under each polarization curve represents the altitude in km. for which that polarization plot is valid. The Earth's magnetic field is directed inward and rotation in the clockwise direction represents right handed polarization. To obtain the direction of rotation the gap in the polarization curve must first be found. That side of the gap which is marked with an "x" represents the beginning point. At 90° from the "x" is a dot and the rotation sense is obtained by proceeding from the "x" to the dot. At each altitude the plot is normalized to the larger of the two components being plotted. Thus in order to determine the relative sizes of plots at different altitudes one must determine the wave field magnitudes from Figure 3.8.

In the x-y plane the electric and magnetic fields are right circularly polarized down to the D region. Due to the mode coupling which produces a separation in the x and y components of the electric

POLARIZATION



H FIELD POLARIZATION
F MODE, FREQUENCY: 100 C/S

E FIELD POLARIZATION
F MODE, FREQUENCY: 100 C/S

Figure 3.9

and magnetic fields in the D region the fields become elliptically polarized in the lower ionosphere. At 50 km. the electric field becomes left elliptically polarized and then changes back to right elliptically polarized at ground level. Thus the fast mode which is polarized in the right hand sense at 4000 km. is also right handed polarized at ground surface.

However, on the Earth's surface the x and y components of the electric field are smaller than the z component by three and four orders of magnitude respectively. Thus the xz and yz planes are more important than the xy plane. In these planes the electric field on the ground is linearly polarized.

The incident slow mode is left circularly polarized throughout the region above the ion cyclotron resonance level.

3.3 Comparison of Plane Wave with Localized Disturbance at 100 c/s

Comparison of the effects of the plane wave and localized disturbance shows very little difference between the incident slow modes. Both are non-penetrating below about 1070 km. and in both cases the downgoing slow wave is reflected in the form of an upgoing slow wave. The major difference seems to be that the wave fields of the plane wave are π out of phase with those of the localized disturbance. However, comparison of the incident fast modes does reveal some differences. Because there is no propagation in the horizontal direction the plane wave propagates vertically through the neutral atmosphere

with a phase velocity equal to the speed of light. Thus the neutral atmosphere behaves like free space for the plane wave but appears as an elastic evanescent region to the localized disturbance.

Also, mode coupling and mode reflection type coupling appear for the localized disturbance in the lower D region but no such coupling appears for the plane wave. Reflection of the slow mode however still occurs throughout the ionosphere for the plane wave just as it does when the localized disturbance effect is introduced. The z components of the electric and magnetic fields are zero everywhere for the plane wave and the electric field polarization in the xy plane remains right circularly polarized throughout the ionosphere and the neutral atmosphere. In contrast the localized effect produces a z component of the magnetic field throughout the ionosphere and atmosphere and a z component of the electric field in the lower D region and neutral atmosphere. The z components are due to the additive interference of the upgoing and downgoing waves. Therefore only the localized disturbance gives rise to charge separation between ground level and the lower ionosphere. Also the localized disturbance wave field polarizations changed considerably in the lower D region due to strong coupling.

Within the Earth the x and y components for both the electric and magnetic fields are equal in the plane wave case but the localized disturbance gives rise to an inequality in these components.

3.4 Ionospheric Electric and Magnetic Field Measurements

Very few field measurements exist for the ELF range around 100 c/s but several experiments have been performed [Maynard et. al., 1969; Shawhan et al., 1968; Scarf et. al., 1968; Gurnett et. al., 1969]. Various difficulties have been encountered and not all measurements are in agreement. Maynard et. al. measured the complete wave characteristics of several whistlers, whose source was the local ionosphere waveguide, between approximately 100 and 200 km. with a Te-Tomahawk sounding rocket. In particular, one whistler measured at 171.2 km. was elliptically polarized and had the lowest frequency component observed, ie. 60 c/s, with an electric field value between 100 and 200 $\mu\text{v}/\text{m}$. Shawhan et. al. measured electric and magnetic fields with the Javelin 8.45 sounding rocket. However, the measurements were rather broadband (30-650 c/s) and indicated electrostatic noise (ie. no magnetic field). Also Shawhan et. al. were not sure if these measurements were indicative of a natural phenomena or due to payload interaction with the ionosphere. Scarf et. al. performed electric and magnetic field measurements with sensing equipment on board the OV3-3 satellite. Most observations were electrostatic but one case was electromagnetic. At an altitude of 364 km. the maximum magnetic field strength was 80 milligammas at a frequency of 525 c/s. The electric field strength was on the order of 100 microvolts/meter. Low frequency measurements were hampered by spacecraft noise. Gurnett et. al.

obtained observations of electric and magnetic fields with the Injun 5 satellite, launched on August 8, 1968, into an elliptical polar orbit with an apogee of 2528 km. and a perigee of 677 km. The Injun 5 experiment had the capability of measuring electric and magnetic fields of plasma wave phenomena over two frequency bands, 0.3 to 10 kc/s and 30 to 350 c/s. The maximum magnetic field strengths for the latter band were about 50 milligammas. The maximum electric field strengths were on the order of 3.5 mv/m for the lower frequency band but in general the wide-band electric field strengths are much less, of the order of 100 uv/m or less. These electric field strengths are smaller than those reported by Scarf et. al. Gurnett et. al. found that the electric and magnetic field strengths vary together, suggesting that the field variations are due to electromagnetic waves, possibly ELF hiss where the variations are smooth, and discrete emissions (chorus) where the fluctuations are rapid.

A typical value of 100 milligammas is assumed for the magnetic wave field strength at 360 km. and is used in conjunction with the full wave results to predict electric and magnetic wave field strengths at other altitudes (See Table 5.7, Chapter 5).

4.0 THE TRANSMISSION OF ULF WAVES THROUGH THE IONOSPHERE

4.1 Localized Disturbance at 3.0 c/s

4.1.1 Booker Quartic Roots

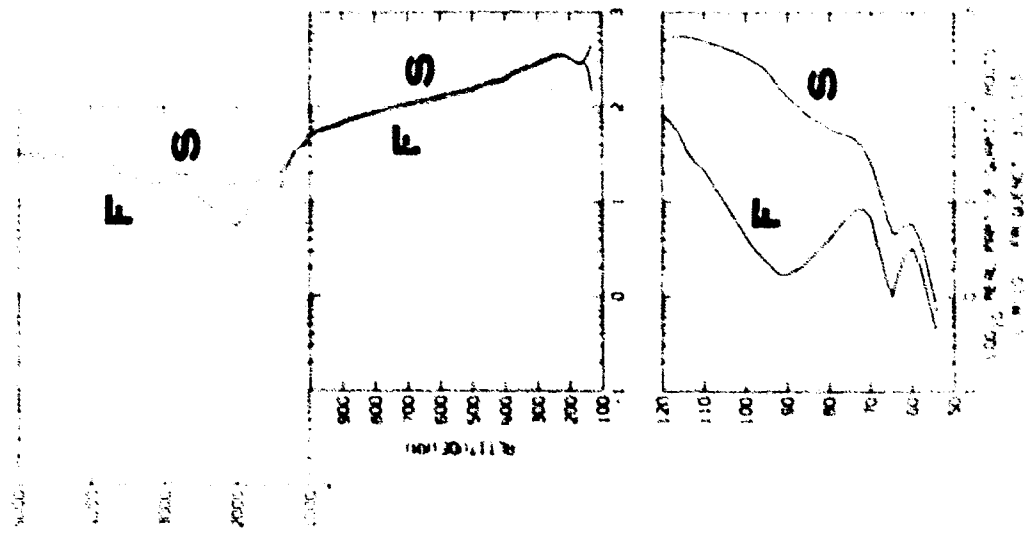
Table 4.1 summarizes the properties of the slow and fast wave disturbances at 3.0 c/s in the ionosphere, neutral atmosphere and the Earth's interior. The Booker quartic roots are presented in Figure 4.1. The labeling used in this figure is the same as that explained in section 3.21. The actual values of the index of refraction for propagation in the vertical direction are obtained by multiplying the values read from the curves in Figure 4.1 by a factor of 2.50.

Comparison of the real and imaginary parts of the quartic roots reveals that both the slow and fast modes are propagating down to about 150 km. The region above 1000 km. is quasi-isotropic. At 1000 km. mode switching occurs and the slow wave becomes a fast wave and the fast wave becomes a slow wave. At 150 km. mode switching again occurs with the slow mode changing back to the fast mode and vice versa. In section 4.15 we shall see that the wave fields undergo a polarization reversal at 1000 km. but not at 150 km. This region between 1000 km. and 150 km. is essentially isotropic. Between 220 km. and 150 km. the real parts of the slow and fast wave quartic roots are indistinguishable. However, the fast wave is evanescent between 150 km. and the Earth's surface. The slow wave is propagating down to about 70 km. at which it becomes

REGION	REFRACTIVE INDEX	PROPAGATION CHARACTERISTICS	
		SLOW WAVE	FAST WAVE
Magnetosphere and upper Ionosphere	Quasi-isotropic	Propagating	Propagating
Transition 160 Km - 220 Km	Isotropic $\text{Re } q_s = \text{Re } q_f$ $\text{Im } q_s \neq \text{Im } q_f$	Propagating	Propagating
Lower Ionosphere	Anisotropic	Propagating	Evanescent
Transition 52 Km - 67 Km	Quasi-isotropic	Evanescent	Evanescent
Neutral Atmosphere	Isotropic $\text{Re } q = 0$	Evanescent $\text{Im } q = 14$	Evanescent $\text{Im } q = 14$
Earth's Interior	Isotropic $\text{Re } q = \text{Im } q$	Propagating $ q \sim 10^3 - 10^4$	Propagating $ q \sim 10^3 - 10^4$

TABLE 1.1 Medium characteristics at 3.0 c/s for a localized disturbance incident at an oblique angle from the vertical at 5000 Km.

QR



QI

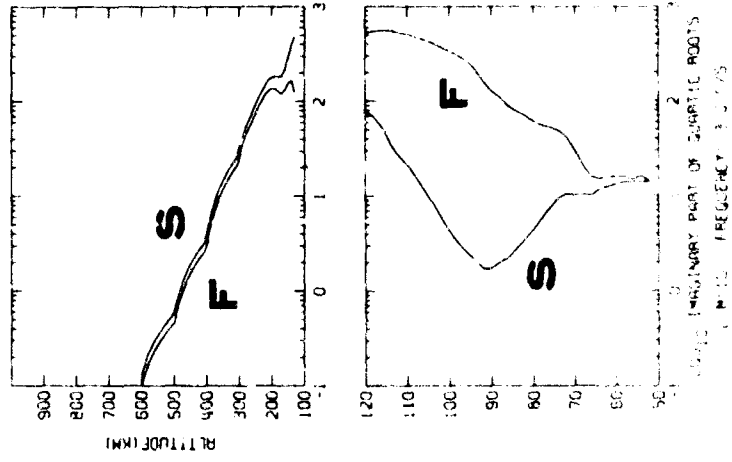
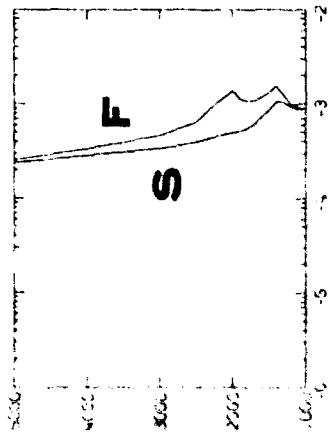


FIGURE 1.1

evanescent and remains as such down to ground level. The lower D region between about 70 km. and 50 km. is quasi-isotropic. The phase velocities of the fast and slow waves reach their minimum values around 250 km. and 120 km., respectively.

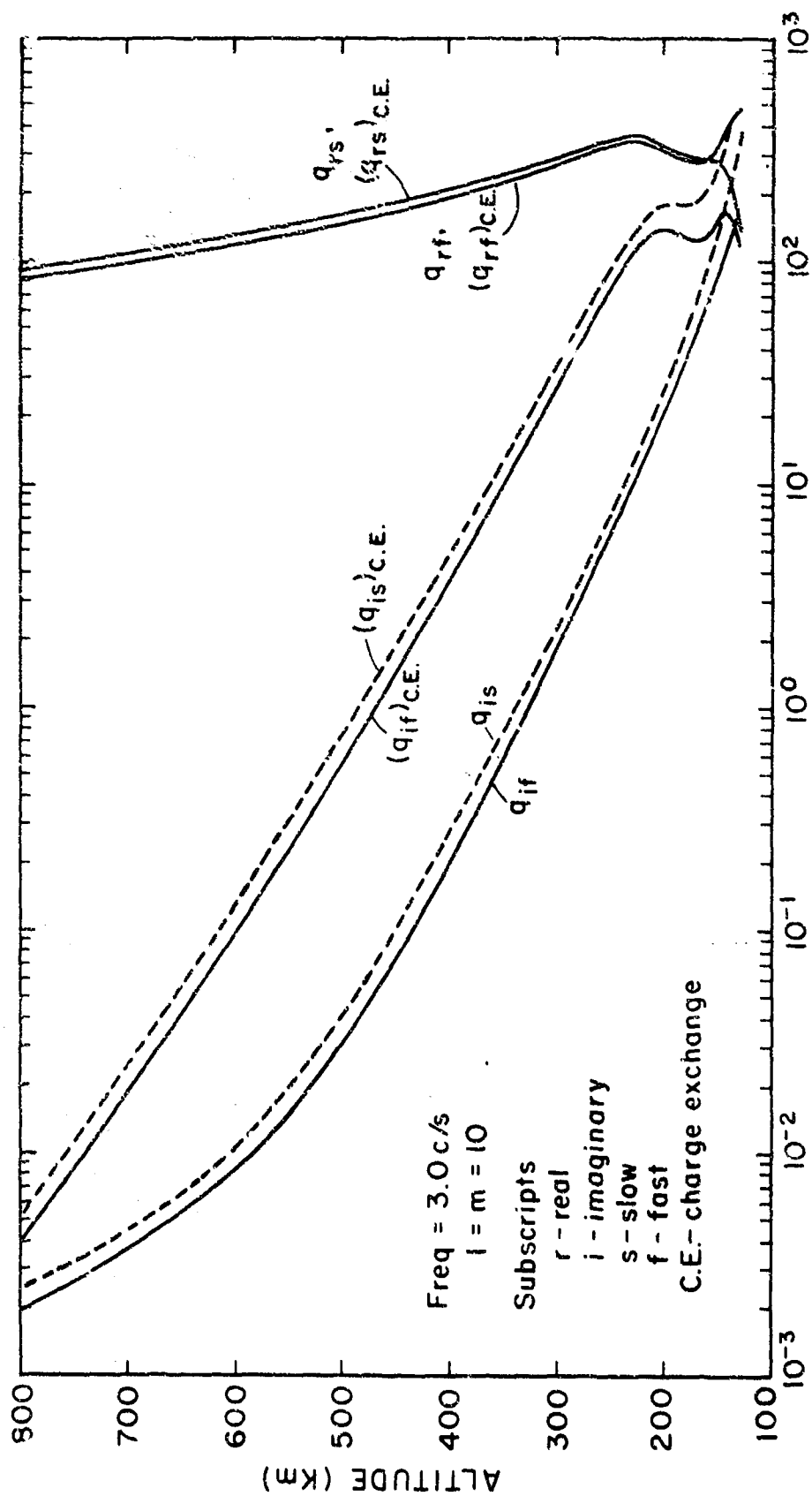
The neutral atmosphere is isotropic and the quartic roots for this region are pure imaginary due to the localization of the disturbance (See section 3.21). The interior of the Earth is also isotropic and behaves as a metal.

4.111 Effect of Charge Exchange on the Booker Quartic Roots

Comparison of the quartic roots obtained by including charge exchange with the quartic roots obtained by excluding charge exchange collisions is shown in Figure 4.2. The real parts of the quartic roots are essentially unaffected by charge exchange between 150 and 800 km. altitude. On the other hand the imaginary parts of the Booker quartic roots are enhanced by as much as an order of magnitude. In the altitude range 150 to 250 km. the imaginary parts of the quartic roots with charge exchange included are the same order of magnitude as the real parts. Hence inclusion of charge exchange collisions significantly enhances the absorption of the disturbance in the region 150-250 km., where charge exchange of O^+ with O is the dominant process. Figure 4.5 and 4.6 show that the electric and magnetic wave fields are indeed greatly reduced in amplitude in this region.

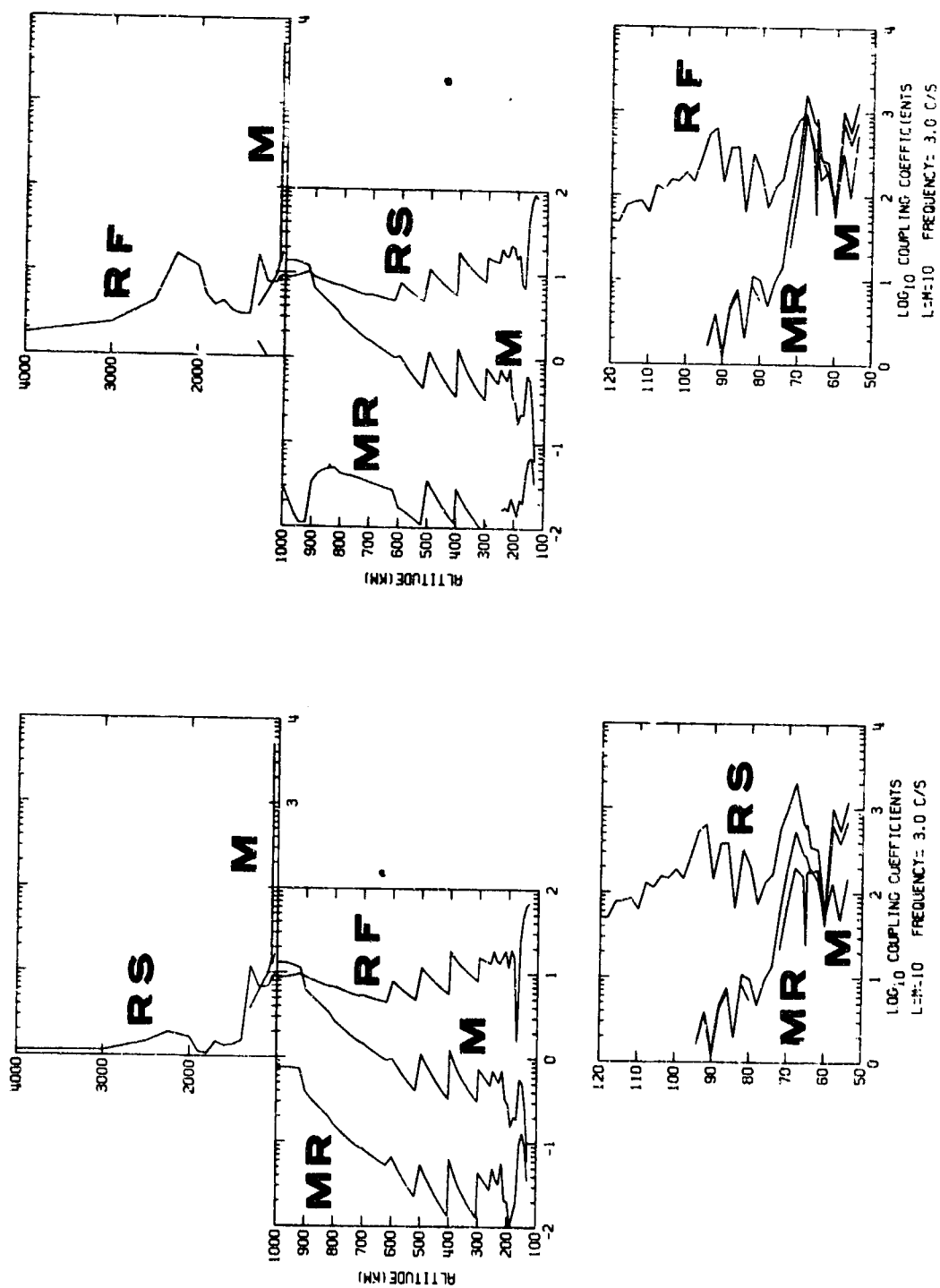
4.12 Magneto-ionic Coupling Coefficients

Figure 4.3 reveals the altitude dependence of the magneto-



Booker Quartic Roots
Effect of charge exchange on the Booker Quartic Roots

Figure 4.2



MAGNETO - IONIC COUPLING

Figure 4.3

ionic coupling coefficients for the localized disturbance at 3.0 c/s. These curves have the same nomenclature attached to them as that explained in section 3.22.

Reflection type coupling is dominant down to about 1000 km. At this altitude there is a strong mode coupling layer caused by the equality of the fast and slow wave quartic roots, ie. the medium rapidly approaches isotropic conditions. Reflection type coupling for both the slow and fast modes once again becomes the major coupling process below about 900 km. and remains dominant down to the lower D region. In the F region mode coupling and mode reflection type coupling are also present due to the quasi-isotropic nature of the F region. These coupling processes become small in the E region because the medium is anisotropic and reappear in the lower D region due to the localized disturbance (See section 3.22). Thus coupling is of importance in the D and F regions but not in the E region. The quartic roots are larger than the coupling coefficients throughout the F region except for the region around 1000 km. where mode coupling becomes very large. The fast wave quartic roots are smaller than the coupling coefficients throughout the D and E regions. The coupling coefficients become larger than the slow wave quartic roots below about 95 km. Coupling in the neutral atmosphere is, of course, zero.

As with the 100 c/s case, reflection type coupling occurs in the surface layer of the Earth and reaches a maximum at a depth of about 2.5 km. This reflection process corresponds to the rapid

change in the ground conductivity. The coupling coefficients in this region are smaller than the quartic roots but become of similar magnitude around a depth of 2.5 km. The medium inside the Earth is isotropic and behaves as a metal.

4.13 Characteristic Wave Mixing Ratios

The characteristic wave mixing ratios for the incident slow and fast waves at 3.0 c/s are depicted in Figure 4.4. The labeling used for these curves is explained in section 3.23.

In the region above 1000 km. the resultant wave for the incident slow mode consists primarily of the downgoing slow wave. The presence of the upgoing slow wave is indicative of reflection taking place throughout the region. The downgoing and upgoing fast waves are also present and are generated by mode coupling and mode reflection type coupling. In the F region below 1000 km. the downgoing fast and downgoing slow waves are nearly equal in magnitude due to the strong coupling associated with this quasi-isotropic region. The upgoing fast and upgoing slow waves are also present due to reflection from the F region maximum. The standing wave formation in these upgoing waves is quite obvious. Around 200 km. the real and imaginary parts of the quartic roots are equal as in a conductor. Therefore this level will behave as the upper conducting wall of a cavity with the other conducting wall being the Earth's surface. This fact is borne out when we look at the standing wave formation observed in the wave fields in the next section. Below this level in the D and E regions the downgoing slow and

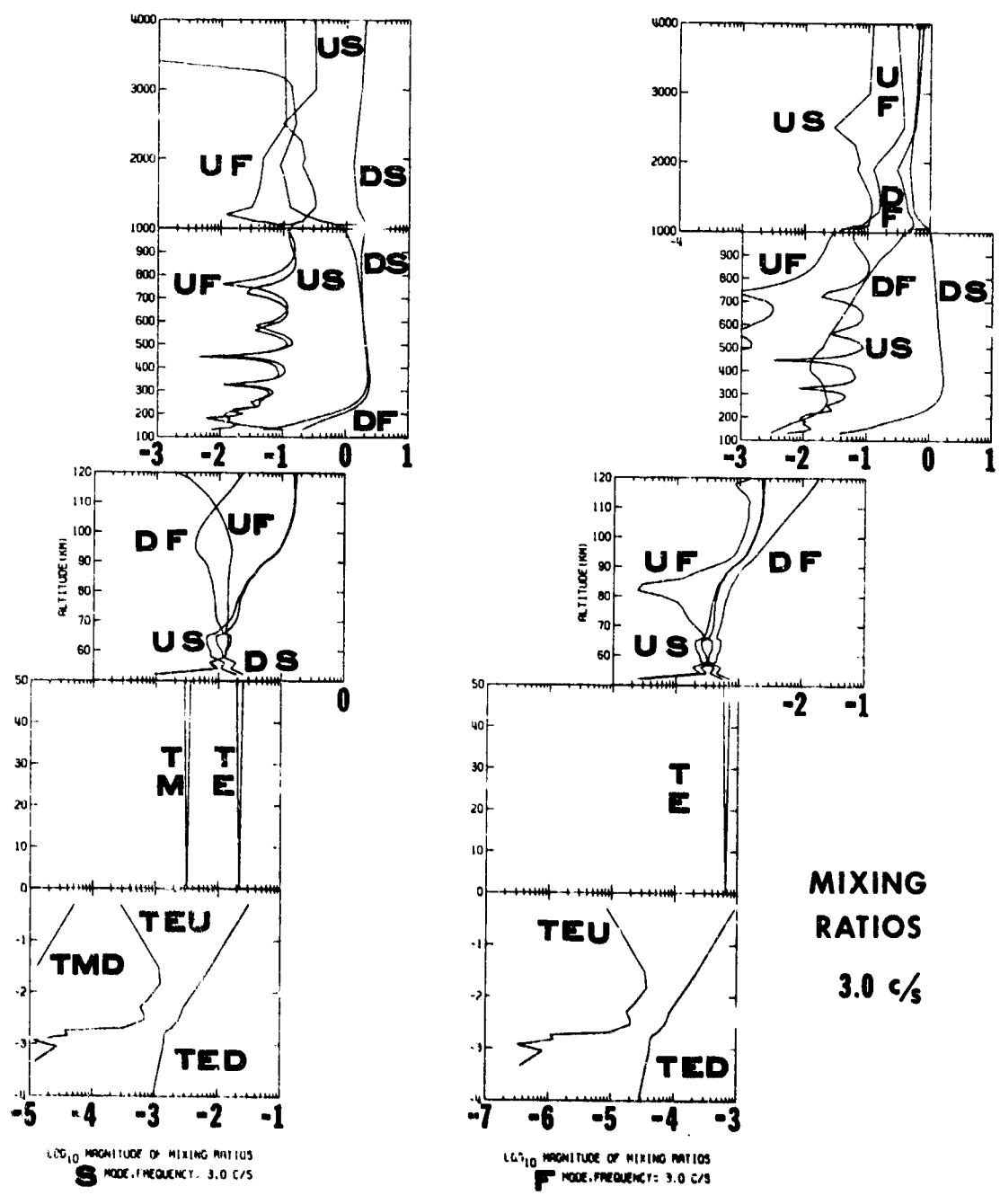


Figure 4.4

upgoing slow waves are almost equal, indicating that reflection is continuously taking place. In the neutral atmosphere the incident slow wave is comprised of both transverse electric and transverse magnetic waves with the transverse electric being dominant. Both the TE and TM modes are reflected quite well at ground surface.

Reflection of the transverse electric wave is also seen to take place within the Earth and the maximum of the reflected wave occurs at a depth of about two km., near the conductivity maximum.

For the incident fast wave above 1000 km. all of the characteristic waves are of the same order of magnitude. The upgoing waves are generated by reflection and mode reflection type coupling. Although this region is anisotropic it is sufficiently close to being isotropic that mode coupling and mode reflection type coupling are important. In fact the downgoing slow wave is at times larger than the downgoing fast wave. In the F region below 1000 km., where the slow wave becomes a fast wave and vice versa, the downgoing slow wave is dominant and a standing wave formation occurs in the reflected upgoing slow wave. The downgoing fast and upgoing fast waves are also present due to mode coupling and mode reflection type coupling, respectively, resulting from the quasi-isotropic nature of this region. In the D and E regions the reflected upgoing fast wave is smaller than the downgoing and upgoing slow waves, which are generated by mode coupling and mode reflection type coupling, respectively. Thus the D and E regions will not act to store energy for the incident fast wave as readily as for the

incident slow wave. This fact will be easily seen from inspection of the wave fields. In the neutral atmosphere the incident fast wave is transverse electric and is reflected quite well at the Earth's surface. Inside the Earth the incident fast wave is primarily comprised of the downgoing transverse electric mode. However reflection produces a small amount of the upgoing transverse electric mode which reaches a maximum at a depth of about two km., near the conductivity maximum.

4.14 Wave Fields

The wave fields of the incident slow wave are shown in Figure 4.5. The magnitudes of the electric and magnetic fields are all relative to the values at 4000 km. If the magnetic field values are multiplied by a factor of 8.33 the B field is then obtained in gammas. The electric field is read directly in volts/meter.

The incident slow wave disturbance is primarily transverse magnetic at the top of the ionosphere and becomes transverse electric in the ground. In the region above 1000 km. a standing wave character is exhibited and is due to reflection from the interface separating the anisotropic region above 1000 km. from the quasi-isotropic region below 1000 km. Standing waves are also seen in the region between 150 and 1000 km. and are due to reflection within this isotropic region.

Standing waves are still discernible down through the D region and neutral atmosphere but are of considerably longer wavelengths than were seen in the F region. The y component of the magnetic field

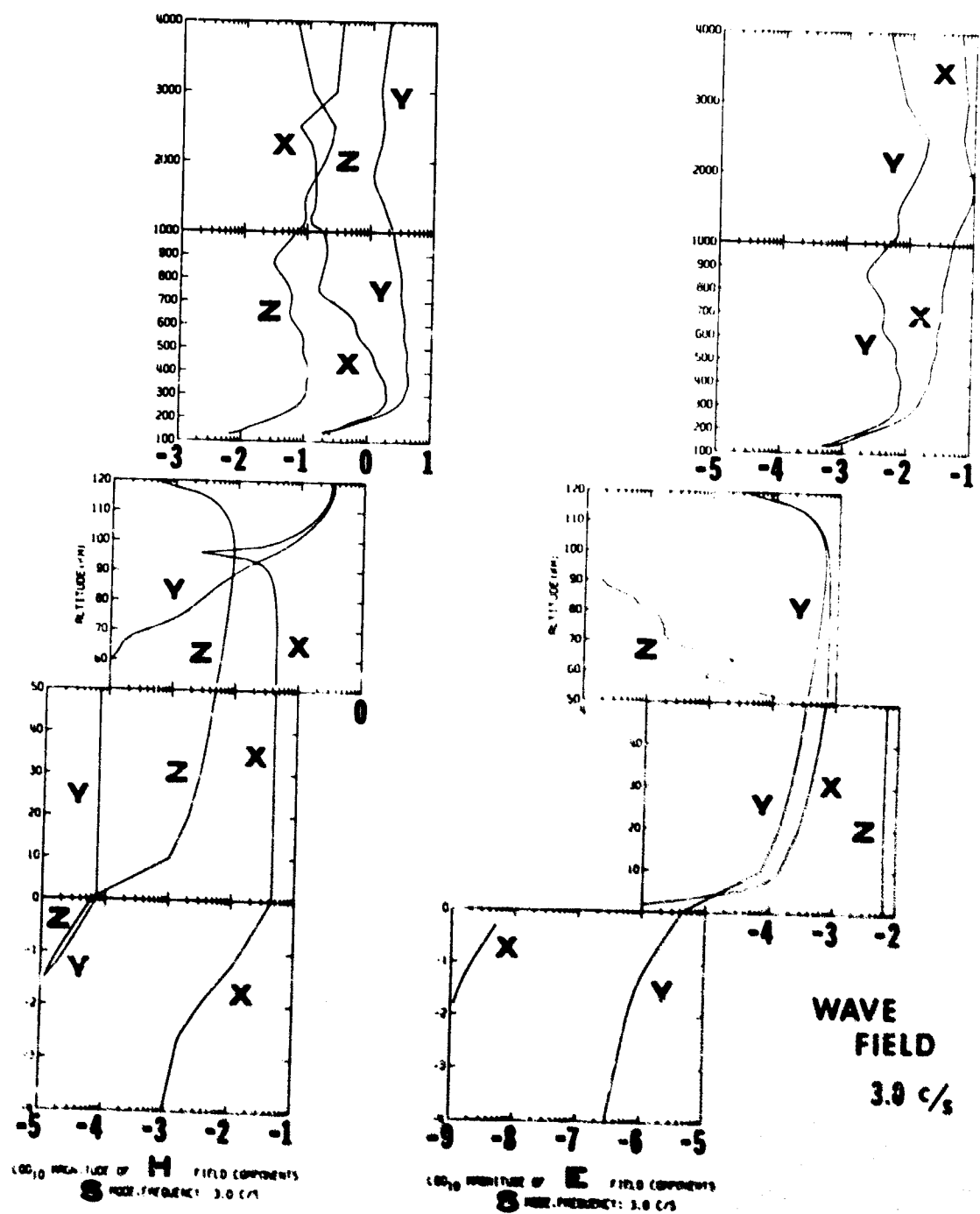


Figure 4.5

decreases and the z component of the electric field increases through the D region due to coupling caused by the localized disturbance. In the neutral atmosphere the z component of the electric field persists and must result in charge separation between the lower ionosphere and ground level.

The x component of the magnetic field grows gradually throughout the F region and becomes nearly equal to the y component in the E region. The x and y magnetic field components are again separated in the D region due to coupling. Inspection of the magnetic component change with altitude reveals that whenever the x - component is dominant on the ground, the y - component is dominant at 4000 km.

The electric field has a similar behavior with the x and y components being well separated in the D and F regions because of coupling. In the E region the x and y electric field components are nearly equal due to the E region anisotropy.

Within the Earth the electric and magnetic fields are horizontal, suggesting the properties of a conductor. The skin depth for these fields within the Earth's surface is less than one km.

The wave fields for the incident fast wave are depicted in Figure 4.6. At the top of the ionosphere the disturbance is neither transverse magnetic nor transverse electric. However, the disturbance is transverse electric at all altitudes below 110 km. As was true of the incident slow wave, standing waves are discernible above 250 km. with the magnetic field envelope reaching a maximum around the F region electron density

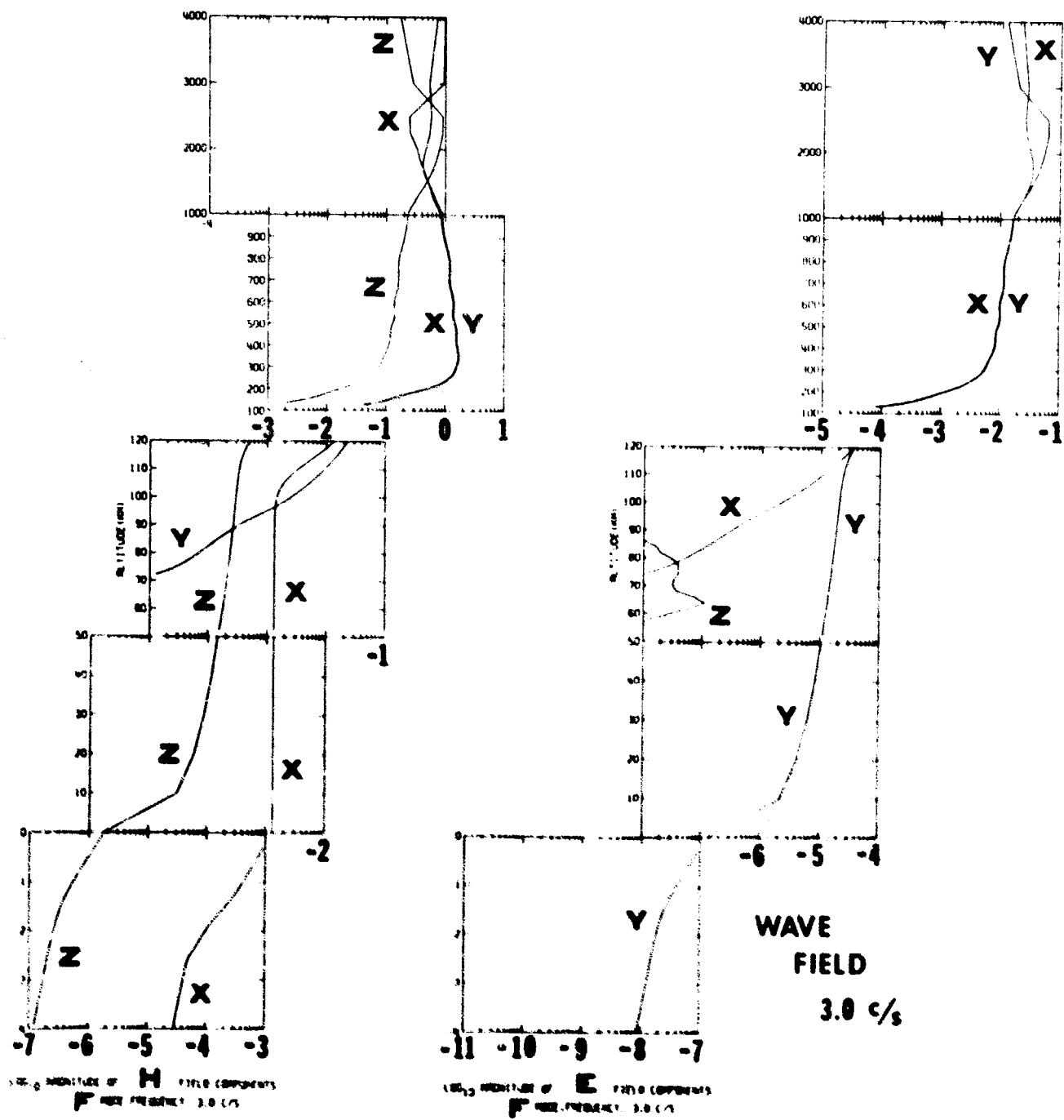


Figure 4.6

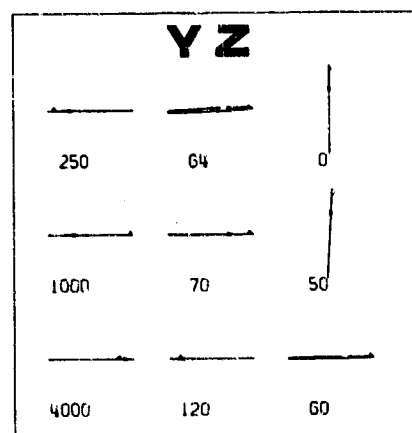
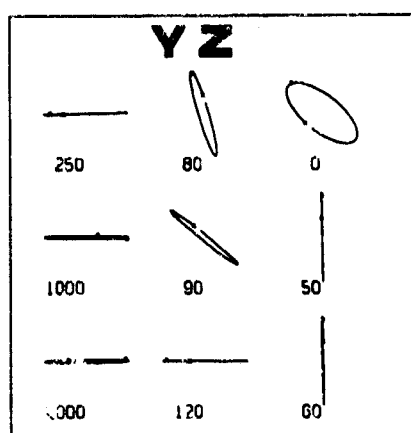
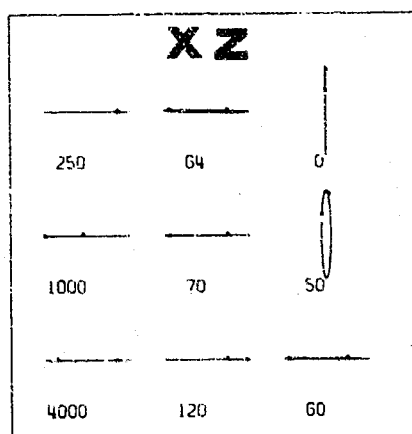
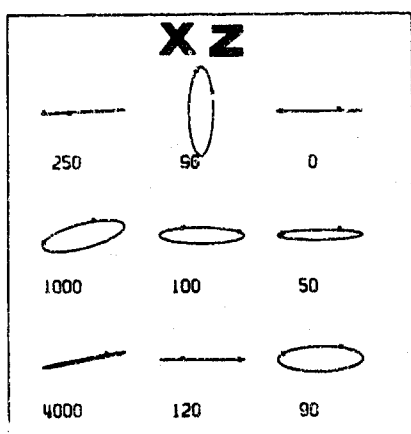
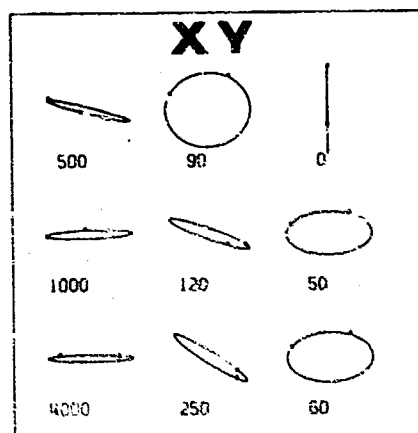
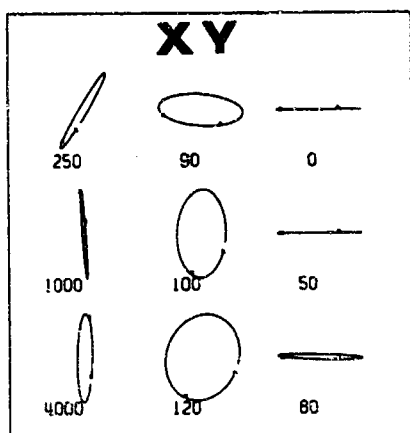
maximum. The field components become well separated in the D region due to the continuation of the TE mode in free space. At ground level the magnetic field is primarily in the x direction and the electric field is in the y direction. Unlike the incident slow wave no electric field z component is generated in the neutral atmosphere. Therefore the incident fast wave will not generate charge separation between the ground and the lower ionosphere. Also, the electric field is attenuated by five orders of magnitude between 4000 km. and the ground. Therefore, the electric field of a disturbance generated at 4000 km. may be difficult to observe on the ground.

The disturbance within the Earth is also transverse electric.

4.15 Wave Field Polarization

The wave field polarizations for the incident slow and fast waves are given in Figures 4.7 and 4.8, respectively. The labeling of these graphs is explained in section 3.25.

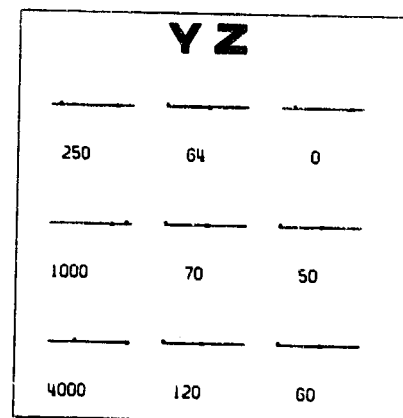
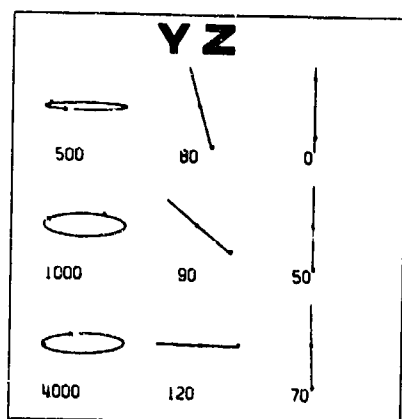
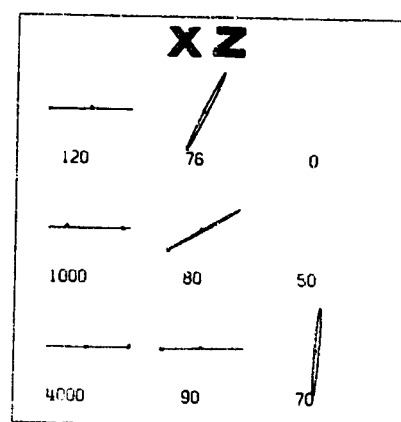
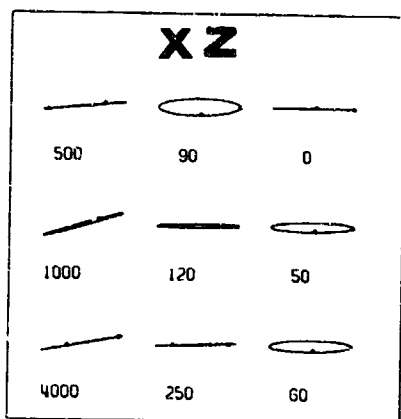
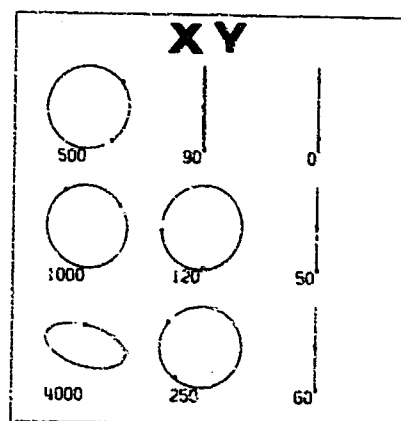
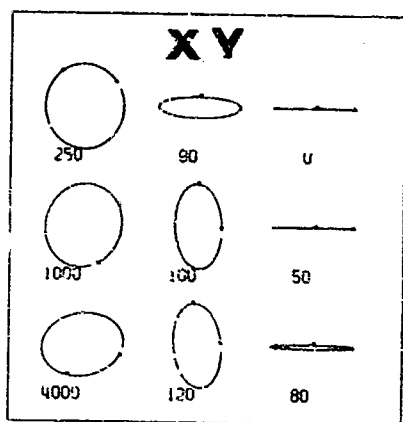
The electric field of the incident slow wave is left elliptically polarized in the xy plane at 4000 km. with the major axis in the x direction. The electric field of the incident fast wave is also elliptically polarized at 4000 km. but in the right hand sense. Thus the slow and fast waves at 4000 km. may be discriminated by observation of the electric field polarization. The slow and fast modes at 4000 km. may also be differentiated by observing the magnetic field polarization, which is left elliptically polarized for the incident slow wave and right elliptically polarized for the fast wave. However, on the ground the



H FIELD POLARIZATION
S MODE, FREQUENCY: 3.0 C/S

E FIELD POLARIZATION
S MODE, FREQUENCY: 3.0 C/S

Figure 4.7



H FIELD POLARIZATION
F MODE, FREQUENCY: 3.0 C/S

E FIELD POLARIZATION
F MODE, FREQUENCY: 3.0 C/S

Figure 4.8

electric and magnetic field polarizations in the xy plane are linear in the same fashion for both the incident slow and incident fast waves. The two disturbances may be identified on the ground only by observation of the z component of the electric field, which is zero for the incident fast wave and non-zero for the incident slow wave.

The electric and magnetic fields of both the incident slow and fast waves undergo a polarization reversal in the xy plane at approximately 1000 km. This polarization reversal is due to the sudden change of the medium from anisotropic above 1000 km. to quasi-isotropic below 1000 km. Also the magnetic field of the incident slow wave changes back to left elliptically polarized in the xy plane at 90 km., which corresponds to the point at which the x component of the magnetic field becomes larger than the y component.

The incident fast wave electric field is left circularly polarized between 1000 km. and 100 km. and then becomes linearly polarized in the y direction. The incident slow wave electric field is right elliptically polarized between 1000 km. and ground surface, at which it becomes linearly polarized in the y direction in the xy plane.

Experimental observations indicate that at high latitudes the Pc 1 signals received on the ground during the day are primarily left elliptically polarized [Campbell, 1965, 1967, 1968] but that frequently the signals are right, linearly, or irregularly polarized [Heacock, 1970]. Some evidence [Heacock, 1970] suggests that Pc 1 events are a superposition of two or more events and Pope [1964] has attempted to explain

the polarization behavior of Pc 1 events in terms of a superposition of successive rising tone signals, the resultant polarization sense of which is determined by the relative magnitudes of the signals and the relative inclination of their polarization axes. More recently Campbell [1967] has concluded from observational evidence of Pc 1 attenuation characteristics and excellent geomagnetic conjugacy that the signals received at ground level are L waves having R wave characteristic absorption.

Experimental workers (e.g., Heacock [1970]) indicate a complexity in the polarization of Pc 1 signals observed at auroral zone stations. The results of the present work indicate that the first independent wave, having left handed elliptical polarization at the top of the ionosphere, shows less attenuation in the course of ionospheric transmission than the second independent wave, the polarization of which is right handed and almost circular at the top of the ionosphere. This result agrees with Campbell's implication, which was in contradiction with the expectation from the case of an infinite plane wave in a uniform plasma. Although this agreement comes essentially from the consequence of magneto-ionic coupling the actual process is not so simple.

In the present model of the ionosphere, together with the localization of the disturbance in the x-direction, mode interchange happens at slightly above 1000 km. and at 150 km. Between these levels, the medium is essentially isotropic, so that there is no

appreciable difference in the attenuation of two characteristic waves. The differentiation of attenuation occurs only in the E and D regions. As seen from Figure 4.4 the incident "L" wave consists mainly of the slow mode, whereas the incident "R" wave is comprised of both the fast and slow modes. By virtue of the mode coupling around the upper mode-interchange level, the incident "L" wave becomes a composite wave of slow and fast modes with the same magnitude in the upper F region, while the incident "R" wave becomes a rather pure slow mode in that region. Then, a mode interchange again occurs at 150 km. Below this level, the differentiation in the attenuation of different modes becomes obvious. As a result, the incident "R" wave is more attenuated, compared to the incident "L" wave.

In contrast with Heacock's observational findings, which show a change of the rotation sense of wave polarization from one location to another and from one occasion to another, the present analysis gives only linear polarization in the x-direction on the ground. The same result was obtained at different frequencies in the ULF range. This is a consequence of the assumption that the disturbance is localized only in the x-direction. In other words the one dimensional localization is equivalent to the specification of the dominant TE mode in the free space between the ionosphere and the Earth's surface. From this analysis the conjecture may be made that if the disturbance function is of the form $e^{-\lambda x} \cdot e^{ik_y y}$ the resultant polarization can be elliptical and the sense of rotation is determined by the sign of the ratio $\frac{m}{\lambda}$.

Also, there is observational evidence showing the structural ionization across the auroral zone, in particular, during auroral events, so that Pc 1 wave disturbances may be confined in the vicinity of the structural ionization, such as the auroral column and/or the auroral arc. On some occasions, Pc 1 waves can be trapped between two sheets of the auroral arcs. Therefore, in order to clarify the spatial change of the polarization rotation sense, the wave guide mode propagating along the structural ionization observed in the auroral zone must be examined by taking into account a certain bi-directional disturbance function. Thus, as far as auroral zone phenomena are concerned, the assumption of an infinite plane wave in a uniform plasma is not sufficient to account for various complexities in the nature of the phenomena.

Also, the present results give larger attenuation for both the incident "L" and "R" waves than given by previous investigations. In addition, the present work shows a greater difference between the incident "L" and "R" wave attenuations than predicted by previous investigators. These differences are attributed to the inclusion of the ion resonant charge exchange processes.

Theoretical studies [Altman and Fijalkow, 1963, 1969; Altman and Cory, 1969] have suggested that intermode coupling channels energy from L to R modes in the upper E region. These studies have concluded that the coupling increases as the angle between the wave normal and the magnetic field increases. Heacock [1970] reconciles his dual-site

(College and Kotzebue, Alaska) polarization differences by invoking Altman and Fijalkow's L-to-R coupling, assuming that College and Kotzebue are both at the feet of the disturbance source lines, and assuming that flaring out of the L-wave ray bundle occurs as the waves propagate through the F region. Large amplitude L sense should then be observed near the center of the disturbed field line region and the polarization should change gradually to R sense with decreasing amplitude as the distance increases radially from the center of the disturbed region.

4.2 Localized Disturbance at $1/3$ c/s.

4.21 Booker Quartic Roots

Table 4.2 summarizes the properties of the slow and fast wave disturbances at $1/3$ c/s in the various regions of the Earth's environment. The Booker quartic roots are presented in Figure 4.9. The labeling of these curves is the same as that used in section 3.21. The actual values of the indices of refraction for propagation in the z -direction are obtained by multiplying the values obtained from the curves by a factor of 22.5.

Above 600 km. the region is anisotropic and the slow wave is propagating and the fast wave is evanescent. From magneto-ionic theory one would expect that both the slow and fast modes would be propagating through this region because the wave frequency is less than the ion cyclotron gyrofrequency. However, the dispersion relation given in section 2.2 shows that above 600 km. the Booker

REGION	REFRACTIVE INDEX	PROPAGATION CHARACTERISTICS	
		SLOW WAVE	FAST WAVE
Magnetosphere Alt > 600 Km	Anisotropic	Propagating	Evanescent
Upper Ionosphere 250-600 Km	Quasi-isotropic	Propagating	Propagating
Lower Ionosphere 70-250 Km	Anisotropic	Propagating	Evanescent
Transition 52-70 Km	Quasi-isotropic	Evanescent	Evanescent
Neutral Atmosphere	Isotropic Re q = 0	Evanescent Im q = 14	Evanescent Im q = 14
Earth's Interior	Isotropic Re q = Im q	Propagating $ q \sim 10^3 - 10^4$	Propagating $ q \sim 10^3 - 10^4$

TABLE 4.2 Medium characteristics at 1/3 c/s for a localized disturbance incident at an oblique angle from the vertical at 5000 Km.

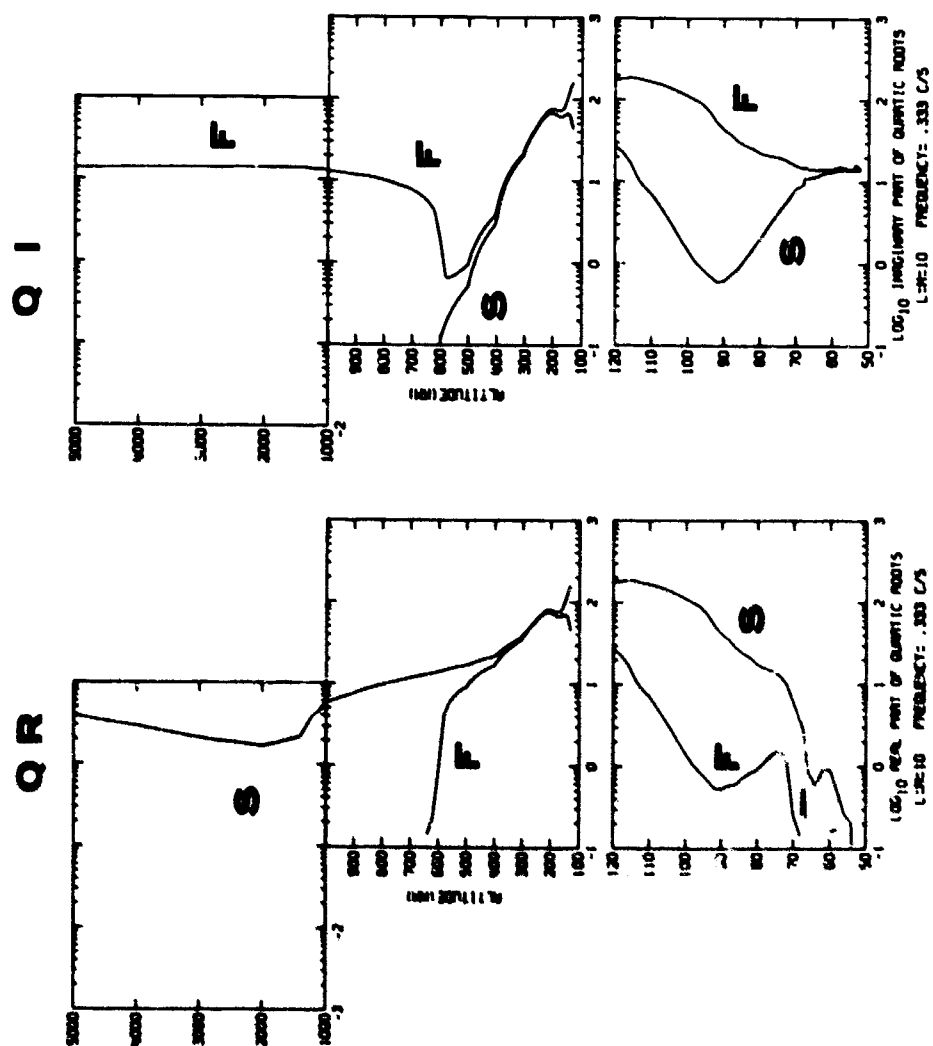


Figure 4.9

quartic roots for the fast and slow waves are given approximately by

$$q_f = i l$$

$$q_s = \left[r^2 |\sum_{\pm i}| \right]^{\frac{1}{2}}$$

respectively, where l is the Fourier number,

$$\sum_{\pm i} = \frac{\sigma_{\pm i}}{\omega \epsilon_0}, \text{ and } r = \frac{2\pi R_e}{\lambda_0}$$

At 500 km. these waves are given by

$$q_f = \left[r^2 \left(|\sum_{\pm i}| - \frac{l^2}{r^2} \right) \right]^{\frac{1}{2}}$$

$$\approx \left[r^2 \left(\frac{2}{3} |\sum_{\pm i}| \right) \right]^{\frac{1}{2}}$$

$$q_s = \left[r^2 |\sum_{\pm i}| \right]^{\frac{1}{2}}$$

Thus the imaginary part of the Pedersen conductivity increases sufficiently to overcome the localization factor $\frac{l^2}{r^2}$ and enables the fast wave to become propagating. This effect holds true for the region 200-600 km., which is quasi-isotropic and both modes are propagating. The real parts of the quartic roots become nearly equal to the imaginary parts and this region therefore is similar to a metal. Later in the analysis this conducting region will be seen to serve as a waveguide for the fast mode.

Between about 200 km. and 70 km. the slow mode is propagating and the fast mode is evanescent. Therefore the propagating region

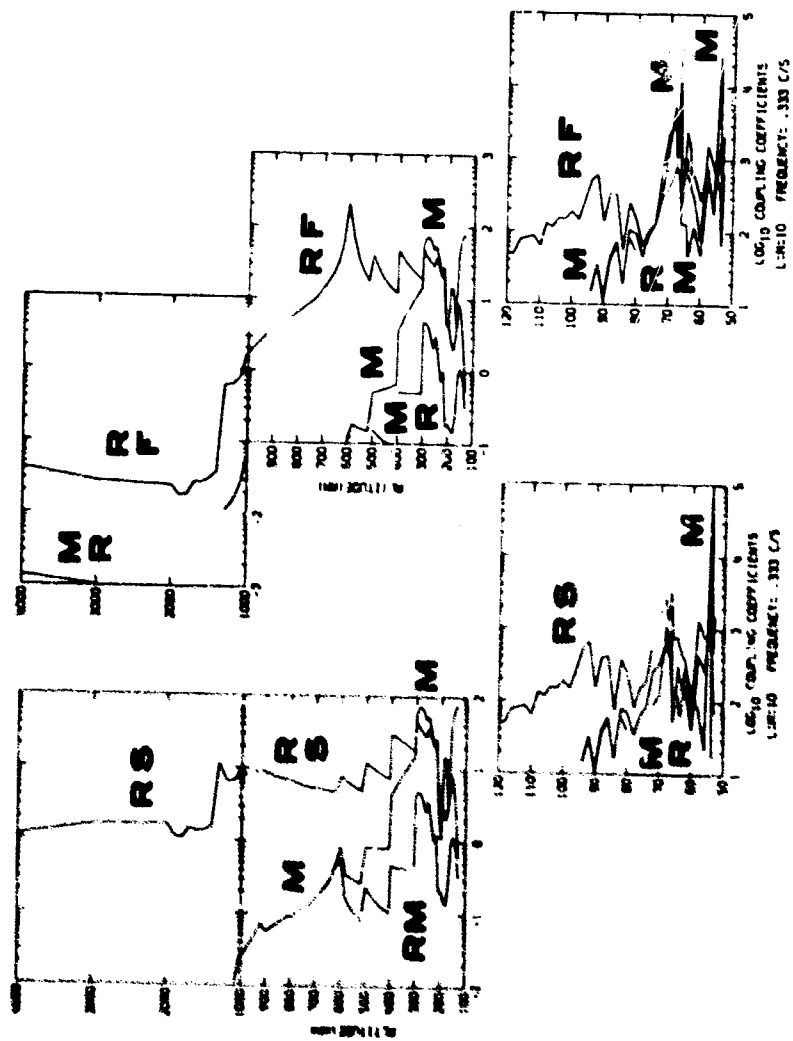
for the fast mode is sandwiched between two strongly evanescent regions and energy trapping of the fast wave occurs between approximately 200 and 600 km.

Charge exchange has basically the same effect on the quartic roots at 0.333 c/s as at 3.0 c/s. However, at the lower frequency the coupling coefficients are becoming comparable in magnitude to the quartic roots and may somewhat mask the effects of charge exchange. Nevertheless some absorption still takes place between about 160 km. and 220 km. where the quartic roots are still larger than the coupling coefficients.

Both the slow and fast modes are evanescent in the quasi-isotropic portion of the D region below 70 km. The neutral atmosphere and the Earth's interior are isotropic. The quartic roots for the neutral atmosphere are once again pure imaginary due to the localized nature of the disturbance.

4.22 Magneto-ionic Coupling Coefficients

Figure 4.10 shows the altitude dependence of the magneto-ionic coupling coefficients for the localized disturbance at 1/3 c/s. These curves have the same labeling as those analyzed in section 3.22. Reflection type coupling is most important down to 300 km. Coefficients for the reflection of the slow wave are greater than those for the reflection of the fast wave above about 700 km. The reflection coefficients for the fast mode increase rapidly between 1000 km. and 600 km. due to the rapid change in the medium character



MAGNETO-IONIC COUPLING

Figure 4.10

from highly anisotropic to isotropic in the region between 200 and 600 km. The coupling coefficients for reflection of the slow wave are the same order of magnitude as the slow wave quartic roots throughout the F region. The coupling coefficients for reflection of the fast wave are smaller than the fast wave quartic roots above 700 km. but become larger than the quartic roots in the region 200-600 km. Thus energy from the fast wave is trapped in this conducting region, which behaves as a waveguide for the fast wave. Mode coupling continuously increases throughout the F region and reaches a maximum around the F region maximum. Mode reflection type coupling also appears in the F region but is of less importance than pure mode coupling. Once again in the E region reflection type coupling is important. In fact, for both modes the reflection coupling coefficients are larger than the quartic roots. There is little mode coupling in the E region as evidenced by the good separation of the quartic roots for the slow and fast modes. Mode coupling and mode reflection type coupling both become much larger than the quartic roots in the lower D region. Thus mode coupling is important in the D and F regions and unimportant in the E region. This result seems to be in contradiction to the suggestion made by Heacock [1970].

Reflection type coupling occurs within the surface layer of the Earth and is a maximum at a depth of about 2.5 km. This reflection region corresponds to the rapid change in the earth conductivity. In this region the coupling coefficients are smaller than the quartic roots

but are of comparable magnitude at a depth of 2.5 km.

4.23 Characteristic Wave Mixing Ratios

The mixing ratios for the incident slow and fast waves at $1/3$ c/s are given in Figure 4.11. The labeling of these curves is the same as that used in section 3.23.

For the incident slow wave the downgoing and upgoing slow waves are of similar magnitude throughout the F region, indicating that reflection is continuously taking place. The downgoing and upgoing fast waves are gradually generated by mode coupling. In the D and E regions the upgoing and downgoing waves are of similar magnitude which indicates that standing waves are formed and that the D and E regions behave as a waveguide for the incident slow wave. In the neutral atmosphere the transverse electric mode is dominant over the transverse magnetic mode. Also almost complete reflection takes place at ground surface. Thus the Earth is a good conductor even at such a low frequency. Inside the Earth the downgoing transverse electric mode is dominant but the upgoing transverse electric mode is also present due to reflection.

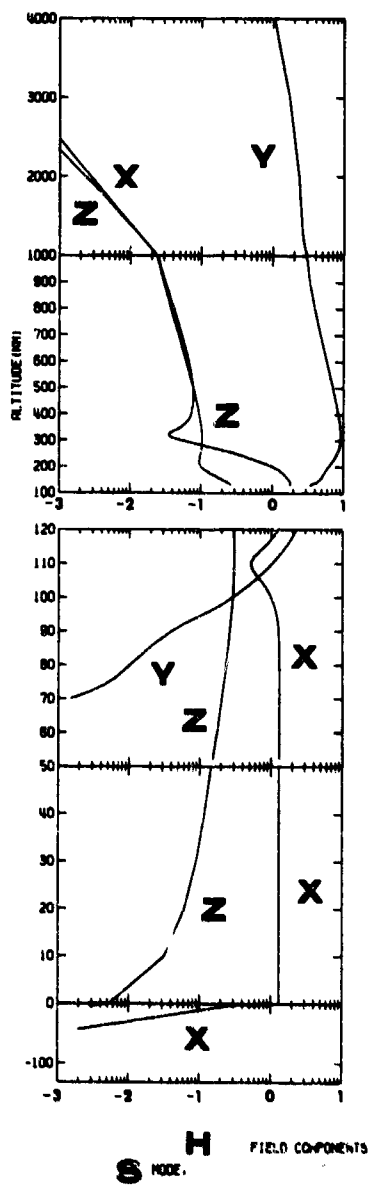
The mixing ratios for the fast mode decrease by three orders of magnitude between 4000 km. and 1000 km. and by four orders of magnitude between 4000 km. and ground level. Therefore even if a disturbance arrives as a fast wave at 4000 km. it might not be seen on the ground. If the fast mode is generated by a disturbance below 1000 km. the wave is more likely to be observed on the ground. Below

600 km. the downgoing and upgoing waves become similar in magnitude and show that the region between about 250 km. and 600 km. serves as a waveguide for the fast wave. In the neutral atmosphere the transverse electric mode is the only mode present and almost complete reflection of this mode takes place on the ground. The downgoing transverse electric mode is dominant in the Earth but the upgoing transverse electric mode is also present to a small degree due to reflection.

4.24 Wave Fields

The wave fields of the incident slow mode are shown in Figure 4.12. The magnitudes of the electric and magnetic fields are all relative to the values at 4000 km. If the magnetic field values are multiplied by a factor of 75 the B field is then obtained in gammas. The electric field is read directly in volts/meter.

The incident slow mode disturbance is transverse magnetic at the top of the ionosphere and becomes transverse electric within the ground. The y component of the magnetic field increases through the F region and reaches a maximum around 300 km. Magnetic energy is being stored in the region 200-600 km. The y component of the magnetic field then decreases in magnitude through the D and E regions. The x and z components of the magnetic field increase through the F region due to mode coupling and exhibit somewhat of a standing wave character below about 300 km. The x and z components of the magnetic field become dominant over the y component below 100 km. The x component of the magnetic field is seen in Figure 4.12 to be dominant on the



WAVE FIELD
.333 c/s

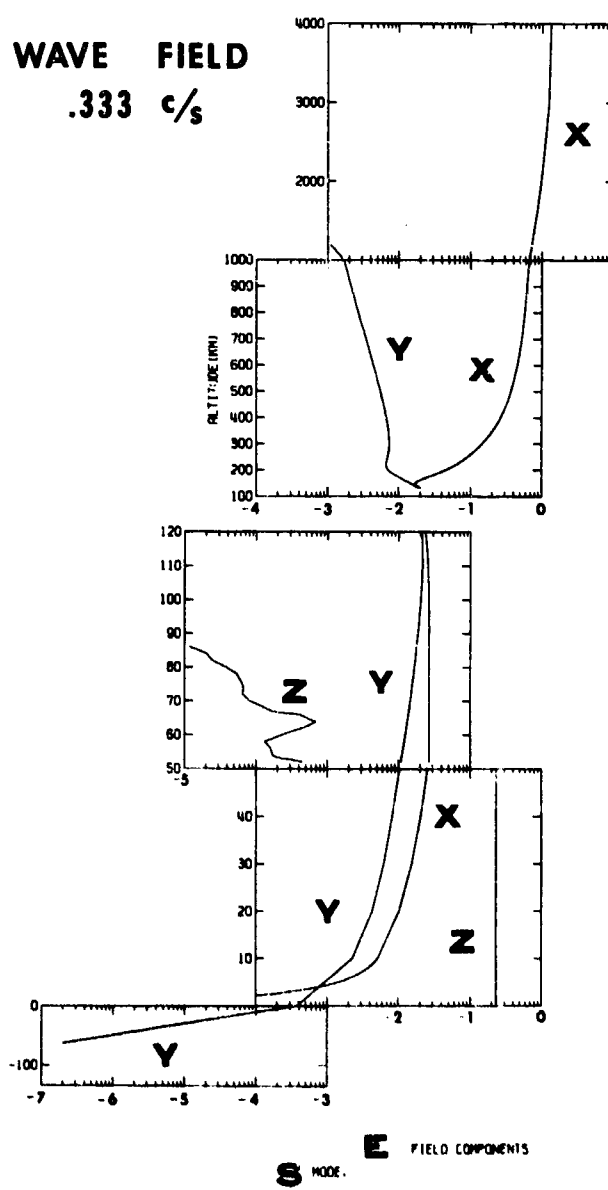


Figure 4.12

ground whereas the y component is dominant at 4000 km.

The electric field is in the x direction at the top of the ionosphere but in the z direction at ground level. The y component grows in magnitude through the F region and becomes equal to the x component around 150 km. Below this level the x and y components exhibit a standing wave formation. Below about 90 km. the x and y components become somewhat separated in the D region. The z component also increases in magnitude through this low conducting region and becomes dominant in the neutral atmosphere. Therefore charge separation must occur between the Earth's surface and the lower ionosphere. Both the electric and magnetic fields decrease logarithmically within the Earth. Even at this low frequency the Earth is a good conductor.

The wave fields for the incident fast wave are shown in Figure 4.13. Both the electric and magnetic fields of this disturbance are attenuated by three orders of magnitude between 4000 and 1000 km. The magnetic field is attenuated by four orders of magnitude between 4000 km. and ground level and the electric field is attenuated by seven orders of magnitude in the same altitude range. Therefore an incident fast wave arriving at 4000 km. may be difficult to observe on the ground. A fast mode disturbance generated below 1000 km. would be more easily observed. The incident fast wave is transverse electric throughout the ionosphere, neutral atmosphere and the Earth's interior, with the exception of the region between 200 and 600 km. altitude where strong coupling causes the x and y components of the electric

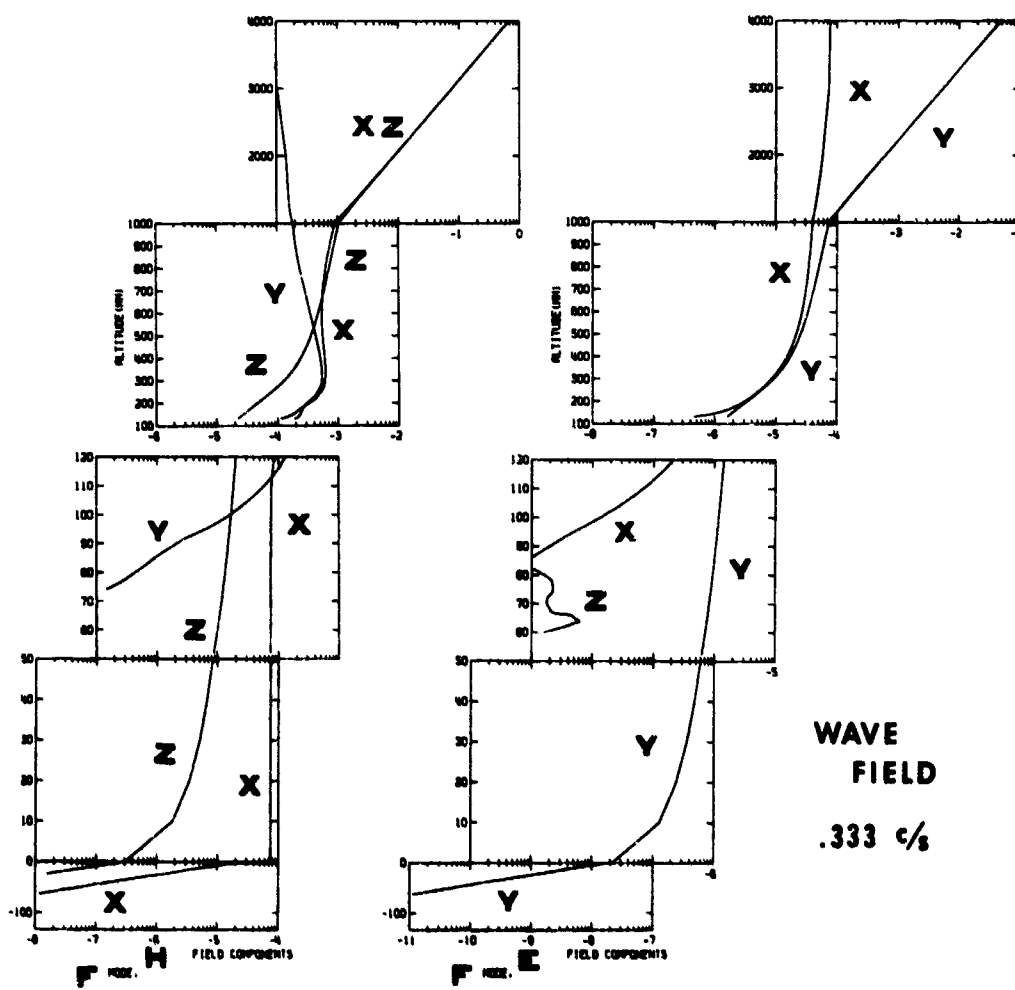


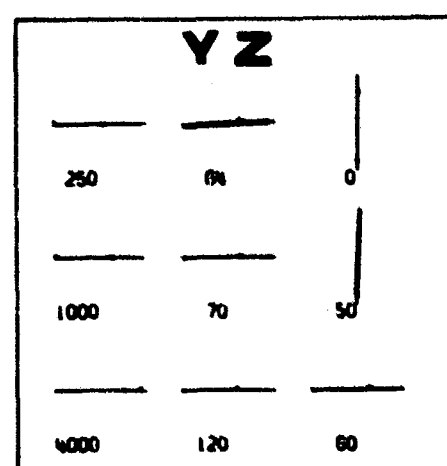
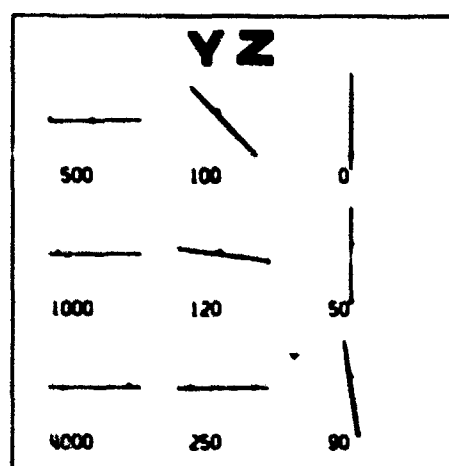
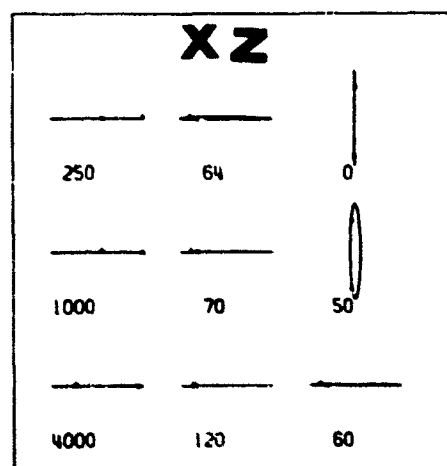
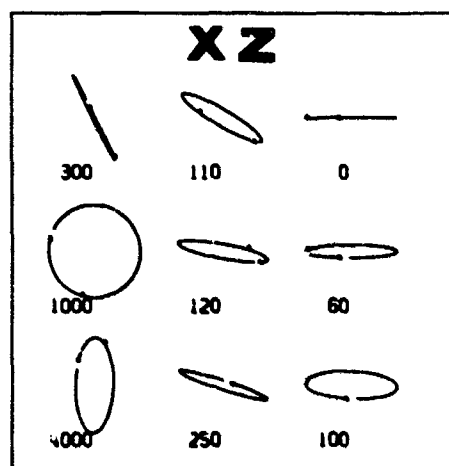
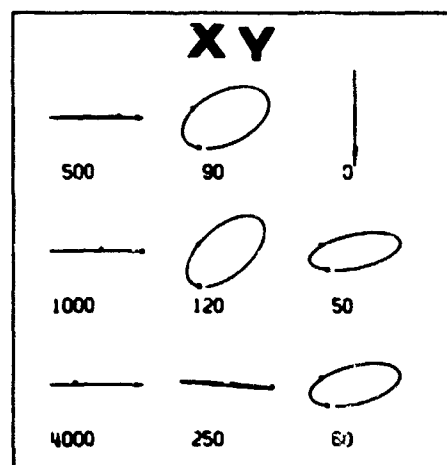
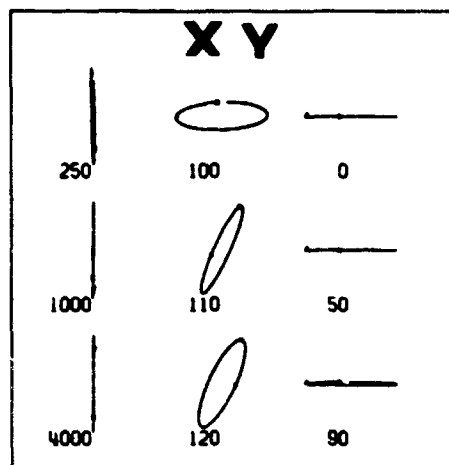
Figure 4.13

field to be nearly equal. A z component of the electric field is generated in the lower D region but unlike the incident slow mode the z component of the electric field does not appear in the neutral atmosphere or on the ground.

4.25 Wave Field Polarization

The wave field polarizations for the incident slow and fast waves are given in Figures 4.14 and 4.15, respectively. These figures are interpreted in the same manner outlined in section 3.25. The polarization characteristics of the resultant waves at this frequency (0.333 c/s), which is near the lower limit of the Pc 1 frequency range, are also in agreement with Campbell's [1967] suggestion that the signal observed on the ground represents a disturbance which has propagated through the ionosphere with R mode attenuation. The incident slow mode magnetic field is linearly polarized down to 250 km. where it then becomes right elliptically polarized. At 110 km. the magnetic field changes to left elliptically polarized and then to linearly polarized in the D region. The electric wave field of the incident slow mode is linearly polarized down to 250 km. and then becomes right elliptically polarized, remaining as such down to ground level where the polarization is linear. Thus the incident slow mode basically has R mode characteristics and is less attenuated than the incident fast wave.

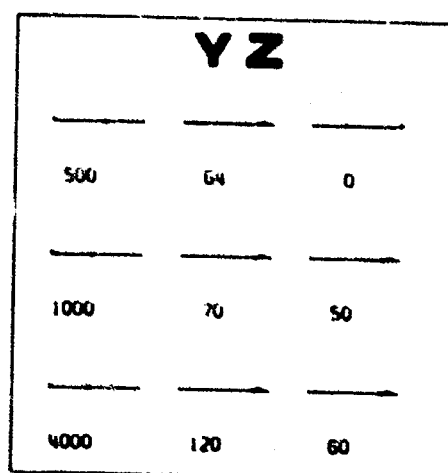
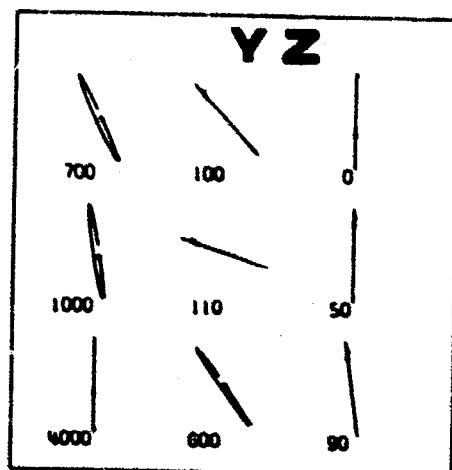
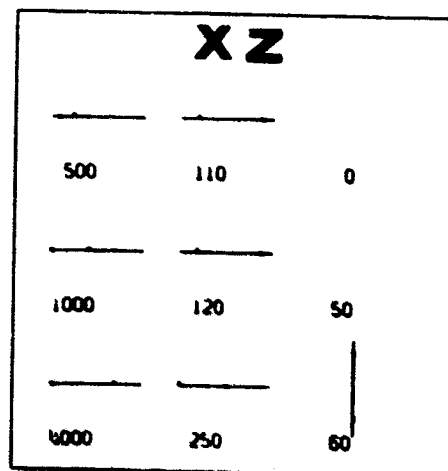
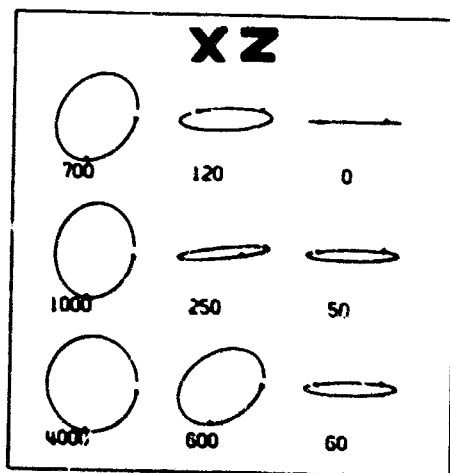
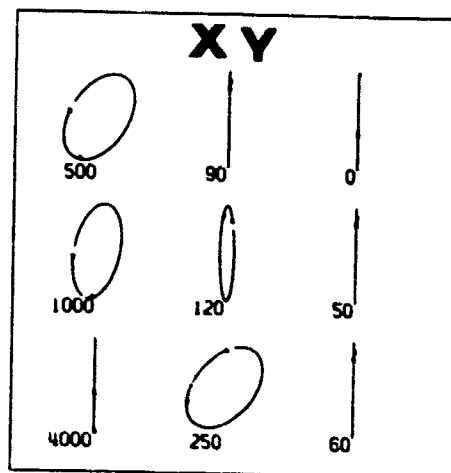
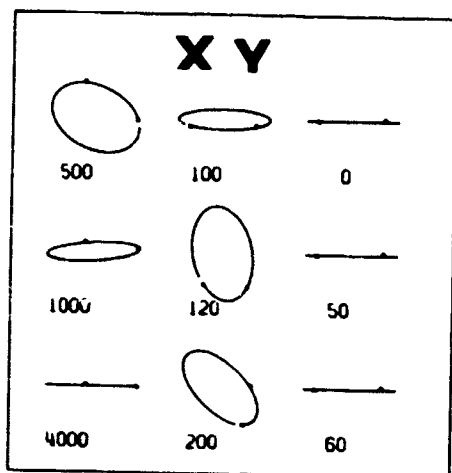
The incident fast wave magnetic field is linearly polarized at 4000 km., changes to left elliptically polarized at 1000 km., and remains left elliptically polarized down to the D region where it becomes



H **S** POLARIZATION
MODE, FREQUENCY: .33 75

E **S** POLARIZATION
MODE, FREQUENCY: .333 C/5

Figure 4.14



H **F** POLARIZATION
MODE.FREQUENCY: .333 C/S

E **F** POLARIZATION
MODE.FREQUENCY: .333 C/S

Figure 4.15

linearly polarized again. The wave electric field has the same polarization characteristics as the magnetic field in the xy plane except that the major axes of the polarization curves are approximately at 90° to each other. Therefore the incident fast mode is found to be in the L mode throughout most of the ionosphere and is more attenuated than the incident slow wave.

If the bi-directional disturbance function is assumed to be of the form $e^{-\lambda x} \cdot e^{ik_0 m y}$, an elliptically polarized wave may then appear at ground level.

4.3 Localized Disturbance at 1/300 c/s

4.31 Booker Quartic Roots

Table 4.3 summarizes the properties of the slow and fast wave localized disturbances at 1/300 c/s in the various regions of the Earth's environment. Figure 4.16 shows the altitude dependence of the Booker quartic roots. The indices of refraction for propagation in the z-direction are obtained by multiplying the values obtained from the curves in Figure 4.16 by a factor of 2.25×10^3 .

The quartic roots reveal that the ionosphere is anisotropic throughout. The slow wave is propagating down to about 80 km, where it becomes evanescent. The fast wave is highly evanescent throughout the entire ionosphere. This is similar to the fast wave disturbance at 1/3 c/s, which was evanescent above 600 km. The same reason given to explain the evanescence of the fast wave in the Pc1 frequency range may also be given to explain the evanescence of the fast wave in the

REGION	REFRACTIVE INDEX	PROPAGATION CHARACTERISTICS	
		SLOW WAVE	FAST WAVE
Magnetosphere Alt > 600 Km.	Anisotropic	Propagating $\text{Re } q_s > \text{Im } q_s$	Evanescant
Upper Ionosphere 150-600 Km.	Anisotropic	Propagating $\text{Re } q_s \approx \text{Im } q_s$	Evanescant
E region 86-150 Km.	Anisotropic	Propagating $\text{Re } q_s > \text{Im } q_s$	Evanescant
D region	Anisotropic	Evanescant	Evanescant
Neutral Atmosphere	Isotropic $\text{Re } q = 0$	Evanescant $\text{Im } q = 14$	Evanescant $\text{Im } q = 14$
Earth's Interior	Isotropic $\text{Re } q = \text{Im } q$	Propagating $ q \sim 10^2$	Propagating $ q \sim 10^2$

TABLE 4.3 Medium characteristics at 1/300 c/s for a localized disturbance incident at an oblique angle from the vertical at 5000 Km.

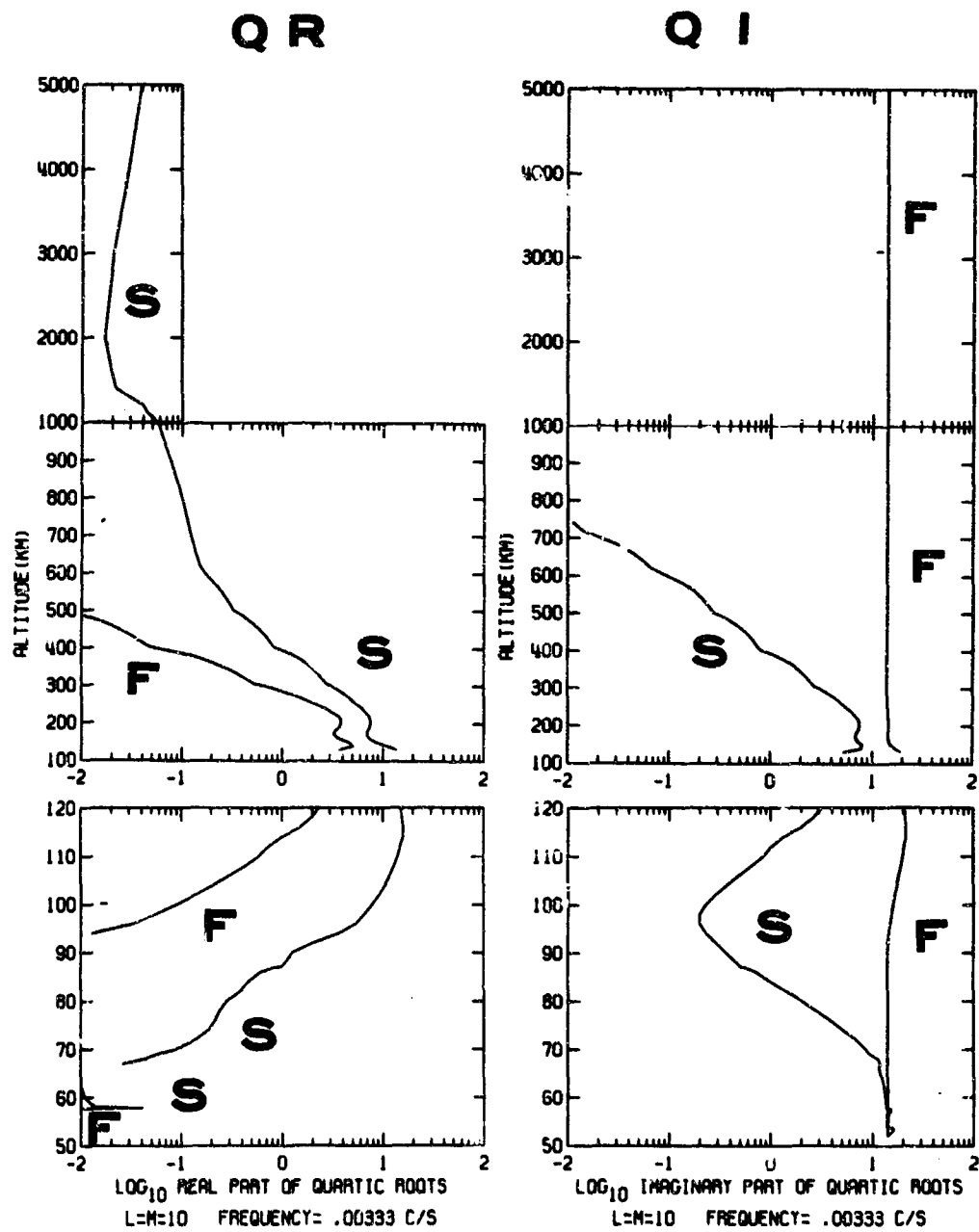


Figure 4.16

Pc 5 frequency range. The dispersion relation given in section 2.2 predicts that above 200 km. the Booker quartic roots for the fast and slow waves are given approximately by

$$q_f = i\ell$$

$$q_s = \left[r^2 \left| \sum_{\perp} i \right| \right]^{\frac{1}{2}}$$

Thus the disturbance factor ℓ is sufficiently large to cause the fast wave to become evanescent.

At approximately 200 km. the real and imaginary parts of the quartic roots for the slow wave become nearly equal. Also the real part of the quartic root of the fast wave increases rapidly, reaching a maximum at about 150 km. but remaining a factor of two less than the imaginary part. Consequently mode coupling becomes large in this region.

From the dispersion relation it may be shown that at 200 km. the fast and slow waves are approximated by

$$q_f = \left[-\ell^2 + ir^2 \sum_{\perp r} \right]^{\frac{1}{2}}$$

$$q_s = \left[ir^2 \sum_{\perp r} \right]^{\frac{1}{2}}$$

The rapid increase of the real part of the Pedersen conductivity with decreasing altitude causes the real part of the fast wave quartic root to approach the imaginary part, but the increase in $\sum_{\perp r}$ is not

sufficient to overcome the disturbance factor \mathcal{L} and to allow the fast wave to become propagating.

Between 150 km. and 600 km. Σ_{r} is enhanced by as much as an order of magnitude when the effect of charge exchange of O^+ with O is included. Therefore the effect of charge exchange is to cause the slow wave to become more propagating and the fast wave to approach more rapidly toward propagating conditions.

The real and imaginary parts of the quartic roots for the slow wave again become unequal in the E region below 150 km. so that the slow wave is highly propagating in this region.

Once again the quartic roots are pure imaginary in the neutral atmosphere due to the presence of localization in the horizontal direction of the disturbance. Also, the interior of the Earth is like a metal.

4.32 Magneto-ionic Coupling Coefficients

Figure 4.17 shows the altitude dependence of the magneto-ionic coupling coefficients for the localized disturbance at 1/300 c/s. These curves have the same labeling as those analyzed in section 3.22.

Reflection type coupling for both the slow and fast waves is seen to be the dominant type of coupling above the F region. In fact the coupling coefficients are everywhere larger than $\text{Re } [q_s]$, indicating that the coupling coefficients are more important than the quartic roots in determining the final wave characteristics. In the region 150-250 km. mode coupling and mode reflection type coupling become important due to the fact that the medium is becoming isotropic.

As will be shown later, across this mode coupling region the incident slow wave changes from quasi-TM at the higher altitudes to quasi-TE at the lower altitudes.

In the E region reflection type coupling once again dominates for the slow wave. Mode coupling becomes very large in the lower D region, which was also true at higher frequencies and was shown to be caused by the localization of the disturbance. For the fast wave mode coupling is most important throughout the lower ionosphere.

Reflection type coupling occurs within the surface layer of the Earth between 1.2 km. and 3.5 km. depth and is a maximum at a depth of 2.5 km. At all depths within this reflection layer the reflection type coupling coefficients are larger than the quartic roots. This reflection region is caused by the rapid change in the earth conductivity. The mixing ratios reveal that a reflected TE wave is generated by the reflection coupling.

4.33 Characteristic Wave Mixing Ratios

The characteristic wave mixing ratios for the incident slow and fast waves are given in Figure 4.18. These curves have the same labeling as those analyzed in section 3.23.

For the incident slow wave the downgoing and upgoing slow waves are approximately equal above the F region, indicating that reflection is continuously taking place. The downgoing and upgoing fast waves are generated around the F region max as a result of mode and mode reflection type coupling. After passing through the strong mode coupling region,

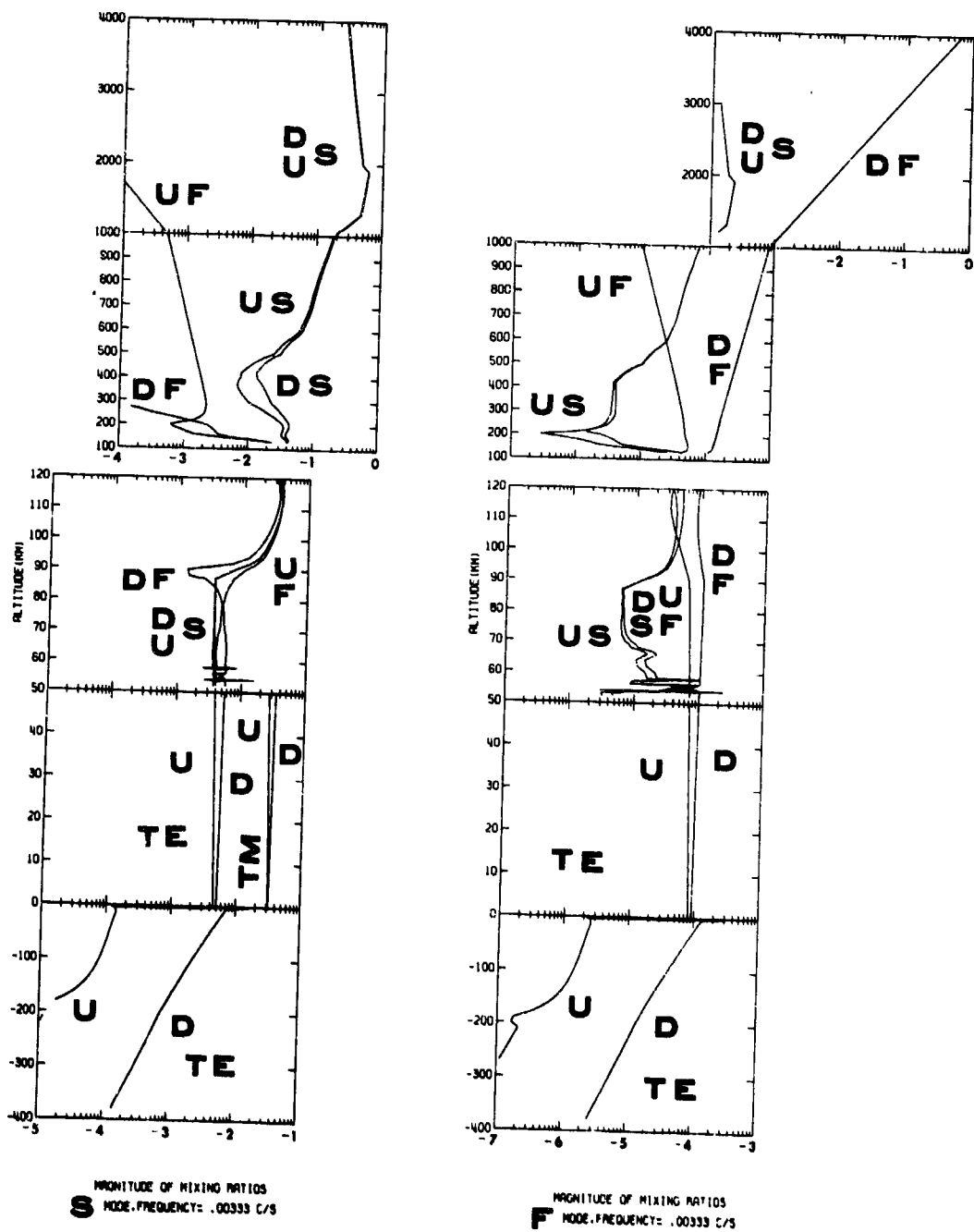


Figure 4.18

all the characteristic waves become the same order of magnitude. Below 150 km. in the D and E regions mixing of the characteristic waves is quite good due to mode coupling and mode reflection type coupling. In the neutral atmosphere the waves are mostly transverse magnetic but with a small amount of transverse electric waves present. The surface of the Earth acts as a good conductor even at Pc 5 frequencies, although the fields are able to penetrate more deeply than at the higher frequencies. Within the Earth the resultant wave is primarily downgoing transverse electric.

The incident fast wave consists primarily of the downgoing fast characteristic wave at the top of the ionosphere. This character predominates down to below the F region maximum, because of the constancy of $\text{Im } [q_f]$ throughout the higher region. Around the F region maximum the slow characteristic waves are generated by the mode and mode reflection type coupling. At higher altitudes a similar behavior is seen in the variation of the slow wave components contained in the initial slow and fast modes. Therefore, the slow wave components in the incident fast wave can be thought of as being included at incidence. The upgoing fast wave originates around the F region maximum where reflection type coupling is strong. The incident fast wave is highly attenuated and has decreased in magnitude by three orders of magnitude at 1000 km.

Although the mixing ratios in the neutral atmosphere show a predominance of the TM mode, the reflection of the TM mode at ground

surface is almost perfect in the sense that the downgoing and upgoing components have the same magnitude and are 180° out of phase. As a result, the TM upgoing and downgoing waves cancel each other. On the other hand, while the TE mode mixing ratios are much smaller than those for the TM mode, the reflection of the TE mode at ground surface is not perfect; the incoming and reflected waves are almost in phase and additive. Consequently, the TE upgoing and downgoing waves interfere constructively in free space, instead of destructively, as is the case of the TM mode. Therefore, the TE - like wave field remains in the neutral atmosphere, as will be seen later.

Within the ground the resultant wave is transverse electric with some reflection taking place. This mode also penetrates to greater depths at this frequency than at higher frequencies.

4.34 Wave fields

The wave fields of the incident fast wave are shown in Figure 4.19. The magnitudes of the electric and magnetic fields are all relative to

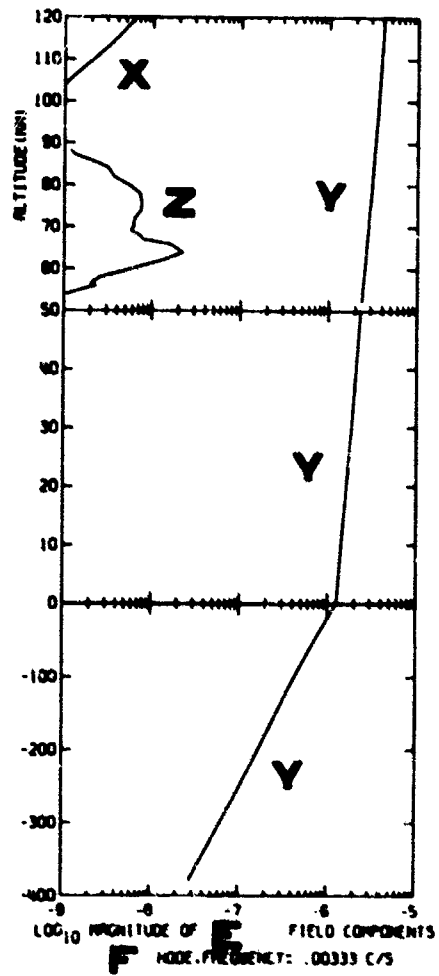
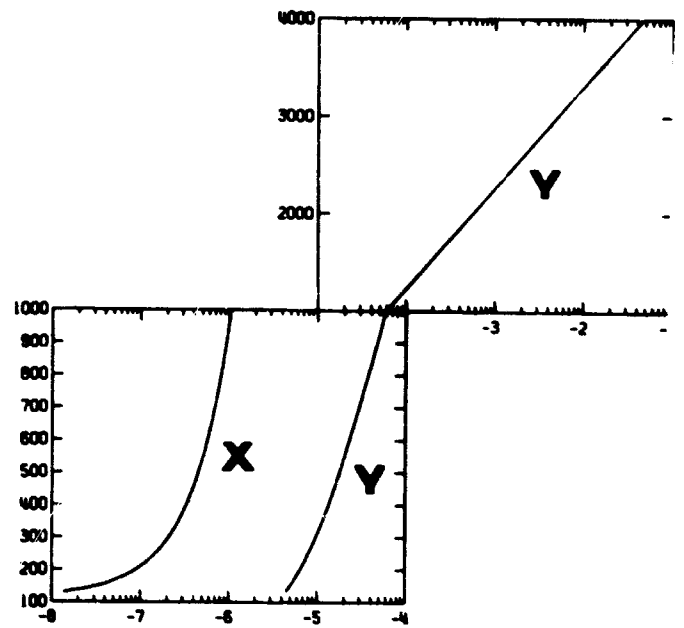


Figure 4.19

the values at 4000 km. If the magnetic field values are multiplied by a factor of 7500 the B field is then obtained in gammas. The electric field is read directly in volts/meter.

The incident fast wave is essentially transverse electric throughout the entire region of consideration. No obvious standing waves are visible in the wave field envelopes as there were at the higher frequencies considered in this investigation. The wave fields are already attenuated by three orders of magnitude at 1000 km. At ground level the magnetic and electric fields are attenuated by four and five orders of magnitude, respectively, compared to the values at 4000 km. Consequently it seems likely that the incident fast wave may be difficult to observe at ground level. A small amount of electric field z-component is generated in the lower D region due to the localized disturbance effect, but no electric field z-component is generated in the neutral atmosphere. Therefore the incident fast wave will not produce charge separation between the lower ionosphere and ground level.

The presence of the z component of the magnetic field throughout the entire region of consideration is also a consequence of the localization of the disturbance. In other words this mode is mostly of TE character and the magnetic z-component persists everywhere. For the plane wave case a z-component of the magnetic field does not appear.

In the ground the fields are attenuated logarithmically but penetrate to greater depths than at higher frequencies.

The wave fields of the incident slow wave are depicted in Figure

4.20. This disturbance is transverse magnetic above the F region maximum and is transformed into transverse electric below the ionosphere. The transition takes place between the F region maximum and 100 km. Within the transition layer the magnetic field character changes from TM to TE due to the presence of mode coupling. However, the character of the electric field does not change across the transition layer. The electric field mode change occurs abruptly at the lower boundary of the ionosphere.

Within the transition layer between 200 km. and 100 km. a horizontal electric current flows rather strongly and gives rise to a steep change in the x and y magnetic components. This electric current layer is necessary for the transition from TM-like at higher altitudes to TE-like at lower altitudes. Also it should be stressed here that whenever the disturbance is specified by a large localizing factor in the x-direction, the wave field ought to behave as a TE mode in the neutral atmosphere, which is bounded by the conducting earth and the ionosphere. Moreover, it is interesting that the electric current layer coincides with the maximum conduction region of the ionosphere (See Part II).

In the lower D region, where the conductivity is rather low, a z-component of the electric field appears as a result of the localized nature of the disturbance. The electric field z-component persists throughout the neutral atmosphere and must cause charge separation to occur between the lower ionosphere and ground surface. This effect is not observed for the incident fast wave or the incident plane wave.

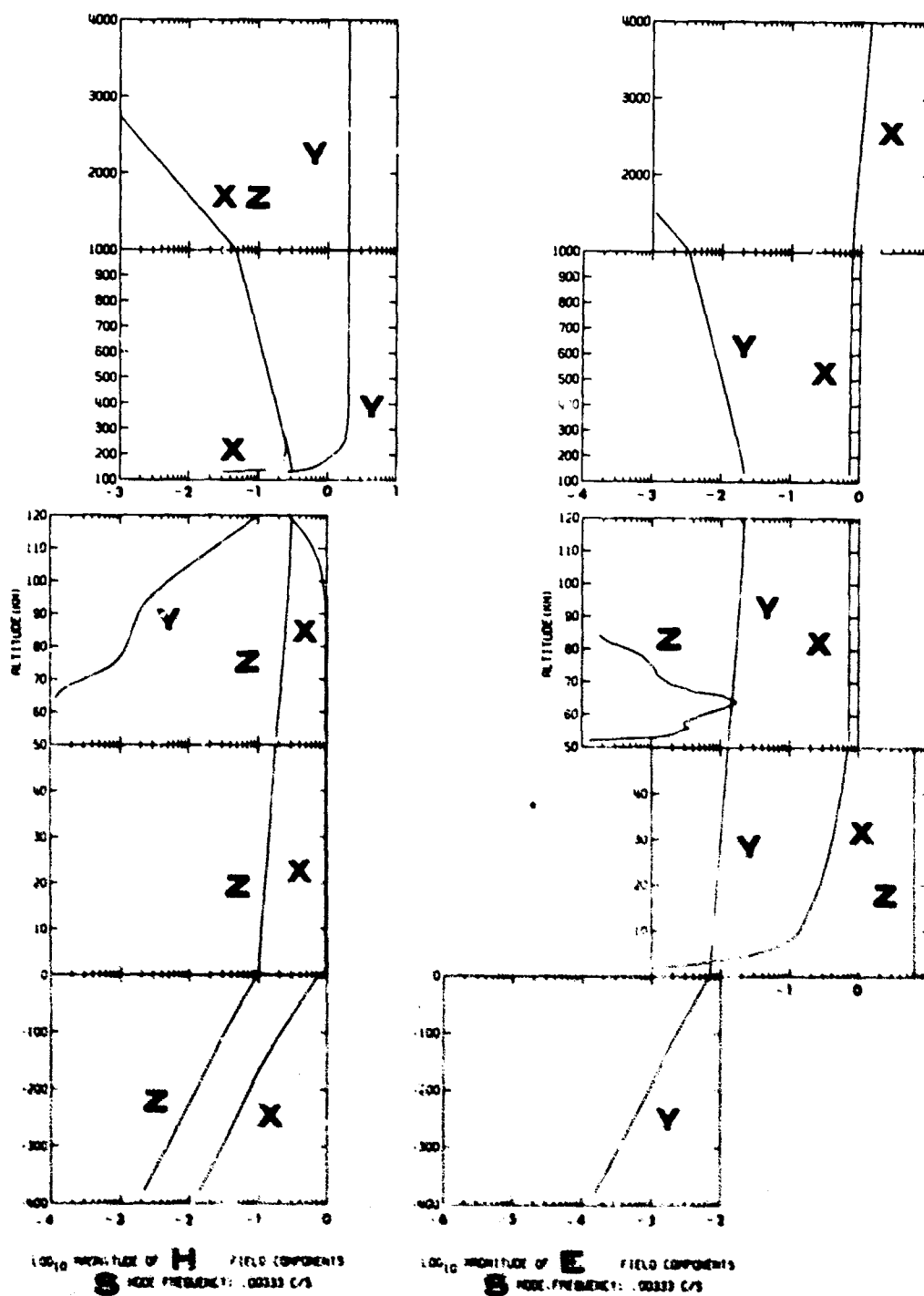


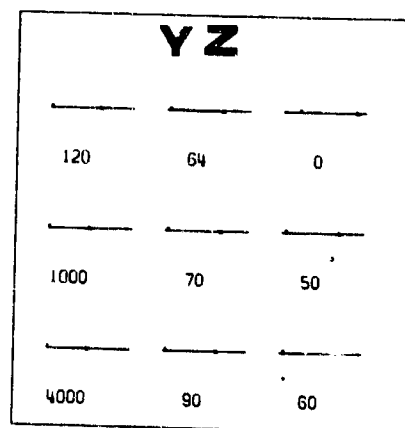
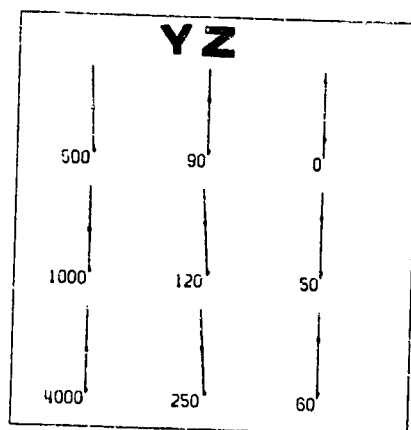
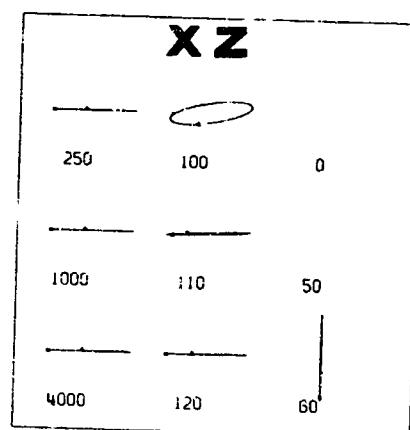
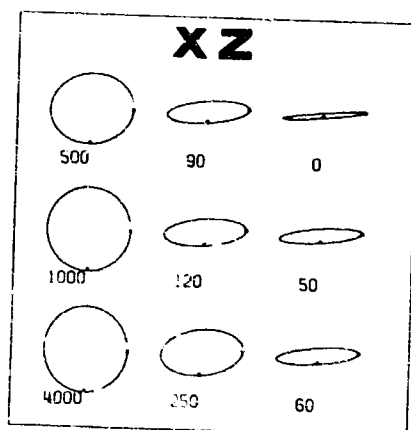
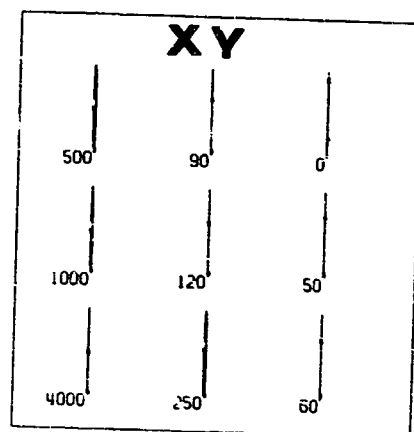
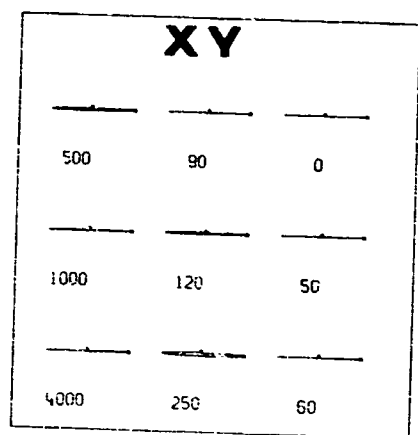
Figure 4.20

The incident slow wave is not severely attenuated between 4000 km. and ground level whereas the incident fast wave is severely attenuated. In fact the value of the electric field z-component of the incident slow wave at ground surface is enhanced by a factor of four over the x-component of the electric field at 4000 km.

4.35 Wave Field Polarization

In Figure 4.21 the incident fast wave is seen to have the magnetic and electric fields linearly polarized in the horizontal plane in the x and y directions, respectively, throughout the ionosphere and at ground level. However, for the magnetic field the xz plane is most important because the x and z magnetic field components are dominant throughout the entire region of consideration. In the xz plane the incident fast wave is right circularly polarized at 4000 km. and right elliptically polarized at ground level. The intervening ionosphere serves to modify the wave from circular to elliptical polarization.

The incident fast wave is seen to be compressive in the presence of the $\vec{E} \times \vec{B}$ drift at high altitudes. As was seen in the wave fields in Figure 4.19, this localized compressive mode is highly attenuated in the form of an evanescent wave, even at high altitudes. Therefore, the conclusion is drawn that a localized disturbance of compressive nature cannot be transmitted along a magnetic field line down to ground surface as long as the cold plasma approximation is made.



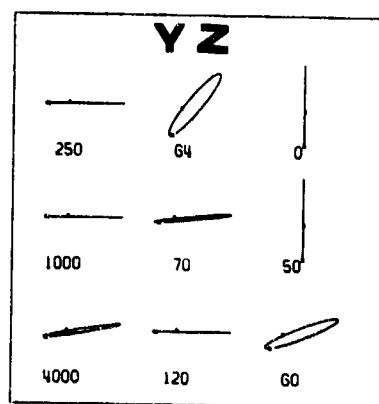
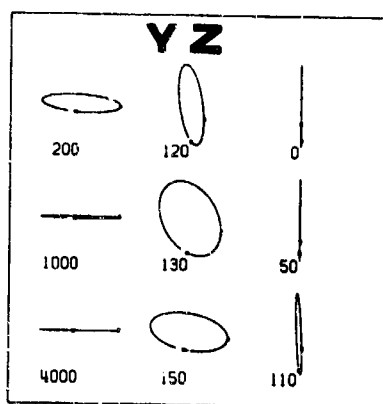
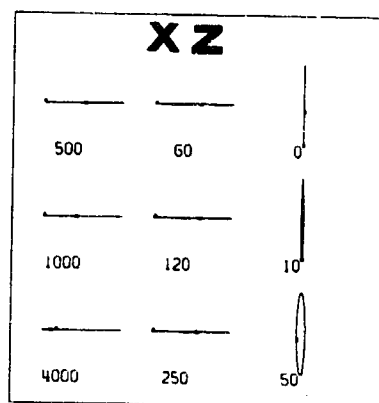
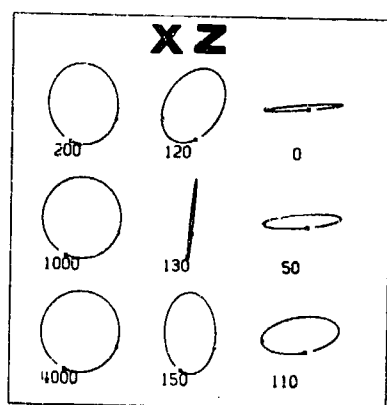
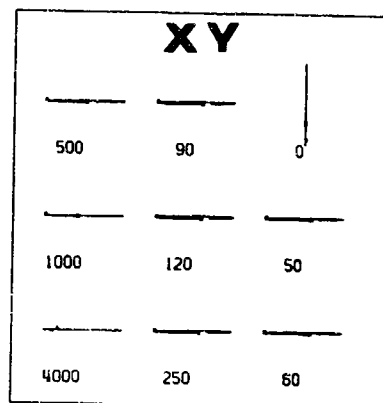
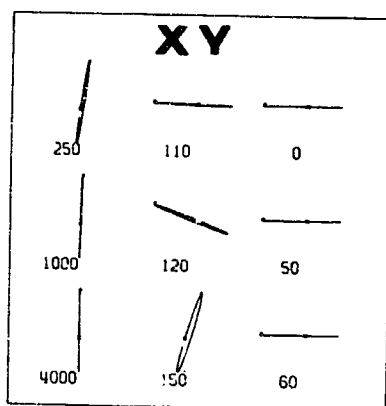
H **F** POLARIZATION
MODE, FREQUENCY = .00333

E **F** POLARIZATION
MODE, FREQUENCY = .00333

Figure 4.21

At 4000 km. the wave normal direction for the incident slow wave is almost perpendicular to the magnetic field line because of the smallness of $\text{Re}[q_g]$. At the higher altitudes this wave is torsional, i. e., an Alfvén wave, and is almost linearly polarized (Figure 4.22). This torsional localized disturbance is quite well transmitted down to ground level. However, as already seen in the wave fields (Figure 4.20), a mode change from torsional at higher altitudes to rather compressional at lower altitudes takes place across the good conducting region centered on 150 km. Therefore, the ionospheric conducting region acts as a surface current layer separating the upper ionosphere of hydromagnetic character from the lower poorly conducting ionosphere. Because of the strong localization in the horizontal direction and of the difference in the reflection at the ground surface between the TE and TM modes, the wave in free space is forced to be of TE character. The mode conversion which takes place between higher and lower regions gives rise to the surface current layer in the good conducting region of the ionosphere. The incident fast wave maintains the TE character throughout the entire region under consideration, so that any obvious surface current layer does not appear.

Thus, from the present analysis, it may be concluded that a torsional disturbance, even if localized, can penetrate from the magnetosphere down to the ground surface. However, a localized compressional disturbance can not be observed at the ground because of its evanescent character in the high f region and in the magnetosphere.



H S POLARIZATION
MODE, FREQUENCY: .00333

E S POLARIZATION
MODE, FREQUENCY: .00333

Figure 4.22

Localized torsional waves resulting from the Kelvin-Helmholtz instability at the magnetopause (Dungey [1955], Parker [1958], and Southwood [1968]) may be observed on the ground. However, those waves should be largely modified in their modes in transmission across the electric current layer of the ionosphere.

In the present work, the disturbance localization is assumed to be in the x-direction only. As a result, the major magnetic component at the ground surface is always in the direction of localization at all the ULF frequencies analyzed, so that linear polarization occurs on the ground. Thus, the wave polarization of the magnetic field on the ground is quite sensitive to the localization of the disturbance.

Consequently, the polarization of the wave disturbances generated in the magnetosphere is difficult to infer from the magnetic polarization observed on the ground unless the localization of the disturbance is precisely known. For example, when a disturbance is localized in two directions and is of the form $e^{-\lambda x} \cdot e^{ik_y y}$ an elliptically polarized wave may possibly result on the ground. Dungey and Southwood [1970] have stressed the importance of the neutral atmosphere and of the localization of the disturbance in determining the modification of hydromagnetic waves transmitted through the ionosphere. The modification of the wave character by different localizations and incident wave polarizations must therefore be carefully examined.

From the present analysis, a vertical magnetic component at

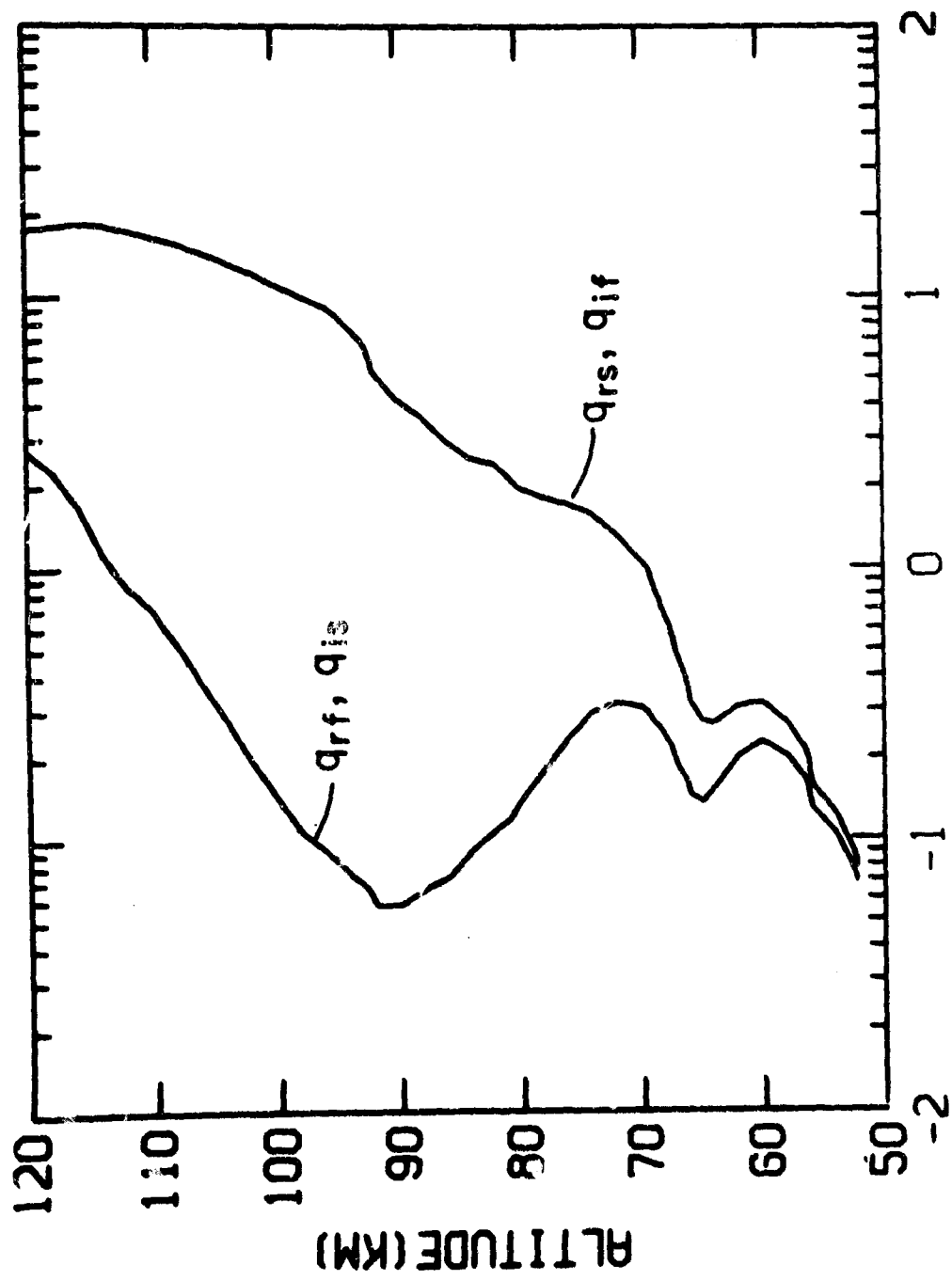
the Earth's surface is found to be associated with all localized disturbance cases. Geomagnetic micropulsations observed in the auroral zones always contain a vertical magnetic component. The inference may then be made that the geomagnetic micropulsations observed at the auroral zone stations are originally localized disturbances.

As Heacock [1970] and Tartaglia [1970] have shown, the wave polarization observed in the auroral zone depends on the location of the observatory relative to the center of the disturbance. This fact also suggests that the disturbances occurring in the auroral zone are localized. Thus, to discuss the observed wave polarization in terms of plane waves in a uniform plasma is not so meaningful.

4.36 Comparison of Localized Disturbance and Plane Wave Cases at $1/300$ c/s

In contrast with the localized disturbance the plane wave case is isotropic above 250 km. Both the slow and fast wave quartic roots have the same values above 250 km. as the slow wave quartic roots of the localized disturbance. Below this level the plane wave case is also anisotropic but the behavior of the plane wave quartic roots is different from the localized disturbance quartic roots in the lower ionosphere (See Figure 4.23). The medium character is summarized in Table 4.4.

The quartic roots indicate the slow mode for the plane wave case is propagating throughout the ionosphere whereas the fast mode is propagating down to about 250 km., below which the fast mode is evanescent. In contrast, for the localized disturbance case the slow



LOG₁₀ QUARTIC ROOTS
L=M=0 FREQUENCY= .00333 C/S

Figure 4.23

REGION	REFRACTIVE INDEX	PROPAGATION CHARACTERISTICS	
		SLOW WAVE	FAST WAVE
Magnetosphere 500 Km. < Alt	Isotropic $\text{Im } q < \text{Re } q$	Propagating	Propagating
Upper Ionosphere 200 < Alt < 500 Km.	Isotropic $\text{Re } q = \text{Im } q$	Propagating	Propagating
Lower Ionosphere 70 < Alt < 200 Km.	Anisotropic	Propagating	Evanescent
Lower D region Alt < 70 Km.	Quasi-isotropic	Propagating	Evanescent
Neutral Atmosphere	Isotropic $\text{Im } q = 0$	Propagating $^{-4}$ $\text{Re } q = 4.45 \times 10^{-4}$ i.e., $n_z = 1.0$	Propagating $\text{Re } q = 4.45 \times 10^{-4}$ i.e., $n_z = 1.0$
Earth's Interior	Isotropic $\text{Re } q = \text{Im } q$	Propagating $ q \sim 10^2$	Propagating $ q \sim 10^2$

TABLE 4.4 Medium characteristics at 1/300 c/s for a plane wave.

mode is propagating down to about 80 km. where it becomes evanescent and the fast mode is evanescent throughout the ionosphere.

From the dispersion relation of section 2.2 the quartic roots for the plane wave case above 800 km. are given approximately by

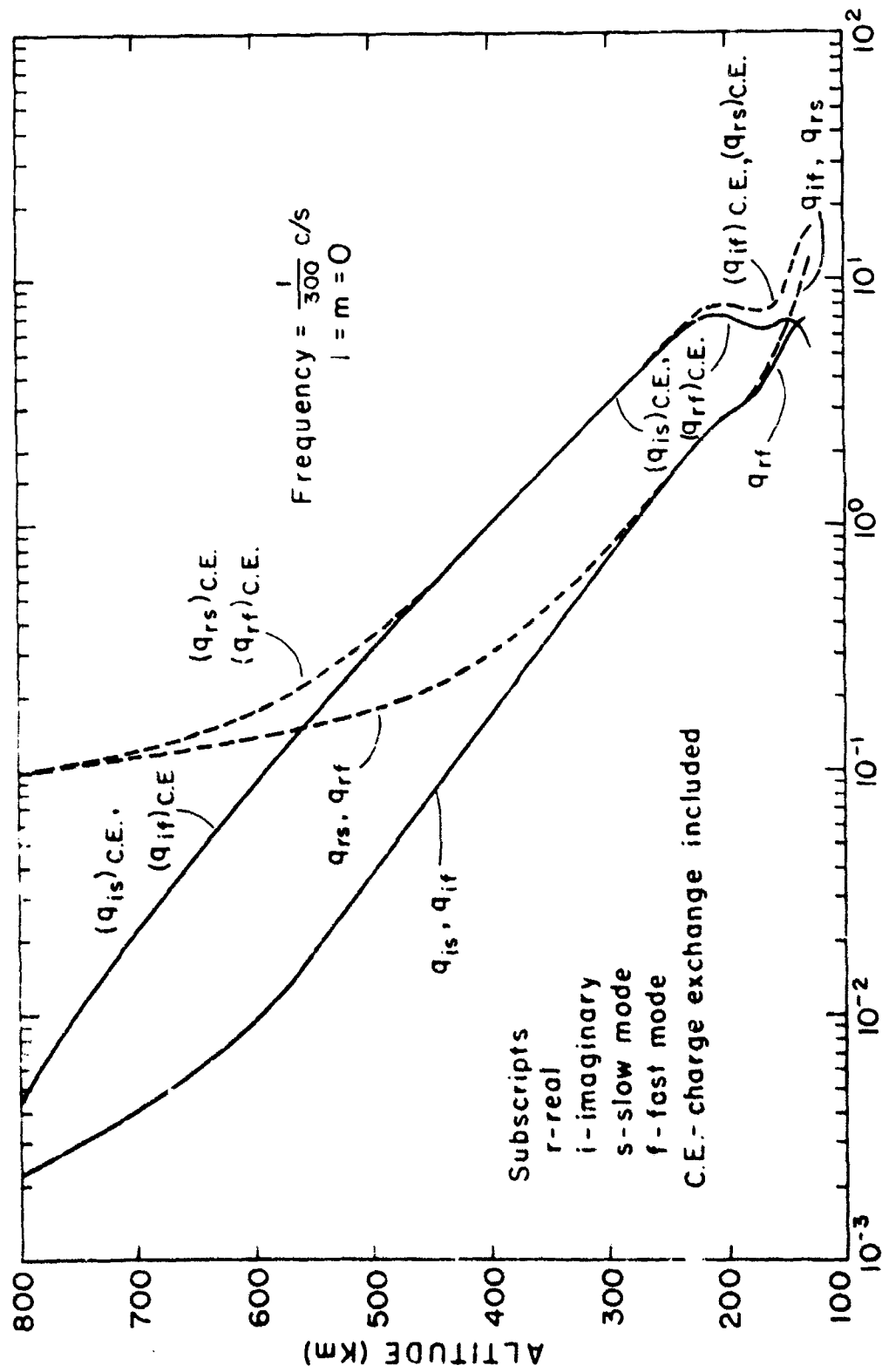
$$q = [r^2 |\Sigma_{\perp i}|]^{\frac{1}{2}}$$

for both the slow and fast waves. Because the disturbance factor f is zero, both modes are propagating. Between 250 km. and 450 km. the slow and fast wave quartic roots are both given approximately by

$$q = [ir^2 |\Sigma_{\perp r}|]^{\frac{1}{2}}$$

The effect of charge exchange on the Booker quartic roots is shown in Figure 4.24. Charge exchange of O^+ with O significantly enhances the real part of the Pedersen conductivity in the region 200-500 km. and causes this region to be metallic, i.e., the real and imaginary parts of the quartic roots are equal. If charge exchange is neglected this metallic region occurs between 200 km. and 250 km.

Although charge exchange considerably enlarges the imaginary parts of the quartic roots, and hence absorption, in this region the wavelength is so large that the ionosphere is still almost completely transparent to the disturbance. Also at this frequency the coupling coefficients are larger than the quartic roots and are the dominant factor in determining the final form of the wave fields.



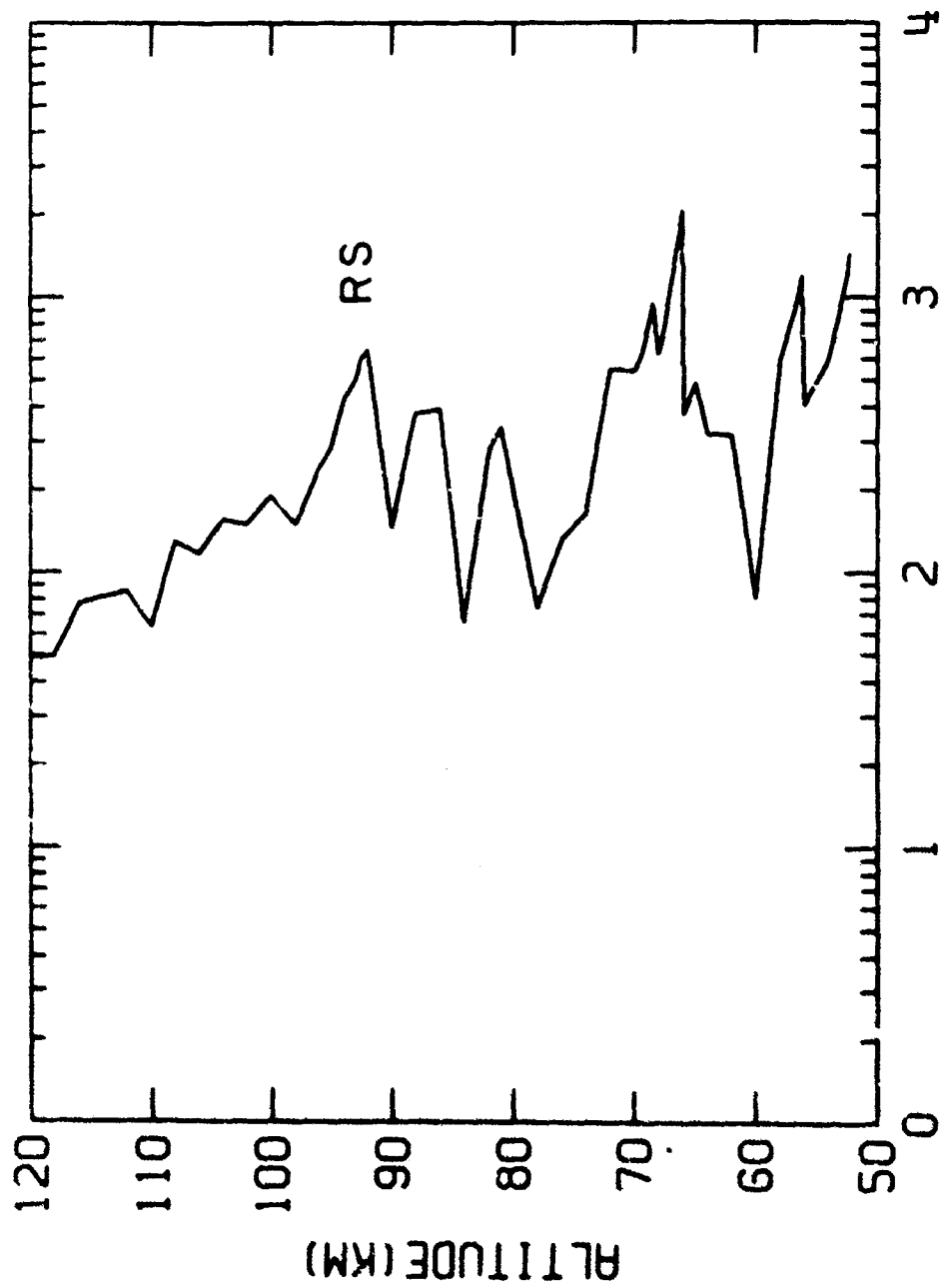
Effect of charge exchange on the Booker Quartic Roots

The neutral atmosphere behaves as free space to the plane wave and as an elastic evanescent region to the localized disturbance. The interior of the Earth is isotropic for the plane wave and the localized disturbance, both of which have the same values for the quartic roots.

For the plane wave the coupling coefficients are the same for both the slow and fast modes. Also, the plane wave coupling coefficients are the same as the coupling coefficients of the localized slow mode except that the mode coupling and mode reflection type coupling terms are absent from the plane wave case (See Figure 4.25). Consequently reflection type coupling is dominant for the plane wave case; mode coupling and mode reflection type coupling are a result of the localized nature of the disturbance.

The mixing ratios reveal that the slow mode plane wave is transverse magnetic at 4000 km. and inside the Earth. This fact is also borne out by the wave fields. The localized slow mode was seen to change from transverse magnetic at 4000 km. to transverse electric inside the Earth. The incident fast mode is transverse electric at all altitudes for the plane wave and localized disturbance cases.

The wave fields for the plane wave (Figures 4.26 and 4.27) reveal that the z components of the electric and magnetic fields are zero. Therefore the plane wave will not induce any surface charge at the bottom of the lower ionosphere and at ground. Also, the electric field of the slow mode plane wave is attenuated by only one order of magnitude between 4000 km. and ground surface and the magnetic field is completely



LOG₁₀ COUPLING COEFFICIENTS

L=M=0 FREQUENCY= .00333 C/S

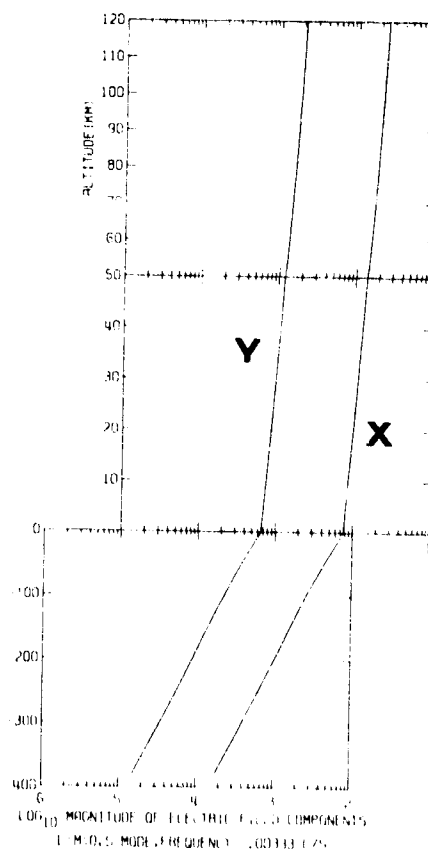
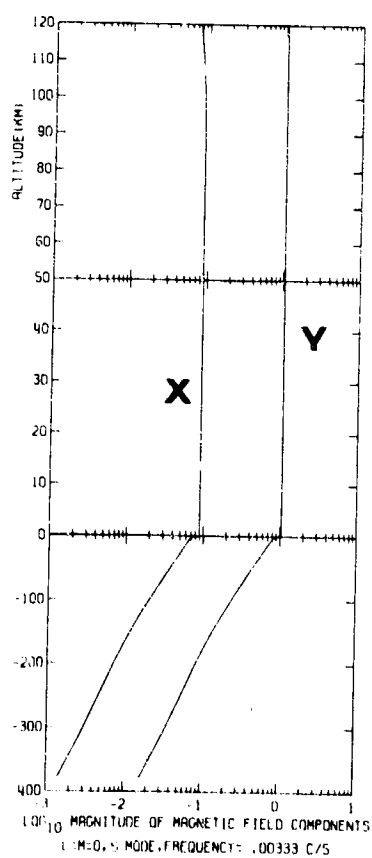
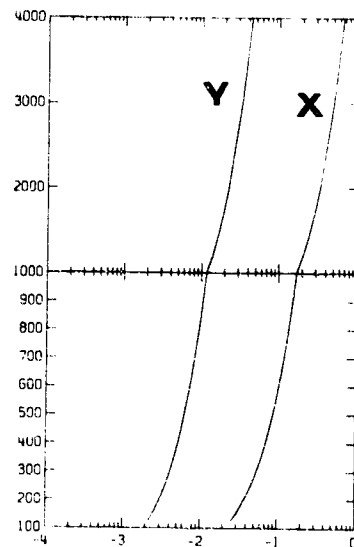
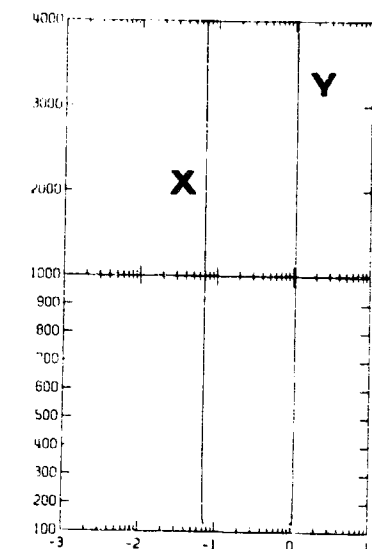


Figure 4.26

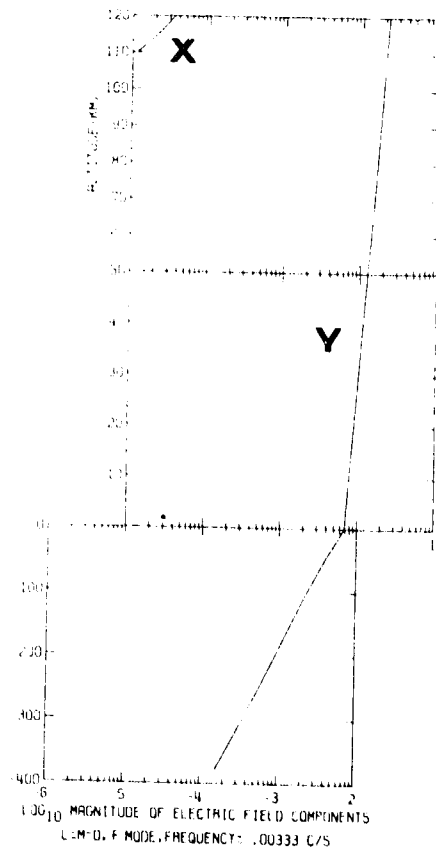
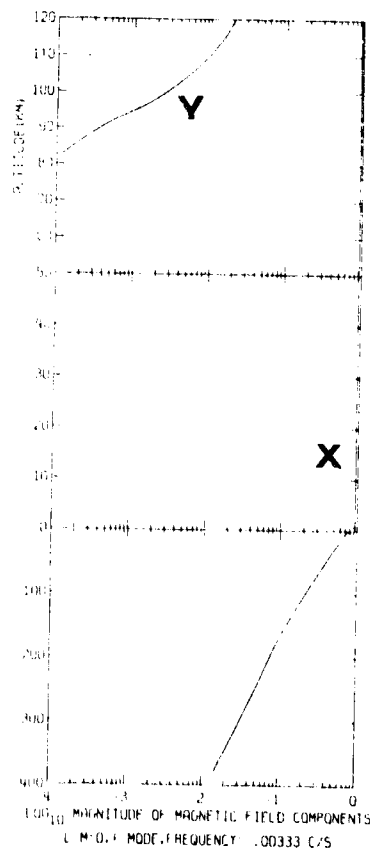
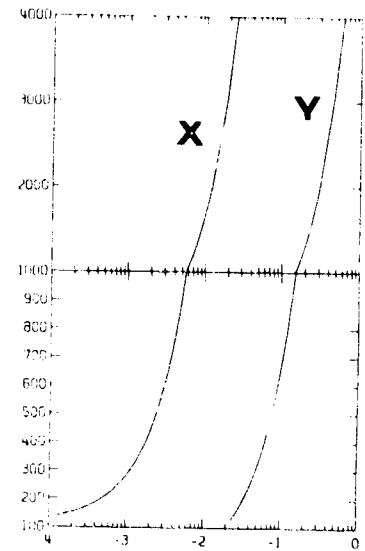
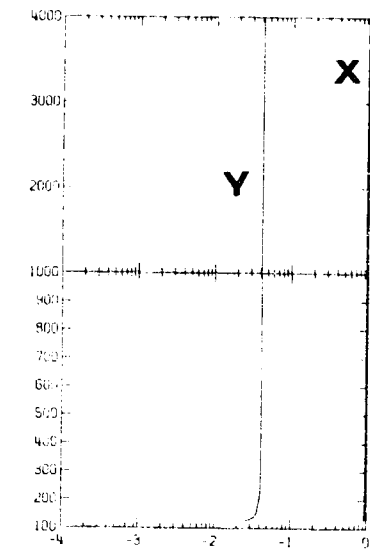


Figure 4.27

unattenuated down to the Earth's surface. Thus the Earth's ionosphere and atmosphere are nearly transparent to the incident slow mode plane wave.

The electric field of the incident fast mode plane wave is attenuated by two orders of magnitude and the magnetic field is completely unattenuated between 4000 km. and ground surface. For the localized case the magnetic and electric wave fields of the incident fast mode were attenuated by four and five orders of magnitude, respectively, between 4000 km. and the Earth's surface. Consequently, introduction of the localizing effect causes the fast mode to be much more severely attenuated.

The wave polarization is almost linear at every height for both the slow and fast plane wave cases. However, at higher altitudes for the fast wave and at lower altitudes for the slow wave, a slight ellipticity is discernible. The rotation sense is right handed for the slow wave and left handed for the fast wave. The hydromagnetic wave polarization in a collisionless cold plasma should be basically linear (See Stix [1962]). However, elliptical polarization may result when collisions are taken into account, because of the greater effect of collisions on the dispersion relation at hydromagnetic frequencies than at higher frequencies. Thus, the small ellipticity in the wave polarization results from the effect of collisions.

5.0 OVERALL COMPARISON OF THE DISTURBANCE PROPAGATION CHARACTERISTICS AT THE VARIOUS FREQUENCIES INVESTIGATED

In Tables 5.1 and 5.2 are found some of the physical parameters of the incident slow and fast modes, respectively, at 5000 km. for all the frequencies considered in this investigation. The propagation angle θ is measured with respect to the magnetic field line, i.e., from the vertical. The quantity δ is the skin depth measured in km. and is given by

$$\delta = \frac{R_e}{q_i}$$

where q_i is the imaginary part of the Booker quartic root and R_e is the Earth's radius in km. The wavelengths λ_x and λ_z in the x and z directions, respectively, are given by

$$\lambda_x = \frac{2\pi R_e}{\ell}$$

$$\lambda_z = \frac{2\pi R_e}{q_r}$$

where ℓ is the Fourier number and q_r is the real part of the Booker quartic root. Notice that at the lower frequencies λ_z is very large, i.e., about $1.6 R_e$ at 1/3 cps. and $160 R_e$ at 1/300 cps. for the incident slow wave.

Reflection coefficients for the various incident slow and fast mode disturbances are tabulated in Table 5.3. The coefficients are

Freq (c/s)	Disturbance	$\Theta(^{\circ})$	$\text{Re } n_z$	$\text{Im } n_z$	λ_x (km)	λ_z (km)	δ (km)
100	Plane	0.0	167.9	5.652×10^{-4}	∞	17.87	8.450×10^5
	Loc.	0.2558	167.9	5.652×10^{-4}	4.003×10^3	17.87	8.450×10^5
3.0	Loc.	15.77	88.45	5.896×10^{-4}	"	1.131×10^3	2.670×10^7
1/3	Loc.	68.59	88.15	5.239×10^{-3}	"	1.021×10^4	2.734×10^7
1/300	Plane	0.0	88.15	5.239×10^{-1}	∞	1.021×10^6	2.734×10^7
	Loc.	89.78	88.15	5.239×10^{-1}	4.003×10^3	1.021×10^6	2.734×10^7

TABLE 5.1 Disturbance parameters for slow mode at 5000 Km.

Freq (c/s)	Disturbance	$\theta(^{\circ})$	$\text{Re } n_2$	$\text{Im } n_2$	λ_x (km)	λ_z (km)	δ (km)
100	Plane	0.0	67.76	3.283×10^{-5}	∞	44.28	1.455×10^7
	Loc.	0.6338	67.76	3.283×10^{-5}	4.003×10^3	44.28	1.455×10^7
3.0	Loc.	17.20	80.70	6.321×10^{-4}	"	1.239×10^3	2.518×10^7
1/3	Loc.	90.00	1.516×10^{-3}	3.058×10^2	"	5.939×10^8	4.685×10^2
1/300	Plane	0.0	88.15	5.259×10^{-1}	∞	1.021×10^6	2.734×10^7
	Loc.	90.00	1.896×10^{-3}	3.171×10^4	4.003×10^3	4.749×10^{10}	4.518×10^2

TABLE 5.2 Disturbance parameters for fast mode at 5000 Km.

Freq (c/s)	Dist	R _{ss}		R _{sf}		R _{fs}		R _{ff}	
		r	$\theta(^{\circ})$	r	$\theta(^{\circ})$	r	$\theta(^{\circ})$	r	$\theta(^{\circ})$
100	Plane	8.228×10^{-8}	280.08	.9940	350.65	.1520	248.13	7.355×10^{-8}	58.91
	Loc.	2.834×10^{-4}	72.411	.9962	209.67	7.069×10^{-2}	283.04	6.718×10^{-4}	249.09
3.0	Loc.	.1580	256.41	5.095×10^{-2}	256.67	.1581	160.95	.3788	354.59
1/3	Loc.	.6802	187.02	3.295×10^{-4}	7.479	2.262×10^{-4}	-203.34	9.000×10^{-3}	1.079×10^{-3}
1'300	Plane	6.450×10^{-2}	187.76	.9990	182.84	.9990	182.84	4.334×10^{-2}	111.17
	Loc.	.9717	182.53	2.331×10^{-6}	196.12	1.494×10^{-4}	102.81	1.154×10^{-6}	319.56

TABLE 5.3 Reflection coefficients for incident slow and fast waves.

defined in terms of the mixing ratios at 5000 km. For example, R_{sf} means the ratio of the upgoing fast wave to the downgoing slow wave at 5000 km., where r is the modulus of the ratio and θ is the phase angle. Thus $R = re^{i\theta}$.

At 100 cps. the incident slow mode is almost entirely reflected due to the ion resonance which is encountered at 1070 km. At 3.0 cps. the incident fast wave is well reflected whereas at 1/3 cps. the incident slow wave is well reflected. At 1/300 cps. the incident slow and fast plane waves are almost completely reflected; Tables 5.4 and 5.5 reveal that the transmission coefficients for these waves are nearly unity at ground level so that most of the reflection takes place at the Earth's surface.

The transmission coefficients for the electric and magnetic wave fields of the fast and slow waves, respectively, are found in Tables 5.4 and 5.5. As an example the transmission coefficient T_{xz}^E is defined as the ratio of the magnitude of the electric field z component at ground level to the magnitude of the electric field x component at 4000 km. T_E is defined as the ratio of the magnitude of the total electric field at ground level to the magnitude of the total electric field at 4000 km. The same definitions apply to the magnetic field transmission coefficients.

In general the incident fast wave transmission coefficients are smaller than the incident slow wave transmission coefficients except at 100 cps. where the slow wave transmission coefficients are zero because the ion resonance condition is encountered at 1070 km. and

Freq (c/s)	Dist	ELECTRIC FIELD TRANSMISSION COEFFICIENTS				MAGNETIC FIELD TRANSMISSION COEFFICIENTS			
		T_{xx}^E	T_{yy}^E	T_{xz}^E	T_E	T_{xx}^B	T_{yy}^B	T_{zz}^B	T_B
100	Plane	1.11×10^{-3}	1.11×10^{-3}	0.0	1.11×10^{-3}	9.71×10^{-2}	9.71×10^{-2}		9.71×10^{-2}
	Loc.	3.37×10^{-3}	1.08×10^{-3}	1.60×10^1	1.13×10^1	8.16×10^{-2}	2.55×10^{-1}	1.08×10^{-3}	1.34×10^{-1}
3.0	Loc.	0.0	1.02×10^{-5}	0.0	1.02×10^{-5}	1.24×10^{-3}	0.0	1.02×10^{-5}	1.06×10^{-3}
1/3	Loc.	0.0	4.43×10^{-7}	0.0	4.43×10^{-7}	1.10×10^{-4}	0.0	4.43×10^{-7}	7.72×10^{-5}
1/300	Plane	0.0	1.14×10^{-2}	0.0	1.14×10^{-2}	9.80×10^{-1}	0.0		9.79×10^{-1}
	Loc.	0.0	2.70×10^{-5}	0.0	2.70×10^{-5}	2.61×10^{-4}	0.0	2.71×10^{-5}	1.84×10^{-4}

TABLE 5.4 Incident fast mode electric and magnetic wave field transmission coefficients.

Freq (c/s)	Dist	ELECTRIC FIELD TRANSMISSION COEFFICIENTS				MAGNETIC FIELD TRANSMISSION COEFFICIENTS			
		T_{xx}^E	T_{yy}^E	T_{xz}^E	T_E	T_{xx}^B	T_{yy}^B	T_{zz}^B	T_B
100	Plane	0.0	0.0	0.0	0.0	0.0	0.0	<div></div>	0.0
	Loc.	0.0	0.0	0.0	0.0	0.0	0.0	0.0	0.0
3.0	Loc.	1.15×10^{-7}	9.46×10^{-4}	1.09×10^{-1}	1.03×10^{-1}	1.27×10^{-1}	3.79×10^{-5}	9.46×10^{-4}	2.25×10^{-2}
1/3	Loc.	7.03×10^{-9}	2.31×10^0	1.73×10^{-1}	1.73×10^{-1}	1.33×10^3	3.10×10^{-5}	2.30×10^{-5}	1.24×10^0
1/300	Plane	1.14×10^{-2}	1.50×10^{-2}	0.0	1.14×10^{-2}	1.30×10^0	9.81×10^{-1}	<div></div>	9.81×10^{-1}
	Loc.	4.67×10^{-10}	1.62×10^3	4.55×10^0	4.55×10^0	1.56×10^4	4.38×10^{-8}	1.62×10^3	4.72×10^{-1}

TABLE 5.5 Incident slow mode electric and magnetic wave field transmission coefficients.

none of the slow wave energy is able to penetrate this barrier. The localized incident fast wave at 100 cps. and the localized incident slow wave at 1/300 cps. are very efficient in storing electric field energy in the neutral atmosphere. The transmission coefficient T_E of the former is 3.5 times larger than T_E for the latter. Also, the incident slow wave at 1/3 cps. is very efficient at storing magnetic field energy below the F region due to energy being reflected back and forth between the Earth and the conducting wall appearing between 200 and 600 km. as a result of charge exchange of O^+ with O, which enhances the Pedersen conductivity.

In Table 5.6 a comparison is made of magnetic field transmission coefficients obtained by various investigators for two different wave frequencies. For the present work L and R correspond to the incident slow and incident fast waves, respectively; these are propagating at 16° and 17° , respectively, at 3.0 cps. and at 0.0° for both modes at 1/300 cps. The results of Altman and Fijalkow [1968] were obtained for vertical propagation but with the magnetic field inclined at 20° from the vertical. The results of E.C. Field [1963] were obtained for vertical polar propagation; L corresponds to the ordinary mode and R corresponds to the extraordinary mode. Notice that the L (R) results of the present work at 3.0 cps. correspond more closely to the R (L) results of Field. This is due to the fact that the incident slow (fast) wave reverses polarization and propagates through the ionosphere primarily in the R (L) mode. Altman and Fijalkow also found that energy

Freq (c/s)	INVESTIGATOR	L	R
3.0	Shaeffer & Inoue	2.25×10^{-2}	1.06×10^{-3}
	E.C. Field	2×10^{-3}	8.5×10^{-2}
	Altman and Fijalkow	2.5×10^{-2}	
1/300	Shaeffer & Inoue	9.81×10^{-1}	9.79×10^{-1}
	Greifinger and Greifinger	2×10^0	

TABLE 5.6 Comparison of magnetic field transmission coefficients obtained by various investigators for two different wave frequencies.

was being fed from L to R in transmission through the ionosphere.

Greifinger and Greifinger also considered polar propagation and found somewhat larger transmission coefficients than what the present investigation reveals.

Campbell [1967] compiled attenuation factors computed by various investigators (Akasofu, 1965; Francis and Karplus, 1960; Greifinger and Greifinger, 1965a; Karplus et. al., 1962; Prince et. al., 1964; Wentworth, 1964) and found that Pcl signals were reduced to about 0.5 - 0.7 at 0.5 cps. and 0.2 - 0.5 at 1.0 cps. of the initial amplitudes at the top of the ionosphere in transmission through the daytime ionosphere at midlatitudes. The present work found transmission coefficients which were much smaller at 3.0 cps. for the incident slow and fast waves and at 1/3 cps. for the incident slow wave; however, the transmission coefficient for the incident slow wave at 1/3 cps. was greater than unity.

The discrepancies of these results with Campbell's conclusions may be attributed to several factors.

1. Previous works divided the medium into thick layers with gross properties, whereas this work considers a large number of slabs in which the ionospheric parameters vary continuously with altitude.

2. Incident plane waves were assumed in previous investigations whereas in this work a localized disturbance was considered.

3. Resonant charge exchange collisions have apparently heretofore been neglected. This process has been found to be important in determining

the final wave fields in the Pc1 range.

4. Campbell's results were based on the measurement of one component only. Table 5.5 shows that this may lead to completely erroneous conclusions. Here, at 3.0 cps. for the incident slow mode, T_{xx}^B is approximately 0.1 but T_B is 2.25×10^{-2} . Thus three component measurements are in general necessary.

In Tables 5.7 and 5.8 are given the magnitudes of the electric and magnetic wave fields, predicted from the full wave calculations, at various altitudes for typical observed values, given in the doubly ruled boxes, at some given height. For the incident fast wave the 100 milligamma magnetic field strength at the altitude h_i (364 km.) is based on the measurements of Scarf et. al. [1968]. At the other frequencies for the incident fast wave typical ground observed magnetic field values are chosen, e.g., see Campbell [1968]. Also, for the Pc1 and Pc5 frequencies the intermediate height h_i is 120 km. Notice that the localized disturbances at 1/3 and 1/300 cps. (Table 5.7) require uncommonly high magnetic field values at 4000 km. in order to observe a typical ground measurement of 0.2 and 50 gammas, respectively. Therefore the incident fast waves with the Fourier number L equal to $10\sqrt{2}$ at 1/3 and 1/300 cps. appear to be banished from the realm of reality.

Consider the case where the magnetospheric plasma at 4000 km. is moving perpendicular to the Earth's magnetic field with a drift velocity of 0.4 km/sec. (values as high as 1 km./sec. have been

Freq (c/s)	Dist.	MAGNETIC FIELD MAGNITUDES (gammas)			ELECTRIC FIELD MAGNITUDES (volts/meter)		
		0.0 Km	h_i	4000 Km	0.0 Km	h_i	4000 Km
100	Plane	4.24×10^{-3}	100×10^{-3}	4.36×10^{-2}	2.85×10^{-7}	1.10×10^{-4}	2.56×10^{-4}
	Loc.	8.52×10^{-3}	100×10^{-3}	4.64×10^{-2}	2.58×10^{-4}	1.06×10^{-4}	2.28×10^{-4}
3.0	Loc.	1×10^{-2}	1.43×10^{-1}	9.43×10^0	7.34×10^{-7}	1.04×10^{-4}	7.20×10^{-2}
1/3	Loc.	2×10^{-1}	3.54×10^{-1}	2.59×10^3	7.74×10^{-7}	5.01×10^{-5}	1.75×10^0
1/300	Plane	5×10^1	5.01×10^1	5.11×10^1	4.90×10^{-5}	1.54×10^{-4}	4.30×10^{-3}
	Loc.	5×10^1	5.49×10^1	2.72×10^5	4.88×10^{-5}	1.56×10^{-4}	1.81×10^0

TABLE 5.7 Electric and magnetic wave field magnitudes of the incident fast wave at various altitudes. The intermediate height h_i is 364 Km for 100 c/s and 120 Km for the other frequencies.

Freq (c/s)	Dist.	MAGNETIC FIELD MAGNITUDES (gammas)			ELECTRIC FIELD MAGNITUDES (volts/meter)		
		0.0 Km	h_i	4000 Km	0.0 Km	h_i	4000 Km
100	Plane	0.0	2.91×10^{-1}	1.0	0.0	2.49×10^{-4}	1.43×10^{-4}
	Loc.	0.0	4.79×10^{-1}	1.0	0.0	3.45×10^{-4}	6.89×10^{-3}
3.0	Loc.	1×10^{-2}	1.01×10^{-1}	4.44×10^{-1}	1.76×10^{-4}	6.29×10^{-6}	1.63×10^{-3}
1/3	Loc.	2×10^{-1}	3.09×10^{-1}	1.61×10^{-1}	4.75×10^{-4}	6.70×10^{-5}	2.75×10^{-3}
1/300	Plane	5×10^1	5.00×10^1	5.10×10^1	4.89×10^{-5}	1.55×10^{-4}	4.29×10^{-3}
	Loc.	5×10^1	2.69×10^1	1.06×10^2	4.42×10^{-2}	5.11×10^{-3}	9.72×10^{-3}

TABLE 5.8 Electric and magnetic wave field magnitudes of the incident slow wave at various altitudes. The intermediate height h_i is 1060 Km for 100 c/s and 120 Km for the other frequencies.

observed, e.g., see Parker [1968], p. 21). For a steady magnetic field value of 10^{-5} wb/m² the electric field generated at 4000 km. by this drifting plasma is given by

$$\vec{E} = \vec{V} \times \vec{B}$$

or $|\vec{E}| = 4 \times 10^{-3}$ volts/m.

If the plasma is modulated at a frequency of 1/300 cps. this electric field value is precisely what is needed by either the incident fast or slow plane wave in order to generate a 50 gamma Pc5 disturbance at ground level. In like manner plasma drift velocities between 0.1 and 1.0 km./sec., modulated at the appropriate frequency, are sufficient for the incident slow waves considered in this investigation (Table 5.8) to excite typical ground observed magnetic field disturbances in the Pc1 and Pc5 frequency ranges.

6.0 CONCLUSIONS AND RECOMMENDATIONS

6.1 Conclusions

A localized disturbance was introduced at all frequencies considered in this investigation and was found to have several effects. If the localization was large compared to the Pedersen conductivity, e.g., at $1/3$ and $1/300$ c/s, then the incident fast wave was evanescent in the upper regions of the ionosphere. Also, the neutral atmosphere became an evanescent region and mode coupling became large in the ionosphere, even for near-vertical incidence, for both the incident slow and fast modes. Localization resulted in a large vertical electric field in the neutral atmosphere for the incident fast wave at 100 c/s and for the incident slow waves at 3.0, $1/3$, and $1/300$ c/s.

Coupling of the various magnetoionic characteristic waves was found to be of importance in determining final wave fields, in particular at $1/3$ c/s and $1/300$ c/s. In fact even for vertical propagation of the plane wave at $1/300$ c/s the coupling coefficients were found to be larger than the Booker quartic roots throughout almost the entire region of interest. Also, at $1/300$ c/s the incident slow mode was transformed from transverse magnetic at 4000 km to transverse electric in the Earth as a result of strong mode coupling which peaked around 150 km.

Inclusion of resonant charge exchange collisions resulted in an enhanced Pedersen conductivity such that the integrated Pedersen conductivity is approximately 1.5 times the integrated Hall conductivity. Thus the ionospheric model of Jacobs and Watanabe [1962] for

hydromagnetic wave propagation which neglected the Pedersen region must be revised to include two conducting layers. Magnetic energy is stored in the ionosphere as a result of reflection from the Pedersen layer, viz., for the incident fast wave at 100 c/s, for the incident slow and fast waves at 3.0 c/s, and for the incident slow wave at 1/3 c/s. Also, at 1/3 c/s magnetic wave energy for the incident fast wave is stored between about 200 km and 600 km, where the upper limit was determined by the localizing factor ℓ which caused the incident fast wave to be evanescent above 600 km.

Charge exchange also enhances the imaginary part of the quartic roots so that some absorption of wave energy takes place in the Pc 1 frequency range between approximately 150 km and 250 km. The absorption effect is not as clear in the Pc 5 frequency range where the coupling coefficients are everywhere larger than the quartic roots.

On the Earth's surface the observable wave field is a residual between the incoming and reflected waves and is usually small because of almost perfect reflection. Also, this residual is sensitive to the conductivity of the Earth's surface. Therefore, the assumption of a perfectly conducting Earth is not appropriate for the purpose of comparison of the wave characteristics on the ground and at the top of the ionosphere. Reflection at the Earth's surface can affect the wave fields in the hydromagnetic frequency range throughout the entire medium being considered. The reflection strongly depends on the form of the disturbance as well as on the conductivity of the ground surface

layer. Thus, it is worthwhile to investigate the resultant wave field from the full wave solution by changing the ground surface conductivity and the functional form of the disturbance. The surface conductivity data obtained by the Dallas geomagnetic station and used in the present analysis are perhaps somewhat high compared to data obtained by stations located in areas of different geological structure.

The incident fast waves with a disturbance factor ℓ value of $10\sqrt{2}$ at $1/3$ and $1/300$ c/s are deemed incapable of being observed on the ground in view of the extremely high field values necessary at 4000 km in order to generate typical ground observed values.

At 4000 km altitude plasma drift velocities between 0.1 and 1.0 km/sec, modulated at the appropriate frequency, are sufficient for the incident slow waves considered in this investigation (Table 5.8) to excite typical ground observed magnetic field disturbances in the Pc 1 and Pc 5 frequency ranges.

At 3.0 c/s (Pc 1) the incident slow (fast) mode was found to undergo polarization reversal at 1000 km and to propagate through most of the ionosphere polarized in the right (left) hand sense, although the polarization at ground level was linear. In view of the fact that the incident fast wave is highly attenuated, this conclusion seems to be consistent with Campbell's [1967] hypothesis that ground observed signals have characteristic R wave absorption in the ionosphere.

6.2 Recommendations

In order to determine more fully the nature of electromagnetic disturbances in the ULF and ELF frequency range the following investigations are considered to be necessary.

1. Narrow band measurements of electric and magnetic wave fields in the ELF frequency range at satellite altitudes.
2. Polarization and wave field magnitude measurements of micro-pulsation disturbances at satellite altitudes.
3. Further full wave analysis at different frequencies and varying ionospheric conditions.
4. Simultaneous observation of satellite and ground based signals.

REFERENCES

- Akasofu, S., Attenuation of Hydromagnetic Waves in the Ionosphere, Radio Sci., 69D, 361-366, 1965.
- Altman, C., and H. Cory, The Simple Thin-Film Optical Method in Electromagnetic Wave Propagation, Radio Sci., 4, 449-457, 1969a.
- Altman, C., and H. Cory, The Generalized Thin-Film Optical Method in Electromagnetic Wave Propagation, Radio Sci., 4, 459-470, 1969b.
- Altman, C., and E. Fijalkow, Mechanism of Transmission of Hydromagnetic Waves through the Earth's Lower Ionosphere, Nature, 220, 53-55, 1968.
- Altman, C., and E. Fijalkow, The Transmission of Electromagnetic Waves Through the Ionosphere at Micropulsation Frequencies, presented at URSI Symposium on Electromagnetic Waves, Stresa, Italy, July 24-29, 1968, published in Alta Frequenza, XXXVIII, 183-188, 1969.
- Barrington, R.E., J.S. Belrose, and W.E. Mather, A Helium Whistler Observed in the Canadian Satellite Alouette 2, Nature, 210, 80-81, 1966.
- Barron, D.W., and K.G. Budden, The Numerical Solution of Differential Equations Governing the Reflexion of Long Radio Waves from the Ionosphere, 3, Proc. Roy. Soc. London, A, 249 (1258), 387-401, 1959.
- Budden, K.G., The Numerical Solution of Differential Equations Governing the Reflexion of Long Radio Waves from the Ionosphere, 1, Proc. Roy. Soc. London, A, 227 (1171), 516-537, 1955.
- Budden, K.G., Radio Waves in the Ionosphere, Cambridge University Press, London, England, 1961.
- Budden, K.G., Full Wave Solutions for Radio Waves in a Stratified Magnetospheric Medium, Alta Frequenza, XXXVIII, 167-179, 1969.
- Campbell, Wallace H., Low Attenuation of Hydromagnetic Waves in the Ionosphere and Implied Characteristics in the Magnetosphere for Pcl events, J. Geophys. Res., 72, 3429-3445, 1967.
- Campbell, Wallace H., Rapid Geomagnetic Field Variations Observed at Conjugate Locations, Radio Sci., 3, 726-733, 1968.

- Campbell, Wallace H., and Ernest C. Stiltner, Some Characteristics of Geomagnetic Pulsations at Frequencies near 1 c/s, Radio Sci., 69D, 1117-1132, 1965.
- Clemmow, P.C., and J. Heading, Coupled Forms of the Differential Equations Governing Radio Propagation in the Ionosphere, Proc. Cambridge Phil. Soc., 50, 319-333, 1954.
- Dawson, John A., Hydromagnetic Wave Propagation Near 1 c/s in the Upper Atmosphere and the Properties and Interpretation of Pcl Micropulsations, NBS Tech. Note No. 342, June 30, 1966.
- Dungey, J.W., The Attenuation of Alfvén Waves, J. Geophys. Res., 50, 323-328, 1954a.
- Dungey, J.W., Electrodynamics of the Outer Atmosphere, Penn State University Ionos. Res. Lab. Sci. Report No. 69, 1954b.
- Dungey, J.W., The Propagation of Alfvén Waves Through the Ionosphere, Penn State University Ionos. Res. Lab. Sci. Report No. 57, 1954c.
- Dungey, J.W., and D.J. Southwood, Ultra Low Frequency Waves in the Magnetosphere, Space Sci. Rev., 10, 672-688, 1970.
- Fejer, J.A., Hydromagnetic Wave Propagation in the Ionosphere, J. Atmos. Terrest. Phys., 18, 135-146, 1960.
- Field, E.C., Hydromagnetic Signals in the Ionosphere, Memo. RM-3830-PR, Rand Corp., 1963.
- Field, E.C., and C. Greifinger, Transmission of Geomagnetic Micropulsations Through the Ionosphere and Lower Exosphere, J. Geophys. Res., 70, 4885-4889, 1965.
- Field, E.C., and C. Greifinger, Equatorial Transmission of Geomagnetic Micropulsations through the Ionosphere and Lower Exosphere, J. Geophys. Res., 71, 3223-3232, 1966.
- Field, E.C. and C. Greifinger, Geomagnetic Fluctuations Due to Impulse Sources with Applications to High Altitude Nuclear Bursts, J. Geophys. Res., 72, 317-329, 1967.
- Francis, W.E., and R. Karplus, Hydromagnetic Waves in the Ionosphere, J. Geophys. Res., 65, 3593-3600, 1960.
- Gantmacher, F.R., The Theory of Matrices, Chelsea Publishing Company, New York, N.Y., 1959.

- Green, A.W., Jr., and A.A.J. Hoffman, Micropulsation Instrumentation Systems at the Dallas Geomagnetic Center, I.E.E.E. Trans. Geosci. Electronics, GE-5, 3-17, 1967.
- Greifinger, C., and P. Greifinger, Transmission of Micropulsations Through the Lower Ionosphere, J. Geophys. Res., 70, 2217-2231, 1965.
- Gurnett, Donald A., and Paul Rodriguez, Observations of 8-amu/unit Charge Ion Cyclotron Whistlers, J. Geophys. Res. 75, 1342-1344, 1970.
- Gurnett, D.A., S.D. Shawhan, N.M. Brice, and R.L. Smith, Ion Cyclotron Whistlers, J. Geophys. Res., 70, 1665, 1965.
- Gurnett, Donald A., G. William Pfeiffer, Roger R. Anderson, Stephen R. Mosier, and David P. Cauffman, Initial Observations of VLF Electric and Magnetic Fields with the Injun 5 Satellite, J. Geophys. Res., 74, 4631-4648, 1969.
- Hayakawa, Masashi, Jinsuke Ohtsu, and Akira Iwai, Dispersion of Waves in the Lower Exosphere with Multiple Ionic Species, Rept. Ionosphere Res. Japan, 23, 233, 1969.
- Heacock, R.R., Micropulsation Pcl Phase and Polarization Comparisons between College and Kotzebue, Alaska, in press, Annales de Geophysique, 1970.
- Inoue, Yuji, and Samuel Horowitz, Magneto-ionic Coupling in an Inhomogeneous Anisotropic Ionosphere, Radio Sci., 1, 427-440, 1966a.
- Inoue, Yuji, and Samuel Horowitz, Numerical Solution of Full-wave Equation with Mode Coupling, Radio Sci., 1, 957-970, 1966b.
- Jacobs, J.A., Geomagnetic Pulsations, Physics and Chemistry in Space, Vol. 1, Springer-Verlag, New York, 1970.
- Jacobs, J.A., and T. Watanabe, Propagation of Hydromagnetic Waves in the Lower Exosphere and the Origin of Short Period Geomagnetic Pulsations, J. Atmos. Terrest. Phys., 24, 413-434, 1962.
- Jacobs, J.A., Y. Kato, S. Matsushita, and V.A. Troitskaya, Classification of Geomagnetic Micropulsations, J. Geophys. Res., 69, 180-181, 1964.
- Johler, J.R., and J.D. Harper, Reflection and Transmission of Radio Waves at a Continuously Stratified Plasma with Arbitrary Magnetic Induction, J. Res. NBS, 66D (1), 81-99, 1962.

Karplus, R., W.E. Francis, and A.J. Dragt, The Attenuation of Hydromagnetic Waves in the Ionosphere, Planetary Space Sci., 9, 771-785, 1962.

Kokubun, S., and T. Nagata, Geomagnetic Pulsation Pc5 in and near the Auroral Zones, Rept. Ionos. Space Res. Japan, 19, 158-175, 1965.

Maynard, N.C., T.L. Aggson, and J.P. Heppner, Electric Field Observations of Ionospheric Whistlers, Goddard Space Flight Center, Tech. Rept. x-645-70-11, Dec. 1969.

Nagata, Takesi, S. Kokubun, and T. Iijima, Geomagnetically Conjugate Relationships of Giant Pulsations at Syowa Base, Antarctica, and Reykjavik, Iceland, J. Geophys. Res., 68, 4621-4625, 1963.

Parker, E.N. Interaction of the Solar Wind with the Geomagnetic Field, Physics Fluids, 1, 171-187, 1958.

Parker, E.N., Dynamical Properties of the Magnetosphere in Physics of the Magnetosphere, edited by Robert L. Carovillano, John F. McClay, and Henry R. Radoski, pp. 3-64, D. Reidel Publishing Company, Dordrecht, Holland, 1968.

Pease, Marshall C., III, Methods of Matrix Algebra, Academic Press, New York, 1965.

Pitteway, M.L.V., The Numerical Calculations of Wave Fields, Reflection Coefficients, and Polarizations for Long Radio Waves in the Lower Ionosphere, 1, Phil. Trans. Roy Soc. London, A, 257 (1079), 219-241, 1965.

Poeeverlein, H., Characteristic Heights for Hydromagnetic Processes in the Atmosphere, J. Geophys. Res., 72, 251-256, 1967a.

Poeeverlein, H. Ionospheric Wave Theory Using Coupled Vacuum Modes, Radio Sci., 2, 905-911, 1967b.

Pope, John H., An Explanation for the Apparent Polarization of Some Geomagnetic Micropulsations (pearls), 69, 399-405, 1964.

Price, A.T., Effects of Induced Earth Currents on Low-frequency Electromagnetic Oscillations, Radio Sci., 69D, 1161-1168, 1965.

Prince, C.E., and F.X. Bostick, Ionospheric Transmission of Transversely Propagated Plane Waves at Micropulsation Frequencies and Theoretical Power Spectrums, J. Geophys. Res., 69, 3213-3234, 1964.

- Prince, C.E., F.X. Bostick, and H.W. Smith, A Study of the Transmission of Plane Hydromagnetic Waves Through the Upper Atmosphere, Univ. of Texas, Elec. Eng. Res. Lab., Rept. No. 134, July 1964.
- Ratcliffe, J.A., The Magneto-ionic Theory and Its Application to the Ionosphere, Cambridge University Press, London, England, 1959.
- Scarf, F.L., R.W. Fredricks, and G.M. Crook, Detection of Electromagnetic and Electrostatic Waves on OV3-3, J. Geophys. Res., 73, 1723-1745, 1968.
- Shawhan, Stanley D., And Donald A. Gurnett, VLF Electric and Magnetic Fields Observed with the Javelin 8.45 Sounding Rocket, J. Geophys. Res., 73, 5649-5664, 1968.
- Smith, R.L., and Neil Brice, Propagation in Multicomponent Plasmas, J. Geophys. Res., 69, 5029-5040, 1964.
- Smith, R.L., N.M. Brice, J. Katsufakis, D.A. Gurnett, S.D. Shawhan, J.S. Belrose, and R.E. Barrington, An Ion Gyrofrequency Phenomena Observed in Satellites, Nature, 204, 274-275, 1964.
- Southwood, D.J., The Hydromagnetic Stability of the Magnetospheric Boundary, Planet. Space Sci., 16, 587-605, 1968.
- Stix, T.H., The Theory of Plasma Waves, McGraw-Hill Book Company, New York, N.Y., 1962.
- Tartaglia, Nunzio Anthony, Irregular Geomagnetic Micropulsations Associated with Geomagnetic Bays in the Auroral Zone, Ph.D. Thesis. University of Pittsburgh, Pittsburgh, Pennsylvania, 1970.
- Walsh, Edward J., Full Wave Solutions in Terms of Coupled Vacuum Modes, Radio Sci., 2, 913-925, 1967.
- Wentworth, R.C., Evidence for Maximum Production of Hydromagnetic Emissions above the Afternoon Hemisphere of the Earth, 1, Extrapolation to the base of the exosphere, J. Geophys. Res., 69, 2689-2705, 1964.

PART II

IONOSPHERIC CONDUCTIVITY

TABLE OF CONTENTS

	<u>Page</u>
List of Figures	2-iii
List of Tables	2-v
1.0 INTRODUCTION	2- 1
1.1 Purpose	2- 1
1.2 Historical Review	2- 1
1.3 Equations of Motion	2- 2
1.4 Definition of the Average Ion	2- 4
2.0 COLLISIONS.	2- 8
2.1 Types of Collisions	2- 8
2.2 Electron-Neutral Collisions	2- 8
2.3 Ion-Neutral Collisions	2-11
2.31 Resonant Charge Exchange.	2-11
2.4 Fokker-Planck Collisions	2-12
3.0 CONDUCTIVITY TENSOR.	2-20
3.1 Conductivity Tensor Derived from the Uncoupled Equations of Motion	2-20
3.2 Conductivity Tensor Derived from the Coupled Equations of Motion	2-22
3.3 Conductivity Profiles for a Model Ionosphere	2-26
3.31 Parallel Conductivity	2-26
3.32 Hall Conductivity	2-30
3.33 Pedersen Conductivity	2-33
3.34 Comparison of the Various Conductivities	2-33
4.0 STIX'S QUANTITIES IN TERMS OF THE CONDUCTIVITY TENSOR ELEMENTS	2-39
4.1 Derivation of P,R,L,D, and S in the Presence of Collisions	2-39
4.2 The Effect of the Coupled Equations of Motion on Stix's Quantities	2-41
REFERENCES	2-43

LIST OF FIGURES

<u>Figure</u>	<u>Page</u>
1.1 A plot of vs. altitude	2- 5
2.1 Charge exchange effect on the ion collision frequency vs. altitude	2-13
2.2 Comparison of Spitzer's collision frequency and reciprocal relaxation times for electrons	2-15
2.3 Comparison of Spitzer's collision frequency and reciprocal relaxation times with Fokker- Planck collision frequency for ions	2-16
2.4 Plasma, cyclotron, and collision frequencies vs. altitude for electrons and ions	2-17
3.1 Comparison of the parallel conductivities obtained with the Spitzer and Fokker-Planck collision expressions	2-27
3.2 Frequency dependence of the parallel conductivity (including charge exchange and Fokker-Planck collisions) vs. altitude	2-28
3.3 Frequency dependence of the parallel con- ductivity (including charge exchange and Spitzer's coulomb collision expression) vs. altitude	2-29
3.4 The Hall conductivities with and without charge exchange vs. altitude	2-31
3.5 Hall conductivity (including charge exchange) for various frequencies vs. altitude	2-32
3.6 The perpendicular conductivities with and without charge exchange vs. altitude	2-34
3.7 Frequency dependence of perpendicular conductivity (with charge exchange) vs. altitude	2-35

3.8	Parallel, Pedersen, and Hall conductivities (with charge exchange and Fokker-Planck collisions) vs. altitude	2-36
3.9	Dimensionless Hall and Pedersen conductivities at 0.00333 cps. plotted on a linear scale vs. altitude	2-38

LIST OF TABLES

<u>Table</u>		<u>Page</u>
2.1	Types of collisions included in the collisional terms of the equations of motion	2- 8
2.2	Electron-neutral collision frequency expressions due to Banks [1966a]	2-10
2.3	Coefficients for charge exchange collision frequency expressions due to Banks [1966b]	2-12

1.0 INTRODUCTION

1.1 Purpose

A study of the electrically conducting properties of the ionosphere is of particular interest in the problem of wave propagation through the ionosphere because the dispersion relation may be written in terms of the various elements of the conductivity tensor. This is effected by writing Stix's quantities P, R, L, S , and D in terms of the ionosphere's electrical conductivity. As a result, the height dependent characteristics of the Booker quartic roots may be examined in terms of the height dependent behavior of the Hall, Pedersen, and parallel conductivities.

1.2 Historical Review

The electrical conductivity of the ionosphere has been of interest to geophysicists ever since Balfour Stewart [1882] suggested that the ionosphere must contain an electrically conducting region in order to explain geomagnetic quiet daily variations. Stewart theorized that the solar heating of the upper atmosphere produced convective motions of conducting air across the Earth's magnetic field lines generating electrical currents by means of a dynamo action.

Stewart's theory was placed on firmer ground by Schuster [1889, 1908] who used a spherical harmonic analysis to show that the quiet daily variation could originate above the earth and also gave a mathematical formulation to Stewart's dynamo theory. Kennelly [1902] and Heaviside [1902] independently inferred the existence of an electrically conducting

layer which reflects radio waves.

Pedersen [1927] concluded that the presence of the geomagnetic field renders the ionospheric conductivity anisotropic. Cowling [1932] then proposed that a transverse component of the electric field not only produced a current parallel to itself (the magnitude of the current being determined by the Pedersen conductivity) but also produced a Hall current in a direction perpendicular to both the electric and magnetic fields.

Application of these ideas has been made to the dynamo theory by various investigators and the altitude distribution of the conductivity tensor elements has been calculated (Baker and Martyn, 1953; Fejer, 1953; H. Maeda, 1953; Chapman, 1956; K. Maeda and S. Kato, 1966).

1.3 Equations of Motion

The ionosphere may be considered a multi-component plasma consisting of several different species of ions and electrons and neutral particles. The macroscopic equations of motion for these particles may be written

$$\rho_k \frac{d\vec{v}_k}{dt} = e_k N_k (\vec{E} + \vec{v}_k \times \vec{B}) - N_k \nu_{kj} m_k (\vec{v}_k - \vec{v}_j) - N_k \nu_{kn} m_k (\vec{v}_k - \vec{v}_n) \quad (1-1)$$

$k = i$

$$\rho_n \frac{d\vec{v}_n}{dt} = -N_e \nu_{en} m_e (\vec{v}_n - \vec{v}_e) - N_i \nu_{in} m_i (\vec{v}_n - \vec{v}_i) \quad (1-2)$$

where the k and j subscripts refer to positively and negatively charged particles, and vice versa. The quantity e is the electronic charge and is considered positive. The quantity ϵ_k is positive or negative depending on whether the charge is positive or negative. The electric and magnetic fields are represented by \vec{E} and \vec{B} , respectively. The particle velocity, density, mass, and mass density are given by \vec{v} , N , m , and ρ , respectively. ν_{kj} refers to the collision frequency for positively and negatively charged particles. The subscripts e , i , and n refer to electrons, ions, and neutral particles.

The terms involving temperature have been neglected. Thus the cold plasma approximation is made and only two modes will be obtained from the dispersion relation. The magnetosonic mode appears only when temperature effects are included. The gravitational force is neglected and has no effect in the micropulsation range. (For a further discussion of this latter point see, for example, Hultqvist [1966]). The ionosphere is considered to be a two component plasma so that $N_e = N_i$.

Also, the neutral particles may be considered to be stationary at least as long as the following condition is fulfilled:

$$\bar{\nu} \gg \omega$$

where

$$\bar{\nu} = \frac{\rho_e}{\rho_n} (\nu_{en} + \frac{m_i}{m_e} \nu_{in}) \quad (1-3)$$

and ω is the angular wave frequency of the disturbance. A plot of the quantity \bar{v} vs. altitude is shown in Figure 1.1. From this figure \bar{v} is seen to be significantly large only around the F layer maximum and even in this region \bar{v} is sufficiently small for the neutral particle motion to be neglected for angular frequencies greater than 2.3×10^{-3} rad/sec.

1.4 Definition of the Average Ion

In general the equations of motion are coupled through collisions. However, coupling of the equations of motion is found (see section 4.2 of chapter 4) to be unimportant in determining the transmission properties of a disturbance originating at 5000 km. and propagating to the Earth. Therefore the equations of motion are assumed to be uncoupled, i.e., the neutral particle velocity is set to zero and the term involving the difference in the electron and ion velocities is replaced by the velocity of the particle whose equation of motion is being considered.

Then the equation of motion for the jth ion species is given by

$$n_j m_j \frac{d\vec{v}_j}{dt} = en_j (\vec{E} + \vec{v}_j \times \vec{B}) - n_j m_j \nu_j \vec{v}_j \quad (1-4)$$

where ν_j is the appropriate collision frequency for the jth positive ion with all other particles, which we see from the original equation of motion to be given by

$$\nu_j = \nu_{je} + \sum_n \nu_{jn}$$

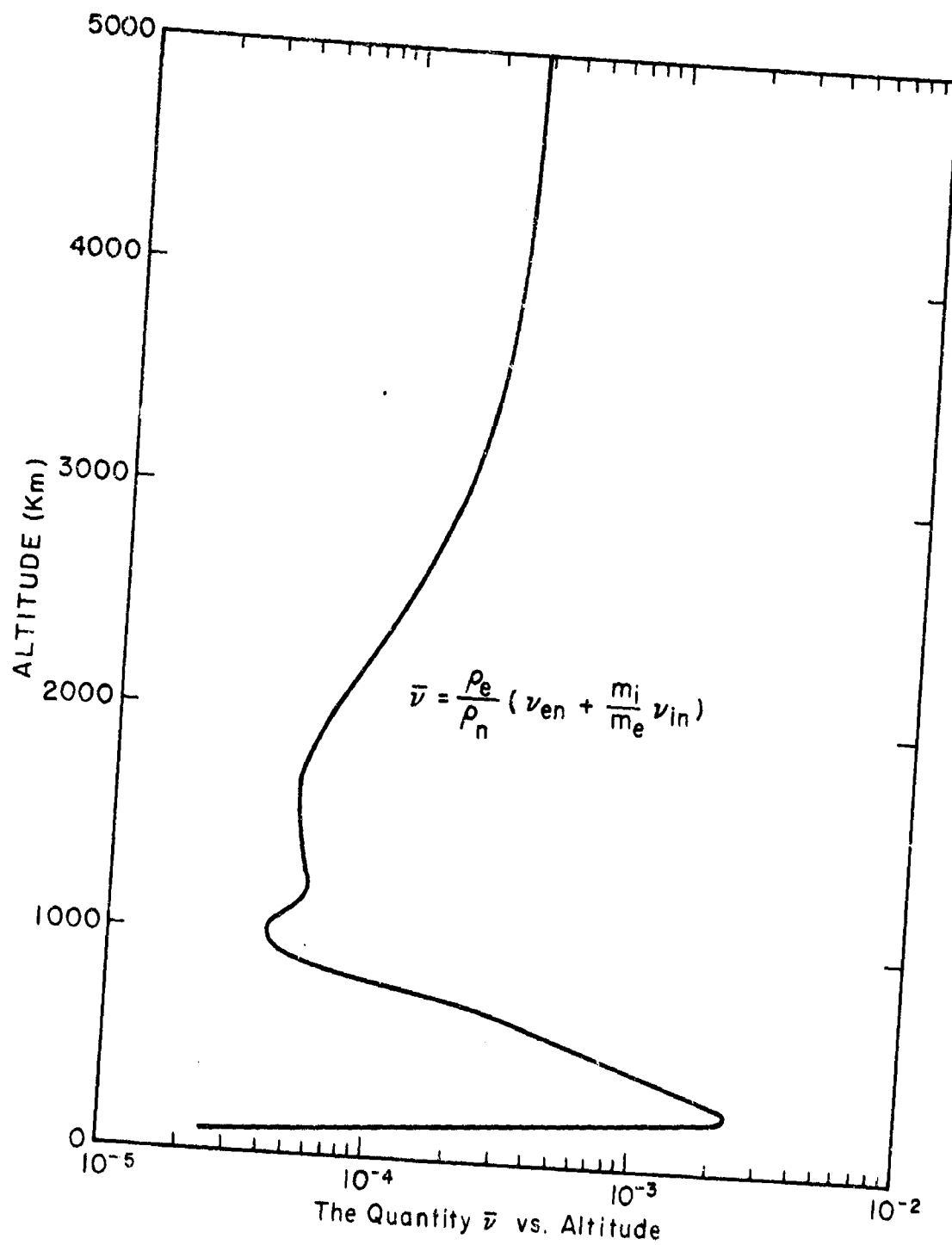


Figure 1.1

where ν_{jn} is the collision frequency of the j th positive ion with the n th neutral particle, due to either resonance charge exchange or polarization. Linearizing and summing all the transport equations for all the ion species:

$$-i\omega \sum_j n_j m_j \vec{V}_j = e \sum_j n_j (\vec{E} + \vec{V}_j \times \vec{B}_0) - \sum_j n_j m_j \vec{V}_j (\nu_{je} + \sum_n \nu_{jn})$$

To simplify matters, we want to reduce to one equation of the form

$$-i\omega N_i M_i \vec{V}_i = e N_i (\vec{E} + \vec{V}_i \times \vec{B}_0) - N_i M_i \nu_i \vec{V}_i$$

The assumption is made that

$$\vec{V}_i = \vec{V}_j$$

i.e., all the ion species are characterized by the same macroscopic drift velocity. Then we obtain the result that

$$M_i = \frac{\sum_j n_j m_j}{N_i} ; N_i = \sum_j n_j \quad (1-5)$$

and the collision frequency is given by

$$\begin{aligned} \nu_i &= \frac{\sum_j [n_j m_j (\nu_{je} + \sum_n \nu_{jn})]}{N_i M_i} \\ &= \nu_{ie} + \nu_{in} \end{aligned} \quad (1-6)$$

where

$$\nu_{ie} = \frac{\sum_j n_j m_j \nu_{je}}{N_i M_i}$$

and

$$\nu_{in} = \frac{\sum_j [n_j m_j (\sum_n \nu_{jn})]}{N_i M_i}$$

The quantities N_i and M_i represent the "average ion" mass and total ion particle density. ν_i is the total averaged ion collision frequency including collisions with electrons and neutral particles.

In the same fashion the linearized electron equation of motion is given by

$$-i\omega N_e m_e \vec{V}_e = -e N_e (\vec{E} + \vec{V}_e \times \vec{B}_0) - N_e m_e \nu_e \vec{V}_e$$

where

$$\begin{aligned} \nu_e &= \sum_k \nu_{en_k} + \sum_j \nu_{ej} \\ &= \nu_{en} + \nu_{ei} \end{aligned} \tag{1-7}$$

i.e., ν_e is the total electron collision frequency, ν_{en_k} is the collision frequency for electrons with the k th neutral species, and ν_{ej} is the collision frequency of electrons with the j th ion species.

We have assumed throughout this discussion that all the positive ions are singly charged.

2.0 COLLISIONS

2.1 Types of Collisions

Table 2.1 shows the types of collisions which are included in the collisional terms of the equations of motion. Resonance charge exchange collisions, heretofore apparently not included in the equations for wave propagation through the ionosphere, are found to be an important process and expressions given by Banks [1966b] are utilized. For electron-ion and ion-electron collisions the Fokker-Planck equation is used to give a slightly improved collision frequency (see section 2.4) over previous expressions.

Table 2.1

Colliding Incident Center Particle	Neutral Particle			Electron	Pos. Ion
	Charge Exchange	Polarization	Empirical	Fokker Planck	Fokker Planck
Electron			X		X
Positive Ion	X	X		X	

In general, electron-electron and ion-ion collisions may be ignored (see discussion in section 2.4).

2.2 Electron-Neutral Collisions

The collision frequency in the friction term of the equations of motion has long been a matter of controversy. In magnetoionic theory [Appleton, 1932; Ratcliffe, 1959] the average number of collisions which an electron makes per unit time is assumed independent of electron velocity.

Experimental evidence indicates that the collision frequency is velocity dependent and that this dependence varies with the type of plasma. Phelps and Pack [1959] have shown that the electron collision frequency in nitrogen gas is proportional to the square of the velocity. This experimental evidence motivated Sen and Wyller [1960] to re-formulate the Appleton-Hartree magnetoionic formulae taking into account the velocity dependence of the electron-neutral collision frequency. They assumed the neutral particle velocity distribution remained Maxwellian under the influence of an alternating electric field and a steady magnetic field and then expanded the electron velocity distribution (using the Chapman-Enskog method) to first order, retaining the zero order isotropic part and the first order anisotropic part. The collision integral on the right hand side of the Boltzman equation was assumed to have the form given by Chapman and Cowling [1958, p. 350] which contains the collision frequency. Sen and Wyller then proceeded to develop the conductivity tensor and indices of refraction in terms of C script integrals which have been tabulated by Dingle, Arndt, and Roy [1957]. These integrals allow one to take into account any functional form of the collision frequency which can be expressed as a power series in the electron velocity. Sen and Wyller found that their absorption factors could differ by as much as 100 per cent from the results of the Appleton-Hartree formulae.

The electron-neutral collision frequency expressions utilized in the present work were adopted from the results of Banks [1966a]. Banks

made a study of elastic collisions between electron and neutral gases characterized by separate Maxwellian velocity distributions and then defined collision frequencies for electrons colliding with N_2 , O_2 , O , H , and He in terms of empirical momentum transfer cross sections, except for the cross sections of O and H which were derived from theoretical calculations of scattering phase shifts.

These collision frequencies given by Banks are as follows:

Table 2.2

<u>Neutral gas</u>	<u>Collision frequency</u>	<u>Electron temperature range</u>
N_2	$\nu = N_{N_2} (1.44 \times 10^{-11}) T_e$ $\nu = N_{N_2} (1.41 \times 10^{-11})$ $\times [1 - (3.13 \times 10^{-3}) T_e^{\frac{1}{2}}] T_e^{\frac{1}{2}}$	$232^\circ K \leq T_e \leq 1160^\circ K$ $1160^\circ K \leq T_e \leq 11,600^\circ K$
O_2	$\nu = N_{O_2} (1.37 \times 10^{-10}) [1 + (2.86 \times 10^{-2}) T_e^{\frac{1}{2}}] T_e^{\frac{1}{2}}$	$232^\circ K \leq T_e \leq 11,600^\circ K$
O	$\nu = N_O [(2.12 \pm 0.623) \times 10^{-10}] T_e^{\frac{1}{2}}$	$T_e < 4000^\circ K$
H	$\nu = N_H (3.41 \times 10^{-9}) [1 - (9.0 \times 10^{-5}) T_e] T_e^{\frac{1}{2}}$	$150^\circ K \leq T_e \leq 5000^\circ K$
He	$\nu = N_{He} [(3.48 \pm 0.373) \times 10^{-10}] T_e^{\frac{1}{2}}$	$T_e \leq 58,000^\circ K$

where the neutral particle densities are measured in cm^{-3} .

For collisions of electrons with argon the hard sphere model is used and the collision frequency is given by

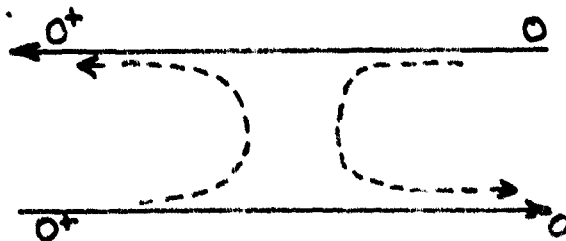
$$\nu = N_A (1.37 \times 10^{-11}) T_e^{\frac{1}{2}}$$

In general theoretical methods do not seem to yield accurate values for momentum transfer cross sections so that Banks relied as much as possible on experimentally obtained values. His collision frequencies have been incorporated into the equations of motion by utilizing equations (1-7). Perhaps a more accurate method would have been to use the velocity dependent momentum transfer cross sections given by Banks in the equations developed by Sen and Wyller [1960].

2.3 Ion-Neutral Collisions

2.31 Resonant Charge Exchange

Banks [1966b] found that resonant charge exchange between an ion and its parent neutral molecule can significantly enhance the magnitude of the momentum transfer cross section. An example of this type of process is $O^+ + O \longrightarrow O + O^+$. There is a transfer of charge between two particles but each approximately retains its original kinetic energy. Therefore, even though the ion has changed its identity the reaction is basically elastic. This reaction provides a means of transforming energetic ions into energetic neutral particles. The enhancement of the momentum transfer cross section is a consequence of the conversion of a grazing collision into an apparently direct impact resulting in significantly large backscattering, as illustrated in the following diagram.



The dotted lines indicate the apparent backscattering.

The resulting charge exchange collision frequency for momentum transfer given by Banks is changed to the form

$$\nu_{C.E.} = (5.93 \times 10^{-10}) \frac{N_n}{\sqrt{M_n}} (T_i + T_n)^{\frac{1}{2}} [E + D \cdot \ln(T_i + T_n)]^2$$

where N_n , M_n , T_n , and T_i are the neutral particle density in cm^{-3} , neutral particle mass in kg, and neutral and ion temperatures in $^{\circ}\text{K}$, respectively. The logarithm is to the base e and the coefficients D and E are given in the table below.

Table 2.3

<u>Molecule</u>	<u>D</u>	<u>E</u>
H	0.144×10^{-7}	-4.14×10^{-7}
O	0.0824	-3.02
N	0.0796	-2.97
He	0.128	-3.32
O ₂	0.0936	-3.04
N ₂	0.118	-4.07

Charge exchange significantly enhances the total ion collision frequency above 150 km (see Figure 2.1).

2.4 Fokker-Planck Collisions

A measure of the ratio of large angle to small angle coulomb collisions is the quantity (see Schmidt [1966], p. 312):

$$R = \frac{\nu_0^2}{\lambda_D^2 - \nu_0^2}$$

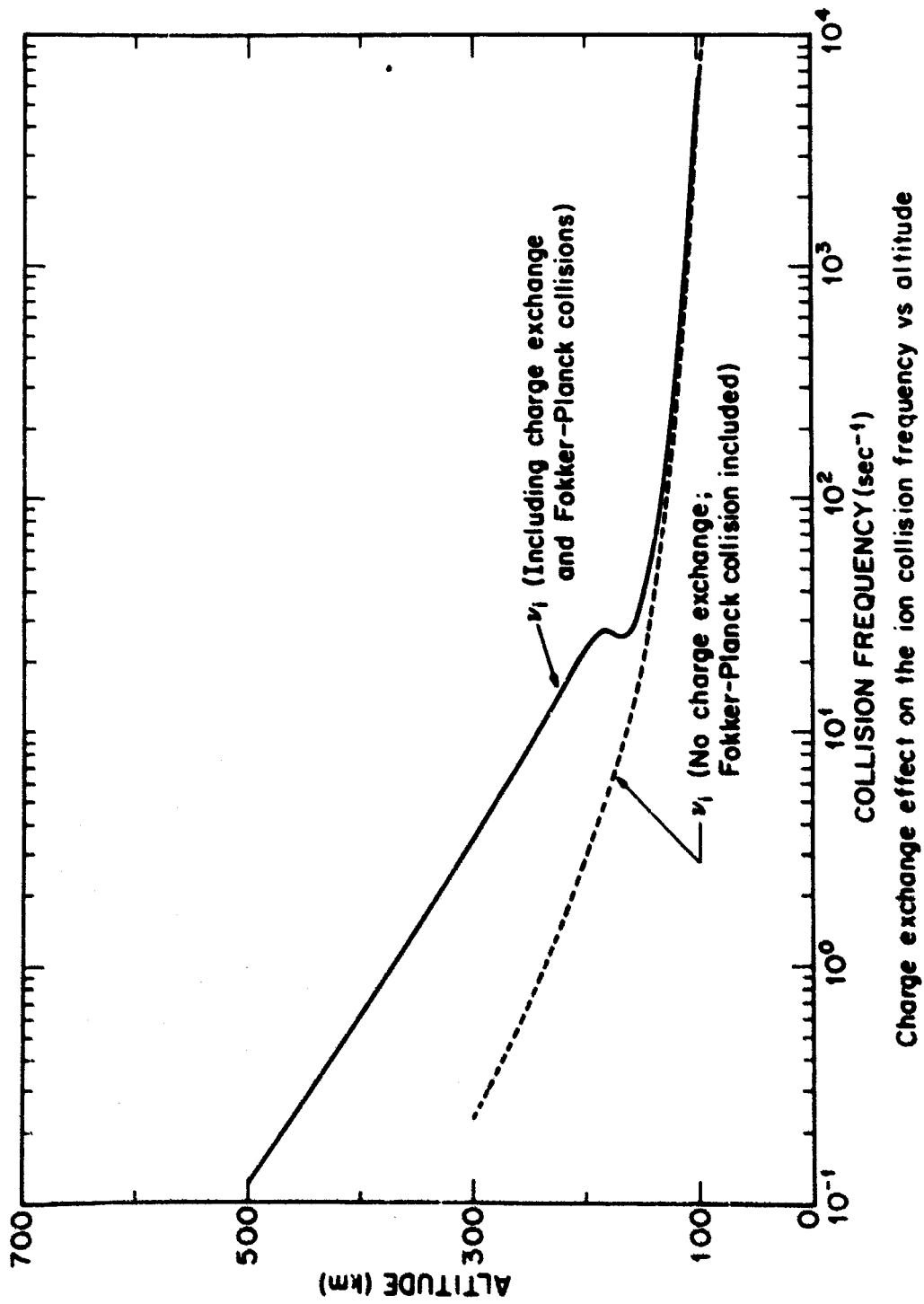


Figure 2.1

with

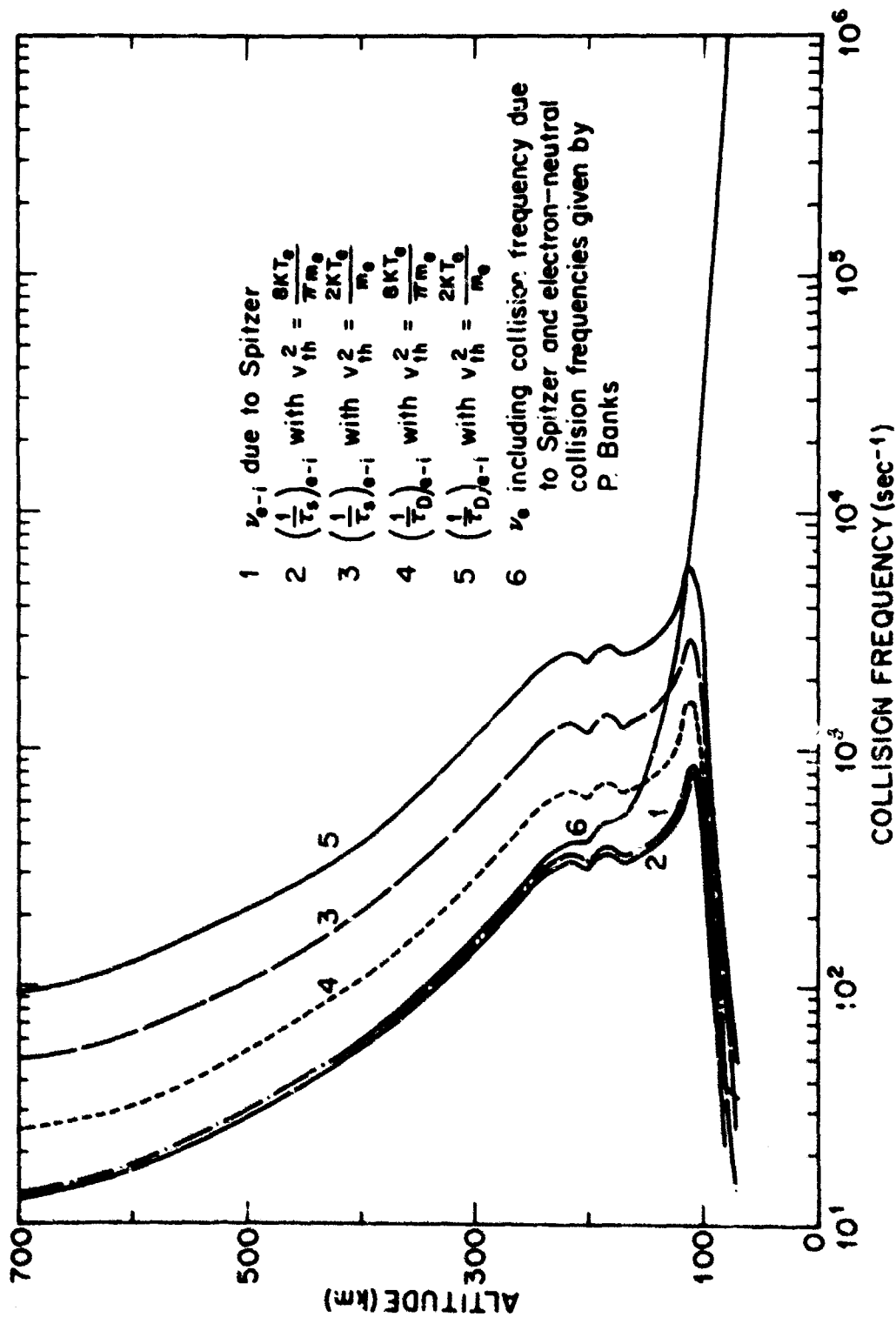
$$\lambda_D = \left[\frac{\epsilon_0 K T}{N e^2} \right]^{\frac{1}{2}}$$

where λ_D is the Debye shielding length and p_0 is the impact parameter for Coulomb collisions when

$$p_0 = \frac{\frac{1}{2} \frac{|q_a q_b|}{4\pi\epsilon_0}}{\frac{1}{2} M u^2}$$

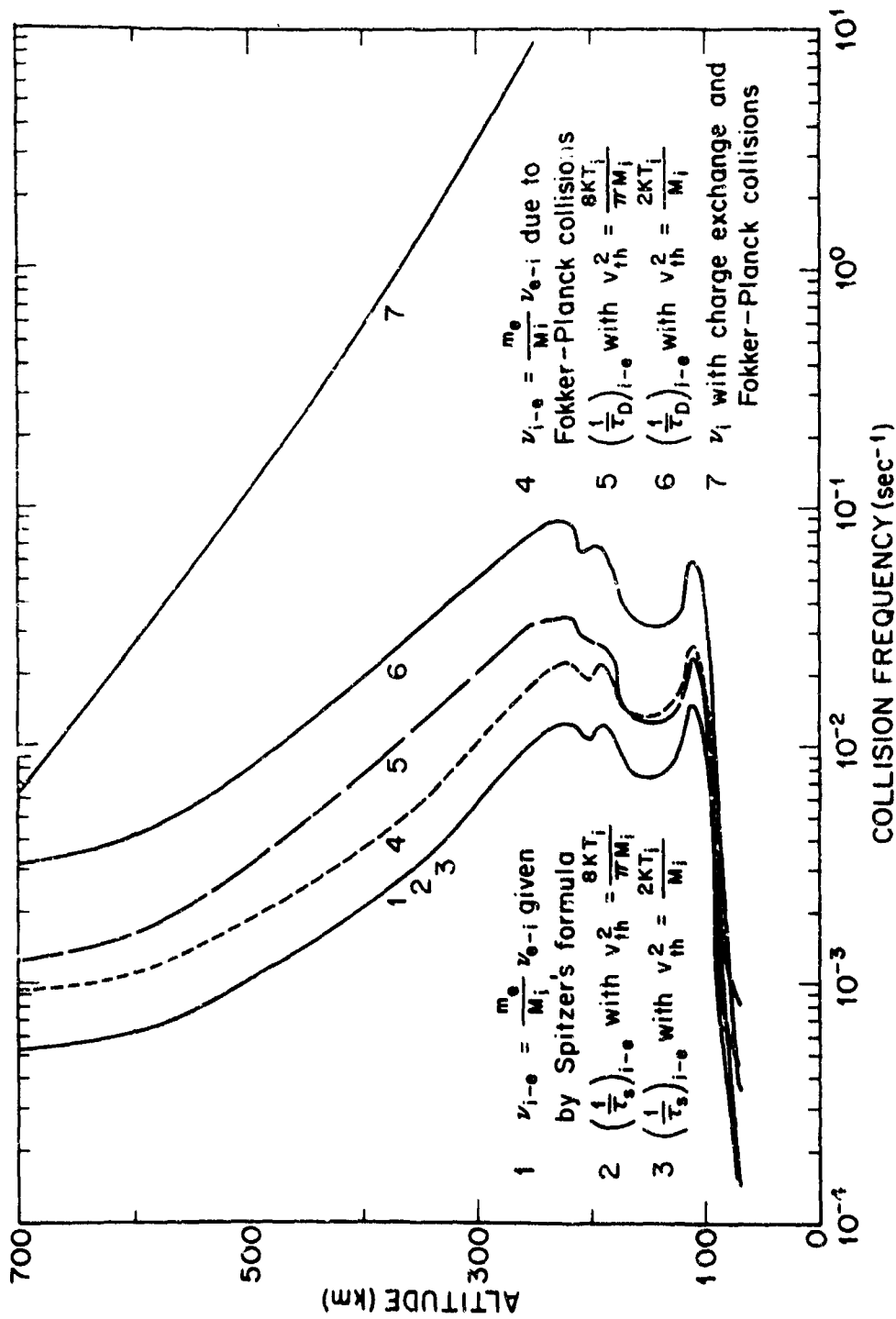
M being the reduced mass and u the relative velocity between charged particles a and b. For conditions existing in the ionosphere, $R \ll 1$. Thus the overwhelming majority of particle encounters in the ionospheric plasma leads to small angle deflections. A Fokker-Planck treatment of charged particle collisions is therefore most appropriate.

One might try to define the small angle collision frequency as the reciprocal of Spitzer's "slowing-down" time or of Spitzer's "deflection" time (Spitzer, 1962, p. 131). These reciprocal relaxation times are plotted in Figure 2.2 and Figure 2.3. Some of the ionospheric parameters used in the calculation of the various collision frequencies are shown in Figure 2.4 where ω_e , ω_i , Ω_e , and Ω_i are the electron and ion plasma frequencies and the electron and ion cyclotron frequencies, respectively. Spitzer's relaxation times are seen to be highly dependent on the choice of the thermal velocity of the test particle.

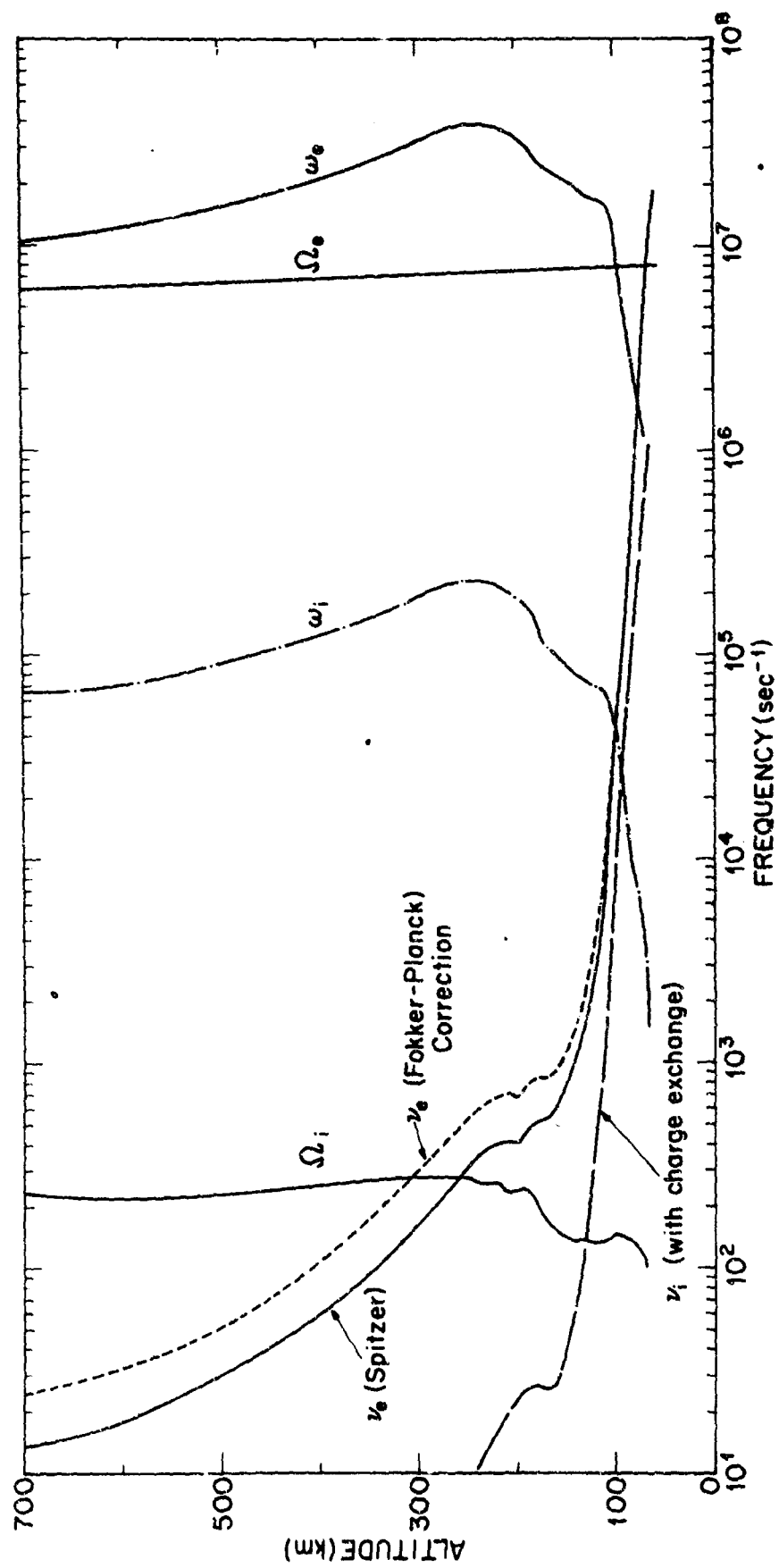


Comparison of Spitzer's collision frequency and reciprocal relaxation times for electrons

Figure 2.2



Comparison of Spitzer's collision frequency and reciprocal relaxation times with Fokker-Planck collision frequency for ions



Plasma, cyclotron, and collision frequencies vs altitude for electrons and ions

Figure 2.4

A more appropriate approach to the determination of the Fokker-Planck collision frequency is as follows. The assumption is made that the electron and ion gases are both represented by velocity distributions which are isotropically distributed in velocity space and are separated by a macroscopic relative velocity \vec{V} . If the velocity distributions are isotropic then when the second moment of the Fokker-Planck equation is taken, only the friction term appears and the diffusion term vanishes. Also electron-electron and ion-ion collisions do not appear. The velocity distribution for ions may be approximated by a delta function unless the ion temperature becomes extremely high. Under these conditions the frictional force per electron is found to be

$$\vec{F} = -m_e \vec{V} \nu_{ei} e^{-x^2} \left(1 + \frac{x^2}{5} + \frac{3x^4}{70} + \dots \right)$$

where

$$x = \frac{V}{\left[\frac{2KT_e}{m_e} \right]^{1/2}}$$

and

$$\nu_{ei} = \frac{4}{3} \left(1 + \frac{m_e}{m_i} \right) \frac{Z^2 e^4}{4\pi\epsilon_0^2 m_e^2} (\ln \Lambda) \left[\frac{m_e}{2KT_e} \right]^{3/2} N_i$$

$$\Lambda = \frac{P_0}{\lambda_D}$$

This expression for the electron-ion collision frequency is $\sqrt{\pi}$ greater than the result given by Spitzer and Harm [1953], which is put

into a more convenient form by Shkarofsky et. al. [1966], and the expression given by Banks [1966a].

In general the quantity $X \ll 1$. The electron and ion macroscopic drift velocities are \vec{V}_e and \vec{V}_i , respectively, and $\vec{V} = \vec{V}_e - \vec{V}_i$. Then conservation of momentum requires that

$$-m_e (\vec{V}_e - \vec{V}_i) \nu_{ei} N_e + m_i (\vec{V}_e - \vec{V}_i) \nu_{ie} N_i = 0$$

Under the assumption that

$$N_e = N_i$$

it follows that

$$\nu_{ie} = \frac{m_e}{m_i} \nu_{ei}$$

The various collision frequencies as a function of altitude are shown in Figures 2.1 to 2.4. The Fokker-Planck correction becomes important above 150 km. for electrons and above 1000 km. for ions.

3.0 CONDUCTIVITY TENSOR

3.1 Conductivity Tensor Derived From the Uncoupled Equations of Motion

The uncoupled equations of motion for electrons and ions under the influence of oscillating electric and magnetic fields are given by

$$m_e \frac{d\vec{V}_e}{dt} = -e(\vec{E} + \vec{V}_e \times \vec{B}_0) - m_e \nu_e \vec{V}_e$$

$$m_i \frac{d\vec{V}_i}{dt} = e(\vec{E} + \vec{V}_i \times \vec{B}_0) - m_i \nu_i \vec{V}_i$$

where \vec{B}_0 is the Earth's magnetic field and ν_i and ν_e are the ion and electron collision frequencies defined by equations (1-6) and (1-7), respectively. The conductivity tensor is now derived under the following assumptions:

1. The equations of motion are linearized assuming the time variation of all quantities is of the form $e^{-i\omega t}$.
2. The zero temperature approximation is made, i.e., the thermal motions of the electrons and ions are ignored.
3. The various ions in the ionosphere are all represented by an "average" singly charged ion.
4. Negative ions are ignored.

The equations of motion are solved for the electron and ion velocities and then plugged into the relation for the current density

$$\vec{J} = eN_e(\vec{V}_i - \vec{V}_e)$$

This result is then compared with the relation

$$\vec{J} = \vec{\sigma} \cdot \vec{E}$$

to obtain the conductivity tensor $\vec{\sigma}$.

After some algebraic manipulation one obtains the result

$$\vec{\sigma} = \begin{bmatrix} \sigma_{\perp} & -\sigma_H & 0 \\ \sigma_H & \sigma_{\perp} & 0 \\ 0 & 0 & \sigma_{\parallel} \end{bmatrix}$$

where σ_{\perp} , σ_H , and σ_{\parallel} are the Pedersen, Hall, and parallel conductivities, respectively, and are given by

$$\sigma_{\perp} = \frac{eN_e}{B_0} \left[\frac{\Omega_e \nu'_e}{\nu_e'^2 + \Omega_e^2} + \frac{\Omega_i \nu'_i}{\nu_i'^2 + \Omega_i^2} \right]$$

$$\sigma_H = \frac{eN_e}{B_0} \left[\frac{\Omega_e^2}{\nu_e'^2 + \Omega_e^2} - \frac{\Omega_i^2}{\nu_i'^2 + \Omega_i^2} \right]$$

$$\sigma_{\parallel} = \frac{eN_e}{B_0} \left[\frac{\Omega_e}{\nu_e'} + \frac{\Omega_i}{\nu_i'} \right]$$

where

$$\nu_j' = \nu_j - i\omega$$

$$\Omega_j = \frac{eB_0}{m_j} \quad j=e,i$$

The magnetic field was assumed parallel to the z -axis in this derivation.

3.2 Conductivity Tensor Derived From the Coupled Equations of Motion

The coupled equations of motion are given by

$$m_k \frac{d\vec{v}_k}{dt} = e_k e (\vec{E} + \vec{v}_k \times \vec{B}_0) - m_k \vec{v}_k \gamma_{kn} - m_k \gamma_{kj} (\vec{v}_k - \vec{v}_j)$$

$k, j = e, i \quad k \neq j$

Use is then made of the Appleton-Hartree quantities

$$\gamma_k = \frac{\Omega_k}{\omega}$$

$$\Omega_k = \frac{e_k e B}{m_k}$$

$$Z_{kn} = \frac{\gamma_{kn}}{\omega}$$

$$Z_k = Z_{kn} + Z_{kj}$$

$$X_k = \frac{\pi_k^2}{\omega^2}$$

$$\pi_k^2 = \frac{(e_k e)^2 N_k}{m_k \epsilon_0}$$

$$U_{kn} = 1 + i Z_{kn}$$

$$U_{kj} = 1 + i Z_{kj}$$

$$U_k = 1 + i Z_k$$

Also, the vector cross product of the velocity and magnetic field is put in the form

$$\vec{V}_k \times \hat{b}_0 = \begin{bmatrix} 0 & b_z & -b_y \\ -b_z & 0 & b_x \\ b_y & -b_x & 0 \end{bmatrix} \cdot \vec{V}_k = \bar{\bar{A}} \cdot \vec{V}_k$$

where $\hat{b}_0 = \frac{\vec{B}}{B_0}$

The equation of motion can then be written in the form

$$\bar{\bar{G}}_k \cdot \vec{V}_k = \gamma_k \frac{\vec{E}}{B_0} + z_{kj} \vec{V}_j \quad k \neq j; \quad k, j = e, i$$

where

$$\bar{\bar{G}}_k = -i \mu_k \bar{\bar{I}} - \gamma_k \bar{\bar{A}}$$

and $\bar{\bar{I}}$ is the unit tensor.

Writing the ion and electron equations separately

$$\bar{\bar{G}}_i \cdot \vec{V}_i = \gamma_i \frac{\vec{E}}{B_0} + z_{ie} \vec{V}_e$$

$$\bar{\bar{G}}_e \cdot \vec{V}_e = \gamma_e \frac{\vec{E}}{B_0} + z_{ei} \vec{V}_i$$

$$\vec{V}_i = \gamma_i \bar{\bar{G}}_i^{-1} \frac{\vec{E}}{B_0} + z_{ie} \bar{\bar{G}}_i^{-1} \vec{V}_e$$

$$\bar{\bar{G}}_e \cdot \vec{V}_e = \gamma_e \frac{\vec{E}}{B_0} + z_{ei} \gamma_i \bar{\bar{G}}_i^{-1} \frac{\vec{E}}{B_0} + z_{ei} z_{ie} \bar{\bar{G}}_i^{-1} \vec{V}_e$$

$$(\bar{\bar{G}}_e - z_{ei} z_{ie} \bar{\bar{G}}_i^{-1}) \vec{V}_e = (\gamma_e \bar{\bar{I}} + z_{ei} \gamma_i \bar{\bar{G}}_i^{-1}) \frac{\vec{E}}{B_0}$$

$$(\bar{\bar{G}}_e \bar{\bar{G}}_i - z_{ei} z_{ie} \bar{\bar{I}}) \vec{V}_e = (\gamma_e \bar{\bar{G}}_i + z_{ei} \gamma_i \bar{\bar{I}}) \frac{\vec{E}}{B_0}$$

$$\bar{\bar{\Gamma}} \equiv \bar{\bar{G}}_e \bar{\bar{G}}_i - z_{ei} z_{ie} \bar{\bar{I}}$$

In like manner,

$$\vec{V}_e = \gamma_e \bar{G}_e^{-1} \frac{\vec{E}}{B_0} + z_{ei} \bar{G}_e^{-1} \vec{V}_i$$

$$\bar{G}_i \vec{V}_i = \gamma_i \frac{\vec{E}}{B_0} + z_{ie} \gamma_e \bar{G}_e^{-1} \frac{\vec{E}}{B_0} + z_{ie} z_{ei} \bar{G}_e^{-1} \vec{V}_i$$

$$(\bar{G}_i \bar{G}_e - z_{ie} z_{ei} \bar{I}) \vec{V}_i = (\gamma_i \bar{G}_e + z_{ie} \gamma_e \bar{I}) \frac{\vec{E}}{B_0}$$

It can be easily shown that

$$\bar{G}_e \cdot \bar{G}_i = \bar{G}_i \cdot \bar{G}_e$$

Therefore

$$\bar{\Gamma} = \bar{G}_e \bar{G}_i - z_{ei} z_{ie} \bar{I}$$

$$= \bar{G}_i \bar{G}_e - z_{ie} z_{ei} \bar{I}$$

$$\vec{V}_i = \bar{\Gamma}^{-1} (\gamma_i \bar{G}_e + z_{ie} \gamma_e \bar{I}) \frac{\vec{E}}{B_0}$$

$$\vec{V}_e = \bar{\Gamma}^{-1} (\gamma_e \bar{G}_i + z_{ei} \gamma_i \bar{I}) \frac{\vec{E}}{B_0}$$

Then

$$\vec{J} = e N_e (\vec{V}_i - \vec{V}_e)$$

$$= e N_e \bar{\Gamma}^{-1} (\gamma_i \bar{G}_e - \gamma_e \bar{G}_i + [z_{ie} \gamma_e - z_{ei} \gamma_i] \bar{I}) \frac{\vec{E}}{B_0}$$

From momentum conservation

$$\mu_{ie} = \frac{m_e}{m_i} \mu_{ei}$$

and therefore

$$z_{ie} \gamma_e - z_{ei} \gamma_i = - \frac{e B_0}{\omega^2} \left[\frac{\mu_{ie}}{m_e} + \frac{\mu_{ei}}{m_i} \right]$$

$$= -2 \gamma_i z_{ei}$$

Then

$$\vec{J} = eN_e \vec{\Gamma}^{-1} (\gamma_i \vec{G}_e - \gamma_e \vec{G}_i - 2\gamma_i z_{ei} \vec{I}) \frac{\vec{E}}{B_0}$$

Now

$$\begin{aligned} \gamma_i \vec{G}_e - \gamma_e \vec{G}_i &= \gamma_i [-i(1 + iz_{ei} + iz_{en}) \vec{I} - \cancel{\gamma_e \vec{A}}] \\ &\quad - \gamma_e [-i(1 + iz_{ie} + iz_{in}) \vec{I} - \cancel{\gamma_i \vec{A}}] \\ &= -i [\gamma_i (1 + iz_{en}) + i\gamma_i z_{ei} \\ &\quad - \gamma_e (1 + iz_{in}) - i\gamma_e z_{ie}] \vec{I} \\ &= -i \vec{I} [\gamma_i (1 + iz_{en}) - \gamma_e (1 + iz_{in}) \\ &\quad + \underbrace{i(\gamma_i z_{ei} - \gamma_e z_{ie})}_{2\gamma_i z_{ei}}] \end{aligned}$$

$$= -i \vec{I} [\gamma_i V_{en} - \gamma_e V_{in} + i2\gamma_i z_{ei}] \vec{I}$$

Therefore

$$\vec{J} = eN_e \vec{\Gamma}^{-1} [-i(\gamma_i V_{en} - \gamma_e V_{in}) + (2\gamma_i \cancel{z_{ei}} - 2\gamma_e \cancel{z_{ei}})] \frac{\vec{E}}{B_0}$$

$$= -i \frac{eN_e}{B_0} \vec{\Gamma}^{-1} (\gamma_i V_{en} - \gamma_e V_{in}) \vec{E}$$

and the conductivity tensor from the coupled equations of motions is

$$\vec{\sigma} = -i \frac{eN_e}{B_0} \vec{\Gamma}^{-1} (\gamma_i V_{en} - \gamma_e V_{in})$$

The dielectric tensor is then

$$\bar{K} = \bar{I} + i \frac{\bar{\sigma}}{\omega \epsilon_0}$$

where

$$\frac{\bar{\sigma}}{\omega \epsilon_0} = \chi_e \bar{F}^{-1} \left(V_{in} + \frac{m_e}{m_i} V_{en} \right)$$

The above expression for the conductivity tensor is not very amenable to solving explicitly and is therefore solved implicitly with the computer.

3.3 Conductivity Profiles for a Model Ionosphere

A model ionosphere for midlatitude and midday at sunspot minimum is used to calculate the ionospheric conductivity profiles presented in the following sections.

3.31 Parallel Conductivity

Figure 3.1 shows that the Spitzer and Fokker-Planck formulas give different results for the real part of the parallel conductivity $\sigma_{\parallel r}$ above 100 km. The Fokker-Planck case is reduced by a factor of $\sqrt{\pi}$ at the higher altitudes. The dashed curves show that the parallel conductivity is only slightly affected in the range 300-600 km. by the inclusion of charge exchange effects.

Figures 3.2 and 3.3 show the frequency variation of the parallel conductivity when the Fokker-Planck and Spitzer formulas are used, respectively. Above 500 km. $\sigma_{\parallel r}$ is only slightly affected by varying the frequency between 10^{-4} and 10^0 c/s. The real part of the parallel conductivity is significantly decreased above 300 km. by increasing the frequency above 10^0 cps. At 700 km., for a frequency of 10^1 cps.,

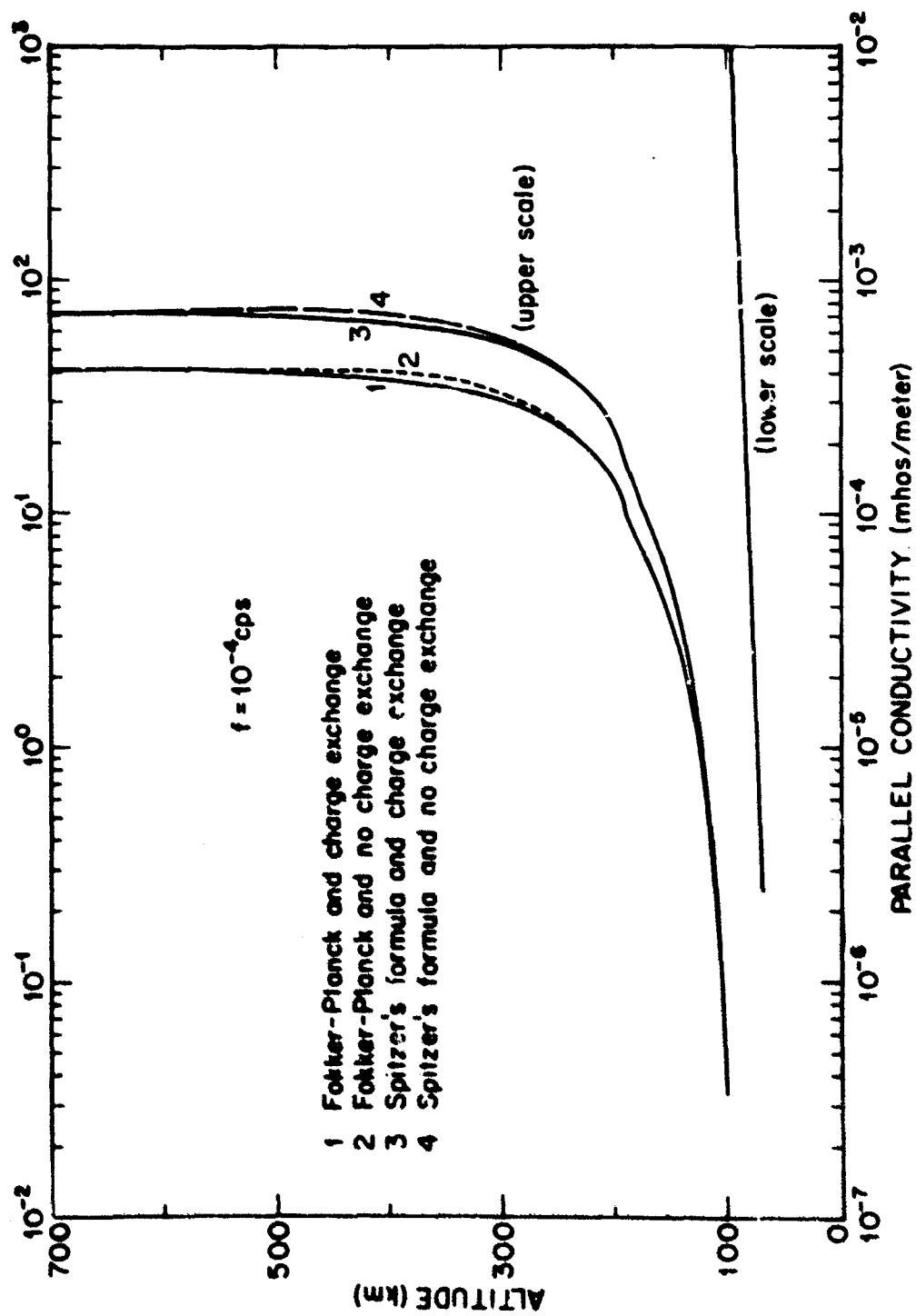
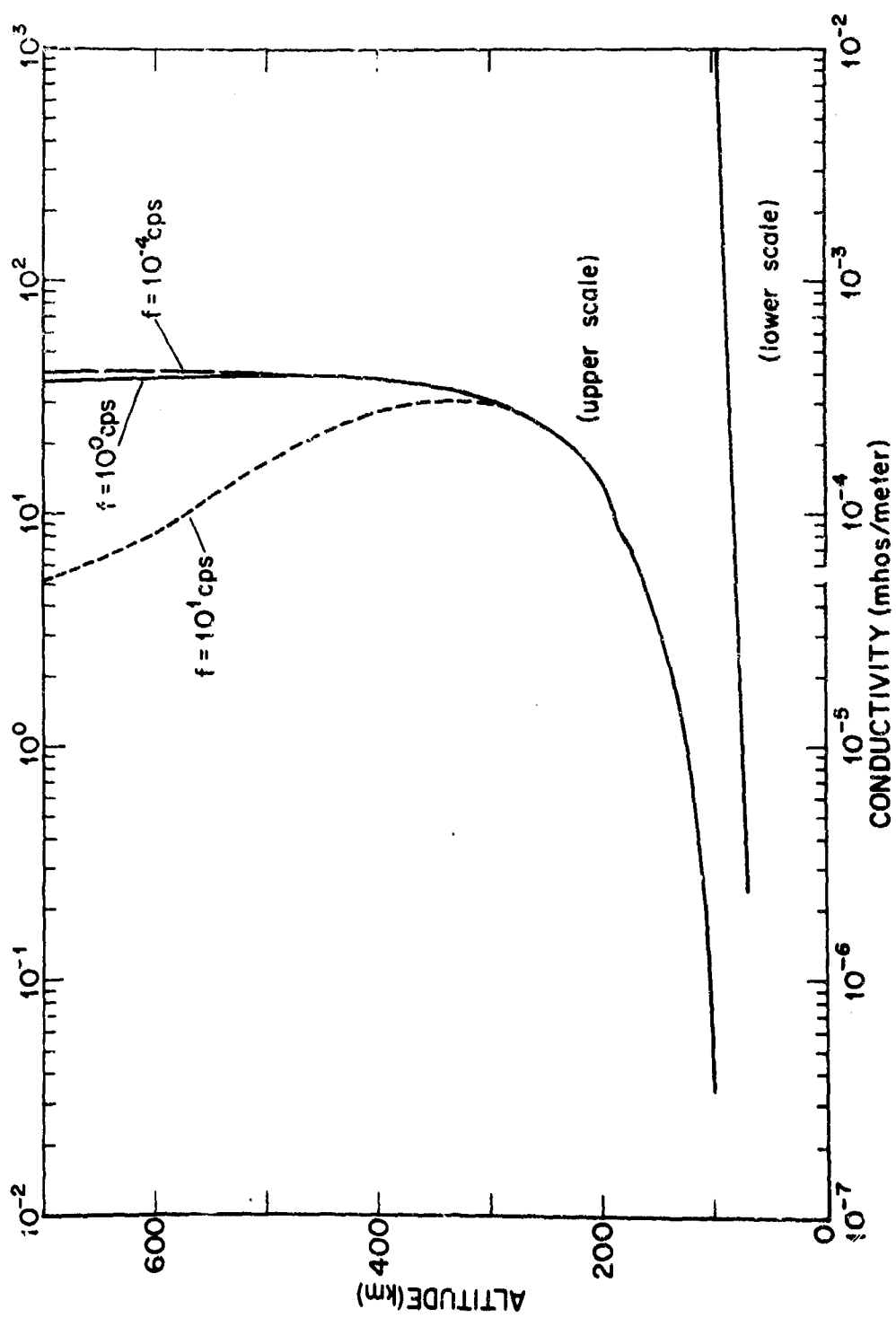
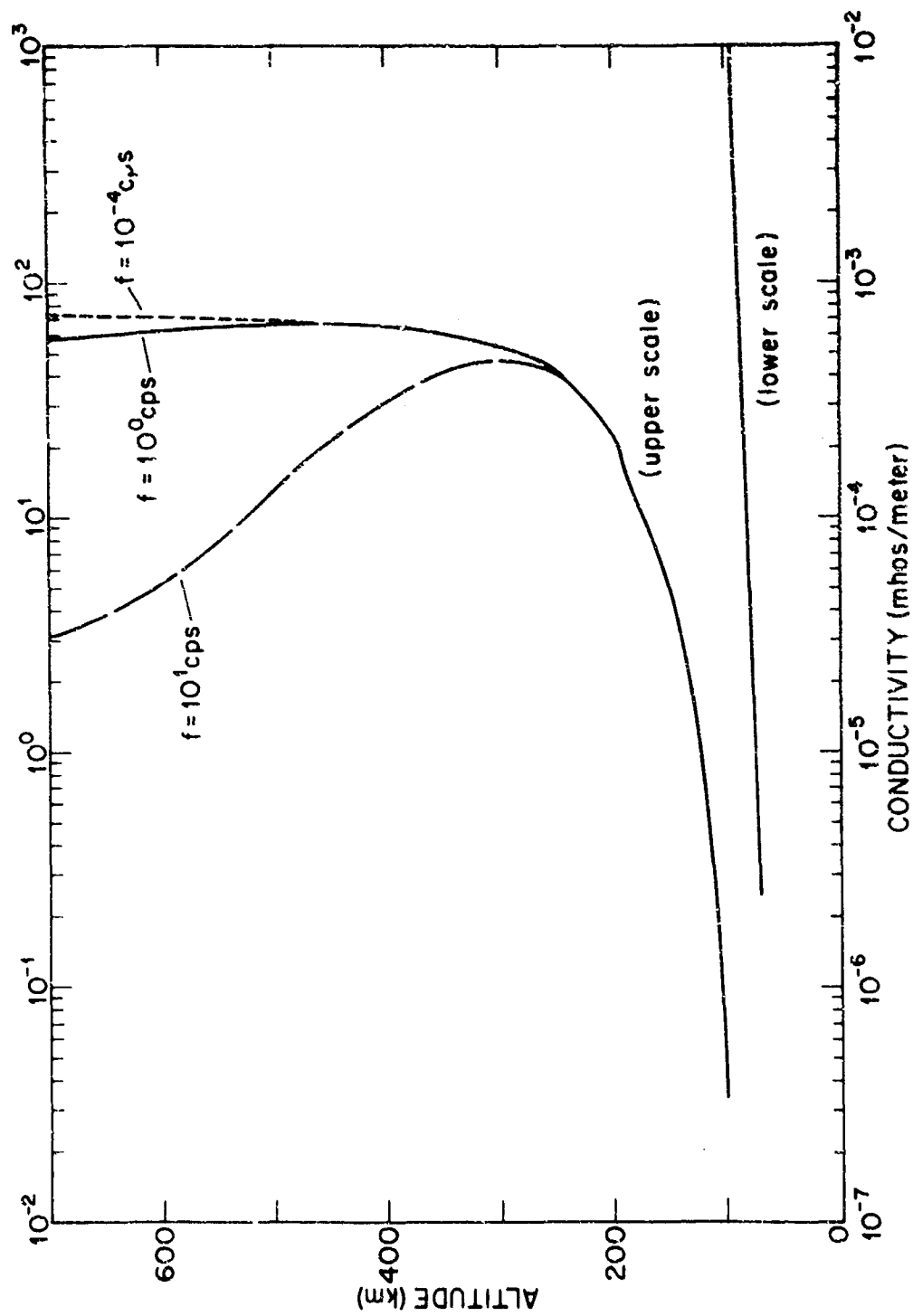


Figure 3.1



Frequency dependence of the parallel conductivity (including charge exchange and Fokker-Planck collisions) vs altitude

Figure 3.2



Frequency dependence of the parallel conductivity (including charge exchange and Spitzer's coulomb collision expression) vs altitude

Figure 3.3

σ_{Hr} is approximately one order of magnitude smaller than σ_{Hr} for frequencies less than 10^0 cps.

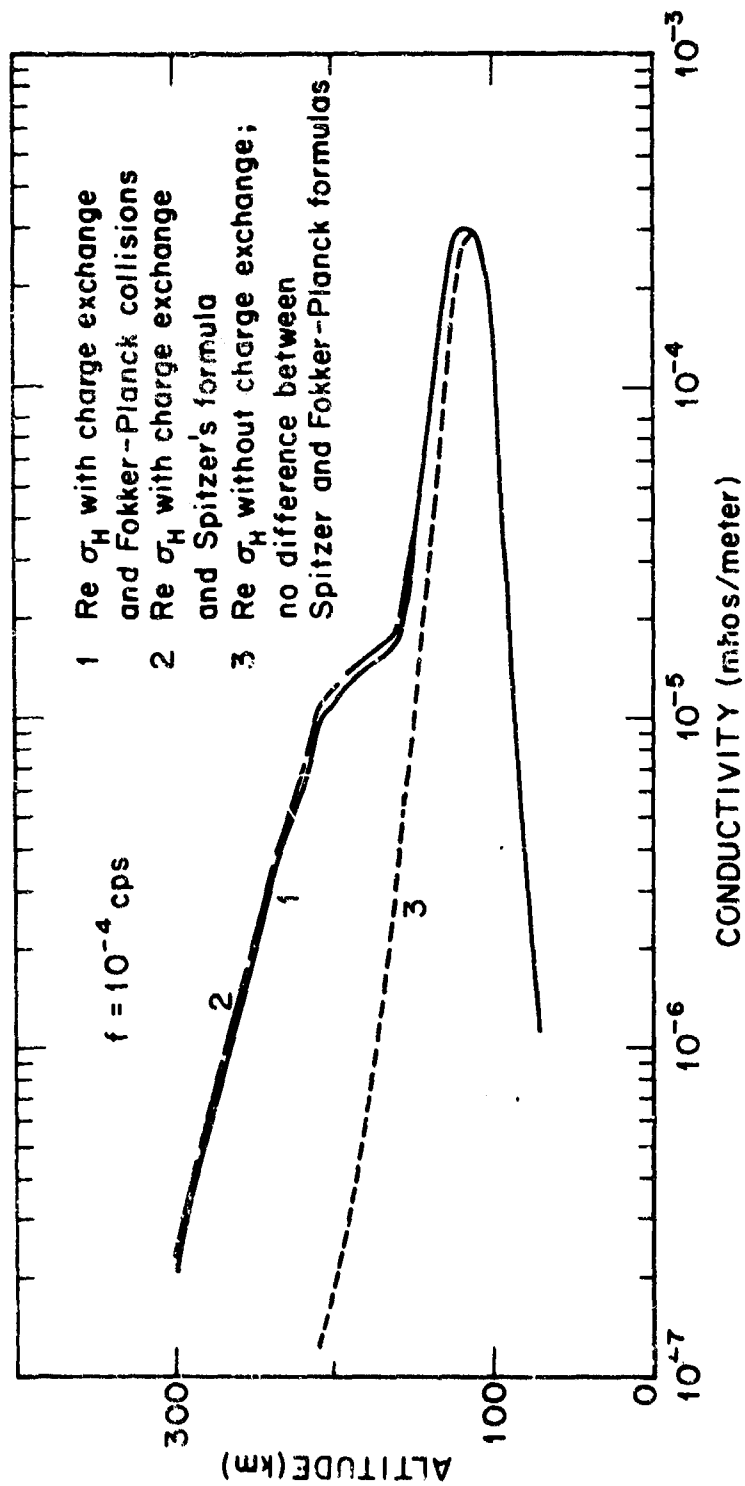
3.32 Hall Conductivity

Figure 3.4 shows that the real part of the Hall conductivity σ_{Hr} is significantly affected above 120 km. if the charge exchange processes are included. The Spitzer and Fokker-Planck formulas give no significant differences in the magnitude of the Hall conductivity. The frequency dependence of σ_{Hr} is depicted in Figure 3.5. For frequencies between 10^{-4} and 10^1 cps., the real part of the Hall conductivity below 150 km. is unaffected by frequency variations. For frequencies between 10^{-4} and 10^0 cps. σ_{Hr} is somewhat diminished for increasing frequency above 150 km. Also, σ_{Hr} actually becomes negative for the frequencies 10^0 and 10^1 cps. at the altitudes 300 and 150 km., respectively. This transition is the ion cyclotron resonance effect in the presence of collisions and is given by the condition

$$Y_i^2 = \frac{(1 + Z_i^2)^2}{1 - Z_i^2} \quad \text{with } \nu_i \ll \omega$$

where Y_i and Z_i are the usual Appleton-Hartree quantities.

The significance of the negative sign is that the ions move faster than the electrons. This is due to the fact that wave energy is being fed into the ion motion with the result that the ion gyroradius increases



The hall conductivities with and without charge exchange are given vs altitude

Figure 3.4

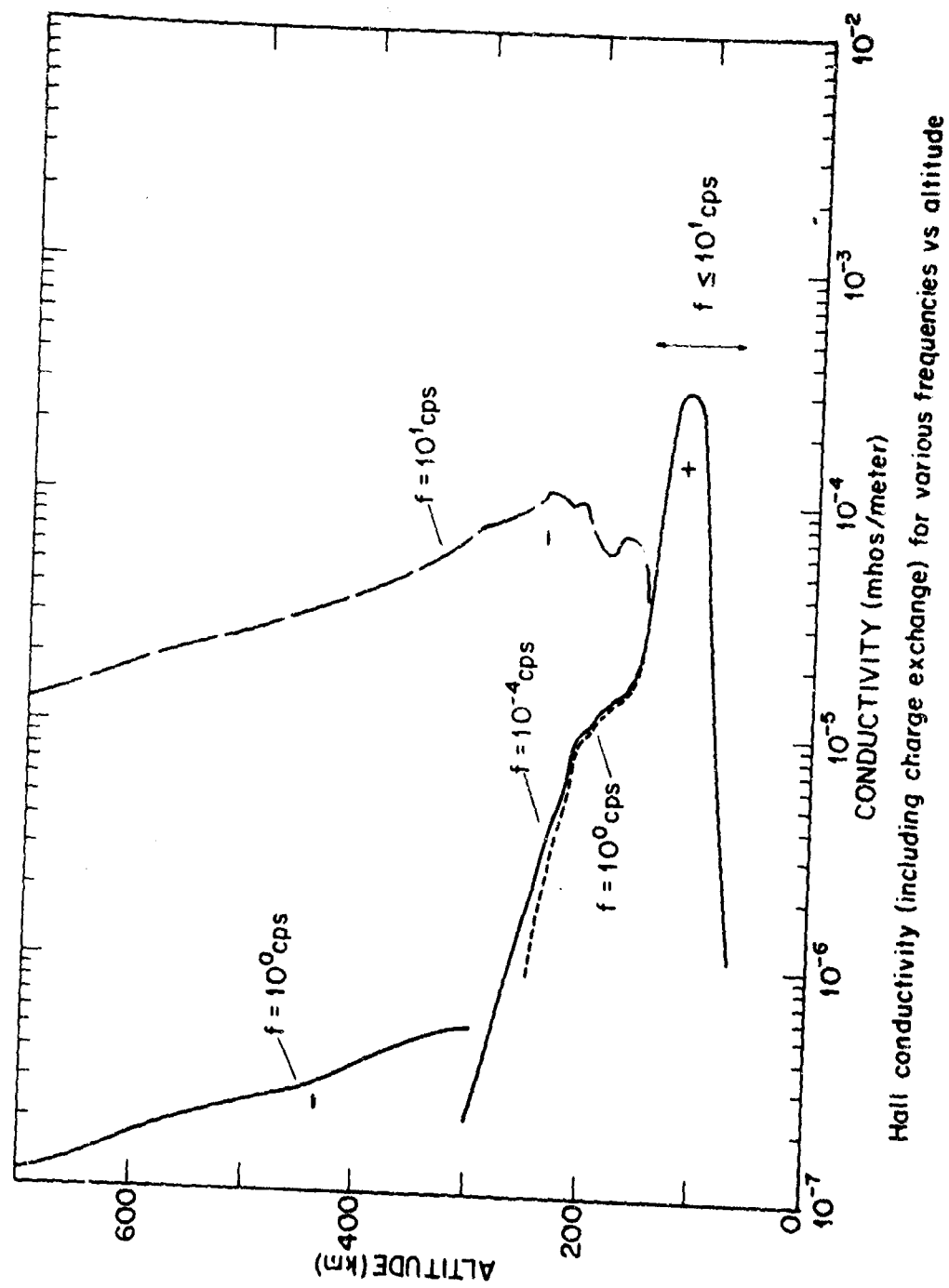


Figure 3.5

and enables the ions to outrun the electrons. Inspection of the imaginary part of the Hall conductivity shows that it is larger than the real part, indicating that wave energy is being absorbed. The effect of ion collisions is to reduce the efficiency with which the ion motion increases.

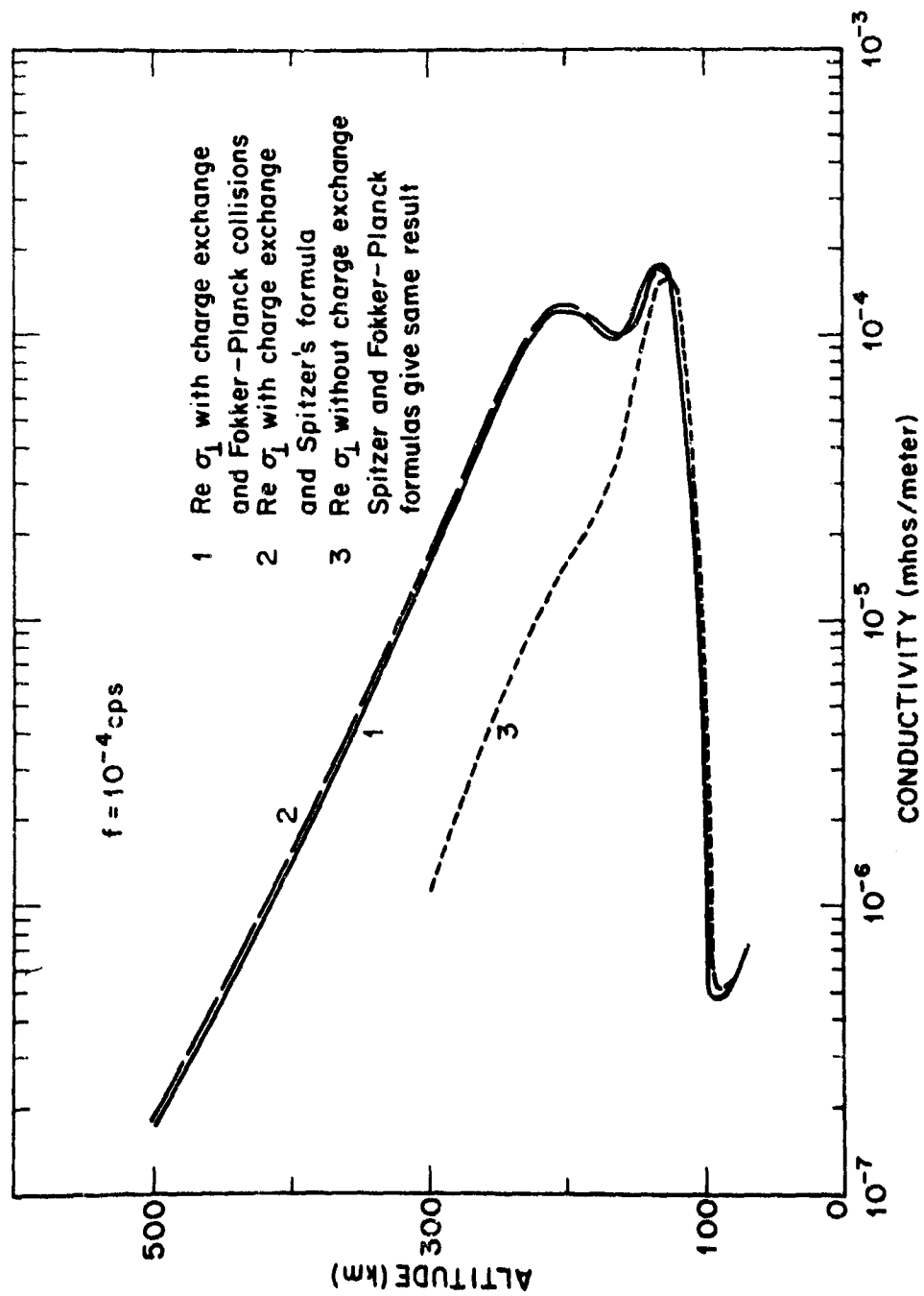
3.33 Pedersen Conductivity

Figure 3.6 shows that the real part of the Pedersen conductivity σ_{1r} is significantly affected above 130 km. by the inclusion of charge exchange effects. Above 200 km. σ_{1r} is enhanced one order of magnitude or more. This enhancement is due primarily to charge exchange of O^+ with O . Although not shown here the same effect is also true for the imaginary part of the Pedersen conductivity σ_{1i} and this is very important in altering the index of refraction for a disturbance propagating through the ionosphere at ULF frequencies (see section 4.2 of Part II and sections 4.11 and 4.31 of Part I).

Figure 3.7 shows that σ_{1r} is unaffected by frequency variations for frequencies less than 10^0 cps. At a frequency of 10^1 cps. σ_{1r} is enhanced slightly at all altitudes above 130 km.

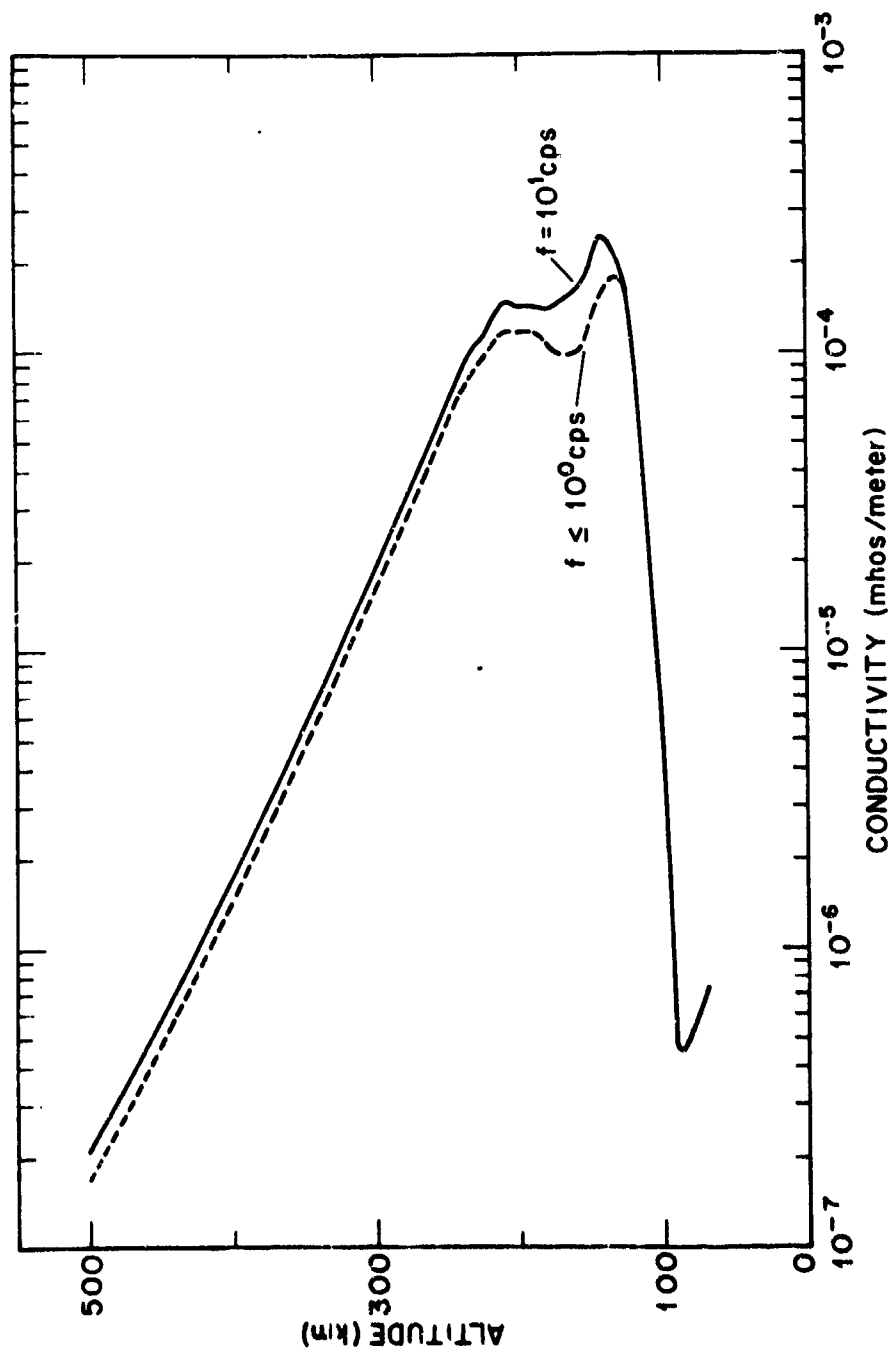
3.34 Comparison of the Various Conductivities

The real parts of all the conductivity elements are shown together for comparison in Figure 3.8. The Hall conductivity is larger than the Pedersen conductivity up to about 130 km. The maximum in σ_{Hr} occurs around 120 km. A primary maximum in σ_{1r} occurs at 130 km. due to charge exchange of O_2^+ with O_2 . A secondary maximum in σ_{1r} occurs around 200 km. due to charge exchange of O^+ with O . The parallel conductivity is



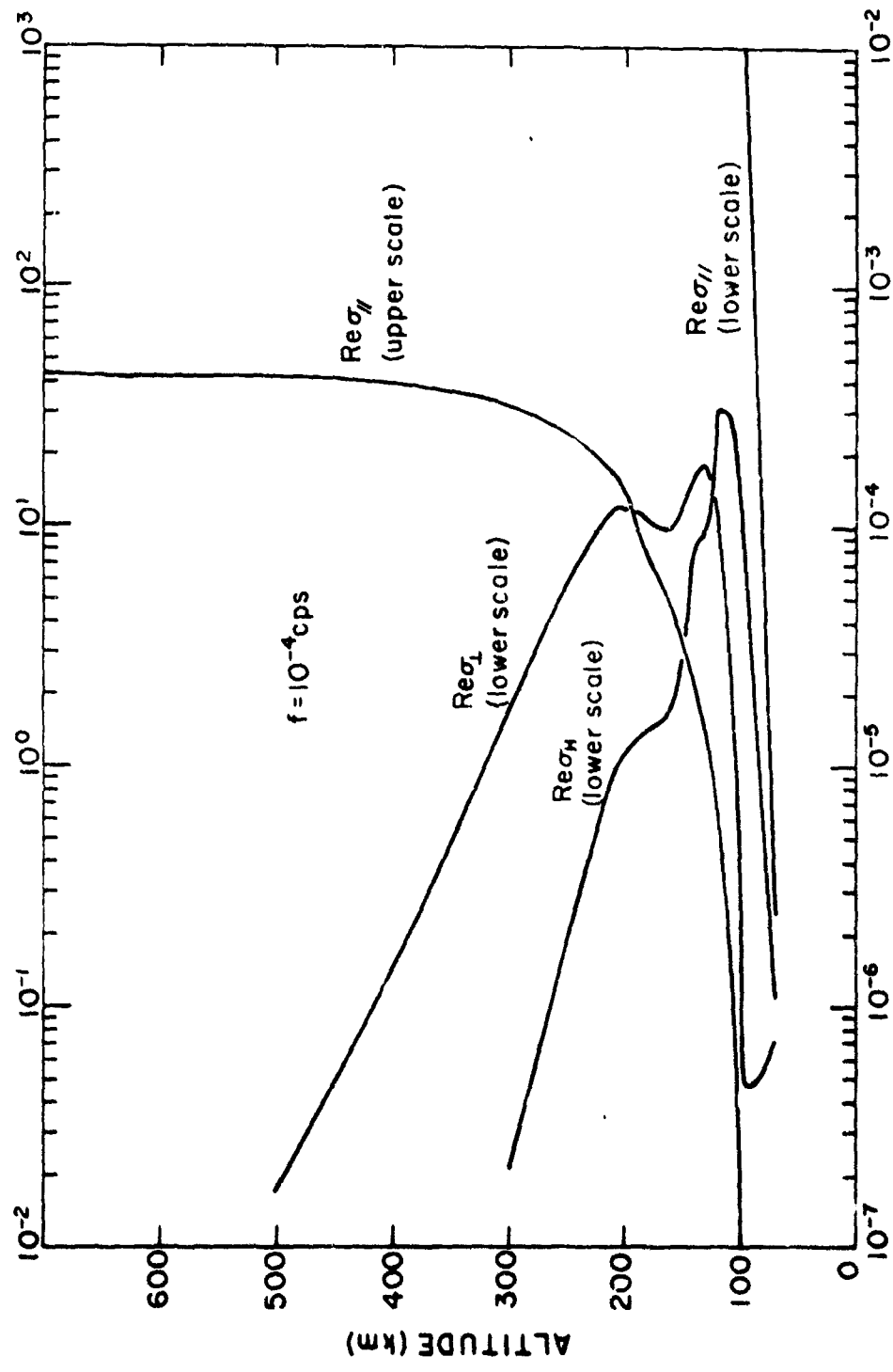
The perpendicular conductivities with and without charge exchange are given vs altitude

Figure 3.6



Frequency dependence of perpendicular conductivity (with charge exchange) vs altitude

Figure 3.7



Parallel, Pederson, and Hall conductivities (with charge exchange and Fokker-Planck collisions) vs altitude

Figure 3.8

much larger than the Hall and the Pedersen conductivities throughout the entire ionosphere.

Figure 3.9 shows the dimensionless Hall $\frac{\sigma_H}{\omega\epsilon_0}$ and Pedersen $\frac{\sigma_P}{\omega\epsilon_0}$ conductivities at the frequency 0.00333 cps. plotted on a linear scale vs. altitude. The integrated Pedersen conductivity (i.e., the area under the curve) for the F region is 1.5 times the integrated Hall conductivity for the E region. This represents a much larger F region conductivity than given by previous investigators.

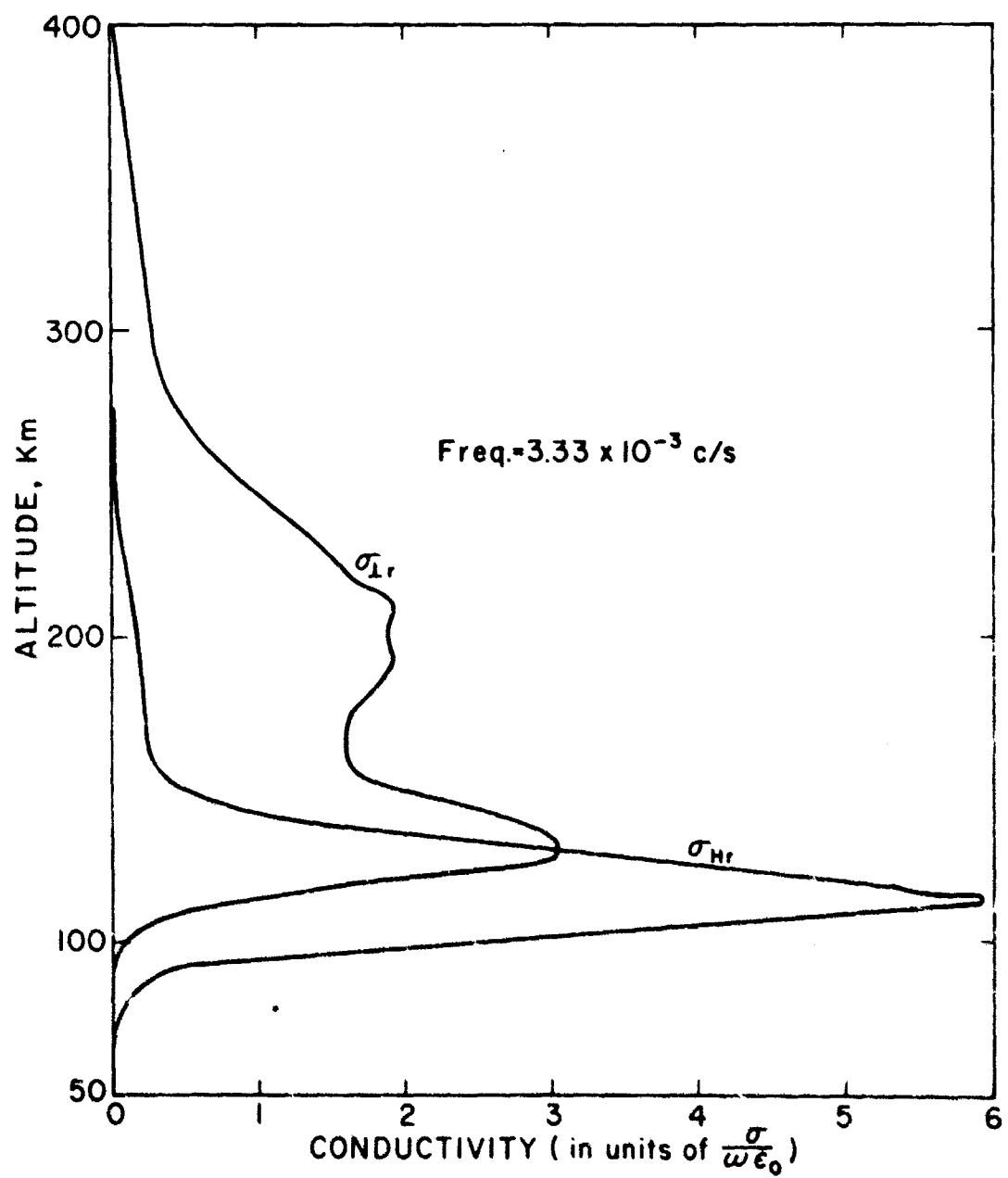


Figure 3.9

4.0 STIX'S QUANTITIES IN TERMS OF THE CONDUCTIVITY TENSOR ELEMENTS

4.1 Derivation of P, R, L, D, and S in the Presence of Collisions

If the uncoupled equations of motion are considered then the quantity m_k representing the mass of the k th particle in the absence of collisions may be replaced by $m_k (1 + iz_k)$ for the case when collisions are included by means of the friction term. It is then straightforward to show that P, R, L, S, and D are given by

$$\begin{aligned} R &= 1 - \sum_k \frac{X_k}{V_k + Y_k} \\ L &= 1 - \sum_k \frac{X_k}{V_k - Y_k} \\ P &= 1 - \sum_k \frac{X_k}{V_k} \end{aligned}$$

$$S = 1/2 (R + L)$$

$$D = 1/2 (R - L)$$

where

$$X_k = \frac{\pi_k^2}{\omega^2} \quad Y_k = \frac{\epsilon_k |\Omega_k|}{\omega}$$

$$z_k = \frac{\nu_k}{\omega} \quad V_k = 1 + iz_k$$

π_k = plasma frequency of k th particle

Ω_k = gyro frequency of k th particle

After some algebraic manipulation these quantities may be written

in terms of the conductivity tensor elements in the following manner

$$\begin{aligned} R &= 1 + \frac{\sigma_{11}}{\omega \epsilon_0} + i \frac{\sigma_{12}}{\omega \epsilon_0} \\ L &= 1 - \frac{\sigma_{11}}{\omega \epsilon_0} + i \frac{\sigma_{12}}{\omega \epsilon_0} \end{aligned}$$

$$P = 1 + i \frac{\sigma_{\parallel}}{\omega \epsilon_0}$$

$$S = 1 + i \frac{\sigma_{\perp}}{\omega \epsilon_0}$$

$$D = \frac{\sigma_H}{\omega \epsilon_0}$$

Separating the real and imaginary parts

$$\sigma_H = \sigma_{Hr} + i \sigma_{Hi}$$

$$\sigma_{\perp} = \sigma_{\perp r} + i \sigma_{\perp i}$$

$$\sigma_{\parallel} = \sigma_{\parallel r} + i \sigma_{\parallel i}$$

then

$$R = \left[1 + \frac{\sigma_{Hr} - \sigma_{\perp i}}{\omega \epsilon_0} \right] + i \left[\frac{\sigma_{\perp r} + \sigma_{Hi}}{\omega \epsilon_0} \right]$$

$$L = \left[1 - \frac{\sigma_{Hr} + \sigma_{\perp i}}{\omega \epsilon_0} \right] + i \left[\frac{\sigma_{\perp r} - \sigma_{Hi}}{\omega \epsilon_0} \right]$$

$$P = \left[1 - \frac{\sigma_{\parallel i}}{\omega \epsilon_0} \right] + i \left[\frac{\sigma_{\parallel r}}{\omega \epsilon_0} \right]$$

$$S = 1 - \frac{\sigma_{\perp i}}{\omega \epsilon_0} + i \frac{\sigma_{\perp r}}{\omega \epsilon_0}$$

$$D = \frac{\sigma_{Hr} + i \sigma_{Hi}}{\omega \epsilon_0}$$

In the absence of collisions

$$\sigma_{Hi} = \sigma_{\perp r} = \sigma_{\parallel r} = 0$$

then

$$R = 1 + \frac{\sigma_{HR} - \sigma_{Li}}{\omega \epsilon_0}$$

$$L = 1 - \frac{\sigma_{HR} + \sigma_{Li}}{\omega \epsilon_0}$$

$$P = 1 - \frac{\sigma_{Hi}}{\omega \epsilon_0}$$

$$S = 1 - \frac{\sigma_{Li}}{\omega \epsilon_0}$$

$$D = \frac{\sigma_{HR}}{\omega \epsilon_0}$$

4.2 The Effect of the Coupled Equations of Motion on Stix's Quantities

In general, for frequencies above 3×10^{-3} c/s, none of the conductivity tensor elements is significantly affected below 700 km. Above about 1000 km, the real part of the Pedersen conductivity and the imaginary part of the Hall conductivity may be seriously affected by the coupling of the equations of motion. However, the imaginary part of the Pedersen conductivity and the real part of the Hall conductivity are more important than the previously mentioned quantities in determining the propagation characteristics of a disturbance and are not seriously affected by the coupling of the equations of motion. Therefore the derivation of P, R, L, S, and D from the uncoupled equations of motions will be sufficient for frequencies of interest in this study.

REFERENCES

- Appleton, E.V., Wireless Studies of the Ionosphere, J. Instn. Elect. Engrs., 71, 642, 1932.
- Banks, Peter, Collision Frequencies and Energy Transfer. Electrons, Planet. Space Sci., 14, 1085-1103, 1966a.
- Banks, Peter, Collision Frequencies and Energy Transfer. Ions, Planet. Space Sci., 14, 1105-1122, 1966b.
- Baker, W.G., and D.F. Martyn, Electric Currents in the Ionosphere, Phil. Trans. Roy. Soc. London, A, 246, 281-294, 1953.
- Chapman, S., The Electrical Conductivity of the Ionosphere: a Review, Nuovo Cimento, 4, Series 10 (Suppl.), 1385-1412, 1956.
- Chapman, Sidney, and T.G. Cowling, The Mathematical Theory of Non-Uniform Gases, Cambridge University Press, (2nd ed., 1952), 1958.
- Cowling, T.G., The Electrical Conductivity of an Ionized Gas in the Presence of a Magnetic Field, Monthly Notices Roy. Astron. Soc., 93, 90-98, 1932.
- Dingle, R.B., D. Arndt, and S.K. Roy, Appl. Sci. Research, 6B, 155-164, 1957.
- Fejer, J.A., Semidiurnal Currents and Electron Drifts in the Ionosphere, J. Atmosph. Terrest. Phys., 4, 184-203, 1953.
- Heaviside, O., Telegraphy, I. Theory, Encyclopedia Britannica, 10th ed., 33, 213-218, 1902.
- Hultqvist, Bengt, Plasma Waves in the Frequency Range 0.001-10 cps. in the Earth's Magnetosphere and Ionosphere, Space Sci. Rev., 5, 599-695, 1966.
- Kennelly, A.E., On the Elevation of the Electrically Conducting Strata of the Earth's Atmosphere, Elec. World Eng., 39, 473, 1902.
- Maeda, H., The Vertical Distribution of Electrical Conductivity of the Upper Atmosphere, J. Geomag. Geoelec., 5, 94-104, 1953.
- Maeda, K., and S. Kato, Electrodynamics of the Ionosphere, Space Sci. Rev., 5, 57-79, 1966.

- Pedersen, P.O., The Propagation of Radio Waves Along the Surface of the Earth and in the Atmosphere, Danmarks Naturv. Samfund, A, 15, 244-262, 1927.
- Phelps, A.V., and J.L. Pack, Electron Collision Frequencies in Nitrogen and in the Lower Ionosphere, Phys. Rev. Letters, 3, 340-342, 1959.
- Ratcliffe, J.A., Magnetoionic Theory, Cambridge University Press, 1959.
- Schmidt, George, Physics of High Temperature Plasmas, Academic Press, New York, N.Y., 1966.
- Schuster, A., The Diurnal Variation of Terrestrial Magnetism, Phil. Trans. Roy. Soc. London, A, 180, 467-512, 1889.
- Schuster, A., The Diurnal Variation of Terrestrial Magnetism, Phil. Trans. Roy. Soc. London, A, 208, 163-204, 1908.
- Sen, H.K., and A.A. Wyller, On the Generalization of the Appleton-Hartree Magnetoionic Formulas, J. Geophys. Res., 65, 3931-3950, 1960.
- Shkarofsky, I.P., T.W. Johnston, and M.P. Bachynski, The Particle Kinetics of Plasmas, Addison-Wesley Publishing Company, Reading, Mass., 1966.
- Spitzer, Lyman, Jr., and Richard Harm, Transport Phenomena in a Completely Ionized Gas, Phys. Rev., 89, 977-981, 1953.
- Spitzer, Lyman, Jr., Physics of Fully Ionized Gases, 2nd ed., Interscience Publishers, John Wiley & Sons, New York, 1962.
- Stewart, Balfour, Terrestrial Magnetism, Encyclopedia Britannica, 9th ed., vol. 16, 159-184, 1882.

PART III

A MODEL IONOSPHERE
FOR MID-DAY AND MID-LATITUDE
DURING SUNSPOT MINIMUM

ABSTRACT

A model ionosphere for daytime conditions at mid-latitudes during the period of solar minimum has been constructed from existing experimental data. The atmospheric parameters obtained from these data include electron and ion densities, electron and ion temperatures, and electron collision frequencies and cross sections for momentum transfer.

TABLE OF CONTENTS	PAGE
List of Figures	3-iv
List of Symbols	3-v
1. Ion Densities	3- 1
1.1 Ion Densities in the F Region	3- 1
1.2 Ion Densities in the D and E regions	3- 4
2. Electron Densities	3- 9
2.1 Electron Densities in the F Region	3- 9
2.2 Electron Densities in the D and E Regions	3-11
3. Electron and Ion Temperatures	3-14
3.1 Electron and Ion Temperatures in the F Region	3-14
3.2 Electron and Ion Temperatures in the D and E Regions	3-17
4. Experimental Electron Collision Frequencies and Cross Sections	3-21
4.1 Electron Collision Frequencies for Momentum Transfer	3-21
4.2 Electron Cross Sections for Momentum Transfer with Neutral Gases	3-23
5. Concluding Remarks	3-26
6. Tables. Model Ionosphere Parameter Data	3-27
1. Charged Particle Densities in the F Region	3-28
2. Charged Particle Densities in the D and E Regions	3-29
3. Neutral Particle Densities	3-30
4. Electron, Ion, and Neutral Gas Temperatures	3-31
5. Electron Collision Frequencies and Average Cross Sections for Momentum Transfer	3-32
REFERENCES	3-33

LIST OF FIGURES

Figure	Page
1. Ion density vs. altitude in the F region	3- 2
2. Ion density vs. altitude in the D and E regions	3- 5
3. Ratio of positive ion density to electron density in the lower ionosphere	3- 7
4. Electron density vs. altitude in the F region	3-10
5. Electron density vs. altitude in the D and E regions	3-12
6. Electron and ion temperature vs. altitude in the F region	3-15
7. Average electron and ion temperature vs. altitude in the F region	3-18
8. Electron and ion temperature vs. altitude in the D and E regions.	3-19
9. Electron collision frequency for momentum transfer vs. altitude	3-22
10. Average momentum transfer cross sections for electrons in neutral gases	2-24

LIST OF SYMBOLS

N_i^+	Total positive ion density
N_i^-	Total negative ion density
N_e	Total electron density
T_e	Electron temperature
T_i	Ion temperature
T_n	Neutral gas temperature
ν_m	Electron collision frequency for momentum transfer
ν_{eff}	Effective electron collision frequency
\bar{S}_{en}	Average momentum transfer cross section for electrons in neutral gases
\bar{F}	10.7 cm solar radiation averaged over five solar rotations

1. Ion Densities

Positive ion density measurements have been extensively made up to 1000 km. Few data are available for higher altitudes. For negative ion densities, only a few rocket measurements have been performed, but existing data seem to indicate that negative ions may be important up to 70 km during the daytime and up to 90 km during the nighttime [Sagalyn, 1965].

1.1 Ion Densities in the F Region

Positive ion densities in the upper atmosphere during solar minimum have been reported by Johnson [1966]. These results are presented in Fig. 1.

Johnson's model is based on two sets of data which were measured with radio frequency ion mass spectrometers that determined the relative ion composition. The first data set is for the region 90-240 km and was measured from an Aerobee 150 rocket launched from White Sands, New Mexico at 1634 UT (0931 MST) on February 15, 1963. The second data set is for the region 400-1200 km and was measured from the Soviet satellite Electron 2. The latter was obtained for the time interval 1400 - 1900 hours LT and for the latitudes 10° - 60° N during the period of February 10-16, 1964.

Notice should be made of the fact that Johnson derived the absolute number densities for various ions from the relative ion composition data by neglecting negative ions and by assuming the electron density was equal to the total ion density. To obtain this normalization Johnson chose three different electron density distributions: For 90-130 km the results reported by Bourdeau et. al. [1966] obtained from a Nike-Apache rocket, NASA 14.117, flown from Wallops Island, Va. at 1207 EST, November 23, 1964 were utilized; the White

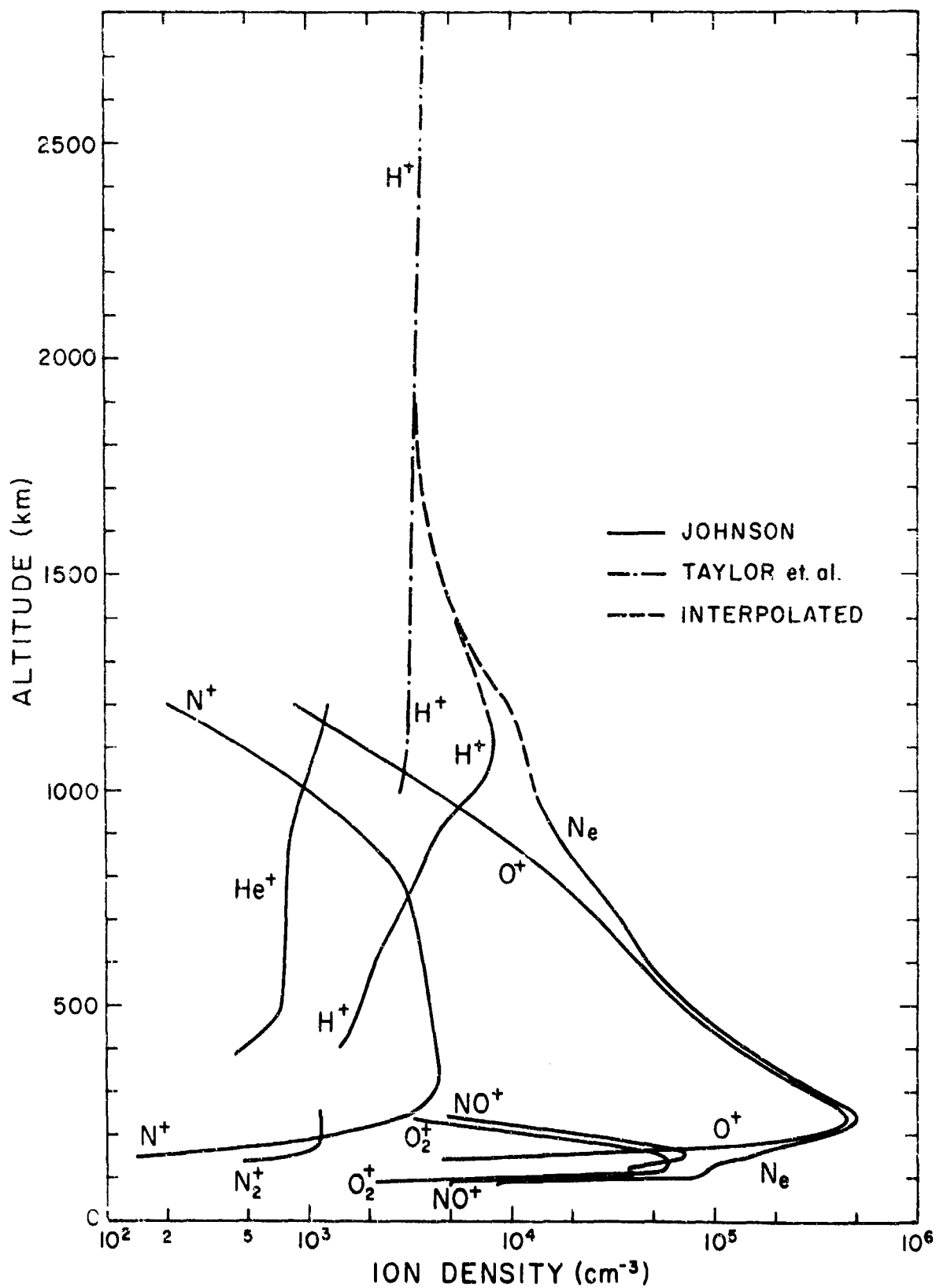


Figure 1. Ion density vs altitude in the F region

Sands ionosonde data reported by Holmes et al. [1965] were used for the 130-240 km region; the electron densities for the 240-1000 km region were obtained by averaging the data from a rocket-borne dispersive Doppler radio propagation experiment and data from Alouette satellite, both data sets being obtained 500 km east of Wallops Island, Va. at 0923 EST (1423 UT) on July 2, 1963. Johnson adopted electron densities for the 1000-1200 km altitudes by extrapolating the lower altitude electron densities.

Johnson presented no data for the 240-400 km region. For these altitudes, an interpolation was made between the high and low altitude portions of the N^+ and O^+ curves. According to Johnson, the maximum deviation required to smoothly connect the three electron density distributions occurred at 240 km and was less than 25%.

At altitudes above 1200 km only a few ion density measurements have been made. Taylor et. al. [1965] measured the H^+ and He^+ densities from 1500 km to 30,000 km with the positive ion spectrometer on board the OGO-A satellite during the period September 23 through December 10, 1964. The He^+ densities were about 1% of the H^+ densities and thus were too small to be shown in Figure 1. This result implies that if we intend to match the data of Taylor et. al. with Johnson's model, then the He^+ concentration must decrease by two orders of magnitude between 1200 and 1500 km. Values for the He^+ densities are given in Table 1.

Also the total positive ion concentration N_i^+ was measured by Hanson [1962] with a retarding potential probe on October 4, 1960 during mid-afternoon. The data are given in Fig. 1. Up to 2400 km these values are larger than those given by Taylor et. al.

All of the data measured at solar minimum seem to indicate that H^+ is by far the dominant ion above 1200 km and that the H^+ concentration is fairly constant between 1200 and 3000 km. Thus in order to make a consistent model we assume that H^+ is the dominant ion above 1200 km and that the H^+ concentration exactly equals the electron density. We therefore extrapolate Johnson's curves for the H^+ and electron densities so that they smoothly connect at about 2000 km with the data given by Taylor et.al. This extrapolation is shown in Figure 1 and values are given in Table 1.

1.2 Ion Densities in the D and E Regions

The ionic composition in the lower ionosphere is complicated by the presence of many minor constituent ions. Fig. 2 shows these minor constituent ions to be 3 or 4 orders of magnitude smaller than the major constituent ions.

In addition to the lower altitude values of Johnson's model, two sets of positive ion density data are presented in Fig. 2. The first set is taken from the results of Sagalyn and Smiddy, as reported by Narcissi [1966], obtained with an electrostatic probe at 1200 hours CST, October 31, 1963 on the Nike Cajun AC6.341 launched from Elgin, Florida. The second data set was obtained by Smith et. al. [1967] with a positive ion Bennett-type mass spectrometer above Wallops Is. at 1330 hours EST in May 1962. Their measurements cover the mass range 7-43 amu.

Both sets of data appear to be in agreement with each other, except for the values of the ion species 24^+ , the values of which given by Sagalyn and Smiddy are about 3 times larger than those given by Smith et. al. We choose the Sagalyn and Smiddy data because they were measured at a time closer to solar

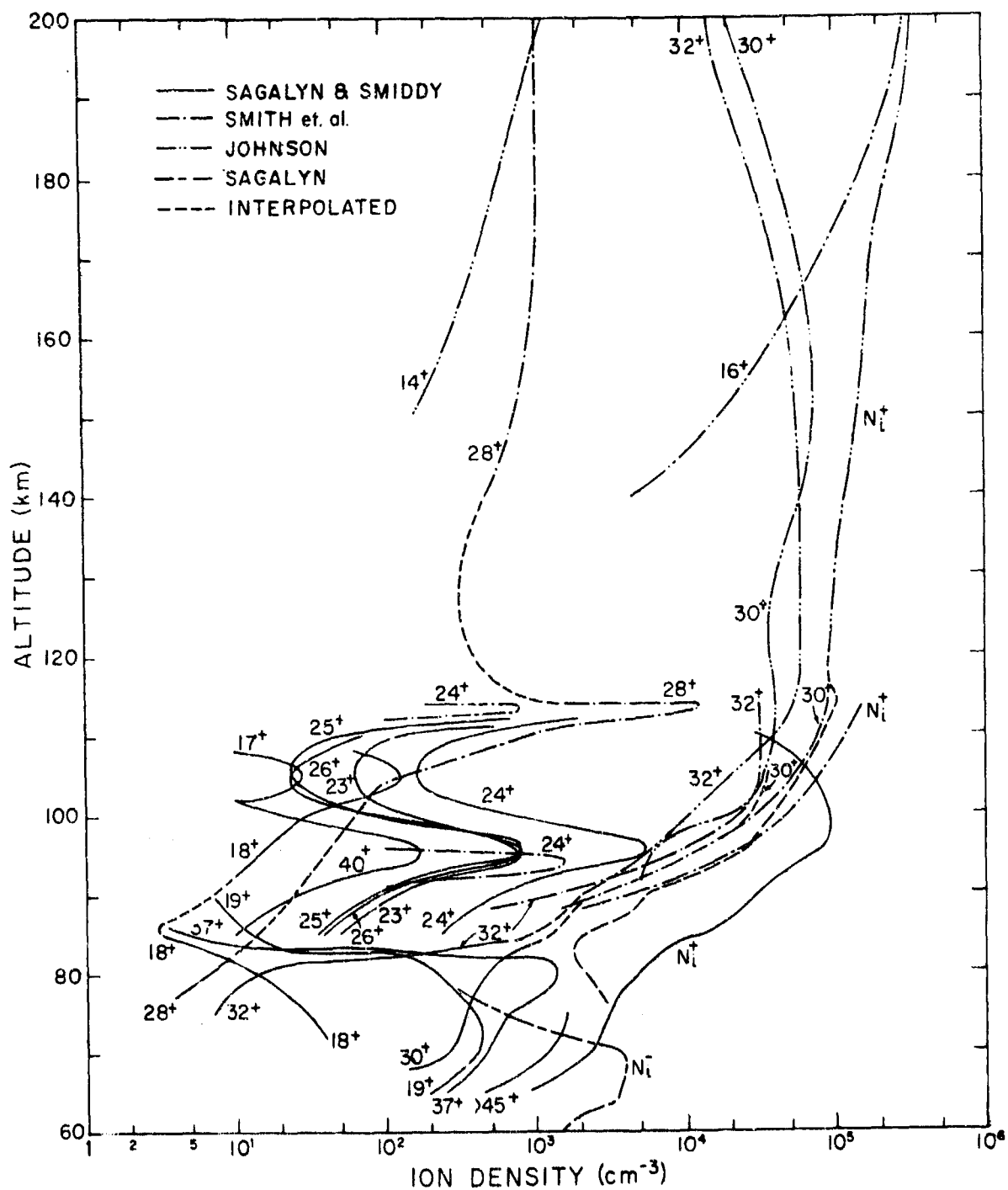


Figure 2. Ion density vs altitude in the D and E regions

minimum. The values of 28^+ given by Smith et. al. are adopted for the altitudes of 104-112 km. Then an interpolation is made between these values and those measured by Sagalyn and Smiddy, whose results for 28^+ extend only up to 82 km. The interpolated values are indicated by the dashed line. We also interpolate between Johnson's values of 28^+ and those of Smith et. al.

The curves for 32^+ and 30^+ given by Smith et. al. are nearly parallel to the corresponding curves of Johnson's model. The 32^+ curve of Johnson is extrapolated down to meet the 32^+ curve of Sagalyn and Smiddy. In the same manner the 30^+ curve of Sagalyn and Smiddy is extrapolated to higher altitudes to join with the 30^+ curve of Smith et al. The latter is then smoothly connected to the 30^+ curve of Johnson's model.

In order to provide a consistent model, we calculate the total negative ion density by subtracting the total electron density (to be discussed in the next section) from the total positive ion density obtained by summing all the densities of the various positive ion species. These results may be compared with the negative ion density data reported by Sagalyn [1965] and are shown in Fig. 2. Her measurements were made using a two probe system on a Nike Cajun II ascent at 1200 hours LT on 11 March 1964. Our negative ion density values do not agree with those of Sagalyn because our adopted altitude distributions of electron and positive ion densities are not the same as those reported by Sagalyn. Taking our calculated values of negative ion densities and plotting the ratio $N_i^+/N_e = 1 + \bar{N}_i/N_e$, we obtain the curve shown in Fig. 3. Comparison of our calculated ratio and the corresponding ratio derived by Sagalyn [1965]

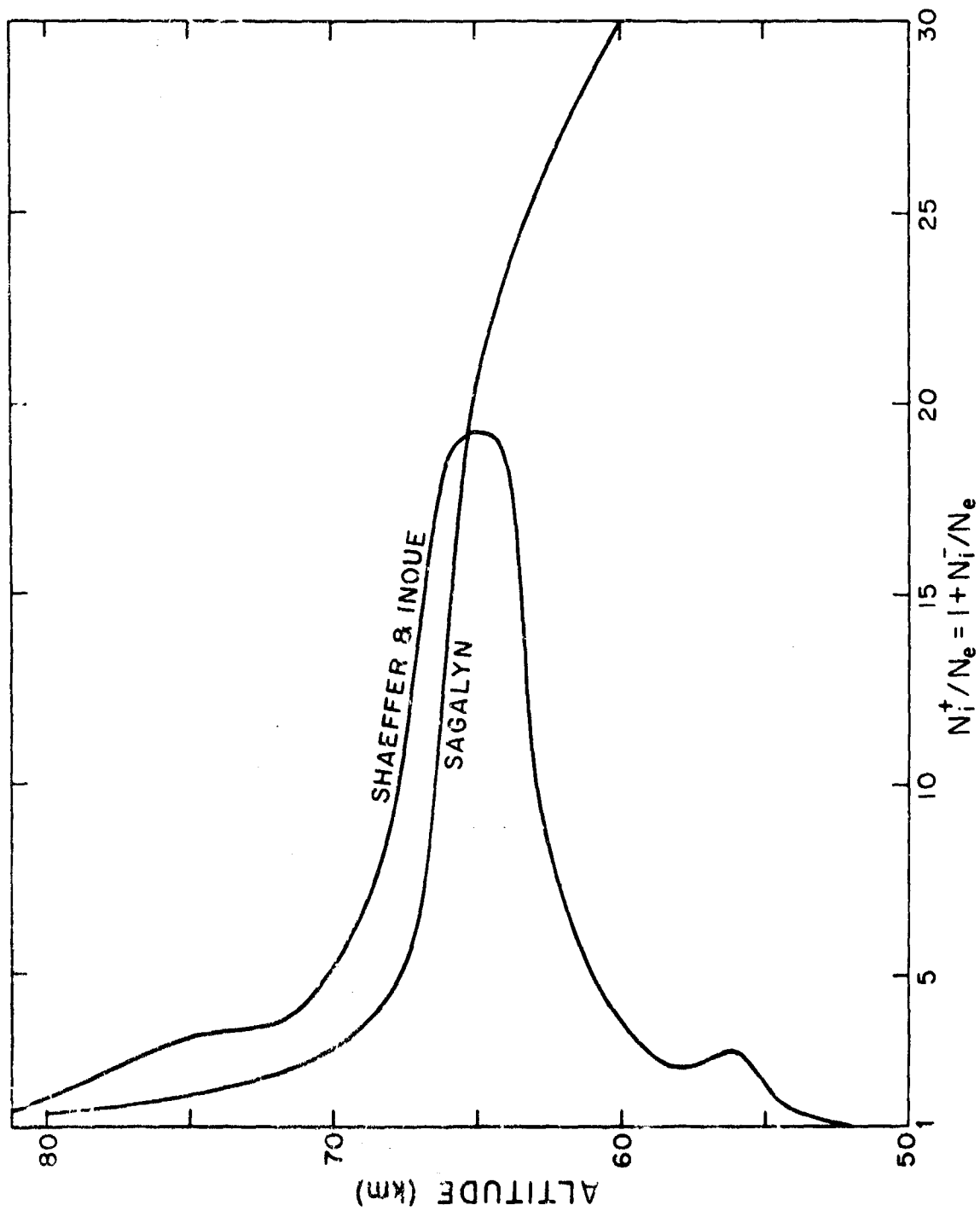


Figure 3 Ratio of positive ion density to electron density in the lower ionosphere

from Nike Cajun II data shows that our calculated altitude distribution of \bar{N}_i/N_e has the same shape above 65 km as that of Sagalyn, although the negative ion density values are considerably different. Below 65 km Sagalyn's ratio of \bar{N}_i/N_e increases with decreasing altitude whereas our calculated values of \bar{N}_i/N_e decrease to zero at about 52 km.

From Fig. 2 we see that for the region below 82 km ions heavier than 45 amu are predominant, with 37^+ , 19^+ , and 30^+ being the next most abundant. Narcissi [1966] has identified these ions as 18^+ (H_2O^+), 19^+ (H_3O^+), 28^+ (N_2^+ or Si^+), 30^+ (NO^+), 32^+ (O_2^+) and 37^+ ($H_5O_2^+$). The heavy ions $> 45^+$, as suggested by Narcissi [1966], may be higher hydrates of H_3O^+ and/or other cluster ions. Narcissi argues that such large quantities of hydrates are not expected from rocket contamination. Also, exact identification of individual negative ion constituents in the lower ionosphere has not yet been made.

At an altitude of about 82 km a transition takes place in the ionic composition. The ions 19^+ and 37^+ decrease sharply while the ions 30^+ and 32^+ become predominant. At about 170 km O^+ becomes the dominant ion species. As shown in Fig. 1, a transition occurs at approximately 1000 km where H^+ becomes the dominant ion and remains as such at greater altitudes. Values of the adopted ion densities for the D and E regions are found in Table 2.

2. Electron Densities

2.1 Electron Densities in the F Region

Several different methods have been used to measure electron densities in the F region. The results of some of these methods are presented in Fig. 4.

The measurements of Ulwick and Pfister [1963] were made with an r.f. impedance probe on a rocket flight at 0100 hours EST on April 12, 1961. The results of Nisbet et. al. [1966] were obtained from measurements of radio signals propagated between sections of a Javelin rocket flown from Wallops Is., Va. on May 19, 1965 shortly after 1600 hours LT. The data of Oya and Obayashi [1967 a] were obtained using the sweep frequency impedance probe technique on the L-3H-2 rocket at 1535-1550 hours JST on July 23, 1966. Jackson and Bauer [1961] used the Seddon CW propagation technique on the NASA 8.10 rocket flown from Wallops Is., Va. at 1502 EST on April 27, 1961. Oya and Obayashi [1967 b] made their measurements at 1725-1730 JST on October 20, 1966.

These data are rather spread but consistently indicate the presence of a peak density in the neighborhood of 240-320 km. Also obvious from Fig. 4 is the variability exhibited by the values of the electron density above about 900 km. However, we must remember that these data were measured during different ionospheric conditions.

Since no negative ions have reportedly been measured at these high altitudes, we are constrained to choose equal electron and ion density values in order to preserve charge neutrality. We have already adopted an ion density distribution for the F region (see Sec 1.1) and must therefore select the same density distribution of electrons. This adopted distribution is shown in Fig. 4

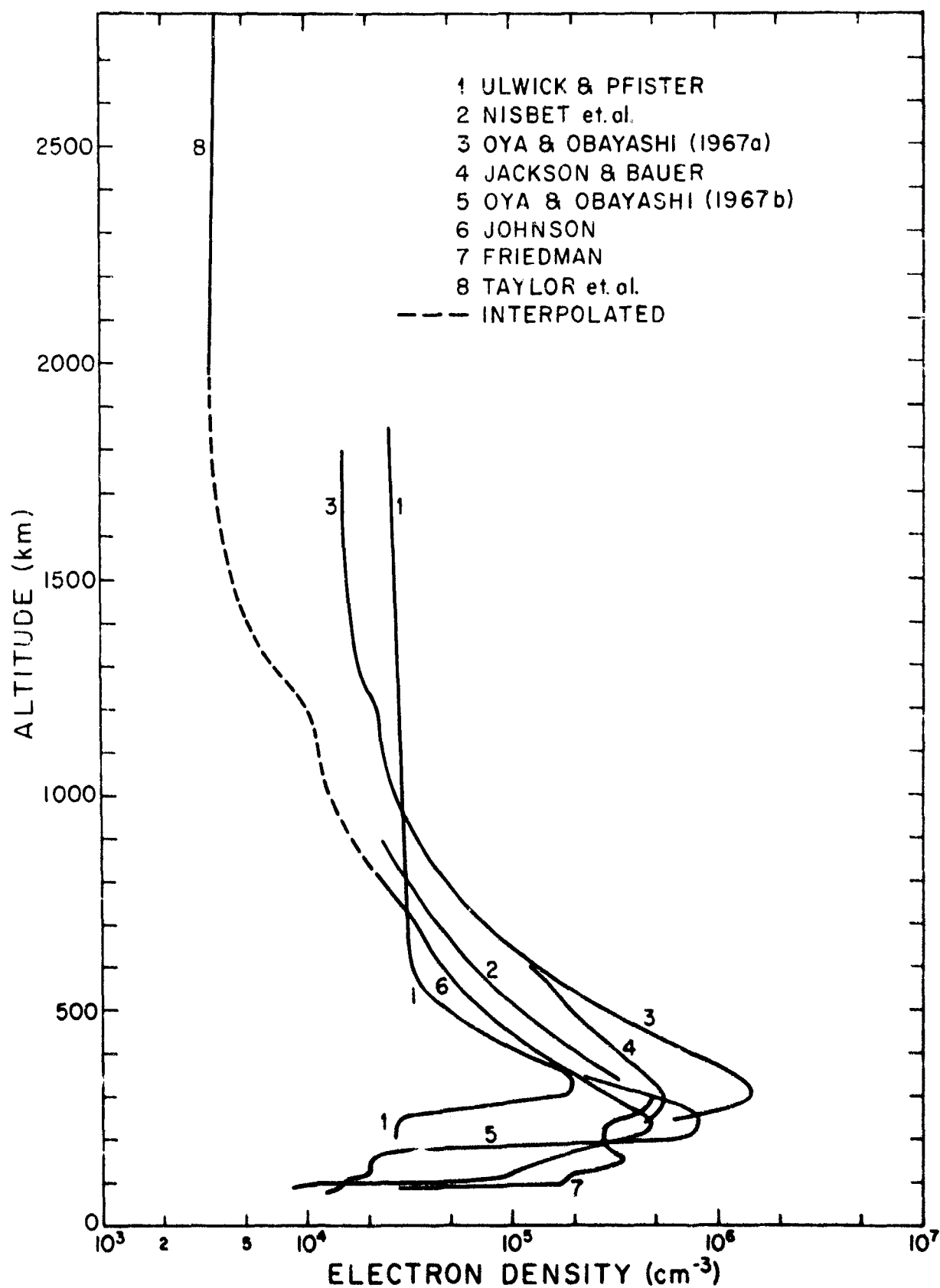


Figure 4. Electron density vs altitude in the F region

and comparison with the previously mentioned electron density data indicates good agreement.

2.2 Electron Densities in the D and E Regions

Various techniques have also been used to measure electron densities in the lower ionosphere. The results of some of these methods are shown in Fig. 5.

Smith [1965a] obtained data with Langmuir probes during the ascent of a rocket launched from Wallops Is., Va. at 1430 hours EST on February 27, 1963. The data of Sagalyn [1965] were measured with a two probe system used on the Nike Cajun II on March 11, 1964 at 1200 hours LT. The data given by Belrose et. al. [1966] were obtained by the partial reflection method. Also, data obtained from Nike Cajun I on October 31, 1963 at 1200 hours LT with spherical electrostatic analyzers are given by Sagalyn et. al. [preprint].

To obtain electron density and collision frequency measurements simultaneously, Salah and Bowhill used a particular radio propagation technique by which the transmitting power and polarization are controlled by the rocket receiver output via telemeter link. The experiment was performed with a rocket fired from Wallops Is., Va. on April 12, 1965 at 1214 EST. Using the same method Mechtly et. al. [1967] obtained data from an experiment performed on Nike Apache 14.143 launched from Wallops Is., Va. on April 16, 1964 at 2100 hours UT.

We choose curve 1, the data obtained by Smith, for our model atmosphere because it seems to be quite representative of the various data given in Fig. 5. The C, D, and E layers are clearly seen in Smith's electron density distribution. Above 82 km curve 1 is in good agreement with our adopted total positive ion

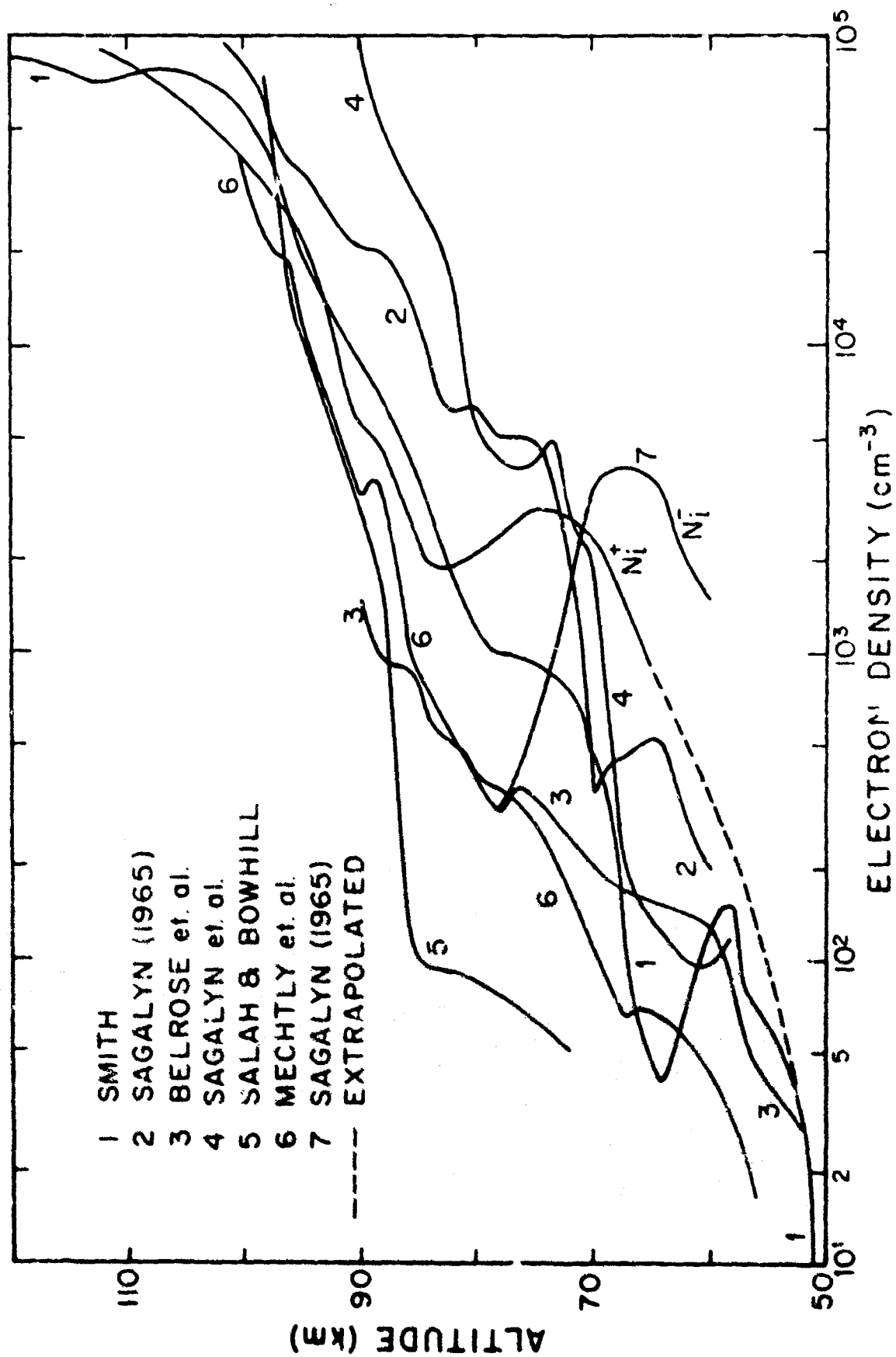


Figure 5. Electron density vs altitude in the D and E regions.

density curve. Below about 82 km Smith's electron densities are considerably less than the positive ion densities. This is to be expected because of the presence of negative ions. The negative ion density is calculated by subtracting Smith's electron density values below 82 km from the adopted positive ion values. Then we extrapolate the positive ion density curve down to 52 km at which altitude the electron concentration is assumed to be equal to the positive ion concentration. For our model ionosphere we also assume that the negative ions disappear above 82 km.

These adopted negative ion and electron density values are listed in Table 2.

3. Electron and Ion Temperatures

3.1 Electron and Ion Temperatures in the F Region

Electron and ion temperatures in the F region have been measured by means of ground based radar backscatter and various types of plasma probes aboard rockets and satellites. A review of these methods and a comparison of the results are given by Evans [1965a]. Discrepancies do exist between the data obtained by the various methods and some of these discrepancies have not yet been resolved. As stated by Evans, rocket and satellite measurements have greater accuracy and better time and height resolution than do radar measurements. However, up to the present time, satellite data are not sufficient to provide the altitude variations of the temperatures. Space vehicles disturb the medium surrounding them. Extensive radar measurements have been made during the solar minimum period and over a wide range of altitudes. For this reason we choose the radar backscatter results for our model.

Ionospheric backscatter results for solar minimum are given by Evans [1965a, 1965b, 1967a, 1967b]. These measurements were made at the Millstone Hill radar observatory (42.6°N, 71.5°W). The results for 1963 and January 1964 [Evans, 1965b] are replotted in Fig. 6. These data were derived on the assumption that only O^+ ions are present at all heights above 200 km.

Later in 1964 Evans [1967b] obtained other electron and ion temperature data with different assumptions. The neutral temperature above 250 km was determined from the radar signal spectra at the altitudes 230, 260, and 290 km. The neutral temperature at altitudes below 250 km was then obtained by assuming

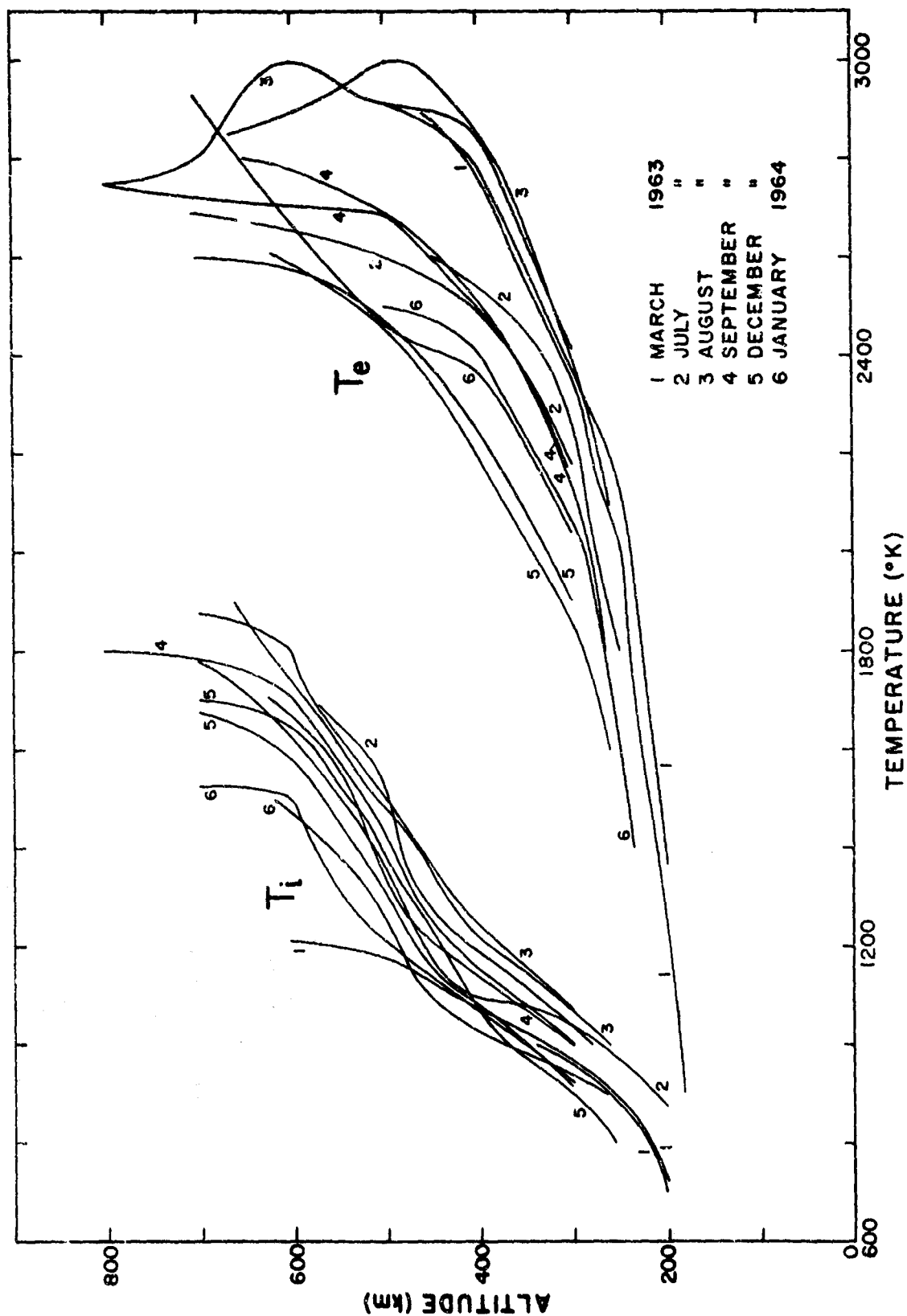


Figure 6. Electron and ion temperature vs. altitude in the F region.

the exponential dependence of T_n on altitude implied by the 1965 CIRA models I and II (see equation (1), Evans [1967b]). Then Evans was able to simultaneously determine T_e and the ratio of (O^+) to $(O_2^+ + NO^+)$ ions for the altitudes 135-250 km. The neutral gas temperatures thus determined are as much as 200 K⁰ lower than the values given by CIRA 1965 for the same solar flux (\bar{F}) of 10.7 cm radiation averaged over 5 solar rotations. Evan's neutral gas temperatures disagree with satellite drag data by 9% [Evans, 1967b].

We choose Evan's data from 1963 and January 1964 for our model for the following reasons:

(1) The ion temperature determined by Evans [1965b] approximately equals the neutral temperature given by CIRA 1965 models I and II ($\bar{F} = 65$ and 75×10^{-22} W/m² c/s, respectively) up to about 300 km. At greater altitudes $T_i > T_n$. This result is in fairly good agreement with theory [Banks, 1966; Dalgarno et. al., 1967; Geisler and Bowhill, 1965 a, 1965b].

(2) A model for the ion composition has already been adopted, as discussed in sec. 1, and agrees with the assumption that O^+ is the dominant ion above 200 km.

(3) The neutral temperatures and corresponding densities given by the CIRA 1965 model I are adopted and there is no need to determine the neutral gas temperatures from radar signal spectra.

Evans concludes from the data of 1963 and January 1964 that the altitude variations of T_e do not indicate a strong seasonal dependence. The ion temperature shows even less seasonal variation than the electron temperature. Evans also points out that the temperatures are fairly stable throughout the daytime. The ratio T_e/T_i is greater than 1.0 throughout the F region and

reaches a maximum value of 2.0 - 2.6 at an altitude of about 300 km soon after dawn irrespective of the season.

As seen in Fig. 6, T_i has a positive gradient at all altitudes. However there remains some uncertainty in the gradient of T_e above 500 km. Twelve different profiles for T_e are depicted. Nine of these indicate near-isothermal conditions above 500 km; three profiles have a definite positive temperature gradient.

Theoretical models [Banks, 1966a; Dalgarno et. al., 1967; Geisler and Bowhill, 1965a, 1965b] predict that T_e becomes isothermal at higher altitudes. Evans [1967a] has developed a theory to explain the discrepancy between observed positive gradients and Geisler and Bowhill's isothermal model. Evans concludes that this positive gradient and the high protonospheric temperatures may be accounted for by the backward scattering of photoelectrons from the ionosphere. This flux is estimated to be about 5×10^8 electrons/cm²/sec with mean initial energies of 14 ev. However, the majority of the cases presented in Fig. 6 indicates that T_i is converging toward T_e and thus does not warrant invoking such a theory. The twelve profiles shown in Fig. 6 are averaged and the resulting average is shown in Fig. 7. The values for these average electron and ion temperatures are given in Table 4.

3.2 Electron and Ion Temperatures in the D and E Regions

Fig 8 shows the measurements of electron and ion temperatures made by several investigators for the D and E regions. The data reported by Brace et. al. [1963] were measured with a dumbbell bipolar probe which was ejected from the rocket vehicle NASA 6.04 flown from Wallops Is., Va. at 1556 hours EST on March 26, 1961. Spencer et. al. [1965] report results obtained with a cylindrical Langmuir probe.

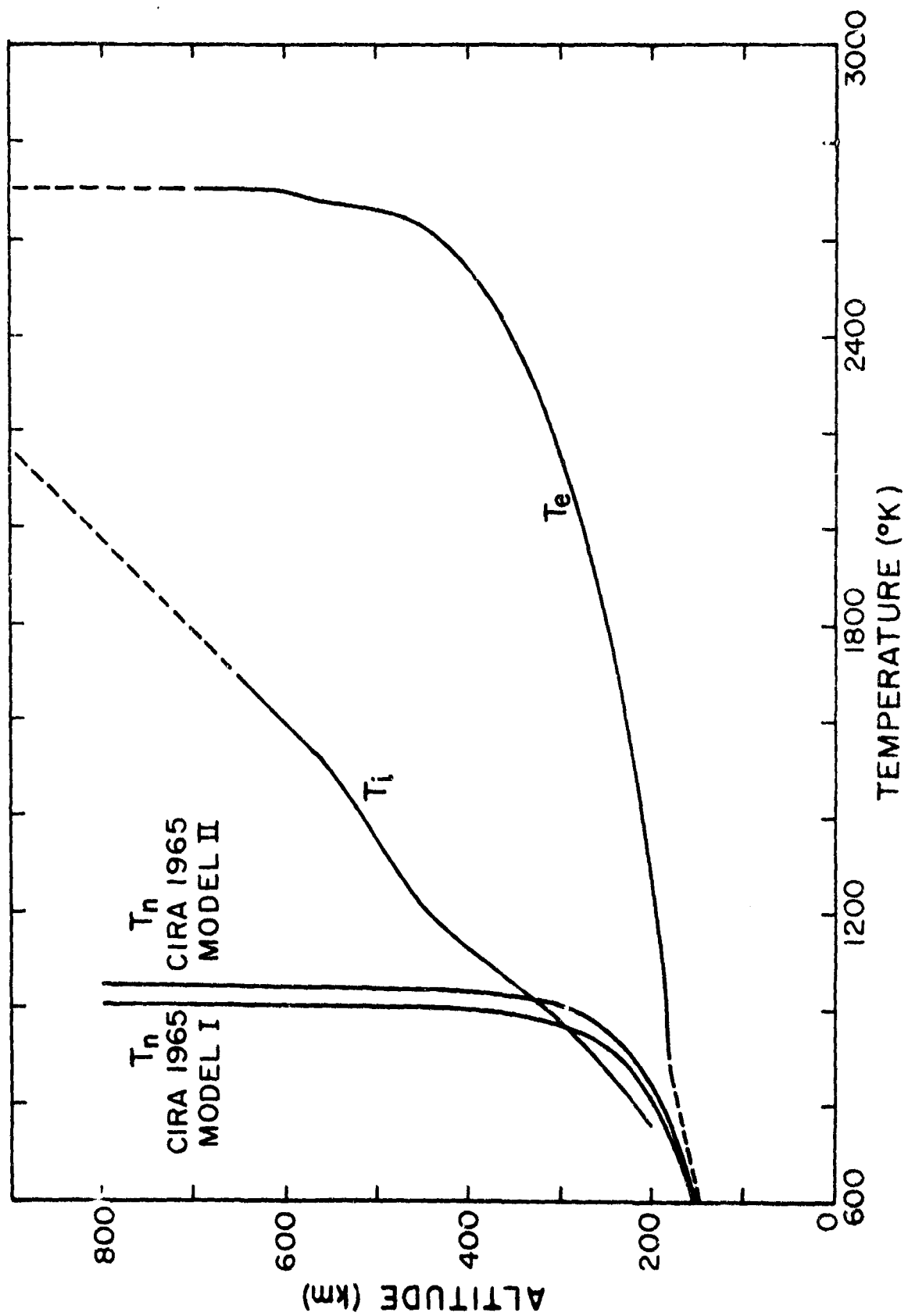


Figure 7. Average electron and ion temperature vs altitude in the F region

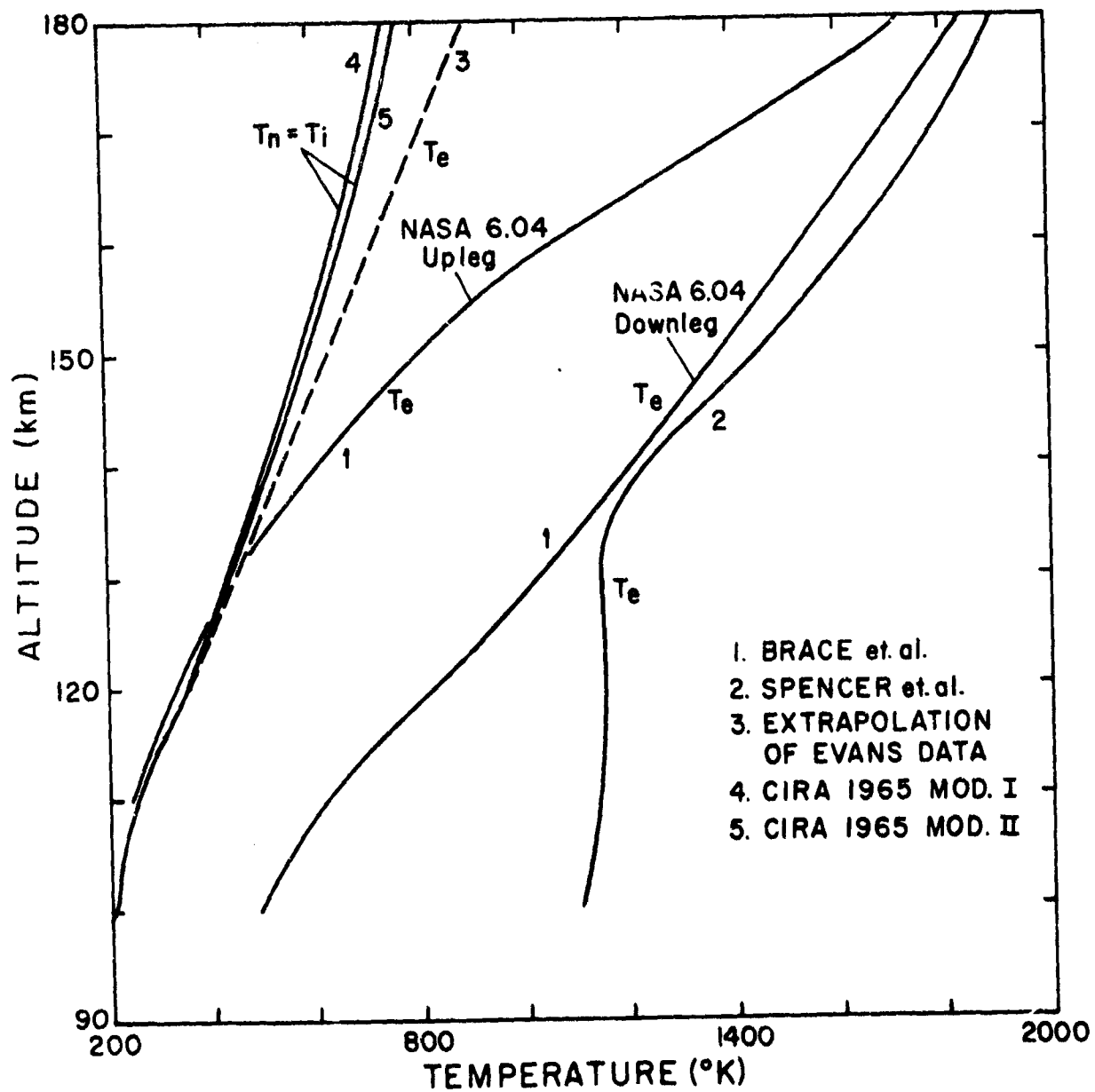


Figure 8. Electron and ion temperature vs altitude in the D & E regions.

The above data indicate a high degree of variability of T_e in the lower regions of the ionosphere. Other data [Nagy et. al., 1963; Aono et. al., 1962; Smith et. al., 1965b] not shown here also substantiate this variability of T_e . Also, the comparison of ascent and descent data (see Fig. 8) from individual flights sometimes reveals large differences in T_e within a time interval of several minutes. This significantly large variation of T_e is not well understood and makes the task of choosing "average" data difficult.

For the sake of consistency we prefer to choose the electron temperatures at these lower altitudes by extrapolating the averaged Evan's data in Fig. 7 down to 120 km where we assume $T_e = T_n$ of the CIRA 1965 model I atmosphere. This assumption is in accord with theory [Dalgarno et. al., 1967; Geisler and Bowhill, 1965 a, 1965b]. Values of T_e and T_n for this altitude range are tabulated in Table 4.

4. Experimental Electron Collision Frequencies and Cross Sections

4.1 Electron Collision Frequencies for Momentum Transfer

In Fig. 9 are reproduced the measured electron collision frequencies for momentum transfer as determined by various investigators. The values given by Benson [1964] were determined with cross modulation experiments at College, Alaska on August 22, 1960, June 29, 1960, and November, 1961. These results agree, within the probable error ($\pm 20\%$), with a formula Benson derived by adding together the collision frequencies in N_2 and O_2 and using the pressure values determined on a rocket flight in July 1957. The values of Jespersen et. al. [1964] were determined in August and December of 1962 from Nike-Cajun rockets (Ferdinand I and II) which were launched from Norway during auroral absorption and which measured the relative amplitude of signals transmitted from the ground and the phase relationship between signals of different frequencies. A marked difference was obtained for the measurements made during the two flights, viz., the highest values were observed during summer. Jespersen et. al. were not sure if this was a seasonal effect or only some variability in the collision frequency values.

Belrose and Burke [1964] obtained collision frequency measurements in 1961 and 1962 at Ottawa, Canada from the recordings of the amplitudes of weak echoes of the ordinary and extraordinary wave components reflected from ionization irregularities. They utilized the Gardner and Pawsey method except that the energy dependence of the collision cross section was employed in the generalized magnetoionic formulas. Belrose and Burke point out that the observed variability in collision frequency data may not be due to a seasonal change but rather a variation with solar activity.

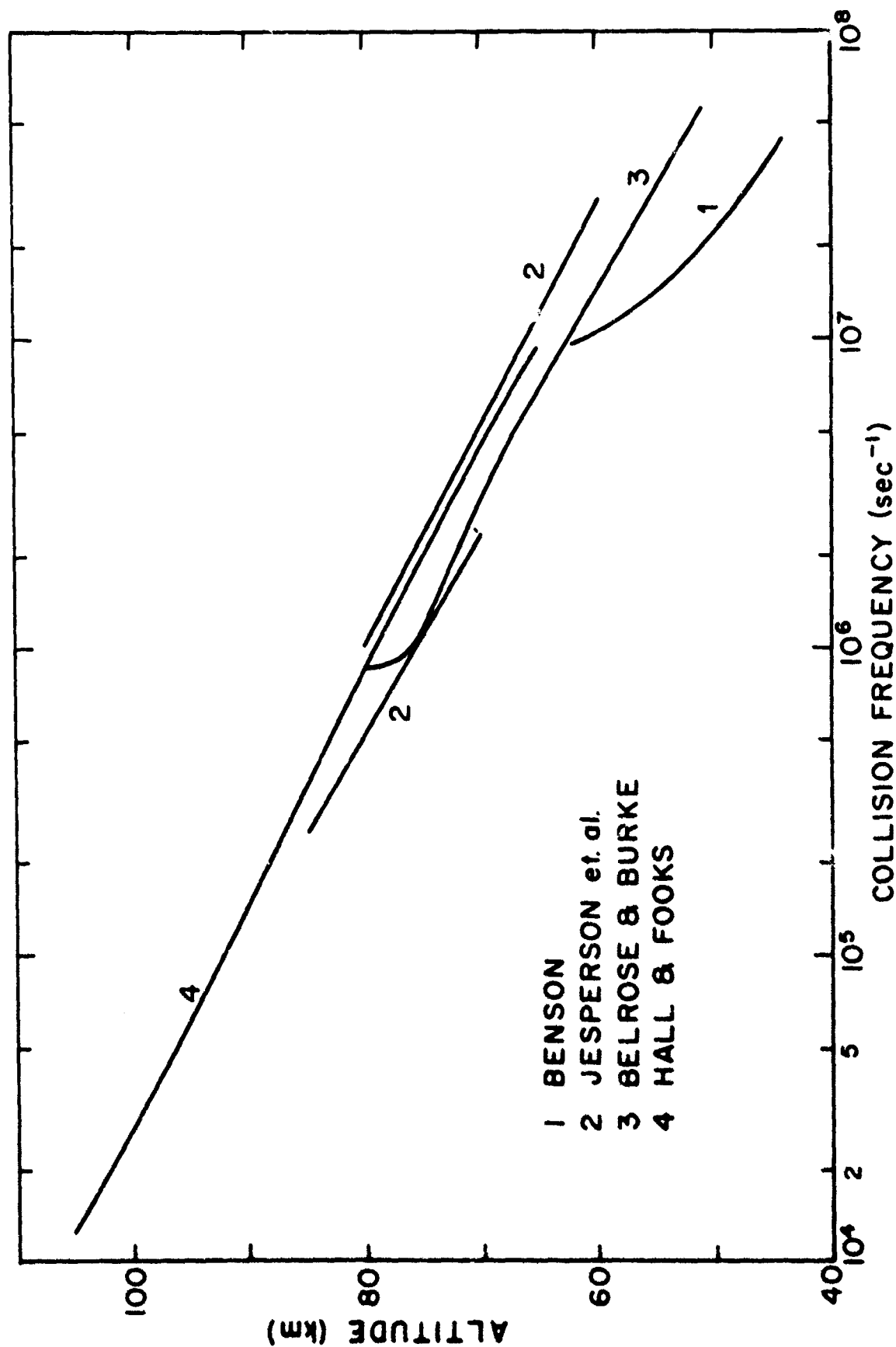


Figure 9. Electron collision frequency for moment transfer vs altitude.

Hall and Fooks [1965] determined the effective electron collision frequency ν_{eff} with a radio propagation experiment on board a Skylark rocket flown from Woomera, Australia (31°S, 137°E, magnetic dip 63°) at 1351 hours LMT on September 20, 1962. Hall and Fooks have taken into account Molmud's [1959] correction for the energy dependence of the collision frequency. At 88 km the collision frequency was calculated from the ratio of the amplitudes of the up-going and reflected parts of the wave transmitted from a ground based transmitter. A curve was then drawn through this point at 88 km and made proportional to air pressure taken from CIRA 1961. Hall's and Fook's values of ν_{eff} must be multiplied by 2/3 to give ν_m , i.e., the collision frequency for mono-energetic electrons of energy KT. The values of ν_m so determined are given in Fig. 9.

Other pertinent data not shown here are those of Salah and Bowhill [1966], Kane [1962], and Landmark [1965].

We choose the data of Hall and Fooks [1965] for our model ionosphere. These values are given in Table 5.

4.2 Electron Cross Sections for Momentum Transfer with Neutral Gases

Inaccurate results yielded by theoretical studies of low energy electron-neutral collision cross sections have necessitated reliance upon experimental measurements of these quantities. Banks [1966b] has made a review of such existing data and has chosen approximate expressions for these cross sections for the energy range appropriate to ionospheric studies. His results are reproduced in Fig. 10. These results were obtained by using an averaging technique described by Banks [1966b].

The largest cross section is associated with H and that of N₂ is the next largest for temperatures greater than about 500°K. The cross sections for He

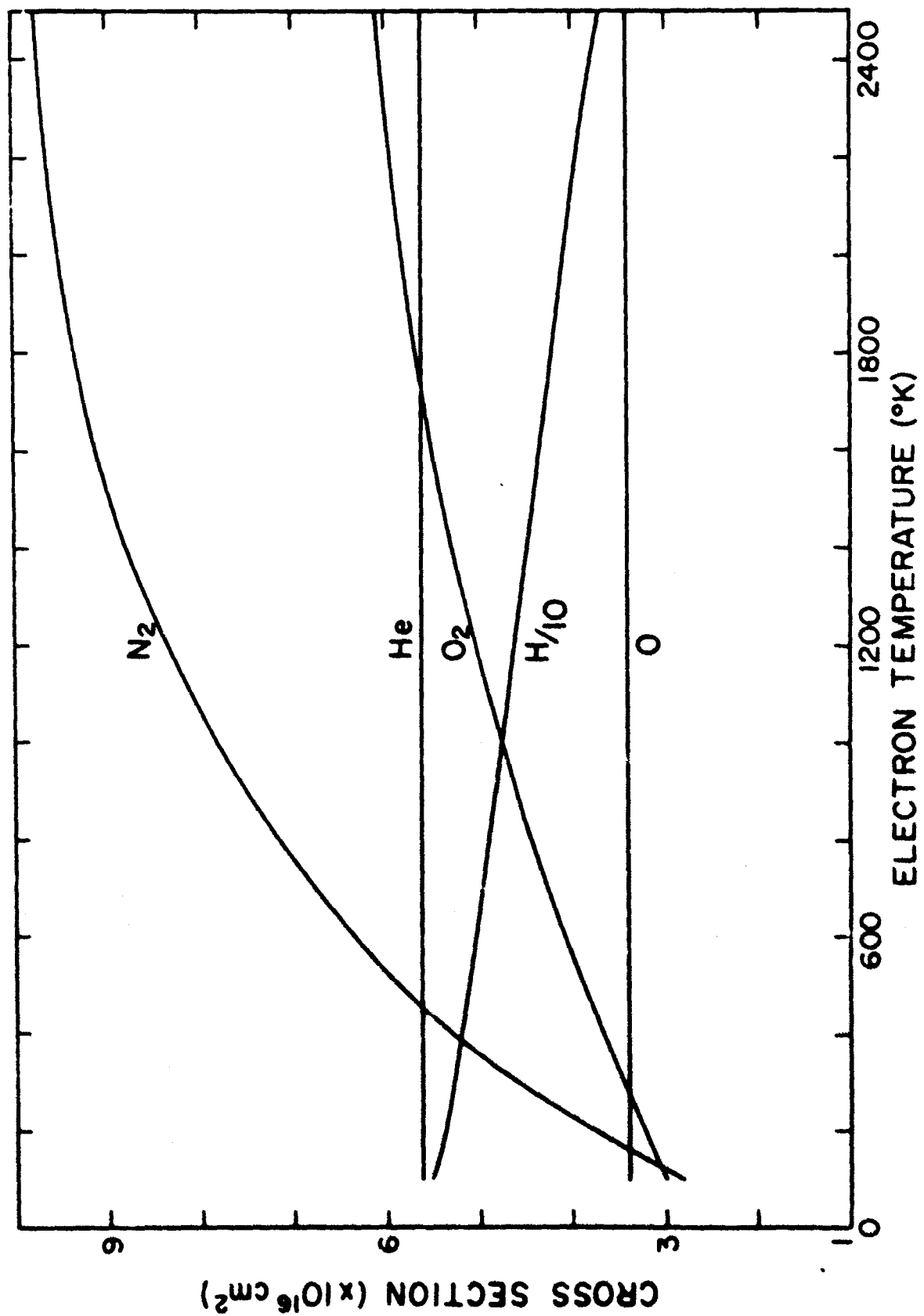


Figure 10. Average momentum transfer cross sections for electrons in neutral gases.

and O are essentially independent of temperature for the temperature range of interest. Banks quotes the uncertainty in \bar{S}_{en} (the velocity averaged electron-neutral cross section) for N_2 and O_2 as being less than 20 per cent. Estimates for the uncertainty in the cross sections for H and O are given by Banks as +25 per cent and +30 per cent, respectively. The cross sections for N_2 , O_2 , and He were based on experimental results whereas the values for O and H were derived from theoretical calculations of scattering phase shifts.

5. Concluding Remarks

No attempt has been made in this report to suggest ionospheric production mechanisms nor to deal with irregularities in ionospheric structure, such as sporadic E. We have also ignored the problem of seasonal variations. Certainly there are seasonal variations in electron and ion densities and in the electron and ion temperatures. There may also be some seasonal variations in the electron collision frequency, although this effect has not yet been resolved. Such simplifying assumptions must be realized when using the data contained herein for problems having a seasonal dependence.

We have attempted to synthesize existing data into a consistent model. Where the experimental data are lacking we have relied on theoretical predictions. For the electron and ion density profiles and the electron collision frequencies, we have referred primarily to the data. For the electron and ion temperatures at altitudes above 1000 km and below 200 km we have been forced to employ theoretical values. Also, the values for the electron cross sections for momentum transfer with atomic oxygen and atomic hydrogen were based on theoretical results.

Ion collision frequencies and cross sections, although important, have not been dealt with in this report. These parameters are considered elsewhere [Shaeffer and Inoue, 1968b].

6. Tables, Model Ionosphere Parameter Data

On the following pages will be found in table form the values of the various model ionosphere parameters obtained from the adopted curves discussed in the previous sections. In addition, the values for the neutral gas densities and neutral gas temperatures from CIRA 1965 Model I atmosphere are tabulated.

TABLE 1.
CHARGED PARTICLE DENSITIES IN THE F REGION

Altitude Km	N_e cm^{-3}	N_i^+ cm^{-3}	$N(\text{O}^+)$ cm^{-3}	$N(\text{NO}^+)$ cm^{-3}	$N(\text{O}_2^+)$ cm^{-3}	$N(\text{N}^+)$ cm^{-3}	$N(\text{He}^+)$ cm^{-3}	$N(\text{H}^+)$ cm^{-3}	$N(\text{H}_2^+)$ cm^{-3}
140	1.20E 05	1.20E 05	4.50E 03	6.00E 04	5.90E 04		4.80E 02		
150	1.40E 05	1.40E 05	1.70E 04	7.00E 04	5.60E 04	1.60E 02	7.50E 02		
160	1.60E 05	1.60E 05	4.00E 04	7.20E 04	5.00E 04	2.80E 02	2.50E 02		
	1.80E 05	1.80E 05	8.50E 04	6.00E 04	4.00E 04	4.30E 02	1.10E 03		
180	2.30E 05	2.30E 05	1.50E 05	4.00E 04	3.00E 04	6.00E 02	1.12E 03		
190	3.00E 05	3.00E 05	2.30E 05	3.00E 04	1.90E 04	8.50E 02	1.13E 03		
200	3.40E 05	3.40E 05	3.00E 05	2.00E 04	1.50E 04	1.20E 03	1.12E 03		
210	4.00E 05	4.00E 05	3.90E 05	1.50E 04	8.50E 03	1.60E 03	1.10E 03		
220	4.80E 05	4.80E 05	4.10E 05	1.00E 04	5.70E 03	1.90E 03	1.10E 03		
230	4.70E 05	4.70E 05	4.40E 05	6.70E 03	4.20E 03	2.40E 03	1.10E 03		
240	4.80E 05	4.80E 05	4.50E 05	4.70E 03	3.30E 03	2.80E 03	1.10E 03		
250	4.60E 05	4.60E 05	4.30E 05			3.30E 03			
300	3.20E 05	3.20E 05	3.00E 05			4.10E 03			
400	1.40E 05	1.40E 05	1.30E 05			4.30E 03	1.40E 03	4.60E 03	
500	7.50E 04	7.50E 04	7.00E 04			4.00E 03	1.80E 03	7.40E 03	
600	4.50E 04	4.50E 04	4.20E 04			3.60E 03	2.10E 03	7.60E 03	
700	3.40E 04	3.40E 04	2.70E 04			3.30E 03	2.70E 03	7.70E 03	
800	2.40E 04	2.40E 04	1.60E 04			2.80E 03	3.40E 03	7.80E 03	
900	1.60E 04	1.60E 04	8.50E 03			1.80E 03	4.30E 03	8.30E 03	
1000	1.30E 04	1.30E 04	4.00E 03			1.00E 03	6.70E 03	9.30E 03	
1100	1.17E 04	1.17E 04	1.90E 03			4.70E 02	8.30E 03	1.10E 04	
1200	9.80E 03	9.80E 03	8.50E 02			2.00E 02	7.50E 03	1.25E 04	
1300	6.70E 03	6.70E 03					6.40E 03		
1400	5.30E 03	5.30E 03					5.30E 03		
1500	4.50E 03	4.50E 03					4.50E 03		
1600	4.00E 03	4.00E 03					4.00E 03		
1700	3.60E 03	3.60E 03					3.60E 03		
1800	3.50E 03	3.50E 03					3.50E 03		
1900	3.45E 03	3.45E 03					3.45E 03		
2000	3.39E 03	3.39E 03					3.40E 03	1.20E 04	
3000	3.88E 03	3.88E 03					3.90E 03	1.90E 04	

TABLE 2.
CHARGED PARTICLE DENSITIES IN THE D AND E REGIONS

Alt km	N_e cm ⁻³	N_1^+ cm ⁻³	N_2^+ cm ⁻³	$N(\text{NO}^+)$ cm ⁻³	$N(\text{O}_2^+)$ cm ⁻³	$N(\text{H}_2^+)$ cm ⁻³	$N(\text{OH}^+)$ cm ⁻³	$N(\text{H}_2\text{O}^+)$ cm ⁻³	$N(\text{H}_3\text{C}^+)$ cm ⁻³	$N(\text{Na}^+)$ cm ⁻³	$N(\text{Ca}^+)$ cm ⁻³	$N(\text{Mg}^+)$ cm ⁻³	$N(\text{Fe}^+)$ cm ⁻³	$N(\text{H}_2\text{O}_2^+)$ cm ⁻³	$N(\text{HCO}^+)$ cm ⁻³	$N(\text{C}_2^+)$ cm ⁻³
52			0.00E 00													
54	5.00E 01	7.00E 01	2.00E 01													
56	7.00E 01	1.40E 02	7.00E 01													
58	1.50E 02	2.30E 02	8.00E 01													
60	1.25E 02	3.50E 02	2.25E 02													
62	7.00E 01	5.00E 02	4.30E 02													
64	4.00E 01	7.40E 02	7.00E 02													
66	5.90E 01	1.10E 03	1.04E 03					2.50E 02						3.00E 02		5.60E 02
68	2.00E 02	1.70E 03	1.50E 03	1.40E 02				3.50E 02						4.00E 02		8.20E 02
70	4.50E 02	2.36E 03	1.91E 03	2.70E 02				4.20E 02						4.70E 02		1.20E 03
72	7.50E 02	2.75E 03	2.00E 03	3.00E 02				4.00E 01	4.20E 02					5.40E 02		1.40E 03
74	8.50E 02	2.95E 03	2.10E 03	3.30E 02				3.20E 01	4.00E 02					6.20E 02		1.55E 03
76	9.50E 02	2.85E 03	1.90E 03	3.65E 02	7.80E 00			2.60E 01	3.65E 02					7.20E 02		
78	1.00E 03	2.40E 03	1.40E 03	4.10E 02	1.00E 01	4.70E 00		2.00E 01	3.00E 02					1.00E 03		
80	1.25E 03	2.10E 03	8.50E 02	4.80E 02	1.40E 01	6.40E 00		1.40E 01	2.20E 02					1.40E 03		
82	1.80E 03	2.00E 03	2.00E 02	6.10E 02	8.30E 01	9.00E 00		1.05E 01	1.50E 02					9.50E 02		
84	1.90E 03	1.94E 03	0.00	1.10E 03	7.10E 02	1.20E 01		5.60E 00	1.70E 01					8.00E 00		
86	3.00E 03	3.00E 03		1.50E 03	1.20E 03	1.50E 01		3.00E 00	1.15E 01	5.70E 01	2.75E 02	3.90E 01	1.60E 01	3.50E 00		
88	3.60E 03	4.60E 03		1.90E 03	1.65E 03	2.00E 01		5.80E 00	9.00E 00	7.40E 01	3.80E 02	5.00E 01	6.30E 01		1.30E 01	
90	5.18E 03	5.48E 03		2.80E 03	2.10E 03	2.40E 01		7.80E 01	7.00E 00	1.20E 02	5.80E 02	8.40E 01	9.30E 01		2.50E 01	
92	1.05E 04	1.08E 04		5.00E 03	3.10E 03	3.00E 01		1.00E 01		6.20E 02	1.70E 03	1.60E 02	2.00E 02		7.00E 01	
94	1.92E 04	1.92E 04		8.20E 03	4.40E 03	3.60E 01		1.25E 01		8.00E 02	5.00E 03	3.80E 02	6.30E 02		1.75E 02	
96	2.63E 04	2.63E 04		1.50E 04	6.00E 03	4.40E 01		1.60E 01		8.20E 02	4.50E 03	3.50E 02	8.00E 02		1.65E 02	
98	3.14E 04	3.14E 04		2.10E 04	8.30E 03	5.40E 01		2.10E 01		3.60E 02	1.80E 03	1.50E 02	3.50E 02		7.00E 01	
100	3.93E 04	3.93E 04		2.70E 04	1.10E 04	6.60E 01		3.10E 01		1.40E 02	6.30E 03		1.00E 01		2.00E 01	
102	4.70E 04	4.70E 04		3.10E 04	1.60E 04	8.20E 01	1.00E 01	4.50E 01		9.00E 01	2.80E 02	3.50E 01	3.30E 01		1.00E 01	
104	5.65E 04	5.65E 04		3.50E 04	2.15E 04	1.00E 02	2.80E 01	7.00E 01		6.60E 01	1.70E 02	2.60E 01	2.40E 01			
106	6.50E 04	6.50E 04		3.70E 04	2.90E 04	2.30E 02	2.50E 01	1.25E 02		6.50E 01	1.70E 02	2.35E 01	2.60E 01			
108	7.60E 04	7.60E 04		3.85E 04	3.70E 04	4.20E 02	1.00E 01	6.40E 01		8.00E 01	4.35E 02	2.80E 01	4.00E 01			
110	8.20E 04	8.20E 04		4.00E 04	4.20E 04	9.50E 02				1.30E 02	3.50E 02	4.90E 01	6.80E 01			
112	9.10E 04	9.10E 04		3.90E 04	4.70E 04	5.00E 03										
114	1.00E 05	1.00E 05		3.80E 04	5.10E 04	5.00E 03										
116	9.70E 04	9.70E 04		3.70E 04	5.50E 04	5.60E 02										
118	9.20E 04	9.20E 04		3.65E 04	5.80E 04	4.50E 02										
120	9.00E 04	9.00E 04		3.70E 04	6.00E 04	4.00E 02										
130	1.00E 05	1.00E 05		4.20E 04	5.95E 04	3.40E 02										

TABLE 3.
NEUTRAL PARTICLE DENSITIES

ALT Km	N(N ₂) cm ⁻³	N(O ₂) cm ⁻³	N(O) cm ⁻³	N(H _e) cm ⁻³	N(A) cm ⁻³	ALT Km	N(N ₂) cm ⁻³	N(O ₂) cm ⁻³	N(O) cm ⁻³	N(H _e) cm ⁻³	N(A) cm ⁻³
52	1.344E 16	3.608E 14			1.606E 14	106	2.950	6.693	3.210	3.886	3.528
54	1.063	2.853			1.274	108	2.174	4.809	2.510	3.656	2.601
56	8.367E 15	2.245			1.002	110	1.620	3.492	2.000	3.450	1.938
58	6.553	1.758			7.851E 13	112	1.164	2.443	1.642	3.171	1.393
60	5.105	1.370			6.117	114	8.606E 11	1.757	1.347	2.934	1.029
62	3.952	1.060			4.735	116	6.513	1.292	1.125	2.731	7.791E 09
64	3.041	8.160E 14			3.644	118	5.057	9.744E 10	9.250E 10	2.554	6.049
66	2.328	6.246			2.789	120	4.008	7.495	7.600	2.400	4.795
68	1.771	4.752			2.122	130	1.455	2.435	3.904	1.889	1.653
70	1.337	3.588			1.602	140	6.378E 10	9.700E 09	2.281	1.565	3.833E 08
72	1.007	2.702			1.207	150	3.140	4.398	1.440	1.333	1.475
74	7.517E 14	2.017			9.007E 12	160	1.691	2.202	9.672E 09	1.164	6.381E 07
76	5.568	1.494			6.671	170	9.757E 09	1.189	6.817	1.036	3.017
78	4.083	1.096			4.892	180	5.928	6.792E 08	4.986	9.359E 06	1.525
80	2.963E 14	7.950E 13	8.500E 10	1.989E 09	3.545	190	3.746	4.051	3.751	8.556	8.108E 06
82	2.072	5.559	8.930	1.391	2.479	200	2.440	2.498	2.883	7.893	4.480
84	1.449	3.888	9.500	9.725E 08	1.734	210	1.627	1.580	2.254	7.334	2.552
86	1.014	2.721	1.015E 11	6.807	1.213	220	1.106	1.020	1.786	6.851	1.489
88	7.095	1.906	1.105	4.761	8.486E 11	230	7.627E 08	6.700E 07	1.431	6.429	8.857E 05
90	4.965	1.332	1.250	3.332	5.939	240	5.326	4.458	1.156	6.055	5.352
92	3.544	9.188E 12	1.680	2.282	4.046	250	3.757	3.000	9.410E 08	5.719	3.277
94	2.349	6.146	2.660	1.568	2.795	300	7.273E 07	4.629E 06	3.610	4.427	3.218E 04
96	1.626	4.296	4.100	1.091	1.945	400	3.514E 06	1.460E 05	6.320E 07	2.834	4.337E 02
98	1.146E 13	2.936	4.800	7.692E 07	1.371						N(H) cm ⁻³
100	8.178E 12	1.994	5.000	5.492	9.800E 10	500	1.979E 05	5.471E 03	1.219	1.873	7.439E 04
102	5.704	1.359	4.760	4.421	6.823	600	1.226E 04	2.284E 02	2.490E 06	1.258	6.729
104	4.060	9.443E 11	4.050	4.138	4.857	700	8.257E 02	1.048E 01	5.331E 05	8.553E 05	6.109

TABLE 4.
ELECTRON, ION, AND NEUTRAL GAS TEMPERATURES

ALT Km	T_c $^{\circ}K$	T_i $^{\circ}K$	T_n $^{\circ}K$	ALT Km	T_c $^{\circ}K$	T_i $^{\circ}K$	T_n $^{\circ}K$
52	265.5	265.5	265.5	106	233.4	233.4	233.4
54	259.9	259.9	259.9	108	242.3	242.3	242.3
56	254.4	254.4	254.4	110	251.1	251.1	251.1
58	248.8	248.8	248.8	112	271.9	271.9	271.9
60	243.3	243.3	243.3	114	292.7	292.7	292.7
62	238.0	238.0	238.0	116	313.1	313.1	313.1
64	232.6	232.6	232.6	118	334.0	334.0	334.0
66	227.3	227.3	227.3	120	355.0	355.0	355.0
68	221.9	221.9	221.9	130	445	437	437
70	216.6	216.6	216.6	140	540	510	510
72	210.5	210.5	210.5	150	630	580	580
74	204.4	204.4	204.4	160	720	644	644
76	198.2	198.2	198.2	170	810	699	699
78	192.1	192.1	192.1	180	900	747	747
80	186.0	186.0	186.0	190	1100	787	787
82	186.0	186.0	186.0	200	1310	821	821
84	185.9	185.9	185.9	210	1400	850	850
86	185.9	185.9	185.9	220	1520	874	874
88	185.9	185.9	185.9	230	1630	895	895
90	185.8	185.8	185.8	240	1730	912	912
92	190.9	190.9	190.9	250	1839	926	926
94	195.9	195.9	195.9	300	2178	985	971
96	200.4	200.4	200.4	400	2541	1121	999
98	204.4	204.4	204.4	500	2665	1356	1006
100	208.1	208.1	208.1	600	2703	1592	1008
102	215.7	215.7	215.7	700	2704	1786	1008
104	224.6	224.6	224.6				

TABLE 5.
ELECTRON COLLISION FREQUENCIES AND AVERAGE CROSS SECTIONS
FOR MOMENTUM TRANSFER

ALT Km	$(\bar{S}_{en})_{N_2}$ 10^{-16}cm^2	$(\bar{S}_{en})_{O_2}$ 10^{-16}cm^2	$(\bar{S}_{en})_H$ 10^{-15}cm^2		ALT Km	$(\bar{S}_{en})_{N_2}$ 10^{-16}cm^2	$(\bar{S}_{en})_{O_2}$ 10^{-16}cm^2	$(\bar{S}_{en})_H$ 10^{-15}cm^2
52	4.30	3.40	5.30		106	4.05	3.30	5.35
54	4.25	3.35	5.30		108	4.10	3.30	5.35
56	4.20	3.35	5.35		110	4.20	3.35	5.35
58	4.15	3.35	5.35		112	4.35	3.40	5.30
60	4.10	3.30	5.35		114	4.50	3.45	5.30
62	4.05	3.30	5.35		116	4.65	3.50	5.25
64	4.05	3.30	5.35		118	4.80	3.50	5.25
66	4.00	3.30	5.35	8.0E 06	120	4.95	3.60	5.25
68	3.95	3.2	5.35	6.0E 06	130	5.55	3.80	5.15
70	3.90	3.25	5.35	4.6E 06	140	6.05	3.95	5.05
72	3.85	3.25	5.35	3.2E 06	150	6.50	4.15	5.00
74	3.75	3.25	5.40	2.3E 06	160	6.85	4.30	4.95
76	3.75	3.25	5.40	1.7E 06	170	7.20	4.45	4.85
78	3.65	3.20	5.40	1.2E 06	180	7.50	4.60	4.80
80	3.60	3.20	5.40	8.6E 05	190	8.10	4.90	4.65
82	3.60	3.20	5.40	6.0E 05	200	8.60	5.20	4.55
84	3.60	3.20	5.40	4.3E 05	210	8.80	5.25	4.50
86	3.60	3.20	5.40	3.0E 05	220	9.00	5.40	4.40
88	3.60	3.20	5.40	2.0E 05	230	9.15	5.50	4.30
90	3.60	3.20	5.40	1.4E 05	240	9.30	5.60	4.25
92	3.65	3.20	5.40	1.0E 05	250	9.40	5.70	4.20
94	3.70	3.20	5.40	7.0E 04	300	9.60	5.90	3.95
96	3.75	3.25	5.40	5.0E 04	400			
98	3.75	3.25	5.40	3.7E 04	500			
100	3.80	3.25	5.35	2.6E 04	600			
102	3.90	3.25	5.35	2.0E 04	700			
104	4.00	3.30	5.35	1.1E 04				

References

- Aono, Y., K. Hirao, S. Miyazaki, Rocket observation of ion density, electron density and electron temperature in the ionosphere, J. Radio Res. Lab., Japan, 9, 407, 1962.
- Banks, Peter M., charged particle temperatures and electron thermal conductivity in the upper atmosphere, Annales De Geophysique, 22, 577, 1966a.
- Banks, Peter M., Collision frequencies and energy transfer. Electrons., Planetary Space Sci., 14, 1085, 1966b.
- Belrose, J.S., I.A. Bourne, and L.W. Hewitt, The winter variability of electron number density in the lower ionosphere over Ottawa. A discussion of results and possible cause, Electron Density Profiles in Ionosphere and Exosphere, ed. by Jon Frihagen, Interscience Publishers, 1966.
- Belrose, J.S., and M.J. Burke, Study of the lower ionosphere using partial reflection. 1. Experimental technique and method of analysis, J. Geophys. Res., 69, 2799, 1964.
- Benson, Robert F., Electron collision frequency in the ionosphere D region, Radio Science, 68 D, 1123, 1964.
- Bourdeau, R.E., A.C. Aikin, and J.L. Donley, The lower ionosphere at solar minimum, J. Geophys. Res., 71, 1966.
- Brace, L.H., N.W. Spencer, and G.R. Carignan, Ionosphere electron temperature measurements and their implications, J. Geophys. Res., 68, 5397, 1963.
- Dalgarno, A., M.B. McElroy, and J.C.G. Walker, The diurnal variations of ionospheric temperatures, Planetary Space Sci., 15, 331, 1967.
- Evans, J.V., A comparison of rocket, satellite, and radar determinations of electron temperature at midlatitudes, J. Geophys. Res., 70, 4365, 1965a.
- Evans, J.V., Ionospheric backscatter observations at Millstone Hill, Planetary Space Sci., 13, 1031, 1965b.
- Evans, J.V., Midlatitude electron and ion temperatures at sunspot minimum, Planetary Space Sci., 15, 1557, 1967a.
- Evans, J.V., Electron temperature and ion composition in the F₁ region, J. Geophys. Res., 72, 3343, 1967b.
- Friedman, H., Proc. Institute Radio Engineers, 47, 2, 1959.

- Geisler, J.E., and S.A. Bowhill, Ionospheric temperatures at sunspot minimum, *J. Atmospheric Terrest. Phys.*, 27, 457, 1965a.
- Geisler, J.E., and S.A. Bowhill, Exchange of energy between the ionosphere and the protonosphere, *J. Atmospheric Terrest. Phys.*, 27, 1119, 1965b.
- Hall, J.E., and Jean Fooks, The electron distribution in the quiet D - region derived from rocket measurements of low-frequency propagation, *Planetary Space Sci.*, 13, 1013, 1965.
- Hanson, W.B., Upper-atmosphere helium ions, *J. Geophys. Res.*, 67, 183, 1962.
- Holmes, J.C., C.Y. Johnson, and J.M. Young, Ionospheric Chemistry, *Space Res.*, 5, 756, 1965.
- Jackson, J.E., and S.J. Bauer, Rocket measurement of a daytime electron-density profile up to 620 kilometers, *J. Geophys. Res.*, 66, 3055, 1961.
- Jespersen, M., O. Petersen, J. Rybner, B. Bjell and, O. Holt, B. Landmark, and J. Kane, Electron and ion density observations in the D region during auroral absorption, *Planetary Space Sci.*, 12, 543, 1964.
- Johnson, C.Y., Ionospheric composition and density from 90 to 1200 kilometers at solar minimum, *J. Geophys. Res.*, 71, 330, 1966.
- Kane, J.A., Re-evaluation of ionospheric electron densities and collision frequencies derived from rocket measurements of refractive index and alternation, *J. Atmospheric Terrest. Phys.*, 23, 338, 1962.
- Landmark, private communication, 1965.
- Mechtly, E.A., S.A. Bowhill, L.G. Smith, and H.W. Knoebel, Lower ionosphere electron concentration and collision frequency from rocket measurements of Faraday rotation differential absorption, and probe current, *J. Geophys. Res.*, 72, 5239, 1967.
- Molmud, P., Langevin equation and the ac conductivity of non-Maxwellian plasmas, *Phys. Rev.*, 114, 29, 1959.
- Nagy, A.F., L.H. Brace, G.R. Carignan, and M. Kanal, Direct measurements bearing on the extent of thermal nonequilibrium in the ionosphere, *J. Geophys. Res.*, 68, 6401, 1963.
- Narcissi, R.S., Ion composition measurements and related ionosphere processes in the D and lower E regions, *Annales De Geophysique*, 22, 224, 1966.

- Nisbet, John S., Thomas P. Quinn, and James Widmaier, Measurements of electron density in the upper ionosphere by propagation measurements between sections of a high altitude rocket, Space Research VII, 422, 1966.
- Oya, H., and T. Obayashi, Rocket measurement of the ionospheric plasma probe, Report Ionosphere Space Res. Japan, 21, 1, 1967a.
- Oya, H., and T. Obayashi, Recombination coefficient of the upper - E and F₁ regions deduced from the electron density profile at sunset measured by rocket borne gyro-plasma probe, Report of Ionosphere and Space Res. in Japan, 21, 9, 1967b.
- Sagalyn, R.C., and M. Smiddy, Electrical processes in the nighttime exosphere, J. Geophys. Res., 69, 1809, 1964.
- Sagalyn, R.C., private communication, 1965.
- Sagalyn, R.C., M. Smiddy, and W.P. Sullivan, Experimental investigation of the nighttime E region, preprint.
- Salah, J.E., and S.A. Bowhill, private communication, 1966.
- Shaeffer, D.L., and Y. Inoue, A model ionosphere for mid-day and mid-latitude during sunspot minimum, SMUP Report No.4, Space Research Coordination Center, University of Pittsburgh, Pittsburgh, Pennsylvania, 1968a.
- Shaeffer, D.L., and Y. Inoue, Theoretical collision frequencies and cross sections for a model ionosphere for mid-day and mid-latitude during sunspot minimum, SMUP Report No. 5, Space Research Coordination Center, University of Pittsburgh, Pittsburgh, Pennsylvania, 1968b.
- Smith, L.G., data from Handbook of Geophysics and Space Environment, ed. by Shea L. Valley, Air Force Cambridge Research Laboratories, 12-5, 1965a.
- Smith, L.G., C.A. Accardo, L.H. Weeks, and P.J. McKinnon, Measurement in the ionosphere during the solar eclipse of 20 July 1963, J. Atmospheric Terrest. Phys., 27, 803, 1965b.
- Smith, C.R., H.C. Brinton, M.W. Pharo, III, and H.A. Taylor, Jr., Lower E-region ion concentration measured at a time of declining solar activity, J. Geophys. Res., 72, 2357, 1967.
- Spencer, N.W., L.H. Brace, G.R. Carignan, D.R. Taeusch, and H. Niemann, Electron and molecular nitrogen temperature and density in the thermosphere, J. Geophys. Res., 70, 2665, 1965.

Taylor, H.A., Jr., H.C. Brinton, and C.R. Smith, Positive ion composition in the magneto-ionosphere obtained from the OGO-A satellite, J. Geophys. Res., 70, 5769, 1965.

Ulwick, J. C., and W. Pfister, Spatial and temporal variations of electron density from an orbiting satellite, Space Research, edited by W. Priester, vol. 3, pp. 194-208, Interscience (John Wiley and Sons), New York, 1963.

Security Classification

DOCUMENT CONTROL DATA - R&D

(Security classification of title, body of abstract and indexing annotation must be entered when the overall report is classified)

1. ORIGINATING ACTIVITY (Corporate author) Space Research Coordination Center University of Pittsburgh Pittsburgh, Pennsylvania 15213		2a. REPORT SECURITY CLASSIFICATION Unclassified
		2b. GROUP
3. REPORT TITLE FULL WAVE SOLUTION FOR THE TRANSMISSION OF ULF AND ELF WAVES THROUGH THE IONOSPHERE		
4. DESCRIPTIVE NOTES (Type of report and inclusive dates) Scientific. Final (1 November 1966 to 30 September 1970)		Approved 7 October 1970
5. AUTHOR(S) (First name, middle initial, last name) Yuji Inoue D. Lynn Shaeffer		
6. REPORT DATE 30 September 1970	7a. TOTAL NO. OF PAGES 245	7b. NO. OF REFS 131
8a. CONTRACT OR GRANT NO. F19628-67-C-0109		9a. ORIGINATOR'S REPORT NUMBER(S) 9b. OTHER REPORT NO(S) (Any other numbers that may be assigned this report) AFCRL-70-0531
b. PROJECT, TASK, WORK UNIT NOS. 5631-16-01		
c. DOD ELEMENT 61102F		
d. DOD SUBELEMENT 601310		
10. DISTRIBUTION STATEMENT 1 - This document has been approved for public release and sale; its distribution is unlimited.		
11. SUPPLEMENTARY NOTES Submitted in partial fulfillment for a Doctorate in Physics, University of Pittsburgh, Pittsburgh, Pennsylvania		12. SPONSORING MILITARY ACTIVITY Air Force Cambridge Research Laboratories (LII) L. G. Hanscom Field Bedford, Massachusetts 01730
13. ABSTRACT Full wave solutions have been found for plane wave and localized disturbances in the ULF (micropulsation) and ELF frequency ranges. Slow and fast wave disturbances incident at 5000 km. altitude at the frequencies 100, 3.0, 1/3, and 1/300 cps. were analyzed. A model ionosphere developed from existing rocket and satellite data for conditions of midday and midlatitude at sunspot minimum was used in the calculations. The cold plasma dispersion relation was written conveniently in terms of the localized disturbance factor and the ionospheric conductivity tensor elements. The localized disturbances were found to produce large vertical electric fields in the neutral atmosphere for the incident slow waves in the micropulsation range and the incident fast wave at 100 cps. Localization causes strong mode coupling in the lower D region and the coupling coefficients are larger than the quartic roots at 1/300 cps. Charge exchange of O ⁺ and O results in an enhanced Pedersen conductivity region which in some cases acts as a cavity wall for wave energy storage. Charge exchange also causes some absorption at Pc1 frequencies in the range 150-250 km. The conductivity of the Earth's surface is included and found to result in almost total reflection at ground level for all frequencies considered. Incident slow mode signals at 3.0 cps. undergo polarization reversal at 1000 km. and then propagate mostly in the E mode through the ionosphere. At 5000 km. plasma drift velocities between 0.1 and 2.0 km/sec. are sufficient for the incident slow waves to excite typical Pc1 and Pc5 ground observed signals.		

Unclassified

Security Classification

14. KEY WORDS	LINK A		LINK B		LINK C	
	ROLE	WT	ROLE	WT	ROLE	WT
Full Wave Solution Hydromagnetic Wave Transmission Micropulsation Transmission Ultra Low Frequency Transmission Extra Low Frequency Transmission Ionospheric Conductivity Model Ionosphere						

Unclassified

Security Classification